

Marquette University

e-Publications@Marquette

Dissertations (1934 -)

Dissertations, Theses, and Professional
Projects

Development of MQCT Method for Calculations of Collisional Energy Transfer for Astrochemistry and Planetary Atmospheres

Bikramaditya Mandal
Marquette University

Follow this and additional works at: https://epublications.marquette.edu/dissertations_mu

 Part of the [Chemistry Commons](#)

Recommended Citation

Mandal, Bikramaditya, "Development of MQCT Method for Calculations of Collisional Energy Transfer for Astrochemistry and Planetary Atmospheres" (2021). *Dissertations (1934 -)*. 1063.
https://epublications.marquette.edu/dissertations_mu/1063

DEVELOPMENT OF MQCT METHOD FOR CALCULATIONS OF COLLISIONAL
ENERGY TRANSFER FOR ASTROCHEMISTRY
AND PLANETARY ATMOSPHERES

by

Bikramaditya Mandal

A Dissertation submitted to the Faculty of the Graduate School,
Marquette University,
in Partial Fulfillment of the Requirements for
the Degree of Doctor of Philosophy

Milwaukee, Wisconsin

May 2021

ABSTRACT
DEVELOPMENT OF MQCT METHOD FOR CALCULATIONS OF COLLISIONAL
ENERGY TRANSFER FOR ASTROCHEMISTRY
AND PLANETARY ATMOSPHERES

Bikramaditya Mandal

Marquette University, 2021

A mixed quantum/classical methodology and an efficient computer code, named MQCT, were developed to model molecular energy transfer processes relevant to astrochemical environments and planetary atmospheres and applied to several real systems. In particular, the rotational energy transfer in $\text{N}_2 + \text{Na}$ collisions was studied with the focus on quantum phase, differential cross-sections, and scattering resonances, and excellent agreement with full quantum results was found. For $\text{H}_2\text{O} + \text{H}_2$, detailed calculations were carried out with the focus on allowed vs. forbidden transitions between the ortho/para states of both collision partners. Again, excellent agreement with full quantum calculations was achieved. Calculations of rotational energy transfer in a collision of two asymmetric-top rotors, a unique capability of this code, were tested using $\text{H}_2\text{O} + \text{H}_2\text{O}$ system where the full-quantum calculations are unfeasible. To make MQCT calculations practical, an approximate, very efficient version of the method was developed, in which the classical-like equations of motion for the translational degrees of freedom (scattering) are decoupled from the quantum-like equations for time-evolution of the internal molecular states (rotational, vibrational). The code MQCT was made publicly available to serve as an efficient computational tool for other members of the community. It can perform scattering calculations on larger molecules and at higher collision energy than it is currently possible with full quantum methods and codes. To study the rotational quenching of isotopically substituted sulfur molecules, such as $^{32}\text{S}^{32}\text{S}$, $^{32}\text{S}^{34}\text{S}$, and $^{34}\text{S}^{34}\text{S}$, a new accurate potential energy surface was developed for $\text{S}_2 + \text{Ar}$ system. Rotational state-to-state transition cross sections were computed using MQCT, and the master equation modeling of energy transfer kinetics was carried out. It is found that isotopically substituted asymmetric molecules such as $^{32}\text{S}^{34}\text{S}$ promote energy transfer due to symmetry breaking and transitions with odd Δj that become allowed. This process may be responsible for mass-independent isotopic fractionation of sulfur isotopes, typical to the Archean surface deposits.

ACKNOWLEDGEMENTS

Bikramaditya Mandal

I would like to express my sincere gratitude to my advisor, Prof. Dmitri Babikov, for giving me the opportunity to show my potential, supporting me always in every situation, helping me in solving research problems, and mentoring me. It would not have been possible without him to make my infinitesimal contribution towards the scientific community.

I would like to thank my committee members, Prof. Scott Reid, Prof. Jier Huang, and Prof. Nicholas Reiter, for their important suggestions to make the quality of my research better. I would also like to thank Prof. Marie-Lise Dubernet and Dr. Alexander Semenov for collaborating and for all their help. I express my gratitude towards Prof. Dmitri Babikov, Prof. Jier Huang, and Prof. Satish Puri for their time to write recommendation letters for me. My thanks to other group members, Alex, Igor, Liza, Dulat, and Carolin.

My sincere thanks to the Eisch family for supporting my research in the last year of PhD. I am honored to be an Eisch fellow. I am also very thankful to the Denis J. O'Brien Fellowship program for supporting my research during Summer 2019. I would also like to acknowledge other financial support, such as Prof. Babikov's grants, Chemistry Department for Teaching Assistantship, and National Energy Research Scientific Computing Center (NERSC) for providing computational resources.

I would like to thank my parents. It would not have been possible to achieve my goals without their lifelong sacrifices, tremendous support, and endless encouragement. I would also like to thank my wife overseas for being with me virtually in every situation and bearing with me.

I would like to express my special thanks to all my friends from India. Especially Arindam, Prasanta, Saumyen, Animesh, Suman, and Aakash. Thanks to all my family relatives for all their contribution in my life. I would also like to acknowledge my friends at the university, Jaydev, Niloufar, Anmol, Nazmus, and Banabithi di.

Finally, a warm thank you to the Marquette University, particularly the Chemistry Department, for everything.

TABLE OF CONTENTS

ACKNOWLEDGEMENTS	i
LIST OF TABLES	vi
LIST OF FIGURES	vii
CHAPTER 1. INTRODUCTION	1
1.1. Significance of the Collisional Energy Transfer.....	1
1.2. Computational Methodologies to Study Collisional Energy Transfer.....	2
1.3. Mixed Quantum/Classical Theory (MQCT) of Energy Transfer	4
1.4. Motivation to Study Energy Transfer in Sulfur Recombination.....	6
1.5. Theoretical Studies of Sulfur Recombination.....	12
1.6. Objectives and Structure of This Dissertation	16
CHAPTER 2. DEVELOPMENT AND TESTING OF A USER-READY PROGRAM FOR CALCULATIONS OF INELASTIC SCATTERING OF TWO MOLECULES	20
2.1. Introduction.....	20
2.2. Three Components of the Input	24
2.2.1. Quantum Degrees of Freedom, Block \$BASIS	26
2.2.2. Classical Degrees of Freedom, Block \$SYSTEM.....	28
2.2.3. Potential Energy Surface Block \$POTENTIAL	30
2.3. Efficient Use of the Code.....	32
2.3.1. Compiling and Running the Code.....	32
2.3.2. Understanding the Output	35
2.3.3. Random Sampling of the Initial Conditions	37
2.3.4. Convergence Studies.....	38
2.3.5. Propagation Options.....	40
2.4. Special Cases of MQCT.....	41

2.4.1. Vibrational States and Transitions	41
2.4.2. Differential Cross Sections and Elastic Scattering	42
2.4.3. Trajectory Analysis and Resonances	43
2.5. Summary	45
2.6. MQCT User Guide for Experts	47
2.6.1. Input Parameters for MQCT calculations	47
2.6.2. Description of user-supplied data files and the corresponding subroutines	55
2.6.3. Options for PES representation and computation of the transition matrix	56
2.6.4. Expansion of the PES over the basis set of analytic functions	58
2.6.5. Computation of coupling matrix and/or potential expansion over the basis set	61
2.6.6. User-supplied PES subroutine	65
CHAPTER 3. APPLICATION OF MQCT TO STUDY ROTATIONAL INELASTIC SCATTERING OF $\text{H}_2\text{O} + \text{H}_2$ AND $\text{H}_2\text{O} + \text{H}_2\text{O}$ COLLISIONS	67
3.1. Introduction	67
3.2. Theoretical Framework	69
3.2.1. MQCT Classical and Quantum Equations	69
3.2.2. Molecular Symmetry	72
3.2.3. Collisions of Identical Molecules	73
3.3. Results	75
3.3.1. Comparison of CC-MQCT with Full Quantum results for $\text{H}_2\text{O} + \text{H}_2$	75
3.3.2. Scattering Calculation of $\text{H}_2\text{O} + \text{H}_2\text{O}$	79
3.4. Summary	83
CHAPTER 4. CALCULATIONS OF DIFFERENTIAL CROSS SECTIONS USING MIXED QUANTUM/CLASSICAL THEORY OF INELASTIC SCATTERING	84

4.1. Introduction.....	84
4.2. Theoretical Approach.....	87
4.2.1. Traditional Approach for Continuous Sampling of Initial Conditions	87
4.2.2. Improved Sampling Method Using Integer Values of J for the Differential Cross Sections	90
4.2.3. Integral Cross Sections Using New Approach.....	92
4.2.4. Description of the Scattering Phase by MQCT Method	94
4.2.5. Inelastic Differential Cross Section Using MQCT	96
4.3. Results and Discussion	98
4.3.1. Elastic Cross Sections for Na + N ₂	98
4.3.2. Resonances at Low Collision Energies	105
4.3.3. Inelastic Cross Sections for Na + N ₂	107
4.4. Summary	110
CHAPTER 5. ADIABATIC TRAJECTORY APPROXIMATION WITHIN THE FRAMEWORK OF MIXED QUANTUM/CLASSICAL THEORY	113
5.1. Introduction.....	113
5.2. Theory	117
5.2.1. Adiabatic Trajectory Approximation.....	117
5.2.2. Adiabatic Step-Size Predictor	121
5.3. Results.....	125
5.3.1. Comparison of AT-MQCT vs CC-MQCT.....	126
5.3.2. Comparison of AT-MQCT vs full-quantum CC method.....	130
5.3.3. Time-dependent insight from AT-MQCT	133
5.4. Discussion	135
5.4.1. Numerical speed-up	135

5.4.2. On a hierarchy of the approximate MQCT methods	138
5.5. Summary	142
CHAPTER 6. ON SYMMETRY-BREAKING IN THE RECOMBINATION REACTION OF TWO SULFUR ATOMS: ROTATIONAL ENERGY TRANSFER ...	144
6.1. Introduction.....	144
6.2. Potential Energy Surface.....	145
6.2.1. <i>Ab Initio</i> Calculations of Pair Interactions for S ₂ and Ar + S	145
6.2.2. <i>Ab Initio</i> Calculation for the Three-Atom System S ₂ + Ar.....	153
6.2.3. Calculation of the Three-Body Interaction Term.....	156
6.2.4. Representation of the Three-Body Term by Fitting.....	162
6.2.5. Representation of the Three-Body Term by Spline Interpolation .	164
6.2.6. The Global 3D PES for the Reaction S + S + Ar → S ₂ + Ar.....	169
6.3. Study of the Rotational Energy Transfer	171
6.3.1. Inelastic Scattering Cross-Sections for Isotopically Substituted S ₂	171
6.3.2. Rotational Energy Transfer Model	176
6.3.3. Kinetics of Energy Transfer and Symmetry-Driven Isotope Effect	180
6.4. Summary	184
CHAPTER 7. SUMMARY AND FUTURE WORK	186
BIBLIOGRAPHY	196

LIST OF TABLES

Table 1. Summary of research on sulfur recombination reaction.	15
Table 2. Types of systems handled by MQCT, with required and optional input data. ...	26
Table 3. Description of keywords for the block \$BASIS	48
Table 4. Description of keywords for the block \$SYSTEM.	51
Table 5. Description of keywords for the block \$POTENTIAL	53
Table 6. Description of the input data files for MQCT calculations.	55
Table 7. Degrees of freedom in the user-supplied PES subroutine.	66
Table 8. Computational speed-up due to employment of the adiabatic step-size predictor in the AT-MQCT calculations, at different values of the kinetic energy of collision, for H ₂ O + H ₂ system.	136
Table 9. Fitting of the <i>ab initio</i> data to obtain the spectroscopic and geometric parameters for S ₂ molecule.	147
Table 10. Computed spectroscopic and thermochemical parameters of the S ₂ molecule.	148
Table 11. Fitting of the <i>ab initio</i> data to obtain the spectroscopic and geometric parameters for S + Ar interaction.	151
Table 12. Computed spectroscopic and thermochemical parameters of the minimum energy point of the S–Ar interaction.	152
Table 13. Morse parameters representing the interaction of S–Ar.	159
Table 14. Fitting parameters for the cross sections of quenching wing of S ₂ molecules.	177
Table 15. Fitting parameters for the cross sections of excitation wing of S ₂ molecules.	178

LIST OF FIGURES

Figure 1: Classical and quantum components of the mixed quantum/classical treatment of molecule-molecule inelastic scattering. Picture is taken from the Journal of Physical Chemistry A.....	5
Figure 2: A volcanic eruption. Taken from the United States Geological survey, downloaded from inhabitat.com.	7
Figure 3: In the year 2000, an active volcanic eruption was observed on Io, a moon of Jupiter. This image was taken from NASA's Galileo spacecraft.	8
Figure 4: Two different pathways of sulfur reactions depending on the abundance of oxygen in the atmosphere. The horizontal axis represents oxidation and reduction states of sulfur. The picture is taken from Ref. 28 by Kasting <i>et al.</i>	9
Figure 5: Performance of MQCT in terms of parallelism. The figure represents the time complexity.....	35
Figure 6: Cross sections for quenching of the excited rotational state 2_{11} of H_2O onto the lower levels: 0_{00} , 1_{11} , and 2_{02} . Black and blue lines represent the elastic H_2 channels with $j_2 = 0$ and $j_2 = 2$, respectively. Red line represents excitation of H_2 from $j_2 = 0$ to $j_2 = 2$ while green line describes quenching of H_2 from $j_2 = 2$ to $j_2 = 2$. Results of MQCT are indicated by symbols; full-quantum results of MOLSCAT are shown by lines.....	75
Figure 7: Cross sections for excitation of the ground state para- H_2O (0_{00}) and ortho H_2O (1_{01}) by para- H_2 ($j_2 = 0, 2$) and ortho- H_2 ($j_2 = 1$). Upper row is for para- H_2O , lower row is for ortho- H_2O . The final state of water is indicated in each frame, while the initial and final states of H_2 are listed along the horizontal axis. Results of MQCT are in red; full-quantum results of MOLSCAT are in blue.....	78
Figure 8: Comparison of results of the semi-classical method (red) vs. those obtained using MQCT method (black) for para- H_2O (left) and ortho- H_2O (right). Thermal distribution of the rotational states in the quencher H_2O and the collision energy corresponds to $T = 800$ K.....	81
Figure 9: Differential cross sections for the elastic scattering channel of N_2 ($j = 0$) + Na at three collision energies: a) $E = 50 \text{ cm}^{-1}$; b) 100 cm^{-1} ; and c) 700 cm^{-1} . Full-quantum data from Ref. 56 are shown by red line, whereas MQCT results are shown by black line (obtained using the older semiclassical sampling approach, with randomly generated non-integer values of l).	86
Figure 10: A set of MQCT trajectories for $E = 16 \text{ cm}^{-1}$, which is the highest collision energy at which one can observe orbiting in the N_2 ($j = 0$) + Na system. This trajectory ($l^* = 31$) is shown by red line. Trajectories with larger impact parameters are green, while trajectories with smaller impact parameters are blue. Here all values of l are integer.....	97

Figure 11: Same as Figure 9 but with MQCT trajectories generated for all integer values of orbital angular momentum l , just as in quantum mechanics. 99

Figure 12: Deflection function (upper frame) and the total phase (lower frame) from MQCT calculations for several values of scattering energy. Red, green, blue & violet lines correspond to $E = 16 \text{ cm}^{-1}$, 50 cm^{-1} , 100 cm^{-1} and 700 cm^{-1} , respectively. In the case of $E = 16 \text{ cm}^{-1}$ the orbiting trajectory is found at $l^* = 31$, where the value of deflection angle is undefined. To compute the phase for this energy, the resonance was “removed”, by linear interpolation of the deflection angle between two neighboring points ($l = 30$ and $l = 32$, where the deflection angle is defined). The phase dependence computed in this way for $E = 16 \text{ cm}^{-1}$ looks rather smooth..... 101

Figure 13: Energy dependence of integral cross section for the elastic scattering channel of $\text{N}_2 (j = 0) + \text{Na}$ in a broad range of energies (a), and in the low-energy scattering regime dominated by resonances (b). Full-quantum data from Ref. 56 are shown by red line, whereas MQCT results are shown by blue line. The spikes in MQCT data are due to looping trajectories, while the gaps (indicated by green arrows) are due to orbiting trajectories. The corresponding values of l are indicated under each gap or spike. Here all values of l are integer. 102

Figure 14: Same as Figure 13 but obtained using single-state MQCT calculations for the elastic scattering process. This is an approximate way of computing the elastic cross section. 103

Figure 15: Same as Figure 11 but obtained using single-state MQCT calculations for the elastic scattering process. This is an approximate way of computing the elastic cross section. 104

Figure 16: Energy dependence of excitation cross sections for $\text{N}_2 (j = 0) + \text{Na}$ in a broad range of energies (a), and in the low-energy scattering regime dominated by resonances (b). Three allowed transitions are indicated on the graph. Full-quantum data from Ref. 56 are shown by red line, whereas MQCT results are in blue. The gaps in blue line correspond to orbiting trajectories, where the final state populations are undefined. These gaps are filled with green line, obtained by averaging state populations over several periods. ... 108

Figure 17: Differential cross sections for inelastic scattering channel into $\text{N}_2 (j = 2)$, starting from $\text{N}_2 (j = 0)$, at two collision energies with Na atom: a) $E = 40 \text{ cm}^{-1}$, and b) 700 cm^{-1} . Full-quantum data from Ref. 56 are shown by red line, whereas MQCT results are shown by blue line..... 111

Figure 18: Comparison of results of the new approximate AT-MQCT method (green dots) against the full-coupled CC-MQCT calculations (red symbols) for the initial state $0_{00}0$ of the $\text{H}_2\text{O} + \text{H}_2$ system. Final states are listed along the horizontal axis. The values of collision cross sections are plotted along the vertical axis using log scale. Eight frames correspond to eight values of the kinetic energy, as indicated. Twenty rotational states of the basis include both ground and excited rotational states of H_2 127

Figure 19: Same as Fig. 1, but for the initial state $1_{11}0$ of the $\text{H}_2\text{O} + \text{H}_2$ system, which is first excited rotational state. 128

Figure 20: Comparison of results of the new approximate AT-MQCT method (empty circles, solid line) against the full-coupled CC-MQCT calculations (filled symbols, dashed lines) for the initial state $0_{00}0$ of the $\text{H}_2\text{O} + \text{H}_2$ system. The values of collision cross sections are plotted along the vertical axis using log scale. Kinetic energy of collision (including Billing's correction) is plotted along the horizontal axis. Color corresponds to five different final rotational states, as indicated in the picture. Excitation thresholds are shown by the vertical dashed lines. 129

Figure 21: Same as Fig. 3 but for the first excited state $1_{11}0$ of H_2O as the initial channel. 130

Figure 22: Comparison of results of the new approximate AT-MQCT method (dashed lines) against the full-coupled quantum calculations (solid lines) of Ref. [42] for the $\text{H}_2\text{O} + \text{H}_2$ system. The values of collision cross sections are plotted along the vertical axis, while the kinetic energy of collision is plotted along the horizontal axis, both in log scale. Black, red, green, and blue color is for $0 \rightarrow 0$, $0 \rightarrow 2$, $2 \rightarrow 0$ and $2 \rightarrow 2$ transitions in H_2 , respectively. In H_2O the transitions are from state 2_{11} to states: 1a) 0_{00} , 1b) 1_{11} , 1c) 2_{02} ; from state 3_{22} to states: 2a) 0_{00} , 2b) 1_{11} , 2c) 2_{11} ; from state 4_{40} to states: 3a) 1_{11} , 3b) 3_{11} , 3c) 5_{24} 132

Figure 23: Time evolution of state probabilities along a typical MQCT trajectory (see text) that indicate a direct exchange of populations between the excited water state and the excited hydrogen state – a quasi-resonance energy exchange process $4_{40}0 \rightarrow 1_{11}$ 134

Figure 24: Comparison of results of the single-state AT-MQCT method (green bars) with calculations where seven rotational states are included in the trajectory prediction (blue bars), and with the full-coupled CC-MQCT calculations in a basis of twenty rotational states (red bars). The initial state is the ground state $0_{00}0$ of the $\text{H}_2\text{O} + \text{H}_2$ system. Collision energy is 200 cm^{-1} . Final states are listed along the horizontal axis. The values of collision cross sections are plotted along the vertical axis using log scale. 140

Figure 25: Potential energy curve of S_2 molecule computed using MRCI/aug-cc-pV(5+d)Z method is shown by the red line while the blue line represents the one computed with CCSD(T)-F12/VTZ-F12 method. The green line with circle is the S_2 curve computed by CCSD(T)-F12/VTZ-F12 method from three atom calculations of $\text{S}_2 + \text{Ar}$ system with Ar moved to a distance of 33.0 Bohr. 146

Figure 26: The red line represents the potential energy curve of $\text{S}-\text{Ar}$ interaction computed by CCSD(T)/aug-CC-pV(5+d)Z method and blue line represents the potential interaction computed by CCSD(T)-F12/VTZ-F12 method.. The green line is representing the analytic fit of the $\text{S}_2 + \text{Ar}$ data as discussed in section 6.2.3. 150

Figure 27: Jacobi coordinates of $\text{S}_2 + \text{Ar}$ system. Here, r is the distance between two sulfur atoms, R is the distance of argon atom from the geometric center of S_2 , and α is the angle of approach. 153

Figure 28: Potential energy surface of the $S_2 + Ar$ system in two degrees freedom. The S_2 bond distance is set fixed for this case at its equilibrium distance of 3.59 Bohr. The global minimum energy point was found to be in T-shaped geometry and the energy of this point is $V = -210.5 \text{ cm}^{-1}$ and the local minimum energy point was at linear geometry with energy $V = -166.1 \text{ cm}^{-1}$ 154

Figure 29: Potential energy surface of the $S_2 + Ar$ system with two degrees freedom. The S_2 bond distance is set fixed for this case at its equilibrium distance of 3.59 Bohr. The minimum energy point at T-shaped geometry and small wells at linear geometry is better reflected in this figure. 155

Figure 30: Slices of the three-body term $U_{3b}(R)$ were computed following the methodology of Peterson and co-workers is shown here. Black, green, red, and blue symbols correspond different S_2 distance: $r = 3.0, 4.0, 5.0$, and 6.0 Bohr respectively. Three different lines for each color corresponds to three different angles of approach: $\alpha = 0^\circ, 45^\circ$ and 90° 158

Figure 31: Three-body terms computed following our methodology. Here again, black, green, red, and blue lines correspond different S_2 distance, $r = 3.0, 4.0, 5.0$ and 6.0 Bohr respectively and three different lines for each color corresponds to three different angles of approach, $\alpha = 0^\circ, 45^\circ$ and 90° 160

Figure 32: Graphical representation of the coordinates for the fitting function. 163

Figure 33: The fitted three-body term for the $S_2 + Ar$ system. The divergence behavior in linear configuration can be seen here. Black, green, red, and blue lines correspond different S_2 distance, $r = 3.0, 4.0, 5.0$ and 6.0 Bohr respectively. Three different lines for each color corresponds to three different angles of approach, $\alpha = 0^\circ, 45^\circ$ and 90° 164

Figure 34: Dependence of kernel on the grid of coordinate. A schematic representation is also provided to determine $r_<$ and $r_>$ 165

Figure 35: The reproducing kernel q_1 for the distance coordinate r . The kernel q_2 for the distance coordinate R is exactly the same. 167

Figure 36: The reproducing kernel q_3 for the angle like coordinate S , where $S = (1 + \cos\alpha)/2$ 167

Figure 37: The fitted three-body term for the $S_2 + Ar$ system. Black, green, red, and blue lines correspond different S_2 distance, $r = 3.0, 4.0, 5.0$ and 6.0 Bohr respectively. Three different lines for each color corresponds to three different angles of approach, $\alpha = 0^\circ, 45^\circ$ and 90° . The behavior is same for all slices. 168

Figure 38: Potential energy surface of the $S_2 + Ar$ system with all degrees of freedom. The dependence of potential on S_2 bond distance can be seen on the top surface of the figure. 170

Figure 39: Energy transfer of rotationally excited S_2 molecule at initial rotational level $j = 51$ as a function of final rotational state (a) and final rotational energy (b). 172

Figure 40: Energy transfer of rotationally excited S_2 molecule for initial rotational level $j = 51, 41, 31$, and 21 in black, blue, green, and red respectively as a function of Δj ... 173

Figure 41: Same as Figure 40, but for isotopically substituted symmetric rotationally excited S_2 molecule $^{34}S^{34}S$ 174

Figure 42: Energy transfer of rotationally excited asymmetric S_2 molecule ($^{32}S^{34}S$) for initial rotational level $j = 21$ as a function of shift of final rotational state is shown here by green, while blue and red represents symmetric S_2 molecule $^{32}S^{32}S$ and $^{34}S^{34}S$, respectively. 175

Figure 43: Analytic representation of the energy transfer of rotationally excited S_2 molecule ($^{32}S^{32}S$) for initial rotational level $j = 51, 41, 31$, and 21 in black, blue, green, and red respectively as a function of Δj . The orange line represents the analytic fit. 179

Figure 44: Analytic representation of the energy transfer of rotationally excited symmetric S_2 molecule ($^{34}S^{34}S$) as Figure 43. 180

Figure 45: Analytic representation of the energy transfer of rotationally excited asymmetric S_2 molecule $^{32}S^{34}S$. The left frame and right frame represent data for even and odd Δj values respectively. 180

Figure 46: Decay of initially populated rotational state $j = 51$. Red, green, and blue line represents $^{32}S^{32}S$, $^{32}S^{34}S$, and $^{34}S^{34}S$ molecule. 182

Figure 47: Comparison of energy relaxation for several isotopic composition of S_2 molecule. Red, green, and blue line represents $^{32}S^{32}S$, $^{32}S^{34}S$, and $^{34}S^{34}S$ molecule. 183

Figure 48: Comparison of complexity of calculations as performed by different codes and methods. The full-quantum code, MOLSCAT, can perform calculations for collision of two water molecules in several months. The CC-MQCT method outperforms MOLSCAT easily and extend the opportunity for users. Finally, the AT-MQCT, as the most efficient methodology, can perform efficiently quite heavy calculations in reasonable amount of time. 187

Figure 49: Comparison of thermally averaged cross-sections obtained by the AT-MQCT (blue) vs. the CC-MQCT method (red) for para- H_2O (left) and ortho- H_2O (right). 191

CHAPTER 1. INTRODUCTION

1.1. Significance of the Collisional Energy Transfer

Inelastic molecular collisions represent a fundamental chemical/physical process,¹ in which the energetically excited molecule in a bath gas exchanges its internal energy with quenchers and finally gets stabilized. The process describes energy transfer between an energetically excited molecule colliding with a quencher, which involves all degrees of freedom, i.e., rotational, vibrational and translational. The energy transfer during an inelastic molecular collision is important in many chemical phenomena like recombination reactions,^{2,3} reactivity of metastable intermediates,^{4,5} enthalpy released by chemical bonds,⁶ photochemistry,⁷ astrochemistry,^{8,9} atmospheric chemistry,^{10,11} in combustion,^{12,13} or in the reaction of ultracold temperature.^{14,15} If the rates of the state-to-state energy transfer processes are known, then many quantitatively accurate predictions about the course of collision dynamics, and about its final result/state, can be made.

First example is the analysis of spectra from a variety of astrochemical environments. The collisional rate coefficients are used as input to analyze the radiative processes in the interstellar medium (ISM) and other cosmic objects.⁶ Analysis of such spectra is crucial for predictions of physical properties of the ISM, such as pressure, temperature, and density, and its chemical composition. This analysis is also very important for understanding evolution of the atmosphere. The modeling of gas-phase recombination reactions helps to find exoplanets with chemical composition/conditions similar to Earth's atmosphere, thus providing crucial information for understanding the

chemical origin of life using molecular signatures. Laboratory experiments are extremely limited in providing this information.

Combustion, such as flames and chemical reactions, is another example of a highly reactive chemical environment where the collisional energy transfer plays an important role in kinetics. The energy released during the bond formation excites the internal states (rotation and vibration), and finally is transferred to the translational motion of the molecules.

The next field of research where inelastic collision plays a crucial role is ultracold physics. This field, the study of collisional energy transfer reactions at ultra-cold conditions of molecular traps, is another hot topic these days. This research is crucial for testing, and eventually employing, the fundamentals of quantum physics, such as quantum computing and communication.

It is rather challenging to study this process near the dissociation threshold since the highly excited molecule exhibits large amplitude of vibrational motion. Also, there is a strong coupling between vibrational and rotational degrees of freedom. Finally, in this situation, scattering resonance, such as Feshbach resonance (when two molecules are trapped together and never leaves the interaction region) or shape resonance (due to quantum tunneling), is a common phenomenon.

1.2. Computational Methodologies to Study Collisional Energy Transfer

Study of this process with classical trajectory method is sometimes implemented to understand the dynamics of collisional energy transfer. But the classical dynamics does not have any quantization of states, so it cannot provide any state specific details of

energy transfer process. It provides only a rough picture. People employ the classical method because it is computationally affordable. However, in some cases, it has other problems as well. The most important issue is the leakage of the vibrational zero-point energy. This could significantly change the collision dynamics near the dissociation threshold. Although, classical trajectory can describe the Feshbach resonance when two molecules are trapped together by exchange of translational and internal (rotational and vibrational) energy. But it cannot describe shape resonance populated by tunneling because tunneling is a quantum mechanical phenomenon. It lacks quantization of energy which is also problematic for the energy transfer process.

Moreover, classical method does not have any symmetry effect. It cannot restrict the process from transferring energy to the states that are forbidden by selection rules of quantum mechanics. Therefore, all the state-to-state transitions are allowed in this method which is physically incorrect. It has been observed that quantum symmetry plays an important role in the energy transfer process in the context of isotope effect, which classical trajectory method cannot describe.

The full quantum method to study the energy transfer is another approach, but it is computationally very demanding. The collision processes of two colliding partners involve not only the state-to-state transition for the vibrational degrees of freedom, but also the rotational states. The vibrational states need to be determined for different values of J , the angular momentum quantum number. So basically, the size of the matrix over the number of the coupled equations depends on the number of states in the system accessed during the collision process.

In practice, it can be easily implemented for those cases when the number of states is relatively small, such as light molecules H_2 , OH , NH and at low collision energies. When molecules become heavier, such as S_2 , CO , CH_3COOH , H_2O and the collision energy is larger, like the room temperature and above, then this is problematic. This leads to huge number of vibrational and rotational states, large size of the state-to-state transition matrix and numerically expensive computation time. As a result, the full quantum method become unaffordable.

1.3. Mixed Quantum/Classical Theory (MQCT) of Energy Transfer

In this work, we develop and implement an alternative method to describe the molecular energy transfer process. It is a mixed methodology of both classical mechanics and quantum mechanics. It takes advantage of the fact that the relative motion of the collision process of two colliding partners can be treated classical mechanically in most cases. Even, rotational motion for some molecule can be treated classically since the energy spacings are rather small between the rotational states and usually, many rotational states are excited. However, in order to stop zero-point energy leakage, we have to treat the vibrational degrees of freedom quantum mechanically.

Our methodology, the mixed quantum/classical theory (MQCT), treats internal degrees of freedom, such as vibration and/or rotations quantum mechanically, while the scattering is treated classically (translational motion). The MQCT equations of motion for classical and quantum degrees of freedom are discussed in Section 3.2.1. Figure 1 describes the components of the mixed quantum/classical theory¹⁶. The picture represents collision of two molecules, $\text{N}_2 + \text{H}_2$. The coordinate Q represents the translational motion

while each diatomic molecule has its own quantum rotational states. This approach of a mixed theory is not entirely new. It was proposed initially by Billing¹⁷ in the 1980s. His method was similar to our methodology. In his work, Billing treated the vibrational motion quantum mechanically while rotation and translational motion classically and applied to a small system, $\text{H}_2 + \text{He}$ with very few rotational states. But our approach is better. It is modified specifically to describe the large amplitude of vibrational motion. The rotational degrees of freedom are coupled with the vibrational degrees of freedom. The energy transfer is allowed between all three degrees of freedom, translational, rotational and vibrational, while the total energy is conserved for the system.

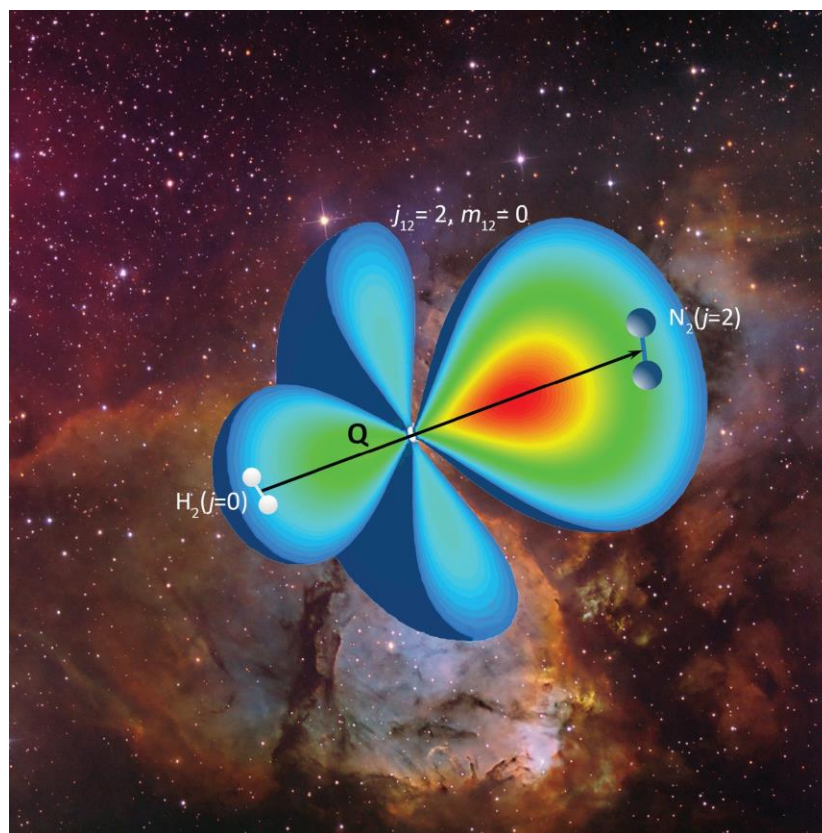


Figure 1: Classical and quantum components of the mixed quantum/classical treatment of molecule-molecule inelastic scattering. Picture is taken from the Journal of Physical Chemistry A.

The energy transfer process is also important in the field of astrochemistry.^{8,9} In terms of astrochemistry, there are more than 200 different molecules and molecular ions found in the ISM till date.^{8,18,19} Few most abundant molecules are CO, H₂ and H₂O. Apart from these, cyano radical (CN)⁸, sulfur-bearing compounds^{20,21}, small organic molecules (HCOOH, CH₃COOH, CH₃OH)²², molecular ions (CH⁺, HCO⁺, SiH⁺)²³ are also found. These molecules are identified by analyzing the radiation from the ISM. This radiation is affected by collisional excitation and quenching with the background gases in interstellar medium (ISM) which are mostly H₂ and He. Therefore, the study of rotational and vibrational energy transfer in the collision of molecule + molecule is important. Some of the molecules found in space can be larger and heavy. For example, methyl formate, CH₃COOH. MQCT method was successfully implemented to treat the rotationally excitation of methyl formate.^{24,25} The collision of H₂O colliding with He, H₂ and other H₂O molecules is very important in this context and MQCT results for the collisional energy transfer of H₂O + H₂ and H₂O + H₂O are reported in this document.

The goal of this work is to develop the mixed quantum/classical theory (MQCT) as a methodology to conduct the computational studies of the collision dynamics and energy transfer and then to apply MQCT to perform scattering calculations of molecular systems relevant to astrophysics (such as H₂O + H₂ and H₂O + H₂O) and atmospheric chemistry (such as S₂ + Ar).

1.4. Motivation to Study Energy Transfer in Sulfur Recombination

Sulfur is one of the most important trace elements in the atmosphere of Earth. In the periodic table of elements, it is under oxygen, and thus is isoelectronic with oxygen,

though it has lower electronegativity. One of the major sources of sulfur in nature is through volcanic eruptions. During the volcanic explosion, sulfur is emitted into the atmosphere (see Figure 2) in the form of hydrogen sulfide (H_2S) and sulfur dioxide (SO_2) gases. Not only on Earth, but sulfur was also found in the atmospheres of Mars, Venus, moons of giant planets (see Figure 3), some exoplanets, and in the shells of some stars as SO_2 , H_2S and S_2 .

Another important property of sulfur is that it exhibits multiple oxidation and reduction states ranging from -2 and up to $+6$, and thus, it can act either as a reducing agent or an oxidizing agent, depending on the environment. The atmospheric chemistry of sulfur is actively studied by geochemists.^{26–28} Depending on the abundance of oxygen in the atmosphere, the chemical and photochemical processes associated with sulfur would follow two distinct pathways (shown in Figure 4 from Ref. 28). In the oxygen-rich atmosphere, sulfur would be quickly oxidized to sulphate, removed from the atmosphere



Figure 2: A volcanic eruption. Taken from the United States Geological survey, downloaded from inhabitat.com.

by rain and be dissolved in the ocean. However, in the anoxic conditions, photolytically produced sulfur atoms would recombine to form S_2 molecule (instead of being oxidized), and then form larger and larger sulfur allotropes such as S_3 , S_4 , S_6 and S_8 :



that are deposited on the surface, react in the bulk, and form minerals like pyrite (FeS_2), gypsum ($CaSO_4 \cdot 2H_2O$) and barite ($BaSO_4$). Analysis of the rock record associated with the Archean eon of Earth indicates that the surface deposits of that time were rich in

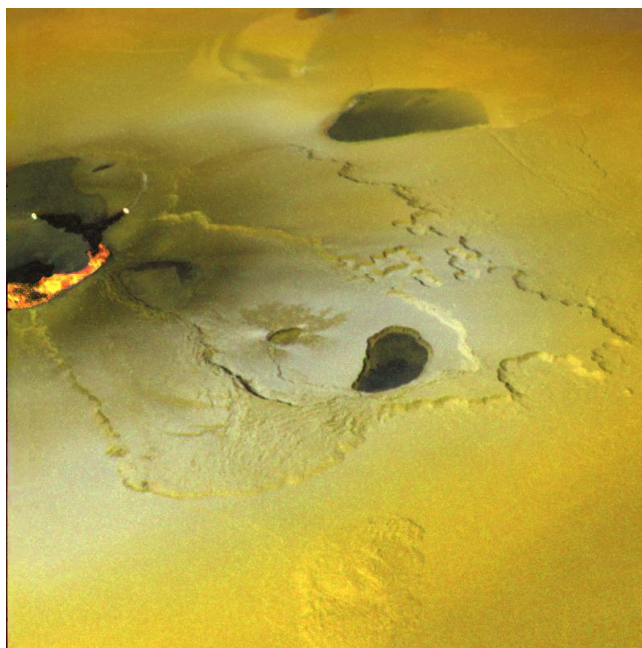


Figure 3: In the year 2000, an active volcanic eruption was observed on Io, a moon of Jupiter. This image was taken from NASA's Galileo spacecraft.

sulfur because these minerals contain a significant amount of sulfur. This was going on before the great oxygenation event that happened about 2.3 billion years ago. The physical, chemical and photochemical processes in such sulfur rich environment are still poorly understood.²⁹

A list of all possible sulfur reactions in the atmosphere was sorted out by Kasting and co-workers^{27,30} over the years. In the kinetics models of the Archean atmosphere there are close to two hundred gas-phase reactions overall. Most of them are redox reactions, but beside that there are also recombination reactions of sulfur allotropes (Eqs 1-6), similar dissociation reactions of sulfur allotropes, atom-exchange and the isotope exchange reactions between sulfur allotropes. Theoretical interpretation of these reactions

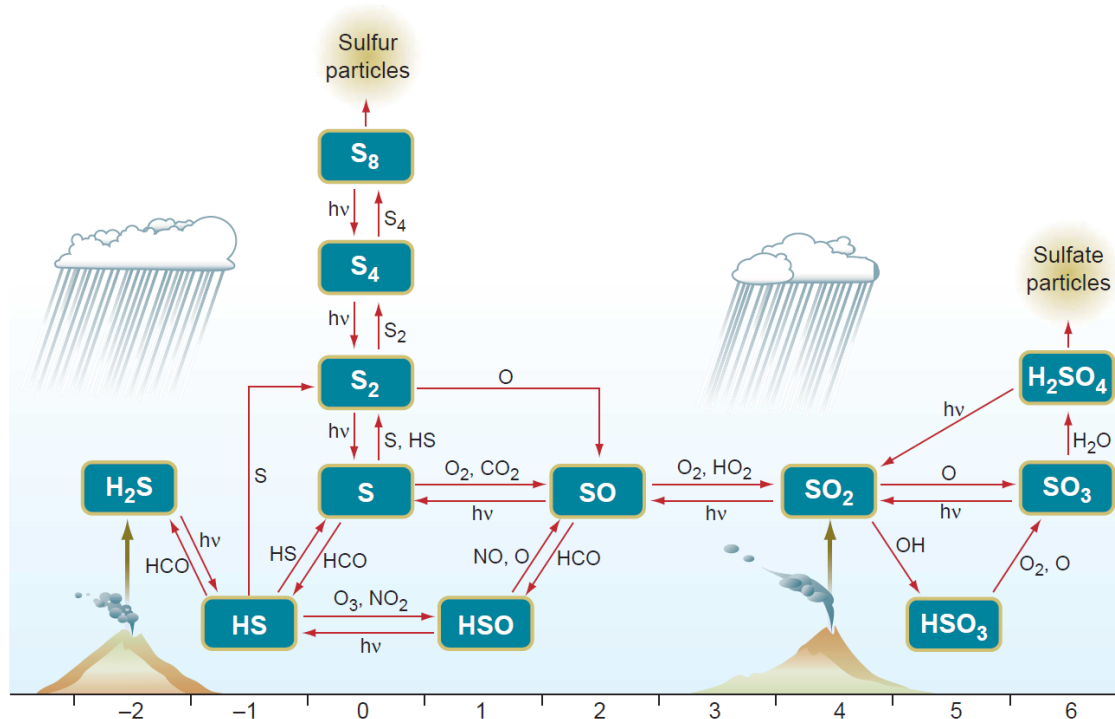


Figure 4: Two different pathways of sulfur reactions depending on the abundance of oxygen in the atmosphere. The horizontal axis represents oxidation and reduction states of sulfur. The picture is taken from Ref. 28 by Kasting *et al.*

requires rate coefficients as input for the kinetics modelling, but they are mostly unavailable as discussed below.

For the rate coefficient, k_1 , of the formation of S_2 , reaction (1), there are two experimental results available. The experiment done by Fair and Thrush³¹ in the year 1968 was a study of chemiluminescence of S_2 in the reaction of $H + H_2S$. It was not even focused on the recombination reaction of S_2 . The derived value of the rate coefficient was $k_1 = 2.8 \times 10^{-33} \text{ cm}^6/\text{s}$. Ten years later another experiment was done by Nicholas *et al.*³² in 1978. This study was done using a special bath gas CS_2 ($S=C=S$) which is an Archean analogue of CO_2 . The derived rate coefficient, $k_1 = 1.19 \times 10^{-29} \text{ cm}^6/\text{s}$, deviates from the former value by four orders of magnitude, creating large uncertainty.

Kasting used the result of Fair and Thrush in his kinetics modelling. There are no available experimental data for the rate constant for the formation of S_3 . So, for reaction (2), the rate coefficient was simply taken as a scaled rate of formation of ozone, since $O + O_2 \rightarrow O_3$ is similar to reaction (2). Namely, the proposed rate constant for reaction (2) was $k_2 = 2.8 \times 10^{-34} \text{ cm}^6/\text{s}$. Then, for the formation of S_4 , S_6 and S_8 , the rate coefficients were set all equal: $k_3 = k_5 = k_6 = 2.8 \times 10^{-31} \text{ cm}^6/\text{s}$, which is empirical.

This empirical approach was used because there are no reliable experimental data available. It is impossible to perform experiment individually for each recombination reaction in the list of Eqs (1-6).³³ The reason for this is that these recombination reactions proceed as a chain of coupled reactions and cannot be studied separately. Namely, two sulfur atoms would form S_2 , but then S_2 would recombine with other atoms or molecules to form S_3 , S_4 , S_6 and S_8 as shown in Eqs (1-6). Another problem is that the vapour pressure of all sulfur allotropes is rather low. So, as soon as a smaller sulfur allotrope is

formed, such as S_2 or S_3 , the deposition on the walls of reaction chamber starts and keep recombining in the condensed phase. So, production and deposition of different sulfur allotropes occurs simultaneously and at the end, we get a mixture of all allotropes which makes the experimental analysis of individual steps rather complicated, basically impossible. Not only the experimental studies are difficult, theoretical studies are also very hard for this process and so far, we are limited to only a few simplified models and several exploratory papers^{29,34,35} that address different aspects of the problem, as discussed in Section 1.5 below.

There are four stable isotopes of sulfur that are found in nature. These are ^{32}S , ^{33}S , ^{34}S , and ^{36}S . About 95% of sulfur is found as ^{32}S . About 4% is ^{34}S , 0.75% is ^{33}S and 0.01% is ^{36}S isotope³⁶. These isotopes are likely to play an important role in the recombination reactions of sulfur since the rate of the reactions could be affected by the isotopic composition of the reactants and/or products. First, the mass of the molecule changes due to the substitution of a rare isotope, which affects the density of rotational and vibrational states and the reduced mass of collisions with bath gas, which in turn affects the speed of collision, the probability of tunneling through activation barrier, and the overall reaction rate. These lead to the mass-dependent isotope effects. Moreover, symmetry of a molecule is distorted due to substitution of an isotope, which may be responsible for the mass-independent isotope effect. As I mentioned earlier, Archean deposits contain a lot of sulfur, but most important is that this sulfur exhibits an unusual mass-independent fractionation (S-MIF), which is in sharp contrast with the mass-dependent fractionation in the oxygen-rich atmosphere of today's Earth. Interestingly, this S-MIF is more similar to the mass-independent fractionation of oxygen (O-MIF) that

we see in the ozone in today's atmosphere. Hence, this study of sulfur recombination reactions is urgently needed to explore several aspects as discussed below.

Modelling the processes of sulfur recombination theoretically will help geochemists to resolve several outstanding problems in the history of Earth. First, it will help atmospheric chemists to analyse the atmospheric condition when early life emerged, and the first microbes started producing and releasing oxygen into the atmosphere (the great oxygenation event). Then, evolutionary chemists will be able to understand the evolution of the atmosphere from the ancient Earth to the present time. Eventually, the same can be applied to the atmosphere of other planets (exoplanets) where a significant amount of sulfur is often found.

1.5. Theoretical Studies of Sulfur Recombination

The formation reaction of the simplest sulfur allotrope, S_2 , in the bath gas of Ar was studied by Peterson and co-workers:³⁴



A potential energy surface was built for $S_2 + Ar$ system and the dynamics study was performed using the method of classical trajectories. It is inefficient to sample the initial conditions for collision of three free moving particles ($S + S + Ar$) such that the diatomic molecule would be produced, because the probability of such reactive event (formation of S_2) would be extremely low. So, for this technical reason, Peterson and co-workers studied this process in the reverse direction, that corresponds to the collision-induced dissociation (CID):



The third order recombination rate constant was then computed using the principle of microscopic reversibility:

$$k = \frac{k_{\text{CID}}}{[\text{Ar}]K} \quad (9)$$

where K is the equilibrium constant computed statistically. The rate constant for the formation of S_2 was found to be $k_1 = 4.19 \times 10^{-33} \text{ cm}^6/\text{s}$. This result agrees quite well with the experiment done by Fair and Thrush,³¹ but disagrees with the other experiment by Nicholas *et al.*³²

This classical trajectory method for the description of recombination correspond only to the direct three-body recombination mechanism, when the reaction (7) goes in one single step (not through any intermediate). However, this mechanism is efficient only at very high concentration of the bath gas, i.e., high pressure of Ar, which is not typical specific to the atmospheric range of pressure values ($\sim 1 \text{ atm}$ and lower) and room temperature.

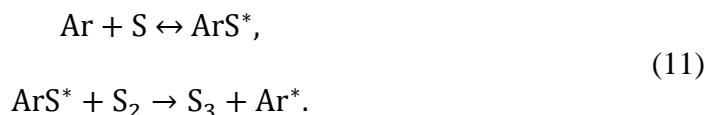
The most important mechanism for recombination at the atmospheric condition is the energy transfer mechanism^{3,29,37} that has two consecutive steps:



The first step describes the formation and decay of the metastable intermediate species, S_2^* , which was studied theoretically by Babikov *et al.*²⁹ In fact, this was the only quantum dynamics study of sulfur recombination where the metastable species, S_2^* , were described as scattering resonances. Moreover, this was the only computational study of the isotope effects in the sulfur recombination reaction (other authors considered only the major sulfur isotope ^{32}S). However, the stabilization step, the second step in this S_2

recombination reaction (9), was not studied by Babikov *et al.* in details because it is harder to study as it involves three atoms. It was treated approximately assigning the same value of stabilization cross section for all states of S_2^* and for all isotopes. But, this second step is the most important in the energy transfer mechanism because this is the rate limiting step, that may also be responsible for the isotope effect. The stabilization step has never been studied by anyone, neither for S_2 , nor for S_3 , nor for any other sulfur allotropes. In fact, there are very few articles associated with accurate theoretical treatment of the stabilization processes. Examples include $H_2^* + He$,³⁸ $Ne_2^* + H$,³⁹ and $O_3^* + Ar$.^{2,3,6,40}

The formation of S_3 molecule through the “chaperone” mechanism in the bath gas Ar was studied by Francisco, Peterson and co-workers.⁴¹ According to this mechanism the reaction could proceed through two alternative pathways. One route is through formation of ArS^* intermediate:



The other path is through ArS_2^* intermediate:



In either case the chaperone mechanism involves two steps. In the first step, one of the reagents forms a weakly bound metastable state with the bath gas, and the collision with the second reagent releases the bath gas atom. Francisco and co-workers used the method of classical trajectories to study the second step, which is the release of the Ar atom from the metastable intermediate complex. The first step in the chaperone mechanism was

studied statistically. They found that the contribution of reaction (12) for the formation of S_3 is dominant while the reaction (11) is minor. The final predicted rate for the formation of S_3 was found to be $k_2 = 2.66 \times 10^{-33} \text{ cm}^6/\text{s}$.

Note that the chaperone mechanism goes through the formation of a non-covalently bonded intermediate (ArS^* or ArS_2^*) and this species is a weakly bound van der Waals complex. At room temperature or even at the reduced temperature specific to the stratosphere, this metastable intermediate is not expected to be stable. This means that the energy transfer mechanism should be considered for S_3 .

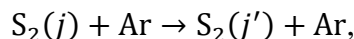
From this survey, we can conclude that the sulfur recombination reactions of Eqs (1-6) are still poorly studied. Table 1 summarises major research done on sulfur recombination reaction. Concerning the potential energy surfaces, only the one for the interaction of S_2 with Ar was constructed in the past. There is no accurate global PES for S_3 , but there was one approximate $\text{Ar} + S_3$ PES used to study the second step in the chaperone mechanism, in reactions (11) and (12). For S_4 , full dimensional 6D PES does not exist yet. Recently Gaidai constructed a simplified two-dimensional PES for a model of $S_2 + S_2 \rightarrow S_4$ process and the construction of 3D PES is in progress. For S_8 , the full

Table 1. Summary of research on sulfur recombination reaction.

Substance	PES	Reaction dynamics		
		Energy transfer mechanism	Chaperone mechanism	Direct three-body mechanism
S_2	Peterson, 2008 Mandal, 2018	Babikov, 2017 (1 st step only)	— —	Peterson, 2008
S_3	Peterson, 2011	— —	Peterson, 2011 (2 nd step only)	— —
S_4	Gaidai, 2018 (2D only)	— —	— —	— —
S_8	— —	— —	— —	— —

dimensional PES for S_8 would need 18 degrees of freedom. Such surface is unlikely to be built with an accurate method but may be an approximate PES can be built using a simplified force-field approach.

More recently, Babikov *et al.*²⁹ studied the first step, i.e., the formation of the S_2^* intermediate, from the point of view of scattering resonances. He identified the mass-dependent and mass-independent isotope effects in this process, and clearly indicated that in order to build a reliable theoretical model, one needs a reliable theoretical description of the second step of the energy transfer mechanism, $S_2^* \xrightarrow{+Ar} S_2$. Our focus here is to study this second step, the energy transfer process for the rotationally excited S_2 molecule:



including both quenching ($j' < j$) and excitation ($j' > j$) in a broad range of the rotational states of S_2 , in order to offer quantitative description of symmetry-driven mass-independent isotope effect. In particular, to study this energy transfer process for different isotopes such as $^{32}S^{32}S$, $^{32}S^{34}S$, and $^{34}S^{34}S$, all collided with Ar bath gas. It is important to realize that half of the rotational states in the homonuclear symmetric molecules $^{32}S^{32}S$ and $^{34}S^{34}S$ are missing, just like in O_2 . While for the case of heteronuclear molecule $^{32}S^{34}S$, all the rotational states are present. These additional states may provide additional energy relaxation pathways, which is expected to facilitate the energy transfer process.

1.6. Objectives and Structure of This Dissertation

The goal of this dissertation is twofold. The first objective is to develop mixed quantum/classical methodology (including theory and computer code) and make it available to other scientists as an efficient tool to study the energy transfer processes in

general. It is important to stress that the methods available to the community nowadays are either computationally demanding (like the full-quantum methods) or not accurate enough (classical trajectory methods). The second objective is to apply this methodology to study the inelastic scattering of molecules relevant to astrophysics (molecular collisions in the interstellar medium) and in the atmospheric conditions (such as gas phase recombination reactions).

In Chapter 2, a description of the mixed quantum/classical methodology and the user-friendly code that we develop and test, named MQCT, is presented. This can be used as a user guide for non-experts to understand the major components of this approach and to perform calculations using the mixed quantum/classical theory of rotational and vibrational transitions for several types of molecule + quencher systems, starting from the simplest diatomic + atom and going to the most general asymmetric top rotor + asymmetric top rotor (such as $\text{H}_2\text{O} + \text{H}_2\text{O}$). Our code is the only one existing that can do this type of calculation.

In Chapter 3, MQCT is applied to study the inelastic scattering of molecules that are important in astrophysics, such as $\text{H}_2\text{O} + \text{H}_2$ and $\text{H}_2\text{O} + \text{H}_2\text{O}$. A rigorous study was performed to prove the accuracy level of the results computed by our code, and the obtained cross sections for state-to-state transitions and thermally averaged cross sections are then benchmarked against available full-quantum methods and experimental results.

In Chapter 4, MQCT is developed further and tested by doing calculations on a well-studied system of astrochemical interest, $\text{N}_2 + \text{Na}$. A benchmark study of the inelastic and elastic integral cross sections is presented. A focused study is performed on the differential cross sections, and the significance of quantum phase and scattering

amplitude is studied in detail. For the first time, the inelastic differential cross section is computed within the MQCT framework. This study also includes the description of the quantum phenomenon of resonance within the MQCT framework.

In Chapter 5, a hierarchy of approximate methods is proposed to solve the equations of motion within the mixed quantum/classical theory (MQCT) framework of inelastic molecular collisions. Of particular interest is a limiting case – the method in which the classical-like equations of motion for the translational degrees of freedom (scattering) are decoupled from the quantum-like equations for time-evolution of the internal molecular states (rotational, vibrational). Trajectories are pre-computed during the first step of calculations, with driving forces determined solely by the potential energy surface of the entrance channel, which is an adiabatic trajectory approximation (AT-MQCT). Quantum state-to-state transition probabilities are computed during the second step of calculations, with an expanded basis and a very efficient step-size adjustment.

Chapter 6 is dedicated to the development of the potential energy surface of the $S_2 + Ar$ system valid up to the dissociation limit in S_2 . Our surface is more accurate than the one of Peterson and co-workers since we consider a broader range of interatomic distances, particularly in the region of close $S + Ar$ encounter where the repulsive interaction is strong. We use an explicitly correlated method CCSD(T)-F12/VTZ-F12 method for the computation of the *ab initio* data points. The dynamics of $S_2 + Ar$ is then studied using the mixed quantum/classical methodology. The rotationally inelastic cross sections are computed for the rotationally excited symmetric molecules $^{32}S^{32}S$ and $^{34}S^{34}S$ to characterize mass-dependent isotope effect and for one asymmetric molecule, $^{32}S^{34}S$, to determine the magnitude of the symmetry-driven mass-independent isotope effect.

Finally, in Chapter 7, I present a summary of the important outcomes of this work together with the description of future projects, made possible by the developments carried out in this dissertation.

CHAPTER 2. DEVELOPMENT AND TESTING OF A USER-READY PROGRAM FOR CALCULATIONS OF INELASTIC SCATTERING OF TWO MOLECULES

2.1. Introduction

Inelastic collisions of molecules in gas phase play important roles in atmospheric chemistry^{3,6,40}, in astrophysical phenomena^{8,42,43} and in combustion^{44–46}. In these processes, energy is exchanged between translational degrees of freedom (kinetic energy of collision) and internal degrees of freedom of the molecules, such as rotations and vibrations. Theoretical treatment of excitation and quenching of rotational-vibrational molecular states requires quantum mechanics, since these states are quantized, and quite often the state-specific information about collision process is needed (*e.g.*, in spectroscopy, for analysis of state populations during absorption and emission of light^{47–49}). The work-horse of theorists today is the coupled-channel approach⁴⁹, in which not only the internal states of molecules are treated quantum mechanically, but also their collision process is described using the quantum scattering formalism⁵⁰. Such full-quantum approach is essential in the ultra-cold physics regime, due to a small number of scattering waves involved in the process and their resultant interference effects^{51,52}, and when the quantum tunneling is important, for example, for description of scattering resonances¹⁵. Two popular computer codes are in use nowadays, MOLSCAT⁵³ and HYBRIDON⁵⁴, that allow users to carry out the full-quantum inelastic scattering calculations for small molecules.

Numerical effort associated with such calculations becomes very significant for larger and heavier molecules, due to their dense spectra of rotational states, and more so at higher collision energies and with heavier collision partners, when many values of the orbital angular momentum states (partial waves) should be taken into account for description of the scattering process. This is because in the full-quantum approach the internal states of molecules couple through partial scattering waves, which leads to a large system of coupled differential equations. Computationally affordable cases include diatomic + atom^{55,56}, triatomic + atom^{9,57}, and diatomic + diatomic^{58,59} collisions. Rotationally inelastic scattering calculations for triatomic + diatomic systems are very demanding^{42,60}. For polyatomic molecules, calculations appear to be affordable at low scattering energies only, and only with the simplest and lightest collision partner, such as He atom^{61–63}. Even more complexity is brought by vibrational (in addition to rotational) excitations, that become possible in larger and floppier molecules (*e.g.*, lower-frequency modes, such as torsions or internal rotations) and/or at higher collision energies, when the vibrational bending modes may also become accessible^{64,65}. There is a strong need for such calculations in the field of chemistry, physics and engineering, but, using the existing methods and codes, they are still outside of our reach.

An astonishing example is a water + water rotationally inelastic scattering process that has never been studied computationally in sufficient detail, $\text{H}_2\text{O} + \text{H}_2\text{O}$ ^{66,67}. Each of the water molecules in this process should be treated as an asymmetric-top rotor, but neither of the codes available to the community today can treat a collision of two asymmetric top rotors^{53,54}. Another representative example includes a group of polyatomic molecules, such as HCOOCH_3 ⁶¹, HC_3N ⁶⁸, H_2CO ⁶⁹, CH_3OH ⁷⁰, C_6H and C_6H^-

^{62,63}. For these and other systems of comparable complexity the potential energy surfaces can be computed nowadays (using the methods and codes of the electronic structure theory), but the scattering calculations are nearly impossible using the standard full-quantum scattering approach.

In the last few years we developed and tested a simplified mixed quantum/classical theory (MQCT) for inelastic scattering in which the relative motion of collision partners is described approximately, classically, whereas their internal motion is still described rigorously using quantum mechanics^{16,24,71–78}. A significant speed up of this approach is achieved by classical-trajectory treatment of the scattering process that uses numerically inexpensive Newtonian mechanics, instead of the Schrodinger equation. Further computational advantage is due to the intrinsic massive parallelism of the MQCT approach, in which different trajectories are independent and can be propagated simultaneously using different processors, without any message passing. The resultant computational gain is very substantial, enabling inelastic scattering calculations for larger molecules and at higher collision energies, compared to the standard full-quantum approach. For example, we could run MQCT calculations for $\text{HCOOCH}_3 + \text{He}$ at collision energies up to 1000 cm^{-1} ²⁴, in contrast to the full-quantum calculations affordable only up to 30 cm^{-1} ⁶¹. Semenov *et al.* also carried out the first ever calculations for $\text{H}_2\text{O} + \text{H}_2\text{O}$ rotational excitations, in a broad energy range⁷⁹. Accuracy of MQCT has been rigorously tested in a series of recent papers^{74,78}, and this question will not be reexamined in this chapter. We recommend “blending” the full-quantum calculations at low collision energies (where those are indispensable and often affordable), with MQCT

calculations at higher collision energies, where they are expected to be accurate, and where no other known method is practical.

In this chapter, we present a user-ready code we named "MQCT", that can be employed for efficient calculations of rotationally inelastic scattering of any two molecules, and for some rotationally-vibrationally inelastic scattering calculations. We want to stress again that, to our best knowledge, no other code can do the inelastic scattering calculations of two general asymmetric top rotors. Potential users of the code are among the members of astrophysics community, atmospheric chemists and, of course, physical chemists. Our code is written in `FORTRAN` and is parallelized using `MP I`. Efficiency of massively parallel calculations (scaling) is explored using the example of water + water rotationally inelastic scattering. Several typical input files are given for calculations on $\text{H}_2\text{O} + \text{He}$, $\text{H}_2\text{O} + \text{H}_2$ and $\text{H}_2\text{O} + \text{H}_2\text{O}$ systems, as examples. Readers will find that MQCT calculations are very easy to set up and run using defaults. The most useful options are discussed in this chapter, but many more are described later in the User-Manual. Current users of the full-quantum code MOLSCAT⁵³ will recognize that our input files are very similar to those they are used to. This was done intentionally, to facilitate familiarization with new program. Indeed, the input files for MOLSCAT calculations can be used for MQCT calculations with minimal modifications. An efficient parser allows communications with the code in a rather efficient way. This would be the first release of the program. This work is done with collaboration with former group member, Alexander Semenov. Its development is ongoing. Several exciting avenues are discussed in Conclusion section.

2.2. Three Components of the Input

MQCT calculations of inelastic scattering include time-propagation of the Newtonian-like equations of motion for collisional degrees of freedom (trajectories driven by the mean-field potential, Eqs. (5-6) in Ref. [78]), and the Schrodinger-like equations for evolution of quantum state populations of the molecules (driven by state-to-state transition matrix and the Coriolis coupling, see Eqs. (2-3) in Ref. [78]). The initial conditions for each of those are defined separately in two blocks of the input file, called `$SYSTEM` and `$BASIS`. The potential energy surface describes interaction between the quantum and classical parts of the system and is defined in the third block of the input file, called `$POTENTIAL`. This block should be the last in the input file, while the order of the first two blocks is interchangeable, since they are independent. Example below sets up input for the default calculations of $\text{H}_2\text{O} + \text{He}$ rotational excitation:

```
$BASIS
    SYS_TYPE=4, A=27.877, B=14.512, C=9.285
$END

$SYSTEM
    MASS_RED=3.2748, RMIN=4.5, RMAX=20.0,
    NMB_ENERGS=1,    U_ENERGY=200.,    JTOTL=0,    JTOTU=20,
    TIME_STEP=15.0,  TIME_LIM=3.5E+6
$END

$POTENTIAL
    LABEL="H2O+He", E_UNITS=A.U., R_UNITS=A.U.,
    GRD_R=50, GRD_ANG1=8, GRD_ANG2=25, GRD_ANG3=25
$END
```

Each block starts with its name and is finalized by the `$END`. All entries inside the block are separated by coma. You can have as many spaces, lines or tabs as you want between the keywords and their values, all is taken care of by the parser.

First keyword of the block \$BASIS indicates type of the system (SYS_TYPE=4 corresponds to the asymmetric-top rotor molecule + atom, see below), followed by three values of the rotational constants of the molecule (in the units of wavenumber). The block \$SYSTEM contains reduced mass of the collision partners (MASS_RED, in atomic mass units), the minimum and maximum values of distance between collision partners to initialize and terminate trajectories (RMIN and RMAX in the units of Bohr), the number of collision energies to compute NMB_ENERGS (here one only) and their effective values (U_ENERGY in wavenumbers), the range of total angular momentum quantum number J (from JTOTL to JTOTU), propagation time-step TIME_STEP and the time limit TIME_LIM to terminate trajectories (both in atomic units). In the block \$POTENTIAL, besides the text LABEL, the units of energy and distance for the potential energy surface subroutine (supplied by the user, see below) are indicated first, followed by the number of quadrature points for integration of matrix elements for state-to-state transitions.

As one can see the default input is very short. Below we discuss the three input blocks in more detail, and some of the most useful options.

2.2.1. Quantum Degrees of Freedom, Block \$BASIS

In this first release of MQCT there are ten system types, summarized in Table 2, from the simplest diatom + atom, to the most general case of two asymmetric top rotor molecules. For each system, the required rotational and vibrational constants are listed in the Table. Those are used by the code to set up and diagonalize Hamiltonian matrix for

Table 2. Types of systems handled by MQCT, with required and optional input data.

SYS_TYPE	Collision Partners	Required Constants	Channel Labels	Optional Input
1	rigid diatom + atom	B_e, D_e	j	
2	vibrating diatom + atom	B_e, D_e, ω_e, x_e	j, v	vibrational functions, grid
3	symmetric top + atom	A, C	j, k	
4	asymmetric top + atom	A, B, C	j, k_a, k_c	expansion over sym. top basis
5	rigid diatom + rigid diatom	$B_{e1}, D_{e1}, B_{e2}, D_{e2}$	j_1, j_2	
6	vibrating diatom + vibrating diatom	$B_{e1}, D_{e1}, \omega_{e1}, x_{e1}, B_{e2}, D_{e2}, \omega_{e2}, x_{e2}$	j_1, v_1, j_2, v_2	vibrational functions, grid
7	symmetric top + rigid diatom	A, C, B_e, D_e	j_1, k_1, j_2	
8	asymmetric top + rigid diatom	A, B, C, B_e, D_e	j_1, k_{a1}, k_{c1}, j_2	expansion over sym. top basis
9	asymmetric top + symmetric top	A_1, B_1, C_1, A_2, C_2	$j_1, k_{a1}, k_{c1}, j_2, k_2$	expansion over sym. top basis
0	asymmetric top + asymmetric top	$A_1, B_1, C_1, A_2, B_2, C_2$	$j_1, k_{a1}, k_{c1}, j_2, k_{a2}, k_{c2}$	expansion over sym. top basis

rotational motion (using basis set of oblate symmetric-top functions), in order to determine rotational states of the system. An option of invoking the externally-computed user-supplied rotational-vibrational states (*e.g.*, vibrational wave functions defined on a grid of points, or vibrationally distorted rotational states, such as those of Kyrö model Hamiltonian, expanded over basis set of the oblate symmetric-top functions) are indicated, where available. When symmetric tops are involved in collisions, the case of an oblate top is handled in a standard way, with rotational constants indicated such that $A > C$, while for a prolate top the input should be in the form $A < C$, opposite to the standard notation. In both cases it is assumed that $B = A$. Although the case of spherical top is not explicitly included, it can be handled also, by indicating $A = C$. By default, the program will form a basis set of six lowest energy channels of the system (and will include all corresponding degenerate states, see below), and will choose the ground state as the initial channel. Alternatively, one can indicate the number of channels, list them explicitly, and choose the initial channel using optional keywords. For example, for the $\text{H}_2\text{O} + \text{He}$ system discussed above, an equivalent input would be:

```
NMB_CHNLS=6,
CHNLS_LIST=0,0,0, 1,0,1, 1,1,0, 1,1,1, 2,0,2, 2,2,1,
INIT_CHNL=0,0,0
```

Here the rotational states of the asymmetric top rotor are labelled using the standard notation: j, k_a, k_c (where k_a and k_c are projections of j onto the principal axis with smallest and largest moments of inertia, respectively). Another useful optional keyword allows forming basis set out of all states below given energy, for example: $\text{EMAX}=135.4$ commands to include in the basis set all states at energies below 135.4 cm^{-1} (which, again, would be the same six channels, see Table C1 in Ref. [79]). Rotational quenching

calculations can be initiated by choosing the excited state as initial, for example (in the $\text{H}_2\text{O} + \text{He}$ system): `INIT_CHNL=2, 0, 2`.

By default, the most general fully-coupled version of MQCT calculations is carried out, in which the transitions due to the Coriolis coupling are included. Such “coupled-channel” calculations are referred to as CC-MQCT. One important option, initiated by the keyword `CS_APPROX=YES`, is to run the so-called *coupled-states* calculations, CS-MQCT^{24,74,78}, where the Coriolis-driven transitions are neglected. Speed up is a factor of ~ 20 , due to a much simpler form of the mean-field potential in this case, and a much smaller number of states accessible from a given initial state^{24,74,78}. Recall that (within each channel) the Coriolis force couples $2j_{12} + 1$ degenerate states labelled by m_{12} , which is projection of j_{12} on the molecule-molecule axis, where j_{12} is the internal angular momentum quantum number of two molecules, also quantized in MQCT^{16,75,78,79}. (If one of the collision partners is an atom, then j_{12} is simply equal to j of the second partner, the molecule.) So, in CS-MQCT these Coriolis couplings and transitions are neglected, and the calculations are done *independently* for various fixed values of m_{12} .

2.2.2. Classical Degrees of Freedom, Block \$SYSTEM

Initial conditions for MQCT trajectories are generated by the code using `RMAX` as the initial distance between the colliding partners at time equal zero. Initial velocity is defined by reduced mass `MASS_RED` and the effective collision energy `U_ENERGY`. If several values of energy are indicated, the program will run `NMB_COLL_ENER` independent calculations, for example:

NMB_ENERGS=4, U_ENERGY=200.5, 345.3, 1203.7, 45.637

Equally spaced collision energies can be defined using the smallest value and an increment:

NMB_ENERGS=6, UMIN=175.0, DU=25.0

Or, alternatively, the largest value and the decrement:

NMB_ENERGS=6, UMAX=300.0, DU=25.0

The last two inputs are equivalent.

Collision impact parameters are generated automatically by the code, using the indicated range of values of the total angular momentum J of the system, and the values of individual angular momenta j_1 and j_2 of collision partners in the initial rotational state (defined by INIT_CHNL or zero by default, see above). Namely, for given j_1 and j_2 the range of possible values of j_{12} which is internal angular momentum quantum number of two molecules is $|j_1 - j_2| \leq j_{12} \leq j_1 + j_2$ (these degenerate states are also quantized in MQCT^{16,75,78,79}). Moreover, for each j_{12} there are $2j_{12} + 1$ space-degenerate states labeled by m_{12} (which is projection of j_{12} on the molecule-molecule axis).

Independent calculations with different initial values of j_{12} and $|m_{12}|$ are required, and all are done automatically by the code. For each of these initial degenerate states the allowed values of orbital angular momentum ℓ (integer, quantized in MQCT) are varied in the range $|J - j_{12}| \leq \ell \leq J + j_{12}$. These are used to initiate MQCT trajectories with different impact parameters, since ℓ is closely related to the collision impact parameter b .

There is an option of setting the maximum value of impact parameter, in the units of Bohr, for example: B_IMPCT=9.50. If this is specified, then the upper and lower limits of J are not required (JTOTL and JTOTU are ignored, even if indicated). This option is convenient for calculations in a broad energy range, since the maximum impact

parameter is less sensitive to collision energy. At each collision energy, the upper limit of J is determined individually, based on the indicated value of maximum impact parameter.

By default, fourth-order Runge-Kutta method is employed to propagate MQCT trajectories (together with quantum equations for state populations) using a constant step-size `TIME_STEP`. Optionally, one can choose an adaptive step-size method from Numerical Recipes⁸⁰, by indicating:

```
PROPAGATOR=ODEINT, MIN_TMSTP=0.0, EPS_ODEINT=1.0E-3
```

This method will adjust time-step in the range between `MIN_TMSTP` and `TIME_STEP` to keep the accuracy below `EPS_ODEINT`.

Trajectories in MQCT are integrated through the interaction region and are terminated when the molecule-molecule distance exceeds `RMAX`. If optional time-limit is indicated (by `TIME_LIM`, as in the example above) the trajectory is terminated as soon as either condition is fulfilled. This is recommended at low collision energies, when orbiting trajectories are possible (analogous to quantum scattering resonances, see below).

2.2.3. Potential Energy Surface Block `$POTENTIAL`

In this block, the units for user-supplied potential energy subroutine must be specified. For the units of distance (keyword `R_UNITS`) Bohr and Angstrom are available, as defined by `A.U.` and `ANGS`, respectively. For energy units (keyword `E_UNITS`) possible values are `CM-1`, `KLVN` and `KCAL` that correspond to wavenumbers, Kelvin and kilocalories per mole, respectively. Note that angles are always assumed to be in radians.

By default, state-to-state transition matrix elements are computed by direct numerical integration over all internal degrees of freedom. The number of Gauss-Legendre quadrature points should be indicated for each angular coordinate, as in the example above (three Euler angles for an asymmetric top rotor, such as H₂O). Integration over angles is carried out at each point of the molecule-molecule distance grid (GRD_R equally-spaced points in the range between RMIN and RMAX). In the collision dynamics calculations, each matrix element is splined over the distance between the grid points, using 3rd-order one-dimensional spline⁸⁰. Optionally, computed matrix elements can be saved to a file, using keyword `SAVE_MTRX=YES`. By default, this would be in the binary form (unformatted). Formatted matrix output can be requested by the keyword `UNFORMAT=NO`, *e.g.*, for visual inspection by the user.

Alternatively, user can expand the potential energy surface over the basis set of spherical harmonics, as it is usually done in the full quantum inelastic scattering calculations, and is implemented in the existing popular codes MOLSCAT⁵³ and HYBRIDON⁵⁴. We implemented this approach in MQCT as well, as an option, to facilitate comparison with full-quantum calculations. But, users should be aware that although this procedure is routinely done for small molecules, it is known to produce unphysical results for larger molecules due to truncation issues⁶¹, and is also computationally inefficient. For this representation of the PES, the following keywords are needed (*e.g.*, for H₂O + He⁷⁶):

```
EXPANSION=YES, NMB_TERMS=12, TERMS=
0,0, 1,0, 2,0, 2,2, 3,0, 3,2, 4,0, 4,2, 4,4, 6,0, 6,2, 6,4
```

where the expansion terms taken into consideration are explicitly listed (labeled by λ and μ , see Eqs. (11-12) in Ref. [76]). The externally generated file

PES_EXPAN_TERMS.DAT is also needed in this case, which should contain radial dependencies of the expansion coefficients on the equally-spaced or non-equidistant grid of points in the range between RMIN and RMAX. Examples of such files are distributed with the code. These expansion coefficients will be used to compute analytically elements of the state-to-state transition matrix. In the course of trajectory, those will be splined between the grid points by the code. The code can also generate a suitable expansion, using keyword CALC_EXPANSION=YES, for all system types except 2 and 6 where the vibrational motion is included.

2.3. Efficient Use of the Code

2.3.1. Compiling and Running the Code

User supplied subroutine for the PES should be compiled first, to create an object file, for example PES_H2O+He.o. It should be copied into (or linked to) the main program directory /MQCT_v1.01. The MQCT code itself is compiled independently from the PES to create the object file head.o, and then is linked with the desired PES to create an executable file. Examples of this procedure are given in the files comp_MQCT and link_ALL. These can be executed as commands, after changing access:

```
> chmod +x comp_PES comp_MQCT link_ALL
> ./comp_PES
> ./comp_MQCT
> ./link_ALL
```

Input file for MQCT should have the extension *.inp, and its name should be placed in the file INPUT_NAME.inp. This permits user to store multiple input files (e.g., for different molecules) in the program directory, but run actual calculations with one specific input file.

There are two general ways of running the code. In the straightforward approach, which is also the default, the program computes elements of the state-to-state transition matrix and then propagates trajectories for collisions, all in a single run. In the optional two-step approach, which we recommend following, the program is run first with small number of processors to compute transition matrix, save it into the file and stop (without doing the calculations of collision). This is done by indicating the following optional keywords:

```
SAVE_MTRX=YES, PROG_RUN=NO
```

Then the program is run again to read the transition matrix (computed previously) and perform massively parallel trajectory calculations using large number of processors. Keywords required for this are:

```
READ_MTRX=YES, PROG_RUN=YES
```

This approach is also convenient when multiple calculations are needed with different input parameters (such as collision energy, initial state, number of trajectories, time step, *etc.*) but with the same basis set, which determines the matrix size. Clearly, the matrix must be computed only once, can be saved in the file, and then reused later as many times as needed. The file name is `MTRX_UF.dat` for the binary form (unformatted) and is `MTRX.dat` for the formatted option of the matrix. Note that all intermediate data files created or used by in the code have extension `*.dat`.

There are two levels of parallelization in the code. At the first level, propagation of each trajectory can be done by multiple processors used as a group (*e.g.*, all processors of a node) to compute right-hand sides of the classical and quantum equations of motion. This requires some minimal message passing. At the second level, propagation of different trajectories can be assigned to different groups, which requires virtually no

message passing. The program attempts to evenly split all requested trajectories between the groups. For example, if the code is submitted for execution using 60 nodes of the machine with 32 cores per node (1920 processors total) the following option, indicated in the `$SYSTEM` block:

```
MPI_PERTRAJ=32, NMB_TRAJ=300
```

will result in formation of 60 groups, and assignment of 5 trajectories per group.

Typically, trajectories with larger impact parameters are shorter and faster to propagate. Thus, for an equalized load, and optimal use of resources, it is recommended to assign several trajectories per group, not just one. Note that `NMB_TRAJ` is an optional keyword used only in conjunction with Monte-Carlo sampling of the initial states (see below). If it is not used, the code automatically determines the required number of MQCT trajectories and attempts to split them evenly between the groups.

The equations of motion represent a system of ordinary differential equations, and their right-hand sides contain a matrix-vector product (for quantum degrees of freedom) and a vector-matrix-vector product (for classical degrees of freedom). Calculations of these right-hand sides are parallelized very efficiently in our code using inter-communication protocol within MPI. In Figure 5 we present the wall-clock data collected from Cray XC40 machine at NERSC (the Cori, <http://www.nersc.gov/systems/cori/>). They represent CC-MQCT calculations for the $\text{H}_2\text{O} + \text{H}_2\text{O}$ system⁷⁹ with 91 channels (3483 states total, including the degenerate states), using one head-on collision trajectory with kinetic energy 8000 cm^{-1} . The figure shows a nearly perfect scaling of MQCT code up to 256 processors. With 1024 processors some small overhead becomes visible. These data correspond to a well parallelized code.

Overall, the two levels of parallelization discussed above (first distributing trajectories over the groups of processors, and then distributing the load of trajectory propagation between processors of a group) enable massive parallelization of MQCT calculations. If the number of trajectories varies from say 100 to 1000 (depending on the system, degeneracy of the initial state and the collision energy), then one can employ rather efficiently, without any significant overhead, on the order of ten thousand to hundred thousand processors using the present version of MQCT code.

2.3.2. Understanding the Output

All output files have extension `*.out`. System setup is written into the file `USER_INPUT_CHECK.out` and should be checked by user for correctness. The file `STATES.out` (written if the option `PRNT_STATES=YES` is chosen) contains the list of

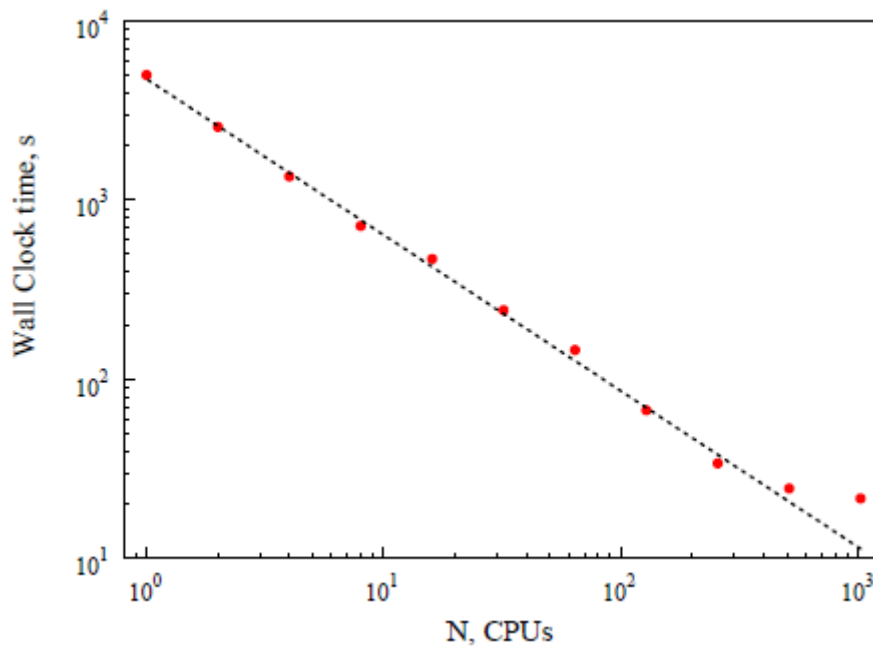


Figure 5: Performance of MQCT in terms of parallelism. The figure represents the time complexity.

all quantum states involved in calculations, including the channel number, the values of j_{12} and m_{12} , and the assigned quantum numbers. Major results are found in `CROSS_SECTIONS.out`. Other, problem-specific output files are discussed in the next section. Here we cover only the major parts of the output.

Examples of output files for the $\text{H}_2\text{O} + \text{He}$ system are also distributed with the code. Cross sections for transitions from the initial state to the final states (all states of the basis, including the elastic channel) are listed in the output file `CROSS_SECTIONS.out`, for each effective collision energy specified in the input. For each transition, the actual collision energy E_{COLL} is also given in the output file, which depends on the effective collision energy U_{ENERGY} and the state-to-state energy difference. These are different for different transitions (particularly at lower collision energies), which is a property of the mixed quantum/classical approach, discussed in detail in several recent papers^{72,75}. Next in the output file goes an important information about the largest values of energy conservation error, and the probability conservation error (both given as % of the initial value) encountered during the propagation. User should check these numbers to ensure that they are reasonable (say below $1.0\text{E}-03$). Excessive values indicate that modification of the propagation parameters in the input file is needed. The last in the output file is CPU-time statistics of the code execution.

More detailed information about propagation accuracy can be found in the file `INTEGRATOR_ERRORS.out`, where the data collected for the less accurate (worst) trajectory in the batch are printed, for each collision energy. Other generally useful information about behavior of MQCT trajectories (classically-treated translational degrees of freedom) is found in the file `DEFLECTION_FUNCTION.out`. Final

probability amplitudes of the internal states (quantum degrees of freedom) can be found in the file `OPACITY_FUNCTIONS.out`. These files are generated by default. We recommend that users inspect all these dependencies after each program execution, to make sure that the overall behavior of the system is reasonable.

2.3.3. Random Sampling of the Initial Conditions

For larger and heavier molecules (with large J and ℓ) and/or highly excited rotational states (with large j_1 and/or j_2), the number of initial states that should be taken into account may become prohibitively large, especially at high energies. Running MQCT trajectories for all possible initial states, which is a default in our code, may become computationally expensive and, in fact, unnecessary. In such cases, it is more efficient to sample the values of J , ℓ , j_{12} and m_{12} randomly and simultaneously, using an efficient multi-dimensional Monte-Carlo procedure^{16,74,75}. This option is initiated by the following keywords:

```
MONTE_CARLO=YES, NMB_TRAJ=300
```

where `NMB_TRAJ` is the user-defined number of trajectories to compute. In such calculations, the semi-classical values of J and ℓ as well as quantum numbers j_{12} and m_{12} are all integers. Also note that in the case of Monte-Carlo sampling the elastic cross section is computed only approximately, while the differential cross section is not computed (due to the lack of accurate phase information, see below).

Evolution of the Monte-Carlo errors during this sampling process is written into the file `MONTE_CARLO_ERROR.out` for each state of the system individually and can be monitored by user. The final standard errors of transition cross sections are written

into the main output file `CROSS_SECTIONS.out`, for each transition individually.

Also, the projection is made for the number of trajectories needed to reach the desired accuracy, as indicated by the keyword `EPS_MONCAR`. After one Monte-Carlo run, the user can increase the value of `NMB_TRAJ` accordingly, set `RESTART=YES` and run the code again to finalize calculations, starting from the checkpoint file

`CHECK_POINT.DAT`.

2.3.4. Convergence Studies

Convergence studies with respect to several input parameters should be carried out by user. For the quantum part of the system sensitivity of results (cross section values) should be checked with respect to the basis set size `NMB_CHNLS`, the range of molecule-molecule distances used to compute transition matrix elements `RMIN` and `RMAX`, the corresponding number of points `GRD_R`, and the number of integration points for each internal degree of freedom (*e.g.*, parameters `GRD_ANG1`, `GRD_ANG2` and `GRD_ANG3` in the case of $\text{H}_2\text{O} + \text{He}$ system). If the PES is represented by expansion over spherical harmonics, then the convergence parameter is the number of terms `NMB_TERMS` (and, of course, what terms are included). For trajectory propagation, sensitivity of energy and probability conservation errors should be checked with respect to step size `TIME_STEP`, and, if the adaptive step-size is used, the value of tolerance `EPS_ODEINT`. For sampling of the initial conditions, convergence parameter is the upper limit of total angular momentum `JTOTU` (or, optionally, the maximum value of collision impact parameter `B_IMPCT`). If optional Monte-Carlo sampling of the initial states is chosen (`MONTE_CARLO=YES`) then the number of trajectories `NMB_TRAJ` is

also a convergence parameter. The value of `RMAX` may also affect MQCT trajectories, since it is used to set up the initial molecule-molecule separation. Note that `RMAX` can be specified larger than the range of the PES. In this case, the code will automatically extrapolate matrix elements using an attractive $-1/R^6$ function in the asymptotic range of distances (a linear function is used for extrapolation in the repulsive short-distance range).

Often, user will want to increase the number of channels relative to the previously run calculations, for example, in order to check convergence with respect to the basis set size, or to do calculations at higher collision energy, where the number of channels is typically larger. In this case our code allows to add new needed elements to the existing transition matrix, without re-computing the entire matrix. This is achieved, simply, by rerunning the code with new increased number of channels, using any method of channel specification available, for example, increasing the value of keyword `NMB_CHNLS` and adding new channels to the list `CHNLS_LIST` (or increasing the value of keyword `EMAX`, or using other appropriate keywords indicated in Table 3 of Section 2.6). The code will read the existing matrix from file, check whether all needed matrix elements are present, automatically compute the missing elements, update the matrix file and/or proceed with trajectory calculations, depending on what options are indicated by the user. One requirement is that *R*-grid remains identical to the one used in the previous calculations. However, the way of computing elements of the state-to-state transition matrix can be changed, for example, by increasing the number of integration points for the internal coordinates, or increasing the number of terms in the PES expansion. The

only requirement is that new channels are added at the end of the list, not at the beginning or stuffed in the middle (automatically taken care of if `EMAX` is used).

Also, user can always run calculations of dynamics with the number of channels smaller than that in the saved matrix file `MTRX_UF.dat`. The code will read the file and chose only those matrix elements that are necessary for this run. Again, the requirement is that the active channels are listed continuously from the beginning of the list, and only the channels at the end of the list can be omitted. If the user wants to exclude some states from the beginning or from the middle of the list, the keyword `EXCLUDE_STATES` can be used (the corresponding data file should be provided).

2.3.5. Propagation Options

Besides the default RK4 propagator, one can choose an adaptive step-size method by indicating:

```
PROPAGATOR=ODEINT, TIME_STEP=500.0, MIN_TMSTP=10.0,
EPS_ODEINT=1.0E-3
```

This method adjusts time-steps along each trajectory trying to keep accuracy below `EPS_ODEINT`, and is a slightly modified version of the code from Numerical Recipes¹.

Our version of this propagator enforces `MIN_TMSTP` to avoid an excessively long integration near the turning point. We recommend that users run their first calculations using the default RK4 propagator to determine a suitable value of `TIME_STEP` for their system and collision conditions, (by monitoring energy and norm conservation in the output file). Then, one can try to switch to the `ODEINT` by simultaneously setting `MIN_TMSTP` equal to this value, and increasing the value of `TIME_STEP` by an order of

magnitude or even more (which in `ODEINT` plays the role of the maximum time step allowed). We found that for the systems with deep molecule-molecule attraction potentials, such as dipole-dipole, this approach gives a considerable computational advantage. Also, the `ODEINT` propagator has an option `SINGLE_STEP` that commands to integrate the entire trajectory in one step. In this case the code automatically estimates the termination time for each trajectory (based on the impact parameter, the initial separation of collision partners, and the collision energy) and uses this number as maximum time step. This is the most efficient propagation option recommended for the production runs. Note that if `SINGLE_STEP` is chosen, then no propagation information is printed along the trajectory, no phases are computed, and thus no elastic or differential cross sections are calculated.

2.4. Special Cases of MQCT

2.4.1. Vibrational States and Transitions

For the vibrating-diatom cases, `SYS_TYPE=2` and `6`, the code will automatically generate a specified set of vibrational states using Morse parameters indicated in the input file. Vibrational energies are computed using a standard Dunham's formula. Vibrational wave functions are computed using recurrent relations⁸¹, and then are used to compute matrix elements for the corresponding state-to-state transitions. Integration is between the points `RMIN_VIBGRID` and `RMAX_VIBGRID` (indicated in the block `$BASIS`) using a constant-step quadrature of `GRD_VIB` points (indicated in the block `$POTENTIAL`). These are convergence parameters and should be checked by the user.

Note that this way of describing ro-vibrational transitions is expected to be reasonably accurate for low to moderate rotational and vibrational excitations, since it neglects ro-vibrational interaction. More reliable approach, accurate up to dissociation limit, is to compute numerically accurate ro-vibrational states using an external code (not provided) and feed them as input for the MQCT code. This is achieved by the keyword `LEVELS_FILE=YES`. If specified, the file named `USER_DEFINED_BASIS.DAT` is also required (copied or linked to the code directory), that should contain energies and wave functions of pre-computed states. The number of states in the files should be equal to `NMB_CHNLS` (indicated in the block `$BASIS`). The values and weights of grid points for numerical integration (can be non-equidistant) should also be specified. The number of points should be equal to `GRD_VIB` (indicated in the block `$POTENTIAL`).

2.4.2. Differential Cross Sections and Elastic Scattering

Calculations of differential cross sections involves phase information and computation of a coherent sum over all partial scattering waves⁷⁴, and thus requires propagation of MQCT trajectories for *all* allowed integer values of J and ℓ ⁸², which is default in the code. The keyword `DIFF_CROSS=YES` that can be used to request construction of the differential cross section. Angular resolution of the differential cross section is defined by `ANG_RES`. Angular dependence of differential cross section is printed into the file `DIFF_CROSS.out`.

However, when the Monte-Carlo sampling of the initial conditions is requested (for numerical efficiency, see above) the values of J and ℓ will be chosen randomly and only a few of them may be available for each initial degenerate state ($j_{12} m_{12}$). In this case

the meaningful determination of the deflection function, scattering phase and the differential cross section is technically challenging and is not implemented in the code. So, MONTE_CARLO=YES should not be used simultaneously with calculations of the differential cross section. Same considerations apply to the integral cross section for the elastic scattering channel, since it also requires the scattering phase. If the MONTE_CARLO=YES option is used, the value of elastic cross section should normally be ignored. In this case, the code prints the value of elastic cross section as zero. In many applications, the elastic and/or differential cross section are not needed. Then MONTE_CARLO=YES is the best option.

If the elastic and/or differential cross sections are needed for complex systems, the most efficient and robust approach is to use the optional keyword DL, in order to skip some values of ℓ and thus make the overall calculations more affordable. For calculation of the differential cross section the code still computes a coherent sum over all ℓ , but within the “boxes” of size DL the same values of scattering phase and probability amplitudes are used. The magnitude of DL becomes a convergence parameter in this case and should be carefully checked by convergence studies. Note that the full-quantum calculations often follow a similar approach, by skipping some values of the total angular momentum J of the system.

2.4.3. Trajectory Analysis and Resonances

There are several options in the code that allow users to visualize MQCT trajectories, or their most important properties. Opacity functions and deflection functions are printed by default, which gives dependencies of transition probabilities and scattering

angle on ℓ and b (but only for MONTE_CARLO=NO, which is default). Another useful option is to use keyword PRN_TRJCT to print out all information for a trajectory with indicated value of ℓ . By default, the information from trajectories with the initial $j_{12} = \max(j_1, j_2)$ and $m_{12} = 0$ is printed. Other values of the initial j_{12} and $|m_{12}|$ can be specified using optional keyword, for example: PRN_J12M12=3, 3. Plotting and inspecting the deflection function, opacity functions and trajectories is recommended, particularly at low scattering energies, when trajectories may be trapped at certain values of ℓ .

There are options in the code to deal automatically with trapped trajectories, if those occur. For such trajectories the number of loops (due to mutual rotation of collision partners around the origin), and the number of periods (due to mutual oscillations of collision partners along the intermolecular distance R) is determined. The option NMB_LOOPS=2 commands to stop propagation of orbiting trajectories after two full loops (the default value is 1). The option NMB_OSCIL=5 commands to stop propagation at the fifth outer turning point (the default value is 1). When such trapped trajectory is forced to stop, it is still analyzed in a standard way. However, the result of such analysis is somewhat arbitrary, since the termination point is also arbitrary. The option NO_RESONANCE=YES tells the code to remove looping and oscillating trajectories from analysis, which can be used for calculation of non-resonant contribution to the integral cross sections.

Note that differential cross sections and the elastic channel integral cross sections can't be computed rigorously at collision energies when at least one resonant trajectory is present, since in such cases the deflection function is undefined in the range of small

values of ℓ ^{74,82}. Good recipe for extracting resonance information from trapped trajectories is yet to be found⁸². In any case the code automatically detects trajectories that exhibit resonant behavior and prints some basic information about these trajectories in the file `RESONANCE_TRAJECT.out`, including the relevant values of ℓ . Then, if desired, the user can rerun the code with the option `PRN_TRJCT` employed, to obtain more detailed information for each resonant trajectory.

2.5. Summary

In this chapter we presented the code `MQCT` for calculations of rotationally inelastic scattering of molecules using mixed quantum/classical theory. `MQCT` calculations are now possible for collision of two general asymmetric top rotors, which is a feature unique to this code, unavailable in other existing codes, to our best knowledge. Vibrational states of diatomic molecules can be included in the basis set expansion, to carry out ro-vibrational calculations of excitation and quenching. The simplest input for our code uses defaults and thus is very short, easy to set-up and run by non-experts. The options available to expert users are listed in Section 2.6. The code was tested and debugged under Unix environment using two different compilers, Intel and GNU (Cori machine at NERSC), under the Linux on Cray XC30 (Edison at NERSC), but also on a PC under Windows 7 and 10.

The code takes advantage of intrinsic parallelism of the mixed quantum/classical approach, and is suitable for massively parallel calculations. A Monte-Carlo sampling procedure, implemented as option in the code, enables calculations for rather complicated systems. The coupled-states approximation can also be employed, at high collision

energies. Integral and differential cross sections can be computed for the elastic channel, through reconstruction of the deflection function and calculation of the scattering phase. Rotational symmetry of each molecule, and the permutation symmetry of two collision partners are both implemented. Orbiting trajectories can be identified and analyzed to gain some insight into resonant behavior at low collision energies.

Examples of the program input were given for $\text{H}_2\text{O} + \text{He}$ above. Example calculations is presented later for $\text{H}_2\text{O} + \text{H}_2$ in a broad range of collision energies. Performance of the code (scaling) was studied in the most demanding calculations on $\text{H}_2\text{O} + \text{H}_2\text{O}$. The version of the code distributed with this publication includes potential energy surfaces for $\text{H}_2\text{O} + \text{He}$, $\text{H}_2\text{O} + \text{H}_2$, and $\text{H}_2\text{O} + \text{H}_2\text{O}$. Example input files are also provided for these systems, to demonstrate several useful options of the code.

In the future, third level of parallelization can be implemented in the propagation subroutine of the code. Moreover, calculations for different collision energies, that are sequential in this version of the code, could in principle be parallelized, as well as calculations for different initial states of the system (current version starts at one chosen initial state, and should be launched for each initial state). More advanced techniques for propagation of the equations of motion, such as preconditioned Lanczos method⁸³, could also be implemented in MQCT. Another significant development would be to expand the code for calculations of ro-vibrational transitions beyond diatomic molecules, for example, for the bending mode in triatomic molecules, which typically has the lowest frequency and thus is the most important (e.g., in H_2O).

2.6. MQCT User Guide for Experts

2.6.1. Input Parameters for MQCT calculations

Three tables below give a comprehensive list of all required and optional input parameters for three blocks of the program input file: blocks \$BASIS, \$SYSTEM, and \$POTENTIAL. Default values are indicated, where applicable. A keyword has to be specified only if the value different from the default is desired. Datatype “real” corresponds to double precision. The values “YES” and “NO” correspond to logical datatype.

Special note for Table 5: For Gauss-Legendre integration of matrix elements user must indicate the number of quadrature points for each degree of freedom, but this depends on the system type. For all molecule + atom systems (SYS_TYPE=1 to 4) only one integer value should be assigned to each of GRD_VIB, GRD_ANG1, GRD_ANG2, and GRD_ANG3. But for all molecule + molecule systems (SYS_TYPE=5 to 0) two integer numbers should be given sequentially, separated by coma. Note, however, that depending on the system type, some of these numbers are dummy (not used) and can be arbitrary.

Table 3. Description of keywords for the block \$BASIS.

Keyword	Type, Range, Units	Description	Relevant SYS_TYPE
SYS_TYPE	integer, 0 to 9	1 -- rigid diatom + atom 2 -- vibrating diatom + atom 3 -- symmetric top + atom 4 -- asymmetric top + atom 5 -- diatom + diatom (both rigid) 6 -- vibrating diatom + vibrating diatom 7 -- symmetric top + diatom (rigid) 8 -- asymmetric top + diatom (rigid) 9 -- asymmetric top + symmetric top 0 -- asymmetric top + asymmetric top	
NMB_CHNLS	integer	Number of channels	all
CHNLS_LIST	integers	Quantum numbers to specify channels	all
INIT_CHNL	integers	Quantum numbers to specify the initial channel	all
EXCLUDE_STATES	default is "NO"	User can exclude specified states from the basis set, e.g., the weekly coupled states or the states with certain j_{12} , m_{12} .	all
BE, DE	real, positive, cm ⁻¹	Rotational constants B_e , D_e (exp. format for D_e)	1,2,7,8
A, B, C	real, positive, cm ⁻¹	Rotational constants A , B , C	3,4,7,8
BE1, DE1	real, positive, cm ⁻¹	Rotational constant B_e , D_e for molecule #1	5,6

BE2, DE2	real, positive, cm ⁻¹	Rotational constant B_e, D_e for molecule #2	5,6,7,8
A1, B1, C1	real, positive, cm ⁻¹	Rotational constant A, B, C for molecule #1	9,0
A2, B2, C2	real, positive, cm ⁻¹	Rotational constant A, B, C for molecule #2	9,0
WE, XE	real, positive, cm ⁻¹	Vibrational constant ω_e, x_e	2
WE1, XE1	real, positive, cm ⁻¹	Vibrational constant ω_e, x_e for molecule #1	6
WE2, XE2	real, positive, cm ⁻¹	Vibrational constant ω_e, x_e for molecule #2	6
JMIN, JMAX	integer	The range of rotational number j included in the basis set; optional, used to avoid listing all levels individually	1,2
VMIN, VMAX	integer	The range of vibrational number v included in basis set; optional, used to avoid listing all levels individually	2
JMIN1, JMAX1, JMIN2, JMAX2	integer	The range of rotational numbers included in basis sets for molecules #1, 2; option, used to avoid listing the levels	5,6
VMIN1, VMAX1, VMIN2, VMAX2	integer	The range of vibrational numbers included in basis sets for molecules #1, 2; option, used to avoid listing the levels	6
NCHL1, NCHL2	integer	Number of lower energy channels included for molecules #1, 2; optional, used to avoid listing the levels individually	5,6,7,8,9,0
EMAX	real, cm ⁻¹	Channel energy cut-off; only the states below it are included in calculations; option, to avoid listing all levels	all
EMAX1, EMAX2	real, cm ⁻¹	Channel energy cut-offs for molecules #1 and #2; only the states below this energy are included in calculations	5,6,7,8,9,0

SYMMETRY	default is “NO”	If “YES”, only the states coupled to the initial state are retained in the basis (ortho vs para states).	3,4,7,8,9,0
ATOMIC_MASSES	real, positive, amu	Masses of atoms in the diatomic; to determine COM	2,6
MORSE_DEPTH	real, positive, cm ⁻¹	Depth parameter of Morse oscillator (dissociation energy)	2,6
MORSE_WIDTH	real, positive, Bohr	Width parameter of Morse oscillator	2,6
MORSE_POSITN	real, positive, Bohr	Equilibrium Distance of Morse oscillator	2,6
RMIN_VIBGRID	real, positive, Bohr	Minimum diatomic bond length	2,6
RMAX_VIBGRID	real, positive, Bohr	Maximum diatomic bond length	2,6
WGHT_POSPAR	real, positive, ≤1.d0	Weight of positive total parity wave functions in the case of identical particles collision. Default is 1.d0	5,6,0
CHNL_ENERGS	real, cm ⁻¹	User can list energies of states (e.g., computed externally)	all
LEVELS_FILE	default is “NO”	If “YES”, user provides energies, wave functions and assignments of externally-computed states, in a file	all
CS_APPROX	default is “NO”	If “YES”, the coupled-states approximation will be used	all
IDENTICAL	default is “NO”	If “YES”, collision partners are treated as indistinguishable	5,6,0
PRINT_STATES	default is “NO”	If “YES”, prints out states and structure of coupling matrix	all

Table 4. Description of keywords for the block \$SYSTEM.

Keyword	Type, Range, Units	Description
LABEL	text	Name of your job
MASS_RED	real, positive, amu	Reduced mass of two scattering partners
RMIN, RMAX	real, positive, Bohr	Minimum and maximum values of distance between partners
B_IMPCT	real, positive, Bohr	Maximum value of collision impact parameter
JTOTL, JTOTU	integer	Lower and upper limits of total angular momentum J
DL	integer	Step size for orbital angular momentum ℓ , default is 1
NMB_ENERGS	integer	Number of collision energy values U to propagate
U_ENERGY	real, positive, cm^{-1}	List of collision energies U to propagate
UMIN, UMAX	real, positive, cm^{-1}	Minimum and maximum collision energies U
DU	real, positive, cm^{-1}	Step size for setting collision energies U
TIME_STEP	real, positive, au	Propagation time step (for RK4, ODEINT, etc.)
MIN_TMSTP	real, positive, au	Minimum time step allowed in ODEINT
TIME_LIM	real, positive, au	Time limit for propagation
EPS_ODEINT	real, positive, <1.d0	Relative error for step-size control in ODEINT
EPS_MONCAR	real, positive, %	Desirable error in Monte Carlo sampling of initial conditions
PROPAGATOR	text	RK4 is default, ODEINT is optional

NMB_LOOPS	integer, default is 1	Number of full loops (360 deg.) to propagate for orbiting trajectories
NMB_OSCIL	integer, default is 1	Number of outer turning points to propagate for oscillating trajectories
NO_RESONANCE	default is “NO”	If “YES”, orbiting trajectories are removed from analysis
DIFF_CROSS	default is “NO”	If “YES”, differential cross section is computed (elastic only)
ANG_RES	integer, default is 1000	Number of points for angular resolution of the differential cross section
MONTE_CARLO	default is “NO”	If “YES”, initial conditions are sampled randomly
NMB_TRAJ	integer, default is 100	Number of trajectories to sample using Monte Carlo (total number of trajectories)
CHECK_POINT	integer	Wall clock time (minutes after the start) to start writing a checkpoint file
RESTART	default is “NO”	If “YES”, program will start from a check point file
PRN_TRJCT	integer	Indicates the value of ℓ for which all the trajectory data will be printed
PRN_J12M12	two integers	Indicates the desired values of j_{12} and m_{12} for the option above
MPI_PERTRAJ	integer, default is 1	Number of CPUs (MPI tasks) to use for calculations of each trajectory

Table 5. Description of keywords for the block \$POTENTIAL.

Keyword	Type, Range, Units	Description	Relevant SYS_TYPE
READ_MTRX	default is “NO”	If “YES”, read the potential coupling matrix from file	all
SAVE_MTRX	default is “NO”	If “YES”, write the potential coupling matrix to file	all
UNFORMAT	default is “YES”	Saves matrix in binary form; set “NO” to save it as text	all
PROG_RUN	default is “YES”	Propagates trajectories; set “NO” to compute matrix only	all
E_UNITS	text	Energy units of PES: “A.U.”, “CM-1”, “KCAL” or “KLVN”	all
R_UNITS	text	Distance units for supplied PES: “A.U.” or “ANGS”	all
GRD_R	integer	Number of points for R -grid	all
GRD_VIB	integer / two integers	Number of points for vibrational grid / grids	2 / 6
GRD_ANG1	integer / two integers	Number of points for α -grid / grids	1,2,3,4,5/6,7,8,9,0
GRD_ANG2	integer / two integers	Number of points for β -grid / grids	1,2,3,4,5/6,7,8,9,0
GRD_ANG3	integer / two integers	Number of points for γ -grid / grids	3,4 / 5,6,7,8,9,0
VGRID_FILE	default is “NO”	If “YES”, PES values at grid points are stored/read to the file	6,7,8,9,0
EXPANSION	default is “NO”	If “YES”, the PES is represented by expansion over basis	except 2, 6
NMB_TERMS	integer	Number of PES expansion terms	except 2, 6
TERMS	sets of integers	List of the expansion terms (labeled appropriately)	except 2, 6
TERMS_ONFLY	default is “NO”	If “YES”, computes PES expansion on-the-fly for each R	except 2, 6

TERMS_FILE	default is “NO”	If “YES”, reads externally-computed PES expansion terms	except 2, 6
CALC_EXPANSION	default is “NO”	If “YES”, the expansion coefficients are computed.	except 2, 6
IR_BGN, IR_FIN	integer	The range of R -grid points used; defaults are 1 to GRD_R	all
RGRID_EQDS	default is “YES”	If “NO”, non-equidistant R -grid is generated by the code	all
RGRID_FILE	default is “NO”	If “YES”, user-defined R -grid is read from file	all
L_MAX	integer	Maximum value of index l in the expansion of the PES	all
M_MAX	integer	Maximum value of index μ in the expansion of the PES	3,4
L1_MIN, L1_MAX	integer	Min. and max. values of index l_1 in the expansion of the PES	5,7,8,9,0
L2_MIN, L2_MAX	integer	Min. and max. values of index l_1 in the expansion of the PES	5,7,8,9,0
M1_MAX	integer	Maximum value of index μ_1 in the expansion of the PES	5,7,8
M2_MAX	integer	Maximum value of index μ_2 in the expansion of the PES	9,0
PRINT_DIAGONAL	default is “NO”	IF “YES”, prints diagonal elements of transition matrix	all

2.6.2. Description of user-supplied data files and the corresponding subroutines

For several special cases (discussed further below), some of the input data must be generated externally by users and supplied in separate files. The following table gives brief description of these data files (extension `*.DAT`). Examples can be found in the directory `ROUTINES` of the code. In order to create properly formatted files users can employ our subroutines supplied with the code, all located in the file `user_input.f`. They are listed in the table below. Note that these are not ready-to-use utility programs to generate these data, but merely the examples of data formats required by the MQCT code.

Table 6. Description of the input data files for MQCT calculations.

Data File Name	Generating Subroutine	Brief Description
<code>USER_DEFINED_RGRID.DAT</code>	<code>DEFINE_RGRID</code>	Contains user defined (<i>e.g.</i> , non-equidistant) grid for the molecule-molecule distance R . Can be useful for deep short-range interaction potential energy wells.
<code>USER_DEFINED_BASIS.DAT</code>	<code>DEFINE_BASIS</code>	Contains channel labels (quantum numbers), energies, and wave functions of the externally computed ro-vibrational states. For <code>SYS_TYPE=2</code> and <code>6</code> the vibrational wave functions should be pre-computed on a grid. For system types <code>4</code> , <code>8</code> , <code>9</code> and <code>0</code> the rotational states (<i>e.g.</i> , of Kyrö Hamiltonian) should be represented by expansion over the basis set of symmetric-top eigenstates.
<code>PES_EXPAN_TERMS.DAT</code>	<code>EXPAND_PES</code>	Contains R -dependence of the expansion coefficients for analytic representation of the PES using the basis sets of spherical harmonics. Works for all values of <code>SYS_TYPE</code> , except <code>2</code> and <code>6</code> where the vibrational motion is involved.
<code>STATES_TO_EXCLUDE.DAT</code>	<code>EXCLUDE_STATES</code>	Optional. Undesired states can be excluded by listing in this file the state numbers (as they appear in the file <code>STATES.out</code>), and setting the keyword <code>EXCLUDE_STATES=YES</code> .

2.6.3. Options for PES representation and computation of the transition matrix

Within MQCT code there are four ways of computing the potential coupling matrix. Differences are in how the PES is represented and how the data are handled.

Description of the format for four options can be found in the file

`user_suppl_pot.f` in the directory `PES_USER`, and the file `pes_sys_type.f` in the main code directory `MQCT_v1.01`

Option 1: keyword `EXPANSION=NO`, which is the default. In this case user should provide the potential subroutine `USER_DEFINED_PES` that generates the value of potential energy as a function of the molecule-molecule distance R and the internal coordinates (Euler angles in the body-fixed reference frame, and bond lengths). MQCT code will use this subroutine to compute elements of the state-to-state transition matrix directly, by numerical integration over the internal molecular degrees of freedom. Multi-dimensional Gauss-Legendre quadrature is employed with the number of points indicated by the corresponding keyword in the input file (`GRD_VIB`, `GRD_ANG1`, `GRD_ANG2`, and `GRD_ANG3`). Such calculations are done for every grid point of the molecule-molecule distance R and the data are stored in the memory. For calculations of the collision process, when the values of matrix elements and their derivatives (for classical equations of motion) are needed at certain values of R along trajectory, one-dimensional cubic spline of each matrix element is computed.

Option 2: keyword `EXPANSION=YES`. In this case user should provide subroutine `USER_DEFINED_TERMS` that generates coefficients of expansion of the PES over basis set of spherical harmonics (different for different system types, see section 2.6.4). Description of the format can be found in the file `user_suppl_pot.f`. Using

these coefficients MQCT code will calculate elements of the state-to-state transition matrix analytically at every grid point of the molecule-molecule distance R , store them in the memory and finally spline (during the dynamics calculations, just like in the Option 1 above). This option is specifically created for users of MOLSCAT, since an identical subroutine is used there (called VSTAR) and can be employed here without modifications. The other benefit of this approach is that transitions forbidden by symmetry, and the corresponding states, can be excluded *a priori* to ease calculations and slightly improve accuracy. Finally, Option 2 can be used to confirm convergence of Option 1 (where forbidden transitions should show up negligible probabilities), and vice versa.

Option 3: keywords EXPANSION=YES, TERMS_FILE=YES. This case is methodologically equivalent to the Option 2 above, except that here user is required to supply the data file PES_EXPAN_TERMS.DAT that contains the externally computed expansion coefficients at every grid point of the molecule-molecule distance R (instead of the subroutine to compute them). This is convenient when these data are already available, say from literature. Format of the data file is described in the subroutine EXPAND_PES, see section 2.6.2. MQCT code will read these data as input, calculate elements of the state-to-state transition matrix analytically, store them in the memory and then spline for trajectory calculations as needed, like in the Options 1 and 2. Of course, the user-supplied subroutine suitable for Option 2 can also be used to pre-compute the expansion coefficients and create the data file for Option 3. Or, user can pre-run the MQCT code with the optional keyword CALC_EXPANSION=YES to generate the file PES_EXPAN_TERMS.DAT. In this case projection integrals are computed using multi-

dimensional Gauss-Legendre quadrature with the number of points indicated by `GRD_VIB`, `GRD_ANG1`, `GRD_ANG2`, and `GRD_ANG3`.

Option 4: keywords `EXPANSION=YES`, `TERMS_ONFLY=YES`. In this case no grid over the molecule-molecule distance R is employed, no data are stored in the memory, and no splining is involved. The user should supply the subroutine `USER_DEFINED_COEFFS` that will generate *both* the potential expansion coefficients and their R -derivatives at any value of R . The required format is described in the file `user_suppl_pot.f` in the directory `PES_USER`. Using this subroutine MQCT code will compute analytically the matrix elements and their R -derivatives on-the-fly, as requested by propagator along the trajectory. This approach is only practical if generation of the expansion coefficients and their derivatives is computationally inexpensive, for example, if their R -dependencies are described by simple analytic model (e.g., for simple molecular system). Other options, within the `USER_DEFINED_COEFFS` subroutine, would be to spline the expansion coefficients, or to re-compute the expansion at every point by projection, but those, again, would be practical for the simplest systems with smallest basis sets. Moreover, in the current version of the code Option 4 is implemented only for calculations with one processor per trajectory (*i.e.*, without the second level of parallelization). It can be used for debugging, for machines with small number of processors and small memory, and for model systems.

2.6.4. Expansion of the PES over the basis set of analytic functions

In the current version of MQCT we use PES expansions identical to those implemented in the MOLSCAT package for these system types:

SYS TYPE=1: for diatomic + atom the PES is expanded over the basis set of Legendre polynomials⁸⁴. To define the expansion terms by the keyword `TERMS`, user will specify only one integer number for each term, the value of l , which is a rank of Legendre polynomial. The values for different terms are separated by coma. The order of indicated terms defines the order in which they will be handled (read from `PES_EXPAN_TERMS.DAT`, computed by the subroutine `USER_DEFINED_TERMS`, summed into the matrix element, *etc.*). Note, that the total number of terms employed must be specified by the keyword `NUMB_TERMS`, before they are listed one by one. If user does not wish to list all terms, the code can automatically assign them based on the keyword `L_MAX`.

SYS TYPE=3 and 4: for any top + atom the PES is expanded over the basis set of spherical harmonics⁵⁷. User should specify two integer numbers for each term, l and its projection m (in this order, separated by coma), that define spherical harmonic functions. If user does not wish to list all the terms, the code can automatically assign them using the optional keywords `L_MAX` and `M_MAX`. Note that in the literature the symbols λ and μ are often used, instead of l and m .

SYS TYPE=5: for diatom + diatom the PES is expanded over the basis set of generalized spherical harmonics⁸⁵. For each term listed the user should specify three numbers: l_1 , l_2 , and l (in this order, separated by coma). Alternatively, the optional keywords can be employed to generate the terms automatically up to `L1_MAX`, `L2_MAX` and `L_MAX`.

However, for the following system types the PES expansions of MQCT are different from those used in MOLSCAT, since MOLSCAT uses the molecule-fixed reference frame⁵³, while MQCT exploits the body-fixed reference frame²⁵. Namely:

SYS_TYPE=7 and 8: for any top + diatom MQCT code uses expansion over normalized functions which are products of Wigner D -functions and spherical harmonics. Users should indicate four integers for each expansion term: l_1 , m_1 , l_2 and l (in this order, separated by coma). The option of generating these terms automatically is also available, through `L1_MAX`, `M1_MAX`, `L2_MAX` and `L_MAX`. The same expansion was used in the HYBRIDON package⁸⁶ and also in some earlier calculations but with different symbols: p_1 , q_1 , p_2 and p ⁵³. Subroutine `MFTOBF_CONV` (in the file `user_suppl_pot.f`) is available for conversion of the PES from the more standard molecule-fixed reference frame to the body-fixed reference used by MQCT.

SYS_TYPE=9 and 0: top + top collisions have never been studied before, although similar expansion was proposed in the past⁶¹. In the MQCT code the PES is expanded over the basis set of normalized functions which are products of Wigner D -functions for each molecule. The expansion terms are labeled by l_1 , m_1 , l_2 , m_2 and l . Note that value of m_2 can be negative integer and the code will read it without an error message. As in all previous cases, automatic generation of the terms is enabled by `L1_MAX`, `M1_MAX`, `L2_MAX`, `M2_MAX` and `L_MAX`. Note that in the literature symbol η was used, instead of m .

Also note that, if desired, the keywords `L1_MIN` and `L2_MIN` can be used for several system types, as indicated in the Table 5, to define the minimum values of labels for the expansion basis in the case of automatic generation of terms.

2.6.5. Computation of coupling matrix and/or potential expansion over the basis set

Both the direct calculation of transition matrix (default) and the expansion of PES over basis set of analytic functions (optional keyword `CALC_EXPANSION=YES`) deal with numerical integration over the internal degrees of freedom using multi-dimensional numerical quadrature. For both cases, the number of quadrature points should be indicated by user in the input file using keywords `GRD_VIB`, `GRD_ANG1`, `GRD_ANG2`, and `GRD_ANG3`. Integration over vibrational coordinate uses weights indicated for each point in the file `USER_DEFINED_BASIS.DAT`, or uses Gauss-Legendre quadrature for automatically-generated Morse oscillator states. Integration over Euler angles always uses Gauss-Legendre quadrature. Some of these are essential internal degrees of freedom, others are dummy variables, depending on the system, as described below:

`SYS_TYPE=1`: for diatomic + atom integration is carried out along β -angle only, with the number of points `GRD_ANG2`. The values of `GRD_ANG1` and `GRD_ANG3` are dummy. Vibrational degree of freedom is dummy for all `SYS_TYPE` but 2 and 6.

`SYS_TYPE=2`: for vibrating diatomic + atom, besides β -angle described above, the integral includes `GRD_VIB` points for vibration. The values of `GRD_ANG1` and `GRD_ANG3` are dummy, just as in `SYS_TYPE=1`.

`SYS_TYPE=3 and 4`: for any top + atom the number of points for angles β and γ is indicated by `GRD_ANG2` and `GRD_ANG3`, respectively. The value of `GRD_ANG1` is dummy.

`SYS_TYPE=5`: for diatom + diatom the number of points along two β -angles is given by two entries of the keyword `GRD_ANG2`, while the number of points for γ -angle

is indicated by the *first* entry of the keyword GRD_ANG3. The second entry of the keyword GRD_ANG3, and both entries of the keyword GRD_ANG1 are dummy.

SYS_TYPE=6: for vibrating diatom + diatom the number of points along each bond length is indicated by two entries of the keyword GRD_VIB, in addition to the angular coordinates of SYS_TYPE=5.

SYS_TYPE=7 and 8: for any top + diatom the number of points along two β -angles is given by two entries of the keyword GRD_ANG2, the number of points along α is given by the second entry of GRD_ANG1 (the first entry is dummy), while the number of points along γ is given by the first entry of the keyword GRD_ANG3 (the second entry is dummy).

SYS_TYPE=9 and 0: for top + top systems the number of points along α is given by the second entry of GRD_ANG1 (only the first entry is dummy), the number of points along two β -angles is given by two entries of the keyword GRD_ANG2, the number of points along two γ -angles is given by two entries of the keyword GRD_ANG3.

Several practical aspects of multi-dimensional integration for computing transition matrix directly, and/or for expanding the PES over the basis set, should be discussed. First of all, as mentioned previously, it is recommended to compute and store the transition matrix (into the file MTRX.DAT, or MTRX_UF.DAT) in a separate program run, independently from the main run of collision dynamics. This is optional for the case when the matrix is calculated by direct integration (Option 1 of section 2.6.3), but is mandatory in the case when the PES expansion is computed (*e.g.*, prior to using Option 3 of 2.6.3). Moreover, in the first run, initiated by the keyword CALC_EXPANSION to generate the PES expansion coefficients, the number of processors must be equal to the

number of requested expansion terms, since each processor will be responsible for computing one expansion coefficient. The code will compute the expansion coefficients and will stop, without proceeding to calculations of matrix elements or collision dynamics. Then, user should replace `CALC_EXPANSION` in the input file by `EXPANSION=YES` and run the code again with the number of processors appropriate for calculations of matrix elements (keywords `SAVE_MTRX=YES`, `PROG_RUN=NO`). Finally, the code should be run third time for the actual trajectory calculations (keywords `READ_MTRX=YES`, `PROG_RUN=YES`), with an appropriate value of `MPI_PERTRAJ` set up. In this procedure, one should be careful about the units of distance and energy. The file of expansion terms, printed by the code, `PES_EXPAN_TERMS.DAT`, will always contain the distance in Bohr and energy in wavenumber, irrespectively of the units of the potential energy surface routine used for the calculations of the expansion. If the expansion is used further (to compute the state-to-state transition matrix and/or the collision dynamics), the units should be set as Bohr and wavenumber in the `$POTENTIAL` block of the input file, to comply with the expansion file, rather than with the original PES routine that is not anymore used.

If the angular grid (for Option 1) is very large, or the number of expansion terms (for Option 3) is large, and in particular when the number of *R*-grid points is large, it may be convenient to split calculations of the matrix or the PES expansion into several runs. To do that, user can specify the range of *R*-grid to cover in one run, using keywords `IR_BGN` and `IR_FIN`. Results of successive runs are combined automatically into a single file for the matrix, or for the expansion terms and coefficients.

When computing the state-to-state transition matrix by direct integration (Option 1), or computing the PES expansion by projection (e.g., Option 3), it may be advantageous, in terms of CPU time, to keep in the memory the values of potential at the grid points, rather than calling the PES subroutine each time when the value for new point is needed. However, a very large grid (for larger molecules and complicated PES) may not fit as a whole into the memory of one CPU. For this case the option `VGRID_FILE=YES` is recommended. The code first generates the PES at the points of the grid and saves these data to the unformatted file `VGRID_UF.DAT`. The number of processors should be at least equal to the number of points of *R*-grid, or larger. Then the code loads this information into the memory of processors to compute matrix elements (or the expansion coefficients) but does it by slices, sequentially for each value of *R* on the grid, since calculation at each value of *R* is independent. Different processors will be responsible for computing different elements of the matrix, or different expansion terms. Note that if the expansion is being computed the code will save the data file `VGRID_UF.DAT` and will normally stop (except a rare special case when the number of *R*-grid points is equal to the number of the PES expansion terms). It should be run again with the number of CPUs equal to the number of the expansion terms. The code will read the data file `VGRID_UF.DAT` and proceed to calculations of the expansion coefficients, one term per processor. Calculations of matrix elements and the collision dynamics should be done in the following independent runs, as explained above.

In order to take the full advantage of symmetry (when the symmetry is not obvious) the code automatically neglects transitions described by matrix elements with absolute values smaller than `MIJ_CUTOFF=1.d-12`. If needed, an alternative value of

the cut-off criterion can be specified. This keyword can also be used to make calculations more efficient by disregarding transitions between the weakly coupled states. For this, a suitable value of `MIJ_CUTOFF` should be determined by the convergence studies.

Another relevant keyword is `MIJ_SHIFT`. By default, each matrix element is automatically shifted by its value at the last point of R -grid, to ensure that no transitions occur in the asymptotic region. This shift can be disabled by indicating `MIJ_SHIFT=NO`.

2.6.6. User-supplied PES subroutine

Formally, the potential energy surface subroutine `USER_DEFINED_PES` operates with the same coordinates for all system types, but, as it follows from section 2.6.5 (above), for certain system types, some of these coordinates are dummy variables. Namely, the input for the PES subroutine requires, besides the molecule-molecule distance R , one vibrational coordinate and three Euler angles for each collision partner (see the file `user_suppl_pot.f` in the directory `PES_USER`, or the file `pes_sys_type.f` in the code directory `MQCT_v1.01`). However, the vibrational coordinate is a dummy variable for all values of `SYS_TYPE`, except 2 and 6 where the vibrational motion of the diatomic is explicitly described. In the future, our plan is to add one vibrational degree of freedom (such as bending motion in triatomic molecules) for other system types, but this is not yet implemented in the present release of the code. Concerning the angular coordinates, some of them are dummy as described in section 2.6.5. For completeness, we summarized these properties in the Table 7 below, where dash denotes a dummy variable. We want to emphasize one more time that our reference

frame, called the body-fixed reference frame, tied to the molecule-molecule vector, is different from coordinates used in some other codes (such as MOLSCAT) where the reference frame is tied to one of the molecules (see section 2.6.5).

Table 7. Degrees of freedom in the user-supplied PES subroutine.

SYS_TYPE	R	r_1	r_2	α_1	β_1	γ_1	α_2	β_2	γ_2
1	distance	--	--	--	polar	--	--	--	--
2	distance	vibration	--	--	polar	--	--	--	--
3	distance	--	--	--	polar	azimuthal	--	--	--
4	distance	--	--	--	polar	azimuthal	--	--	--
5	distance	--	--	--	polar	azimuthal	--	polar	--
6	distance	vibration	vibration	--	polar	azimuthal	--	polar	--
7	distance	--	--	--	Euler	Euler	azimuthal	polar	--
8	distance	--	--	--	Euler	Euler	azimuthal	polar	--
9	distance	--	--	--	Euler	Euler	Euler	Euler	Euler
0	distance	--	--	--	Euler	Euler	Euler	Euler	Euler

CHAPTER 3. APPLICATION OF MQCT TO STUDY ROTATIONAL INELASTIC SCATTERING OF $\text{H}_2\text{O} + \text{H}_2$ AND $\text{H}_2\text{O} + \text{H}_2\text{O}$ COLLISIONS

3.1. Introduction

Water is one of the key molecules in chemistry. In the nature, water acts as a solvent, temperature buffer, metabolite, and habitat for many creatures.⁸⁷ On Earth it is present everywhere in different physical states (solid, liquid, or gas)⁸⁸ and therefore it played an important role in the appearance and evolution of living organisms. Not only on Earth, but it is also ubiquitous in astrophysical environments. For example, it is one of the main components in cometary ices in the solar system. In the interstellar medium the water molecules in molecular clouds keeps the energy balance and promote star-formation due to significant abundance in the environment as well as strong dipole moment. Water is the third most abundant molecule in the interstellar medium (ISM)⁸⁹, and it is among the molecules that contain most of the oxygen.⁹⁰ It acts as the primary source of oxygen in warm astrochemical environments due to evaporation of the icy grain mantles,^{91,92} and all the gaseous oxygen transforms into the water during an endothermic reaction.⁹³ For all these great many aspects, the modeling of water molecules in space is in the focus of astrochemists.

The study of the energy transfer during collisional excitation and quenching of the water rotational states are crucial in this context. It is found that the most abundant species in cold molecular clouds (where $T = 10$ K roughly) are He or H_2 . On the other hand, atomic or molecular hydrogen and He are found to be most abundant in relatively

warm environments (such as translucent clouds where $T = 70$ K roughly and photon-dominated regions where $T = 200$ K approximately). Thus, the collision of the water molecule with He, H_2 , or even other water molecules in the ISM environments and the theoretical modeling of these rotational energy transfer processes is very important.

The study of rotational excitation and quenching of $H_2O + He$ has been done rigorously using the MQCT method and benchmarked with available full quantum results by Semenov *et al.*⁹⁴ In this chapter, we apply our methodology to study the collision of $H_2O + H_2$ and compare with available full quantum results. As for the collision of $H_2O + H_2O$, I would like to point one more time that none of the full quantum codes available in the community can do calculations on this system. Our code MQCT enables scattering calculations of two asymmetric top rotors, which was not possible in the past.⁷⁹ The results obtained using our method (state-to-state transition cross sections) for $H_2O + H_2O$ collision are then converted to thermally averaged cross sections to compare with other available data.

In this chapter, we first discuss the equations of motion for quantum and classical degrees of freedom of our method and then introduce necessary steps within the mixed quantum/classical framework to appropriately treat the symmetry of molecules, such as inversion symmetry and exchange parity. Cross sections for state-to-state transitions obtained by our method are then benchmarked against full quantum results for $H_2O + H_2$ and thermally averaged cross sections compared with available semi-classical data for $H_2O + H_2O$ system.

3.2. Theoretical Framework

3.2.1. MQCT Classical and Quantum Equations

Here we briefly outline the major components of the mixed quantum/classical theory of inelastic scattering. More detailed description can be found in the recent literature.^{1,79} The collision event can be thought of classically: At the initial moment of time two collision partners are in the asymptotic range, separated by large distance R , that shortens during the time of collision and increases again as collision partners leave the interaction region. The deflection process is determined by change of the azimuthal angle Φ . Time evolution of these continuous *classical* variables and their conjugate momenta P_R and P_Φ is described by the classical-like equations of motion:

$$\dot{R} = \frac{P_R}{\mu} \quad (13)$$

$$\dot{\Phi} = \frac{P_\Phi}{\mu R^2} \quad (14)$$

$$\dot{P}_R = - \sum_n \sum_{n'} e^{i\varepsilon_n^{n'} t} \sum_m \frac{\partial M_n^{n'}}{\partial R} a_{mn'}^* a_{mn} + \frac{P_\Phi^2}{\mu R^3} \quad (15)$$

$$\begin{aligned} \dot{P}_\Phi = & -i \sum_n \sum_{n'} e^{i\varepsilon_n^{n'} t} \sum_m M_n^{n'} \\ & \times \left[a_{m-1,n'}^* a_{mn} \sqrt{j'(j'+1) - m(m-1)} \right. \\ & + a_{m+1,n'}^* a_{mn} \sqrt{j'(j'+1) - m(m+1)} \\ & - a_{mn'}^* a_{m-1,n} \sqrt{j(j+1) - m(m-1)} \\ & \left. - a_{mn'}^* a_{m+1,n} \sqrt{j(j+1) - m(m+1)} \right] / 2 \end{aligned} \quad (16)$$

In these equations $\varepsilon_n^{n'} = E_{n'} - E_n$ is used to label energy differences between the initial (lower index) and the final (upper index) internal states of the system, whereas $a_{mn}(t)$ represent time-evolving probability amplitudes for these *quantized* states:

$$\begin{aligned} \dot{a}_{mn} = & -i \sum_{n'} e^{i\varepsilon_n^{n'}t} \sum_m M_{n'}^n a_{mn'} \\ & - i\dot{\Phi} \left[a_{m-1,n} \sqrt{j(j+1) - m(m-1)} \right. \\ & \left. + a_{m+1,n} \sqrt{j(j+1) - m(m+1)} \right] / 2 \end{aligned} \quad (17)$$

The last term of Eq. (17) describes Coriolis coupling between states with $\Delta m = \pm 1$, driven by classical angular speed $\dot{\Phi}(t)$. Neglecting this term leads to the coupled-states (CS) approximation within MQCT, while retaining this term corresponds to the fully-coupled version of MQCT (or coupled-channel MQCT). Matrix $M_{n'}^n(R)$ in Eqs. (15)-(17) is a potential coupling matrix, its R -dependent elements are real, time independent, and are different for different values of m . The range of m is between $-\min(j, j')$ and $+\min(j, j')$. The total angular momentum of two molecules $\mathbf{j} = \mathbf{j}_1 + \mathbf{j}_2$ is quantized in MQCT. The corresponding eigenfunctions can be formally expressed through states of two coupled rotors:

$$\Psi_{mn}(\Lambda_1, \Lambda_2) = \sum_{m_1 m_2} (j_1 m_1 j_2 m_2 | jm) \Psi_{m_1 n_1}(\Lambda_1) \Psi_{m_2 n_2}(\Lambda_2) \quad (18)$$

Coefficients of this expansion, $(j_1 m_1 j_2 m_2 | jm)$, the so-called Clebsch-Gordan coefficients, are non-zero only if $m = m_1 + m_2$ and $|j_1 - j_2| \leq j \leq j_1 + j_2$, where m is

projection of \mathbf{j} onto the molecule-molecule vector $\mathbf{Q} = (R, \Phi)$. A composite index n is used to label the total set of quantum numbers for the system, $n = \{j, j_1 k_1^A k_1^C, j_2 k_2^A k_2^C\}$. For the two scattering partners the sets of state labels are $n_1 = \{j_1 k_1^A k_1^C\}$ and $n_2 = \{j_2 k_2^A k_2^C\}$, thus, one can also write $n = \{j, n_1, n_2\}$. The rotation of each scattering partner is treated quantum mechanically and is described by a set of usual Euler angles: $\Lambda_1 = (\alpha_1, \beta_1, \gamma_1)$ for molecule one and $\Lambda_2 = (\alpha_2, \beta_2, \gamma_2)$ for molecule two. According to standard notation, rotational states of an asymmetric top are labelled (in addition to j_1 and m_1 for molecule one) by quantum numbers k_1^A and k_1^C that represent projections of \mathbf{j}_1 onto the principal axis of inertia with smallest and largest values of rotational constants, respectively. And similar for k_2^A and k_2^C for the angular momentum \mathbf{j}_2 of molecule two (in addition to j_2 and m_2).

The potential coupling matrix is diagonal in m (*i.e.*, its elements for transition $nm \leftarrow n'm'$ are non-zero only if $m = m'$) but the actual values of non-zero matrix elements do depend on m . For given m the matrix element for transition $n \leftarrow n'$ is:

$$M_{nn'}^n(R) = \langle \Psi_{mn}(\Lambda_1, \Lambda_2) | V(R, \Lambda_1, \Lambda_2) | \Psi_{mn'}(\Lambda_1, \Lambda_2) \rangle \quad (19)$$

Here $V(R, \alpha_1, \beta_1, \gamma_1, \alpha_2, \beta_2, \gamma_2)$ is the potential energy hypersurface for the molecule-molecule interaction, expressed through the same variables.

It should be stressed that here we use the so-called *body-fixed* reference frame, where z -axis is defined to pass through the centers of mass of two molecules (*i.e.*, is tied to the classical molecule-molecule vector \mathbf{Q}). As collision progresses, this axis turns together with collision partners relative to the space-fixed reference frame (same as

vector \mathbf{Q}), and this effect is incorporated into the equations of motion (13)-(17).

Projection m_1 of momentum \mathbf{j}_1 and projection m_2 of momentum \mathbf{j}_2 are made onto this body-fixed z-axis, or equivalently on \mathbf{Q} .

3.2.2. Molecular Symmetry

Rotational states of asymmetric-top molecules are split onto two groups, called para- and ortho-states. We define them based on what values of the quantum number k participate in expansion of wave function over the basis of symmetric-top eigenstates. Namely, for each j even values of k produce para-states, while odd values of k produce ortho-states. Even and odd values of k never mix⁹⁵. For symmetric molecules, such as H_2O , transitions are allowed within each group only, and are exactly forbidden between the para- and ortho-states, due to the symmetry of potential of interaction of the molecule with a quencher (any quencher). Including all states would not cause a problem, but would be meaningless since the efficiency of calculations would be reduced. If the states are specified explicitly as a list, the user should take care of this issue manually (for assignments of rotational states of water as ortho/para see Table C1 in Ref. [79]). But, if the basis set is generated automatically (*e.g.*, using the keyword `EMAX`), user has an option to indicate `SYMMETRY=YES`, for reducing the basis set size to one symmetry only, depending on symmetry of the initial state.

Note that in asymmetric molecules, such as methyl formate⁹⁶, all transitions are allowed, and all states should be included in the basis. Thus, indicating the keyword `SYMMETRY=YES`, would lead to unphysical results in this and other cases with no symmetry, and normally should not be done. In the molecule + molecule case, symmetry

consideration will be applied to the states of each molecule individually, for example, one can compute collisions of para-water with ortho-hydrogen, etc.

3.2.3. Collisions of Identical Molecules

When identical molecules are collided (*e.g.*, $\text{H}_2\text{O} + \text{H}_2\text{O}$) one should choose to treat them as indistinguishable, by indicating the keyword `IDENTICAL=YES` in the input file. In this case only one set of rotational quantum numbers is needed on input, and the unique channels only should be specified. For example, if the state (1,1,1, 0,0,0) of $\text{H}_2\text{O} + \text{H}_2\text{O}$ is already specified, one should not include the state (0,0,0, 1,1,1) since two molecules are treated as indistinguishable.

Symmetry considerations discussed in the previous subsection apply to each molecule individually, which results in three manifolds of uncoupled rotational states for the system of two indistinguishable molecules: para + para, ortho + ortho, and para + ortho collisions. If the basis set is specified explicitly as a list of states, the user should make efforts to exclude the uncoupled states. If the basis set is generated automatically (employing the keyword `EMAX`, or keywords `EMAX1` and `EMAX2`), user has option to minimize the number of channels by choosing `SYMMETRY=YES`. Again, only the states coupled to the initial state would be included, based on symmetry considerations.

For scattering of two identical collision partners there is one more effect of symmetry, related to swapping the two molecules, which can be done in two ways, by adding or by subtracting their wave functions. The resultant states are energetically degenerate, of course, but transitions between them are forbidden⁷⁹. To distinguish between the two manifolds of uncoupled states one should use the *exchange parity* (\pm).

This sign, together with the orbital angular momentum quantum number ℓ of collision, affect the values of state-to-state matrix elements through a factor of $\pm(-1)^\ell$, as it was demonstrated by Eq. (25) in Ref. [79]. It appears that in general, *two* separate MQCT calculations are needed in the case of identical particle scattering: first run for $+(-1)^{\text{even}}$ and $-(-1)^{\text{odd}}$, and second run for $+(-1)^{\text{odd}}$ and $-(-1)^{\text{even}}$. Note that each of these two calculations includes all values of ℓ , both even and odd. The results are converted then into four cross sections: $\sigma^{(+)\text{evn}}$ and $\sigma^{(-)\text{odd}}$ from the first run, and, $\sigma^{(+)\text{odd}}$ and $\sigma^{(-)\text{evn}}$ from the second run, respectively. If IDENTICAL=YES is chosen in the input file, user can also employ the optional keyword WGHT_POSPAR. The default value is one, which leads to the overall cross section computed as $\sigma^{(+)} = \sigma^{(+)\text{evn}} + \sigma^{(+)\text{odd}}$ from results of the two runs (done independently and consequently by the code). The value of zero for WGHT_POSPAR, in contrast, commands to do produce $\sigma^{(-)} = \sigma^{(-)\text{evn}} + \sigma^{(-)\text{odd}}$ based on results of the two runs. For any value of this keyword in the range between zero and one, both $\sigma^{(+)}$ and $\sigma^{(-)}$ will be computed and included into the final cross section with appropriate weights (such that their sum is unity).

Trivial cases occur when both molecules are in the same initial state, such as (0,0,0, 0,0,0) state of $\text{H}_2\text{O} + \text{H}_2\text{O}$ system. In this case, negative values of $\pm(-1)^\ell$ turn wave function of the system into null (since the total internal parity p is positive, (Note, this is different from the total “internal” parity of the state defined in Ref. [79] as $p = (-1)^j(-1)^{\kappa_1+\kappa_2}p_1p_2$, where j is the value of total angular momentum of two molecules, κ_1 and κ_2 are their ortho/para assignments, p_1 and p_2 are their inversion parities. The value of p remains unaffected by the swap.) see Eq. (21) and Table C1 of Ref. [79]).

Thus, only one MQCT run is needed, which produces $\sigma^{(+)} = \sigma^{(+)\text{evn}}$ and $\sigma^{(-)} = \sigma^{(-)\text{odd}}$. Moreover, if the spin weight of the positive parity is one, as indicated by the keyword `WGHT_POSPAR`, then the overall cross section is equal to just $\sigma^{(+)\text{evn}}$, which requires calculations with even values of ℓ only. The case of negative total internal parity of the initial state would be handled similarly and would require only odd values of ℓ . This would be true for $j = 1$ component of the $(1,1,1, 1,1,1)$ state of $\text{H}_2\text{O} + \text{H}_2$ system. Our MQCT code recognizes such special cases and carries out only the necessary calculations.

3.3. Results

3.3.1. Comparison of CC-MQCT with Full Quantum results for $\text{H}_2\text{O} + \text{H}_2$

Here we present new data obtained with MQCT code for $\text{H}_2\text{O} + \text{H}_2$. Note that in the past the mixed quantum classical approach has not been applied to any asymmetric top rotor + diatom system, so, these are the first calculations of this sort.

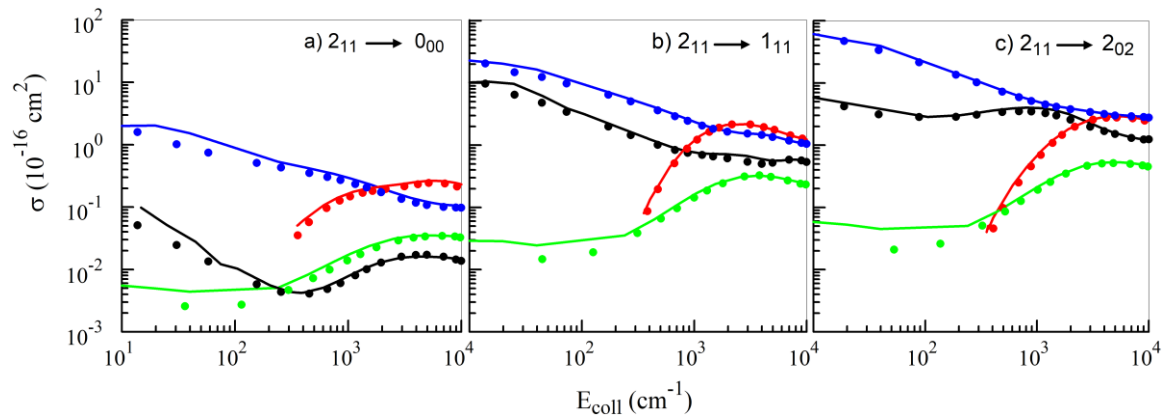


Figure 6: Cross sections for quenching of the excited rotational state 2_{11} of H_2O onto the lower levels: 0_{00} , 1_{11} , and 2_{02} . Black and blue lines represent the elastic H_2 channels with $j_2 = 0$ and $j_2 = 2$, respectively. Red line represents excitation of H_2 from $j_2 = 0$ to $j_2 = 2$ while green line describes quenching of H_2 from $j_2 = 2$ to $j_2 = 2$. Results of MQCT are indicated by symbols; full-quantum results of MOLSCAT are shown by lines.

In Figure 6 we show results for quenching of the excited rotational state 2_{11} of H_2O into three lower energy states: 0_{00} , 1_{11} and 2_{02} . Collision energy varies through four orders of magnitude range of values, from 10 to 10,000 cm^{-1} . Each frame of Figure 6 has four cross section dependencies that correspond to various initial/final states of H_2 . Namely, black and blue symbols describe elastic H_2 channels $j_2 = 0$ and $j_2 = 2$, red symbols describe rotational excitation of H_2 from $j_2 = 0$ to $j_2 = 2$, whereas green symbols describe rotational quenching of H_2 from $j_2 = 2$ to $j_2 = 0$ (all happening simultaneously with rotational quenching of H_2O , as explained above). From Figure 6 one can see that the overall quenching processes (black, green, blue) have no energy thresholds and in the low energy range the values of cross sections slowly grow as collision energy is reduced. In contrast, the overall excitation processes (red in three frames of Figure 6) all have a well-defined threshold energy, where the value of cross section drops sharply as energy is reduced. This happens because the excitation of H_2 from $j_2 = 0$ to $j_2 = 2$ requires more energy than can be released by the quenching of H_2O (2_{11}), so, even when combined these transitions require some minimal amount of energy, which should come from the relative motion of the colliding partners.

In order to benchmark the accuracy of these MQCT predictions we carried out the full-quantum calculations using MOLSCAT package⁵³, for the same collision processes in the $\text{H}_2\text{O} + \text{H}_2$ system. The size of rotational basis set was also the same: for water the states up to $j = 4$ and for hydrogen the states up to $j = 2$ were considered, but only the states with combined rotational energy below 600 cm^{-1} were retained. These full-quantum data are presented in Figure 6 as solid lines (of matching colors), and thus can be compared with MQCT results (symbols). One can see that, overall, the two sets of data

are very similar. The behavior of cross section near threshold energy for the excitation process is predicted correctly by MQCT (red symbols vs lines), as well as the overall dependencies of cross sections on collision energy. At higher energies the results of MQCT become nearly identical to the full-quantum results of MOLSCAT, as expected. At lower collision energies the differences become somewhat larger, as one could also expect, but the relative magnitudes of all state-to-state transition cross sections in the system still remain correct. For simplicity, we removed resonances from Figure 6, but it should be stressed that the mixed quantum/classical approach can offer some useful insight into the resonant phenomena too (through analysis of orbiting trajectories⁸²).

It can also be noted that MQCT data presented above are in very good agreement with results of the most rigorous and complete study of water quenching, carried out by Dubernet and coworkers⁴². Three frames of Figure 6 here can be compared with Figs. 1(a-c) of Ref. [42], which indicates good agreement, although it should be noted that our convergence parameters were not identical to those of Ref. [42], where the basis sets size was progressively increased as a function of collision energy.

We also carried out calculations for the excitation of para- and ortho-water in their ground states, $\text{H}_2\text{O} (0_{00})$ and $\text{H}_2\text{O} (1_{01})$ respectively, by para- and ortho-hydrogen ($j = 0, 1, 2$) for one value of collision energy, 574 cm^{-1} . Again, for the purpose of benchmarking, two sets of calculations were conducted, using our MQCT code and using the full-quantum code MOLSCAT⁵³, with the same rotational basis set as above. The resultant cross sections are presented in Figure 7, in the upper row for the states of para-water, and in the lower row for the states of ortho-water. Their values vary through three orders of magnitude range and demonstrate a systematic very good agreement between

MQCT (red) and MOLSCAT (blue) for all kinds of transitions. This comprehensive survey serves to show that symmetry properties of rotational states are captured correctly by our method and code, describing allowed and forbidden transitions between the ortho- and para- states of molecules. In particular, here we carried out separate calculations for four combinations of allowed transitions between the para and ortho states in water and in hydrogen molecules. But also, we carried out additional calculations where all these states were included to check that, for the transitions forbidden by symmetry (such as between ortho- and para-states of the same molecule), the values of cross sections would come out close to numerical zero. In practice it is also useful to run such test in order to determine the level of convergence of the code.

It can finally be noted that the data presented in Figure 7 are in very good agreement with results of Wiesenfeld and coworkers⁶⁰ computed using MOLSCAT, but

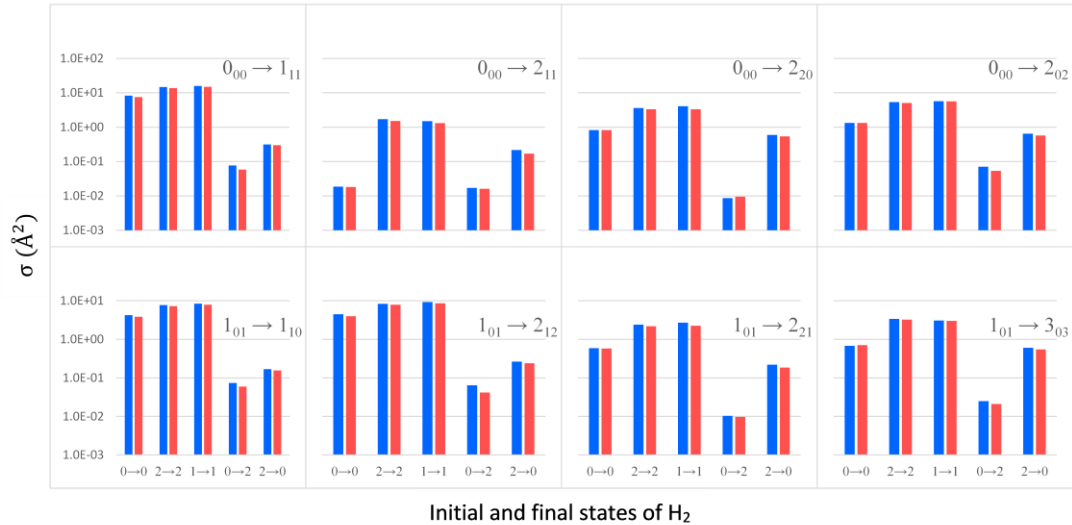


Figure 7: Cross sections for excitation of the ground state para-H₂O (0_{00}) and ortho H₂O (1_{01}) by para-H₂ ($j_2 = 0, 2$) and ortho-H₂ ($j_2 = 1$). Upper row is for para-H₂O, lower row is for ortho-H₂O. The final state of water is indicated in each frame, while the initial and final states of H₂ are listed along the horizontal axis. Results of MQCT are in red; full-quantum results of MOLSCAT are in blue.

with somewhat larger basis set (see Fig. 6 and Table 3 in Ref. [60]). Those data, in turn, were shown to be in excellent agreement with experimental results, and thus we can claim that cross sections obtained by MQCT compare favorably against the available experiments. Therefore, the code MQCT can be used for reliable computational prediction of state-to-state transition cross sections in the inelastic molecular collision processes.

3.3.2. Scattering Calculation of $\text{H}_2\text{O} + \text{H}_2\text{O}$

After successfully testing our code with $\text{H}_2\text{O} + \text{H}_2$ calculations, it was time to apply to the most complicated scattering calculation possible, a system of two asymmetric top rotors. A set of MQCT calculations was carried out for $\text{H}_2\text{O} + \text{H}_2\text{O}$ system at one collision energy $U = 533.3 \text{ cm}^{-1}$ that corresponds to thermal energy at $T = 800 \text{ K}$. We focused on transitions between the states $j = 0, 1$, and 2 of the target water molecules. Since we are here computing the thermally averaged cross-sections, the state-to-state inelastic cross-sections are summed over the final states of the quencher molecule, the ‘Billing correction’ of the collision energy U was not employed. ODEINT integrator was used to propagate MQCT trajectories. First of all, we found that largest contributions to the transition probability come from the relatively large impact parameters b and correspond to the long-range interaction between the two water molecules. We determined that in these conditions we can include only 1 out of 20 values of the orbital angular momentum quantum number, i.e., $\Delta L = 20$ (1 out of 20 trajectories is propagated, skipping 19). The error associated with this approximation is about 6 per cent of the cross-section value on average (4 - 8 per cent for various individual

transitions). We found, however, that we must start these trajectories relatively far, at a distance of $R_{max} = 100$ Bohr between the molecules, and we must cover a broad range of impact parameters, up to $b_{max} = 60$ Bohr.

We have opted to treat the two water molecules as distinguishable and count their degenerate states as belonging to the same channel. Namely, if before the collision the initial states are 0_{00} and 1_{11} for molecules 1 and 2, but after the collision the states are 1_{11} and 0_{00} for molecules 1 and 2 (i.e., swapped), we say that the corresponding probability contributes to the elastic channel, and is not counted in the inelastic transition probability. Note that normally the probability of such transitions (i.e., $0_{00}1_{11} \rightarrow 1_{11}0_{00}$) is large since the states are degenerate. With this ansatz, we tested convergence of the thermally averaged cross-sections with respect to the basis set size of the target molecule and found that if we are looking at the transitions between $j = 0, 1$, and 2 then excluding the states with $j = 3$ and above leads to the differences of cross-section values about 5 per cent on average (0.3 - 13 per cent for individual transitions). It is therefore safe to exclude $j = 3$ and above from the basis set of the target molecule. Then we tested convergence of cross-sections with respect to the basis set size of the projectile molecule and found that this is the most demanding aspect. First, we included the states up to $j = 2$, then up to $E = 200$, 250, and finally 300 cm^{-1} , but we cannot really claim that the result is converged. Indeed, this part of spectrum is within the collision energy. Adding more states to the basis set of the quencher does affect cross-sections. Including more states is computationally expensive, so we stopped without reaching convergence. The results presented in the paper were obtained with the basis set that includes six lowest lying states for the target H_2O (up to $E = 200 \text{ cm}^{-1}$) and 10 lowest lying states of the quencher H_2O (slightly above

$E = 300 \text{ cm}^{-1}$). The overall convergence is estimated to be of the order of 25 per cent of the cross-section values. Numerical cost of these calculations exceeded 100000 CPU hours at the Cori machine at NERSC.

Using MQCT code,¹ we carried out a set of calculations of excitation and quenching of several states of para- and ortho- H_2O by collisions with another H_2O molecule. The target and quencher molecules in these MQCT calculations were considered distinguishable, and a thermal distribution of rotational states was assumed for the quencher H_2O at $T = 800 \text{ K}$. The obtained thermally averaged cross-sections result is presented in Figure 8. One can see that, overall, the results of the MQCT method and

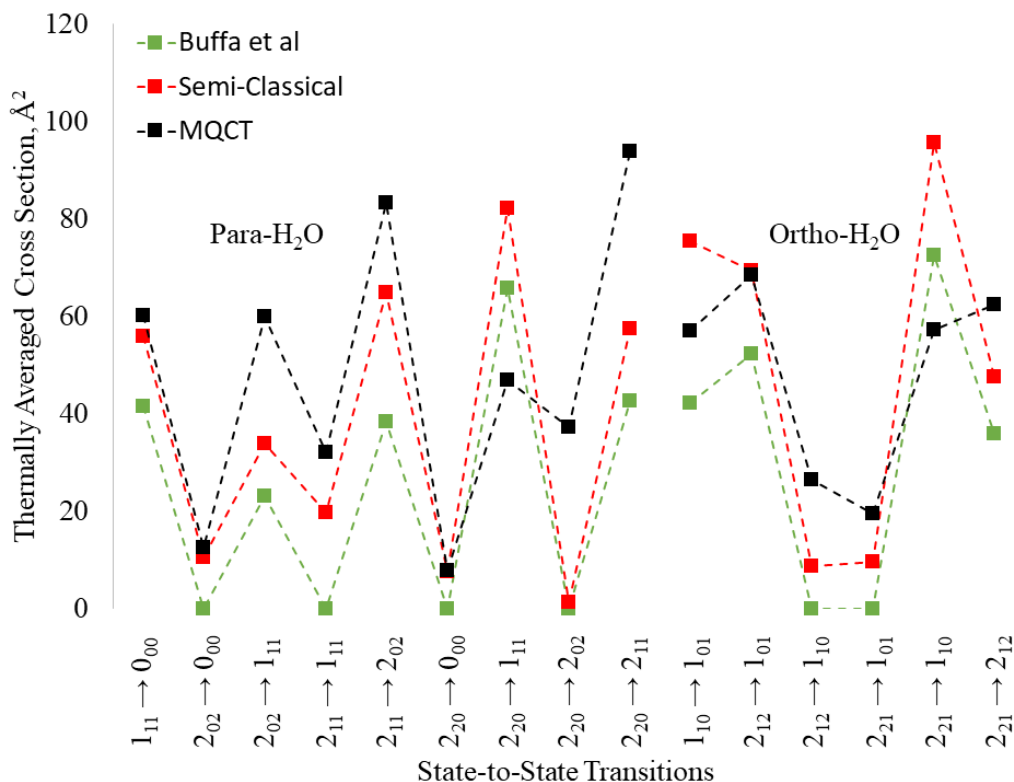


Figure 8: Comparison of results of the semi-classical method (red) vs. those obtained using MQCT method (black) for para- H_2O (left) and ortho- H_2O (right). Thermal distribution of the rotational states in the quencher H_2O and the collision energy corresponds to $T = 800 \text{ K}$.

semiclassical theory developed by Dubernet *et al*⁹⁷. are in good semiquantitative agreement. Importantly, both methods predict the same propensity pattern for state-to-state transitions in $\text{H}_2\text{O} + \text{H}_2\text{O}$ collisions, namely: the transitions with odd $\Delta k_a = 1$ are characterized by systematically larger cross-sections, whereas the transitions with even $\Delta k_a = 0$ and 2 always exhibit smaller cross-sections. Moreover, this trend is found in both para- H_2O and ortho- H_2O . For several transitions that describe quenching to the ground state, such as $1_{11} \rightarrow 0_{00}$, $2_{02} \rightarrow 0_{00}$ and $2_{20} \rightarrow 0_{00}$ in para- H_2O and $2_{12} \rightarrow 1_{01}$ in ortho- H_2O , the two methods gave very similar values of cross-sections (less than 5 per cent difference). Larger differences are typical for other transitions presented in the figure. In particular, we found that for the transition $2_{20} \rightarrow 2_{02}$ in para- H_2O our code gave much larger value of cross-section than the semiclassical method. However, we want to stress that one should not expect a perfect agreement because, first of all, the MQCT code uses a different built-in potential energy surface of Szalewicz and coworkers⁶¹ and therefore some differences are expected. Secondly, MQCT calculations for $\text{H}_2\text{O} + \text{H}_2\text{O}$ system are very demanding computationally and therefore these were carried out with a relatively smaller basis set and with relaxed convergence criteria. For the sake of comparison, the results of Buffa *et al.*⁹⁸ are also included in Figure 8. Transitions dominated by the quadrupole interaction ($\Delta k_a = 0$ and 2) are zero in results of Buffa *et al.* and for most of the $\Delta k_a = 1$ transition, but not all, our results seem closer to the semiclassical results.

3.4. Summary

In this chapter, we applied MQCT to study the inelastic scattering of water molecule with other molecules in the vacuum conditions, such as H_2 and H_2O , specific to astrophysical environment. The rotational excitation and quenching of water molecules are rather important in the field of astrophysics, and the collisional rate constants for these processes would be useful for astronomers. MQCT is the only code in the community that allows the study of the collision of two asymmetric top rotors. Application of this methodology to $\text{H}_2\text{O} + \text{H}_2$ rotationally inelastic scattering shows excellent accuracy as demonstrated by benchmarking against the full-quantum coupled-channel and experimental calculations from literature. MQCT was able to correctly predict the energy threshold observed for rotational excitation of H_2 . Moreover, MQCT appropriately handles the molecular symmetry by properly treating allowed *vs.* forbidden transitions. As for the calculation of $\text{H}_2\text{O} + \text{H}_2\text{O}$, the state-to-state transition cross sections computed by MQCT methodology are converted to thermally averaged cross sections and compared with available results by other methods. The MQCT data are in good agreement with the results of semi-classical methods. In conclusion, it is safe to state that the MQCT methodology proves to be a promising tool for the computational treatment of molecular collisions and energy exchange.

CHAPTER 4. CALCULATIONS OF DIFFERENTIAL CROSS SECTIONS USING MIXED QUANTUM/CLASSICAL THEORY OF INELASTIC SCATTERING

4.1. Introduction

In the last few years the mixed quantum/classical theory (MQCT) for inelastic scattering of gas-phase molecules went through a significant and successful round of revisions, which included careful derivation of equations of motion in space-fixed and body-fixed reference frames,⁷² benchmark studies of rotational state-to-state transitions in simple molecules collided with atoms,⁷⁷ applications to larger molecules,²⁵ extension to molecule-molecule inelastic collisions,¹⁶ and even some work on ro-vibrational transitions.⁷⁷ In such approach to molecular collisions, the internal rotational (and/or vibrational) states of the molecules are treated rigorously using quantum mechanics, whereas the relative motion of scattering partners is treated classically by trajectories. This method allows very efficient scattering calculations for systems and collision regimes inaccessible using the standard full quantum scattering methodology (such as heavier atoms, larger molecules and higher collision energies).

This is an approximate method, and one fundamental question is which quantum features and phenomena “survive” in the mixed quantum/classical treatment of molecular scattering, and what could be done to improve MQCT and make it more general? It is already clear that MQCT is able to give insight into some quantum phenomena. For example, it was demonstrated that state-resolved cross sections computed using MQCT for transitions between quantized rotational states of many molecules remain surprisingly

accurate even at low collision energies, down to the process threshold (if scattering resonances are not present or if they are sufficiently narrow). It was also demonstrated that quantum symmetry can be built into MQCT calculations to describe allowed *vs.* forbidden transitions in a symmetric molecule,¹⁶ and to implement permutation symmetry of two identical collision partners.⁷⁵ Finally, it was shown that quantum oscillations of differential cross section in the forward scattering direction (quantum-scattering regime) can be reproduced well by MQCT.⁷⁴ This is possible due to incorporation of quantum phase, which also enables rigorous calculations of converged cross section for the elastic scattering channel (impossible within purely classical or any known semi-classical framework⁹⁹). All this progress is rather encouraging.

In this chapter, we expand on calculations of differential cross sections using MQCT and propose solution to the problem encountered in the past. Namely, in Ref. [74] we reported calculations of differential (over scattering angle) cross sections for the elastic channel of $\text{N}_2 + \text{Na}$ system, for ground rotational state of the nitrogen molecule, $j = 0$. In the quantum scattering regime (forward scattering) we found excellent agreement between our MQCT results and the full-quantum results of Dalgarno and co-workers⁵⁶ for the same system. But in the backward scattering regime the results of MQCT were incorrect (noisy, see Figure 9 below), which at that time was tentatively attributed to numerical issues.

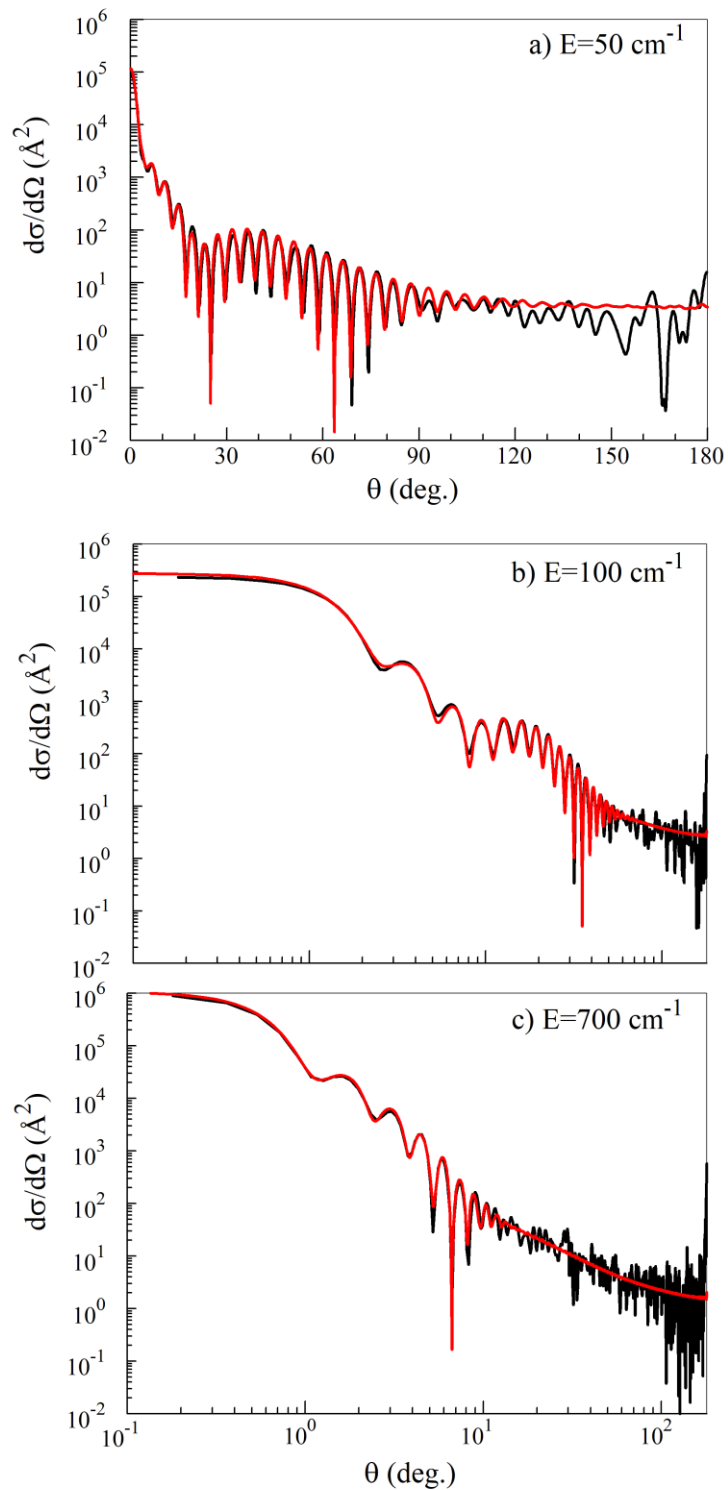


Figure 9: Differential cross sections for the elastic scattering channel of N_2 ($j = 0$) + Na at three collision energies: a) $E = 50 \text{ cm}^{-1}$; b) 100 cm^{-1} ; and c) 700 cm^{-1} . Full-quantum data from Ref. 56 are shown by red line, whereas MQCT results are shown by black line (obtained using the older semiclassical sampling approach, with randomly generated non-integer values of l).

In this chapter, we show that the unphysical behavior of differential cross section we saw in the past was caused by a methodological flaw. We identified the problem, and we found that fixing it allows reproducing quantum differential cross sections through the entire range of scattering angles, from forward to backward scattering, without any further adjustments to MQCT. Moreover, our finding sheds new light on how, in general, the mixed quantum/classical theory should be implemented, and what is the correct correspondence between the quantum and classical moieties in molecular scattering.

4.2. Theoretical Approach

4.2.1. Traditional Approach for Continuous Sampling of Initial Conditions

Consider full-quantum equations for the scattering of an atom off a diatomic molecule in the rotational state jm (such as in the $N_2 + Na$ system). Integral cross sections are computed using elements of scattering matrix in the body-fixed reference frame: ^{57,100–103}

$$\sigma_{j \rightarrow j'} = \frac{1}{2j+1} \sum_{m=-j}^j \sum_{m'=-j'}^{j'} \sigma_{jm \rightarrow j'm'} \quad (20)$$

where

$$\sigma_{jm \rightarrow j'm'} = \frac{\pi}{k_j^2} \sum_{J=0}^{J_{max}} (2J+1) \left| \delta_{jj'} \delta_{mm'} - S_{jj'mm'}^J \right|^2 \quad (21)$$

Here $j'm'$ is the final rotational state. Quantum numbers m and m' correspond to projection of molecular angular momentum onto the rotating z-axis that connects centers of mass of collision partners at every moment of time. Summation in the last formula is

over the values of *total* angular momentum of the system, $0 \leq J \leq J_{max}$, where J_{max} is a convergence parameter that depends on the system and on collision energy.

It was recognized in the past that,^{104–108} in order to be quantitatively comparable to the full-quantum calculations, MQCT method should stay close to these equations, and should attempt to retain (in the mixed quantum/classical theory) as many quantized moieties as possible. Thus, in MQCT we also consider *integer* values the total angular momentum J of the system and vary it in the range $0 \leq J \leq J_{max}$. However, in the mixed quantum/classical calculations elements of the scattering matrix do not depend on J . Instead, they depend on the value of initial *orbital* angular momentum, l , that corresponds to the relative motion of collision partners (to their scattering) and is related to collision impact parameter. In order to take this dependence into account we followed the prescription of Billing,^{14–17} and introduced average over l into Eq. (21):

$$\begin{aligned} \sigma_{jm \rightarrow j'm'} &= \frac{\pi}{k^2} \sum_{J=0}^{J_{max}} (2J+1) \frac{1}{2j+1} \sum_{l=|J-j|}^{J+j} \left| \delta_{jj'} \delta_{mm'} - S_{jj'mm'}^{(l)} \right|^2 \\ &\approx \frac{\pi}{k^2} \sum_{J=0}^{J_{max}} \frac{2J+1}{2j+1} \int_{l_{min}}^{l_{max}} \left| \delta_{jj'} \delta_{mm'} - S_{jj'mm'}^{(l)} \right|^2 dl \end{aligned} \quad (22)$$

For given value j of the internal angular momentum of the molecule, l changes through the range $|J-j| \leq l \leq J+j$, which is $(2j+1)$ values, again, by analogy with full-quantum approach, since $\mathbf{J} = \mathbf{l} + \mathbf{j}$. In our past work,⁷⁴ also following Billing, we adopted a semi-classical approximation for scattering motion, and treated the orbital angular momentum l as a *continuous* (classical, not quantized) variable. Consequently, the sum over l was replaced by the classical-like integral (compare first vs. second lines of Eq. (22)).

This seemed to be logical and attractive, since a numerically efficient Monte-Carlo procedure could be implemented to compute the sum over J and the integral over l in Eq. (22) simultaneously, in one step, as follows: Each trajectory in the batch was initiated with different values of J and l . Namely, for each trajectory, first, an integer value of J was drawn randomly and uniformly from the range $0 \leq J \leq J_{max}$. Then, a non-integer value of l was drawn randomly and uniformly from the range $|J - j| \leq l \leq J + j$, and used to define classical impact parameter b for the trajectory using semi-classical relation $l(l + 1) = k^2 b^2$. The total cross section was simply an average over trajectories in the randomly sampled batch:

$$\sigma_{jm \rightarrow j'm'} = \frac{\pi}{k^2} \cdot \frac{J_{max}}{N} \sum_{i=1}^N (2J^{(i)} + 1) \left| \delta_{jj'} \delta_{mm'} - S_{jj'mm'}^{(i)} \right|^2 \quad (23)$$

Here index i labels trajectories in the batch, the factor $(2j + 1)$ is absorbed by N which is the number of sampled trajectories, $2J^{(i)} + 1$ and $S_{jj'mm'}^{(i)}$ are space degeneracy and scattering matrix element computed for trajectory number i . Obviously, in such quasi-classical sampling procedure the *number of trajectories is a convergence parameter* (and this happens to be related to the critical point, as you will see below). Recently, Eq. (23) was applied to several molecular systems, to compute integral cross section for inelastic transitions,¹⁻⁶ and was found to work well. In such applications the phase of the scattering matrix is unimportant, since the transition probability is simply:

$$P_{jm \rightarrow j'm'} = \left| \delta_{jj'} \delta_{mm'} - S_{jj'mm'}^{(i)} \right|^2 = \left| a_{j'm'}^{(i)} \right|^2 \quad (24)$$

where $a_{j'm'}^{(i)}$ is probability amplitude in the final state $j'm'$ at the end of trajectory i , initiated with the initial population being in the state jm . Phase of scattering matrix

becomes important for the elastic channel, and for the differential cross section, as discussed below.

4.2.2. Improved Sampling Method Using Integer Values of J for the Differential Cross Sections

The semi-classical approach discussed above has a flaw, which becomes obvious if we try to apply this theory to compute scattering amplitude $f(\theta)$ for differential cross section. The full-quantum equations in the body-fixed reference frame are:^{57,100–103}

$$\frac{d\sigma_{j \rightarrow j'}(\theta)}{d\Omega} = \frac{1}{2j+1} \sum_{m=-j}^j \sum_{m'=-j'}^{j'} |f_{jm \rightarrow j'm'}(\theta)|^2 \quad (25)$$

$$f_{jm \rightarrow j'm'}(\theta) = \frac{i}{2k} \sum_{J=0}^{J_{\max}} (2J+1) \left(\delta_{jj'} \delta_{mm'} - S_{jj'mm'}^J \right) d_{mm'}^J(\theta).$$

where $d_{mm'}^J(\theta)$ is an element of the reduced rotation matrix.¹⁰⁹ Let's consider the case of initial $j = 0$, when elements of the reduced rotation matrix can be expressed through associated Legendre Polynomials and their weights:¹⁰³

$$f_{jm \rightarrow j'm'}(\theta) = \frac{i}{2k} \sum_{J=0}^{J_{\max}} (2J+1) \left(\delta_{jj'} \delta_{mm'} - S_{jj'mm'}^J \right) P_J^{|m'|}(\cos \theta) \sqrt{\frac{(J-|m'|)!}{(J+|m'|)!}} \quad (26)$$

The weights turn out to be same for both positive and negative values of m' [see Ref. 109, p. 59)], and the first non-zero weight occurs for $J = |m'| + 1$.

Summation over J in Eq. (26) can be replaced by summation over l , since $j = 0$. Note, however, that Eq. (26) contains coherent sum over partial scattering waves. If the

values of l are sampled *continuously* and randomly for the batch of MQCT trajectories, then it is simply impossible to associate these trajectories with any Legendre polynomials or partial waves! In our previous work on $\text{N}_2(j=0) + \text{Na}$,⁷⁴ we used the following trick: In order to compute differential scattering amplitude $f_{00 \rightarrow 00}(\theta)$ from the batch of randomly sampled MQCT trajectories (already computed for calculation of the integral cross section, see section 4.2.1 above) we simply rounded the value of l for each trajectory to the nearest integer \tilde{l}_i , and used the corresponding Legendre polynomial for that trajectory:

$$f_{00 \rightarrow 00}(\theta) \approx \frac{i}{2k} \cdot \frac{J_{\max}}{N} \sum_{i=1}^N (2J^{(i)} + 1) (1 - S_{00,00}^{(i)}) P_{\tilde{l}_i}(\cos \theta) \quad (27)$$

The sum in Eq. (27) is still over all N trajectories in the batch, labelled by i .

Figure 9(a)-(c) show differential cross sections for the elastic scattering channel of $\text{N}_2(j=0) + \text{Na}$ obtained using MQCT method with large number of randomly sampled trajectories (on the order of $N = 2000$) and employing an *ad hoc* rounding trick described above, in comparison with full-quantum results of Dalgarno and co-workers⁵⁶. We see that rounding the values of l worked well for the forward- and side-scattering regimes, but it did not work for scattering in the backward direction.

At that time we were puzzled,⁷⁴ since back-scattering is considered to be a classical scattering regime, where the mixed quantum/classical theory was expected to work the best. Note, however, that back-scattering corresponds to *small* values of orbital angular momentum. For example, scattering by $\theta = \pi$ is observed for zero impact parameter b , or “head on” collision, which corresponds to $l = 0$. Thus, rounding the values of l to the closest integer \tilde{l}_i does, indeed, have the most adverse effect on the back

scattering. Now it becomes rather clear that the problem was not with MQCT method itself (such as equations of motion for the quantum and classical degrees of freedom⁷²), but rather with the way of sampling the initial conditions for MQCT trajectories. Instead of computing the integral cross section, and then using the same batch of randomly generated trajectories to construct differential cross section, one should go the other way around. Namely, having in mind that we will have to construct differential cross section, let's try to propagate only the trajectories with integer values of l , and include them in the coherent sum of the quantum-like expression below, without any rounding, using the corresponding associated Legendre polynomials (for $j = 0$):

$$f_{jm \rightarrow j'm'}(\theta) = \frac{i}{2k} \sum_{l=0}^{l_{\max}} (2l+1) \left(\delta_{jj'} \delta_{mm'} - S_{jj'mm'}^{(l)} \right) P_l^{|m'|}(\cos \theta) \sqrt{\frac{(l-|m'|)!}{(l+|m'|)!}} \quad (28)$$

Numerical tests of this formula will be presented in section 4.3.1. For $j > 0$,

MQCT version of Eq. (25) can be written as:

$$\begin{aligned} f_{jm \rightarrow j'm'}(\theta) &= \frac{i}{2k} \sum_{j=0}^{J_{\max}} (2J+1) \frac{1}{2j+1} \sum_{l=|J-j|}^{J+j} \left(\delta_{jj'} \delta_{mm'} - S_{jj'mm'}^{(l)} \right) d_{mm'}^J(\theta) \\ &= \frac{i}{2k} \sum_{l=0}^{l_{\max}} \frac{1}{2j+1} \left(\delta_{jj'} \delta_{mm'} - S_{jj'mm'}^{(l)} \right) \sum_{j=|l-j|}^{l+j} (2J+1) d_{mm'}^J(\theta). \end{aligned} \quad (29)$$

This formula will be elaborated and numerically tested elsewhere.

4.2.3. Integral Cross Sections Using New Approach

These same considerations can be applied to the integral cross sections to update Eqs. (22) and (23). Since now l is again integer, and is varied in the range $|J-j| \leq l \leq J+j$, the number of trajectories is not a convergence parameter anymore. We should not

call this a “batch”. The number of trajectories is strictly determined by integer values of J and j . The only remaining convergence parameter is J_{max} , just like in the full-quantum approach. Note that molecular orientations in space are described by rotational wave function (all at once) and, therefore, don’t require a separate sampling in MQCT calculations.

However, it should be realized that the value of total angular momentum J in Eqs. (22-23) does not affect trajectories directly (or their outcome, such as elements of the transition matrix), since initial conditions are defined by the orbital angular momentum l . The values of total angular momentum J only give weights to trajectories. It is possible to account for these weights analytically, which reduces the double sum of Eq. (22) to a single sum, as follows:

$$\sigma_{jm \rightarrow j'm'} = \frac{\pi}{(2j+1)k^2} \sum_{l=0}^{l_{max}} (2j+1)(2l+1) \left| \delta_{jj'} \delta_{mm'} - S_{jj'mm'}^{(l)} \right|^2 \quad (30)$$

where the limit of summation is defined as $l_{max} = J_{max} + j$. Since J_{max} is a convergence parameter, l_{max} can simply be considered as an alternative single convergence parameter. Note that two factors $2j+1$ in numerator and denominator of Eq. (30) cancel, so, only the “geometric” factor $2l+1$ remains. The final expression for degeneracy-averaged cross section, after substitution of Eq. (30) into Eq. (20), is:

$$\sigma_{j \rightarrow j'} = \frac{\pi}{(2j+1)k^2} \sum_{m=-j}^j \sum_{m'=-j'}^{j'} \sum_{l=0}^{l_{max}} (2l+1) \left| \delta_{jj'} \delta_{mm'} - S_{jj'mm'}^{(l)} \right|^2 \quad (31)$$

This formula is valid for any j , for rotationally inelastic and for the elastic scattering processes too (if phase information is properly included in $S_{jj'mm'}^{(l)}$, as explained in the next section).

To our best knowledge, this relatively straightforward approach (with integer values of l within the mixed quantum/classical framework), has not been tried in the past, neither by Billing,^{17,107,108,110–112} nor by his followers^{3,6,120–123,40,113–119}. Application of Eqs. (28) and (30) to the $N_2(j=0) + Na$ system is reported in Results and Discussion section below.

4.2.4. Description of the Scattering Phase by MQCT Method

For completeness, we briefly recap the treatment of scattering phase within MQCT,⁷⁴ since it is important in Eq. (28-30) for differential cross sections, in Eq. (31) for integral cross section in the case of elastic scattering, but also for analysis of scattering resonances, as discussed below.

First, a smooth deflection function $\Theta(l)$ should be constructed from MQCT trajectories.⁷⁴ Then, according to the semi-classical approach,⁹⁹ deflection angle Θ is determined by the total phase shift:

$$\Theta(l) = \frac{d(\delta_j + \delta_l)}{dl} \quad (32)$$

Two components of the total phase are seen in Eq. (32), phase $\delta_j(l)$ of the internal molecular state (*e.g.*, rotational state j in MQCT) and the scattering phase δ_l . The former can be computed from analysis of the probability amplitude $a_{jm}^{(l)}$ at the end of MQCT trajectories, but the latter is absent in MQCT, since scattering is treated classically. However, the differential equation (32) can be integrated over l to determine the missing scattering phase:

$$\delta_l = - \int_{l_{max}}^l \Theta(s) ds - \delta_j(l) \quad (33)$$

This scattering phase can be inserted into the element of scattering matrix to impose coherence into MQCT trajectories in Eqs. (28) and (31), namely:

$$1 - S_{jjmm}^{(l)} = 1 - \exp(i\delta_l) a_{jm}^{(l)} \quad (34)$$

One condition is that l_{max} corresponds to a trajectory that passes through the asymptotic range, where all the phase shifts are zero and the deflection angle is zero. This is always possible to satisfy by choosing large impact parameter. Second condition is that the deflection function $\Theta(l)$ is continuous through the entire range of l_{max} , which is typically the case at higher scattering energies. However, at low scattering energies the trapping of MQCT trajectory in the interaction region can occur, the so-called orbiting, which is a classical analogue of a scattering resonance. In such cases the integration can only be done from l_{max} down to the value of l^* at which the orbiting trajectory occurs, but not through the entire range of l . As result, at these values of collision energies the phase can't be constructed, and the cross section cannot be computed rigorously within MQCT framework. Consequences of this problem are explored in section 4.3 below.

Last point to mention is that, in the case of the elastic scattering channel, equation (34) can be transformed into a more transparent form:

$$\begin{aligned} 1 - S_{jjmm}^{(l)} &= 1 - \exp(i\delta_l) \exp(i\delta_j) |a_{jm}^{(l)}| \\ &= 1 - \exp(i\delta) |a_{jm}^{(l)}| \end{aligned} \quad (35)$$

Here we introduced the total phase $\delta = \delta_j + \delta_l$ determined by the deflection function only:

$$\delta = - \int_{l_{max}}^l \Theta(s) ds \quad (36)$$

This shows that for the elastic scattering channel, for both integral and the differential cross sections, the phase of survival amplitude $a_{jm}^{(l)}$ appears to be not important. The value of cross section is determined by the modulus $|a_{jm}^{(l)}|$, and by the total scattering phase δ that, in turn, depends only on the deflection function $\Theta(l)$.

Finally, one can come out with an approximation:

$$1 - S_{jjmm}^{(l)} \approx 1 - \exp(i\delta) \quad (37)$$

applicable in the case of weak inelastic transitions, when the final probability amplitude in the elastic channel is very close to one. This approximation is also tested in section 4.3 below.

4.2.5. Inelastic Differential Cross Section Using MQCT

Phase information is also important for calculation of inelastic differential cross sections. For transition $jm \rightarrow j'm'$ during the trajectory defined by orbital quantum number l and propagated through time interval t we should write, similar to Eq. (34):

$$S_{jj'mm'}^{(l)} = \exp(i\delta_l) a_{j'm'}^{(l)} e^{-iE_{j'}t} \quad (38)$$

The last time-dependent phase factor in this formula is needed because in practice the time of propagation is finite (rather than $-\infty \leq t \leq +\infty$) and is different for trajectories

with different values of l . Typically, trajectories with large values of l , close to l_{max} , are very short, since they just “touch” the interaction region and stop (see Figure 10 below), while trajectories with intermediate values of l pass through the interaction region and spend there a significant amount of time. The resultant phase shift is taken into account by the last term in Eq. (38), and depends on energies of the final states $E_{j'}$ (energy of the initial state can always be taken as reference $E_j = 0$). This formula can be re-expressed as follows:

$$\begin{aligned}
 S_{jj'mm'}^{(l)} &= \exp\{i(\delta - \delta_j)\} \exp(i\delta_{j'}) |a_{j'm'}^{(l)}| \exp(-iE_{j'}t) \\
 &= \exp\{i(\delta - E_{j'}t + \delta_{j'} - \delta_j)\} |a_{j'm'}^{(l)}|
 \end{aligned} \tag{39}$$

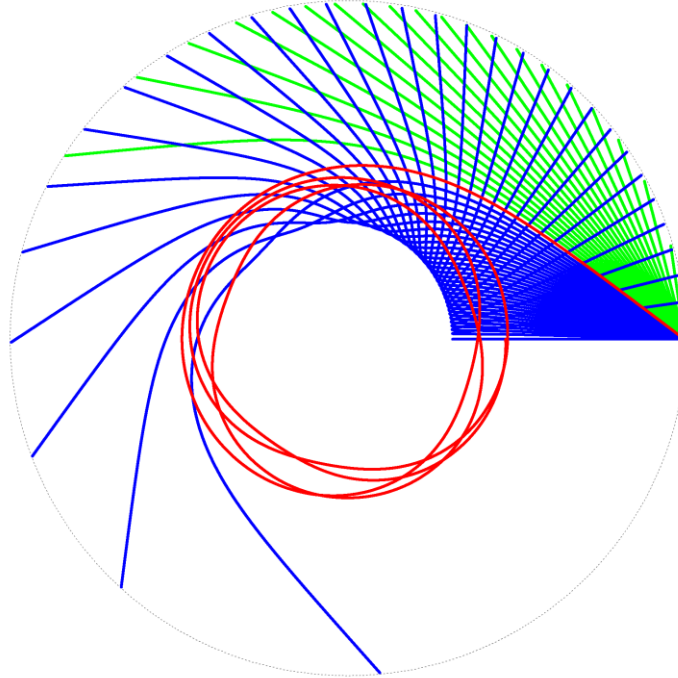


Figure 10: A set of MQCT trajectories for $E = 16 \text{ cm}^{-1}$, which is the highest collision energy at which one can observe orbiting in the $\text{N}_2 (j = 0) + \text{Na}$ system. This trajectory ($l^* = 31$) is shown by red line. Trajectories with larger impact parameters are green, while trajectories with smaller impact parameters are blue. Here all values of l are integer.

Comparing this equation with Eq. (35) for elastic scattering we see that now, for inelastic scattering, in addition to the modulus of transition amplitude $|a_{j'm'}^{(l)}|$ and the total phase δ , we also need phases of the initial and final states δ_j and $\delta_{j'}$, since their difference enters Eq. (39).

4.3. Results and Discussion

4.3.1. Elastic Cross Sections for Na + N₂

Figure 11(a)-(c) show differential cross sections for the elastic scattering channel of N₂($j=0$) + Na obtained using MQCT method with a modified sampling approach, where only integer values of l are employed. Again, the full-quantum results of Dalgarno and co-workers⁵⁶ are shown for comparison, and we see that the agreement between MQCT and the “exact” benchmark is almost perfect. MQCT results are accurate through the entire range of scattering angles, for different scattering energies, and through six orders of magnitude range of cross section values. Not only near the maxima, but even at the dips of cross section dependence, the agreement remains excellent. Every single oscillation is reproduced, in all frames of Figure 11.

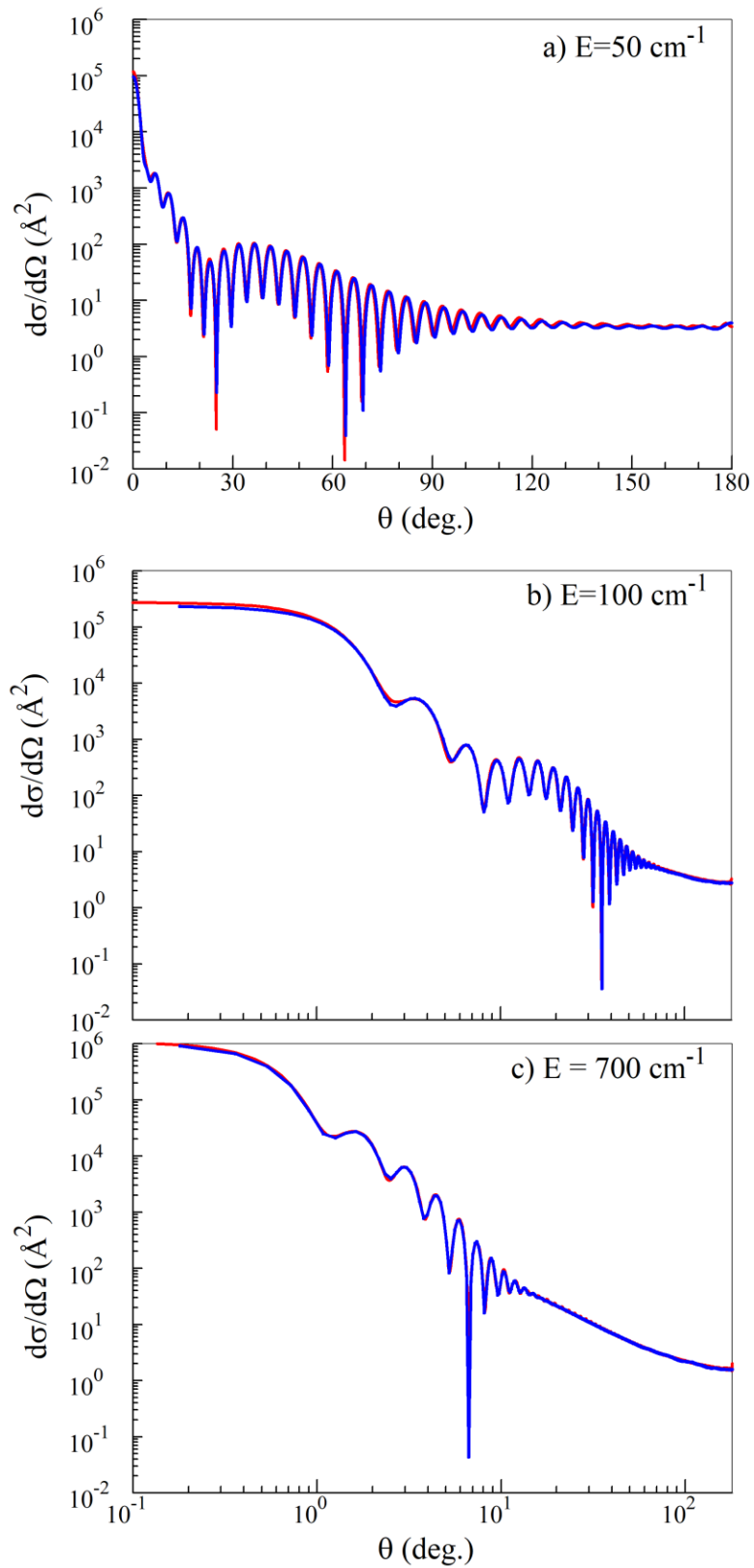


Figure 11: Same as Figure 9 but with MQCT trajectories generated for all integer values of orbital angular momentum l , just as in quantum mechanics.

Figure 11 can be directly compared with Figure 9, where the problem was observed at large scattering angles. We see that now this problem is completely fixed. Remember, results presented in Figure 9 were obtained using randomly sampled non-integer (continuous) values of l . The number of trajectories was a convergence parameter in that case, and was found to be rather large, on the order of 2000. In contrast, in Figure 11 the number of MQCT trajectories is directly determined by J_{max} (equal to l_{max} because $j = 0$ in our case). Here we used only 92 trajectories for collision energy $E = 50$ cm^{-1} (which corresponds to $l_{max} = 91$), only 130 trajectories for $E = 100$ cm^{-1} ($l_{max} = 129$) and only 343 trajectories for $E = 700$ cm^{-1} ($l_{max} = 342$). In fact, the proposed new implementation of MQCT requires fewer trajectories, and less numerical effort.

Note that the horizontal axis of Figure 11(a) is linear, while it is logarithmic for Figure 11(b) and (c). This is done to reveal in detail the forward scattering peak in Figure 11(b)-(c), but also to make visible the rainbow point in Figure 11(a), that occurs at ~ 66 degrees. One can see that the differential cross section dependence given by MQCT method remains regular near the rainbow point, just as the full-quantum result, in contrast to other known semiclassical ways of treating the differential cross section.

Integral elastic cross section can be obtained either by integrating the differential cross section over scattering angle,⁹⁹ or by using the same set of MQCT trajectories in the sum of Eq. (31) directly. Both ways require building the deflection function and reconstructing the scattering phase using Eq. (33-36). Examples of deflection functions $\Theta(l)$ and scattering phase dependencies $\delta(l)$ are given in Figure 12(a)-(b), respectively, for several values of collision energy. The resultant integral cross section for the elastic scattering of $\text{N}_2(j=0) + \text{Na}$ is presented in Figure 13(a) in a broad range of scattering

energies. Comparison with full-quantum results of Dalgarno and co-workers⁵⁶ is again very good. As expected,⁷⁴ MQCT is somewhat more accurate at higher collision energies, but even at lower collision energies the results are reasonable.

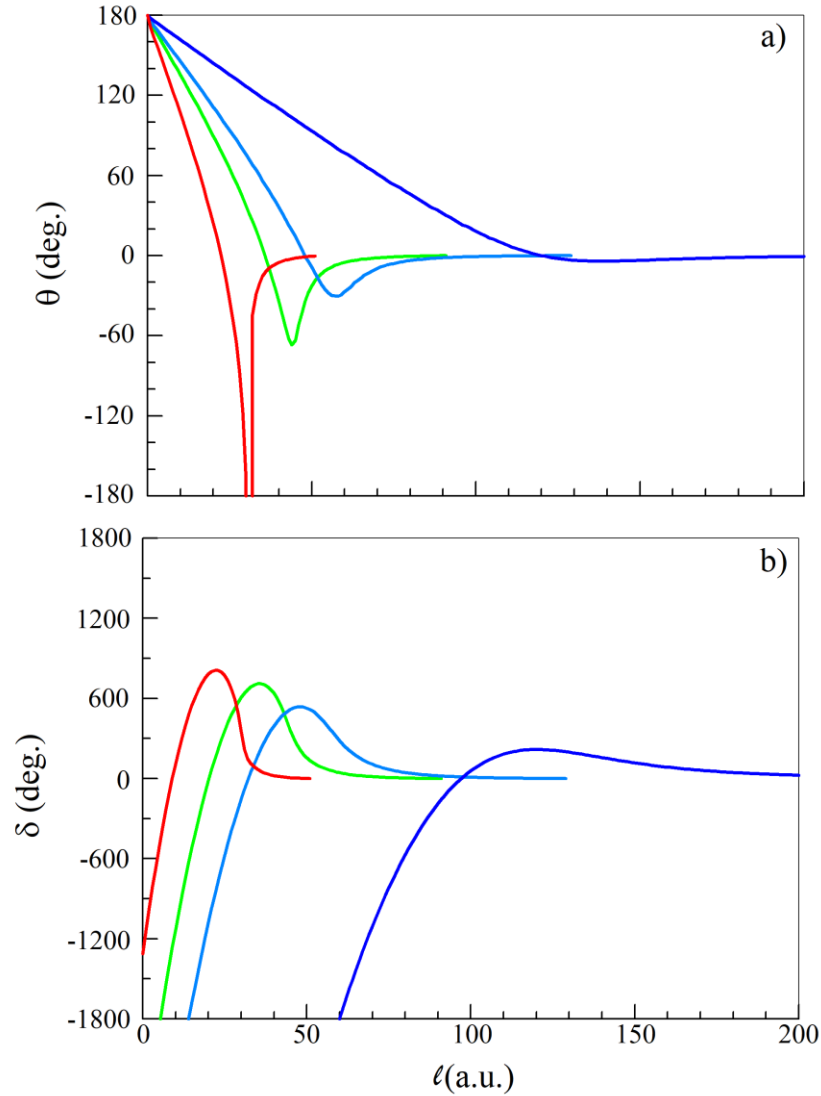


Figure 12: Deflection function (upper frame) and the total phase (lower frame) from MQCT calculations for several values of scattering energy. Red, green, blue & violet lines correspond to $E = 16 \text{ cm}^{-1}$, 50 cm^{-1} , 100 cm^{-1} and 700 cm^{-1} , respectively. In the case of $E = 16 \text{ cm}^{-1}$ the orbiting trajectory is found at $\ell^* = 31$, where the value of deflection angle is undefined. To compute the phase for this energy, the resonance was “removed”, by linear interpolation of the deflection angle between two neighboring points ($\ell = 30$ and $\ell = 32$, where the deflection angle is defined). The phase dependence computed in this way for $E = 16 \text{ cm}^{-1}$ looks rather smooth.

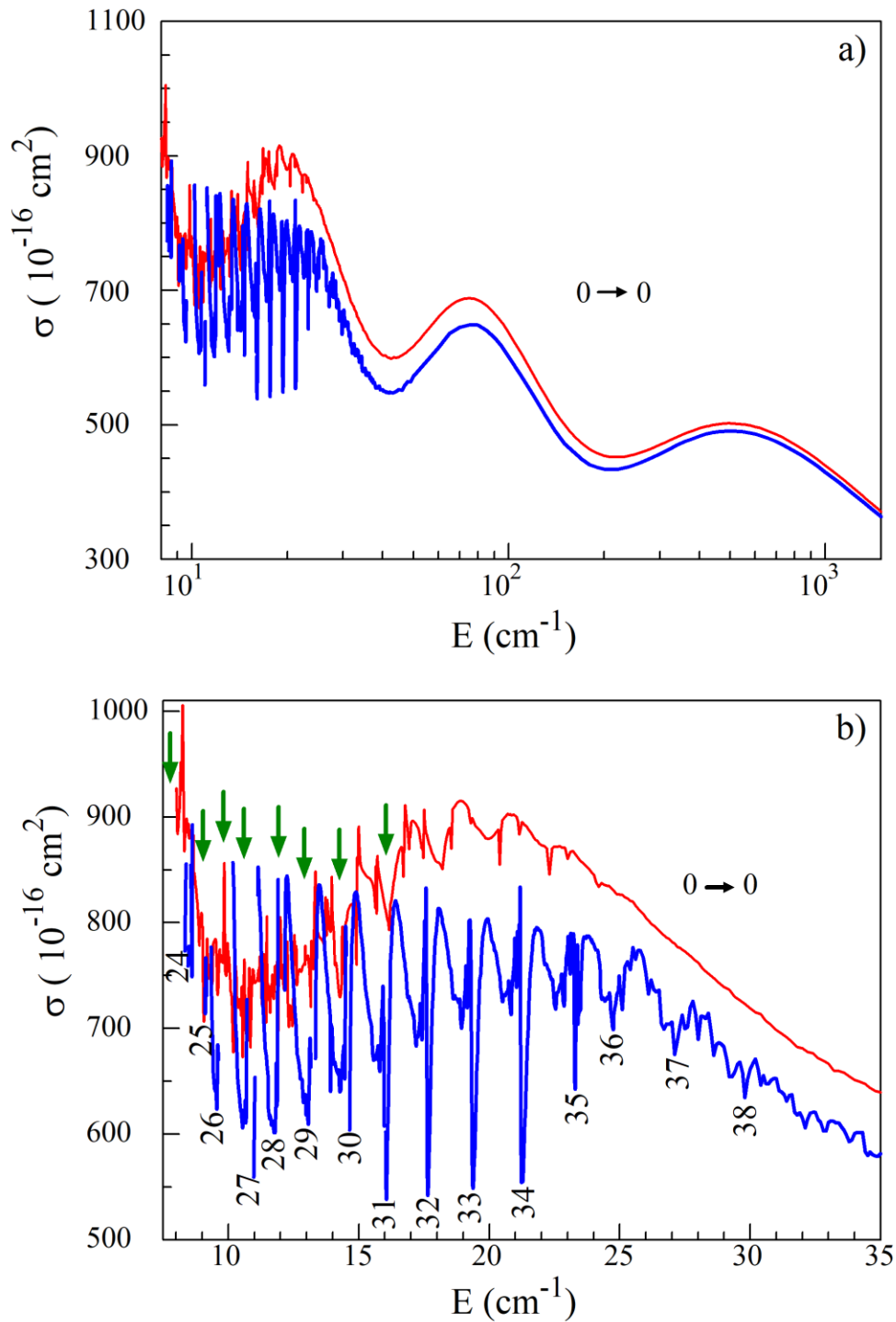


Figure 13: Energy dependence of integral cross section for the elastic scattering channel of N_2 ($j = 0$) + Na in a broad range of energies (a), and in the low-energy scattering regime dominated by resonances (b). Full-quantum data from Ref. 56 are shown by red line, whereas MQCT results are shown by blue line. The spikes in MQCT data are due to looping trajectories, while the gaps (indicated by green arrows) are due to orbiting trajectories. The corresponding values of l are indicated under each gap or spike. Here all values of l are integer.

We also tried to explore the validity of the approximate formula of Eq. (37). We did it in two ways. In one set of calculations, we simply ignored the value of survival probability amplitude and used only the phase, just as Eq. (37) prescribes. In the other set of calculations, we removed all the excited states from the rotational basis, keeping only the elastic scattering channel of $N_2(j=0) + Na$ and running one-state scattering calculations only, that give unitary survival probability by construct. We obtained very similar results that are also in good agreement with the full quantum results (see Figure 14 and Figure 15). This demonstrates very clearly that the dominant factor in the elastic scattering is the scattering phase, rather than probability amplitude neglected in the approximate formula of Eq. (37), and this phase is well captured by MQCT calculations. It also gives a rather powerful way of computing elastic scattering cross sections, including the differential cross sections for elastic scattering, by running just one-state MQCT calculations, that would be very efficient for virtually any molecular system and any collision energy.

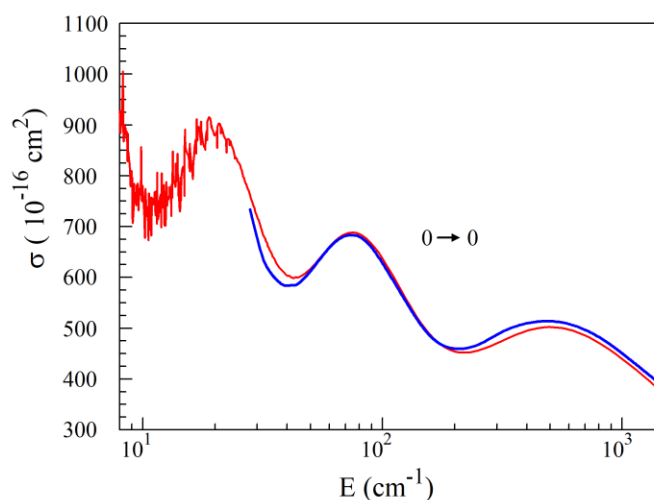


Figure 14: Same as Figure 13 but obtained using single-state MQCT calculations for the elastic scattering process. This is an approximate way of computing the elastic cross section.

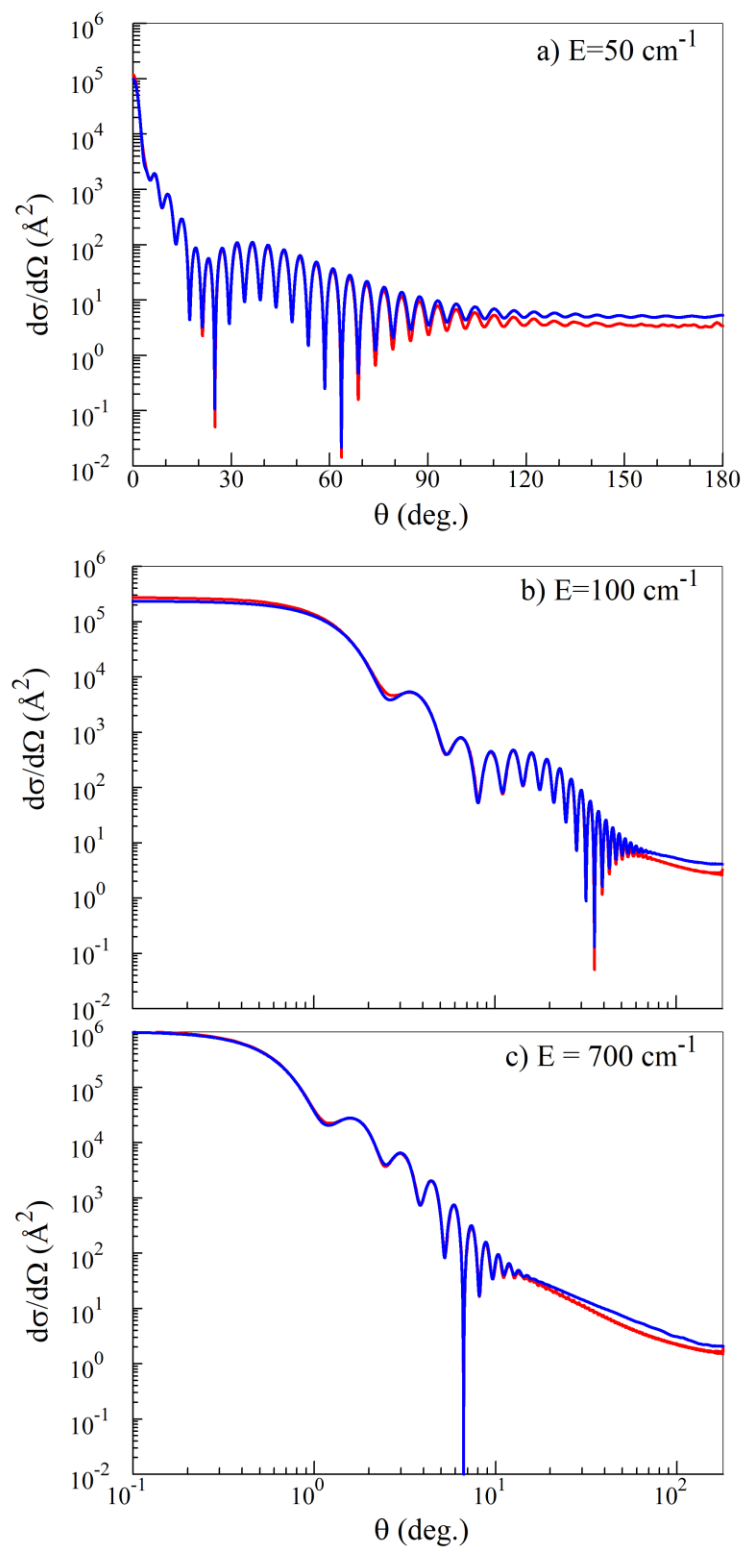


Figure 15: Same as Figure 11 but obtained using single-state MQCT calculations for the elastic scattering process. This is an approximate way of computing the elastic cross section.

4.3.2. Resonances at Low Collision Energies

At very low collision energies, below $E = 30 \text{ cm}^{-1}$ in Figure 13(a), multiple features similar to scattering resonances are predicted by MQCT calculations. This is emphasized by Figure 13(b). We analysed MQCT trajectories in order to understand why these spiky features occur in the cross-section dependence as the collision energy is reduced. We found that in the energy range from $E = 30 \text{ cm}^{-1}$ down to 17 cm^{-1} there are well resolved periodically occurring resonant structures (see Figure 13(b)). We looked closer at those energy points and found that in each case there is one value of l at which the MQCT trajectory makes a *loop* around the interaction region, with the effective deflection angle going over 180 degrees. Those values of l are indicated next to each spike in Figure 13(b). For energies between $E = 17$ and 25 cm^{-1} the values of orbital quantum number between $l = 32$ and 36 are found to produce looping trajectories. Such trajectories leave the interaction region at the end, so, the deflection angle can be determined, the phase reconstructed, and the differential and elastic integral cross sections computed.

However, below 17 cm^{-1} we start seeing trajectories that are trapped in the interaction region. One example of *orbiting* trajectory is shown in Figure 10. Such trajectories don't leave the interaction region within a reasonable number of cycles, say, even after ten loops. And again, they occur at one value of the orbital quantum number which seem to follow the previous progression. Namely, in the range of energy between $E = 10$ and 16 cm^{-1} the values of orbital quantum number between $l^* = 27$ and 31 are found to produce orbiting trajectories. In Figure 13(b) these values of energy are seen as gaps in the cross-section dependence, because if the trajectory keeps cycling and never

leaves the interaction region the deflection angle can't be uniquely specified. The deflection function is discontinuous (see Figure 12a), it cannot be integrated in Eq. (33) or (36), the scattering phase is undefined and neither the differential, nor the integral elastic cross section can be computed within MQCT framework. One can argue that the mixed quantum/classical description of inelastic scattering breaks down at this point (locally, at this collision energy and for this value of l^*).

Nevertheless, the overall picture given by MQCT seems to be semi-quantitatively correct even down to collision energies of 8 cm^{-1} or so, and thus is practically useful. It shows a sharp growth of cross section at very low energies, and a smoother “hill” near $E = 20 \text{ cm}^{-1}$, all superimposed with periodically occurring resonant structures. Looking at the numbers, one sees that in the middle of the resonance region, say around $E = 15 \text{ cm}^{-1}$, the value of MQCT cross section is 20% lower than the quantum result, on average. This is very reasonable. It is hard to expect more from the classical-like approach in the quantum scattering regime, with multiple resonances. Moreover, the finding that our “resonances” occur at one selected value of the orbital quantum number l^* is consistent with recent analysis of resonances in the full-quantum scattering calculations,¹²⁴ where it was found that quantum resonances also occur due to contribution of one particular value l^* into each resonance.

Another important question is a nature of “resonances” observed in MQCT calculations. Typically, one defines either Feshbach resonances that occur because of the loss of translational energy (due to excitation of the internal states of collision partners), or shape resonances populated by tunneling through centrifugal barrier (and trapped behind it). These are often said to be two different types, although in the rotationally

inelastic processes the transfer of kinetic energy into rotation also leads to increase of the centrifugal barrier, so, the two types of resonances may finally be closely related.

Leaving these fine questions on aside, one can argue that since translational motion is treated classically by MQCT, we cannot possibly have resonances populated by tunneling, so the only option is a Feshbach-type process, due to the kinetic-to-internal energy transfer. In order to prove this statement, we carried out an additional set of MQCT calculations with only one internal state in the basis, the initial state (here, the ground rotational state $j=0$ of N_2). This removes possibility of rotational excitation, and the loss of kinetic energy into the internal states of the molecule and is expected to eliminate the Feshbach-type processes. Results of such calculations showed no trajectory trapping (although looping trajectories were still observed at low energies), which demonstrates clearly that in MQCT calculations we are dealing with Feshbach-type resonances.

4.3.3. Inelastic Cross Sections for Na + N₂

The same approach of MQCT with trajectories defined by integer values of l was applied to compute inelastic integral cross sections for rotational excitation of $N_2(j=0)$ by Na. Results are presented in Figure 16(a) in a broad range of collision energies. Three processes are shown, all with even Δj values, because odd values are forbidden by symmetry (this quantum selection rule is perfectly captured by MQCT). One of these cross sections decreases as a function of energy, the second increases, while the third passes through the maximum, according to the full-quantum results of Dalgarno and co-workers⁵⁶. Figure 16(a) demonstrates that MQCT describes all these features really well,

giving nearly perfect results at higher energies and reasonable results at energies near the process threshold. Our focus, again, will be on scattering resonances.

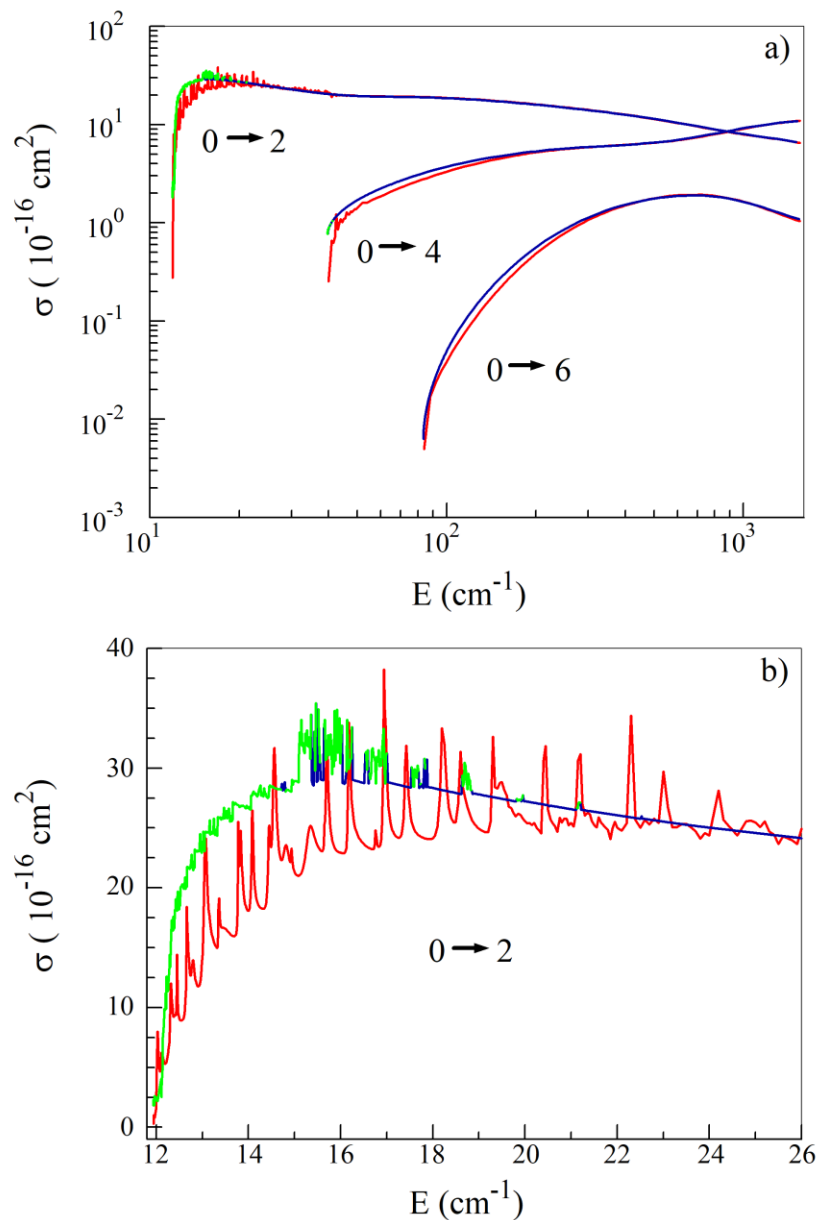


Figure 16: Energy dependence of excitation cross sections for $\text{N}_2 (j = 0) + \text{Na}$ in a broad range of energies (a), and in the low-energy scattering regime dominated by resonances (b). Three allowed transitions are indicated on the graph. Full-quantum data from Ref. 56 are shown by red line, whereas MQCT results are in blue. The gaps in blue line correspond to orbiting trajectories, where the final state populations are undefined. These gaps are filled with green line, obtained by averaging state populations over several periods.

Resonances are more pronounced near threshold of the excitation channel $0 \rightarrow 2$, which is emphasized by Figure 16(b). Full-quantum calculations indicate multiple resonances at collision energies below $E = 30 \text{ cm}^{-1}$, down to the process threshold at $E = 12 \text{ cm}^{-1}$. In MQCT calculations the orbiting trajectories start showing up at energies around $E = 22 \text{ cm}^{-1}$, and become more common at lower energies. Below $E = 15 \text{ cm}^{-1}$ all trajectories show orbiting (see Figure 16(b)). The phase is not important for the integral cross section of the inelastic channel, but the question of transition probability still requires some discussion, since orbiting trajectories never stop, and the final moment of time cannot be rigorously defined. Populations of rotational states keep evolving.

We tried to monitor evolution of state populations during twenty periods or so, and found that state populations oscillate periodically. Thus, the values of state populations averaged over some period of time could serve as a reasonable measure of transition probabilities. Here we propagated resonant trajectories for 15-20 periods and averaged the values of state populations over the last ten periods. These average values were used to fill the gaps in energy dependence of the excitation cross section in Figure 16(b), when orbiting occurs. These data are shown in Figure 16b by green color, mostly at low scattering energies, near the process threshold. At these conditions, the results of MQCT agree qualitatively with full-quantum results.

Differential cross sections obtained by MQCT method for excitation of $\text{N}_2(j=2)$ starting from $\text{N}_2(j=0)$ are presented in Figure 17 for two energies of Na impact. Upper and lower frames of the Figure 17 correspond to low energy collision, $E = 40 \text{ cm}^{-1}$, and high energy collision, $E = 700 \text{ cm}^{-1}$, respectively. The full-quantum benchmark data of Dalgarno and co-workers (red curves) are again presented, for comparison. Overall, the

agreement is very good, although it is not as good as that for the elastic scattering channel (*e.g.*, in Figure 11). The frequency of cross section oscillations seems to be reproduced correctly by MQCT at both high and low energies. The largest differences are observed at lower collision energies for scattering angles near the forward scattering peak, in the most quantum scattering regime. At higher energy, and for deflection angles above $\theta \sim 10^\circ$, when quantum oscillations vanish, the agreement is nearly perfect.

4.4. Summary

In this chapter, we demonstrated that mixed quantum/classical approach to molecular scattering is considerably improved by refraining from description of the orbital angular momentum as classical continuous moiety. It should be kept integer, just like in the quantum theory. Excellent accuracy of the modified theory for prediction of differential cross sections (at various values of collision energy) strongly supports this conclusion and justifies new sampling strategy, in which one MQCT trajectory is generated for each integer value of l . One can argue that trajectories in MQCT calculations serve to represent partial scattering waves, rather than merely to sample the collision conditions (such as continuous impact parameter). The new approach requires less MQCT trajectories, compared to the Monte-Carlo random sampling. The only convergence parameter in MQCT is l_{max} , similar to J_{max} in the full quantum theory. This applies to both elastic and inelastic scattering channels.

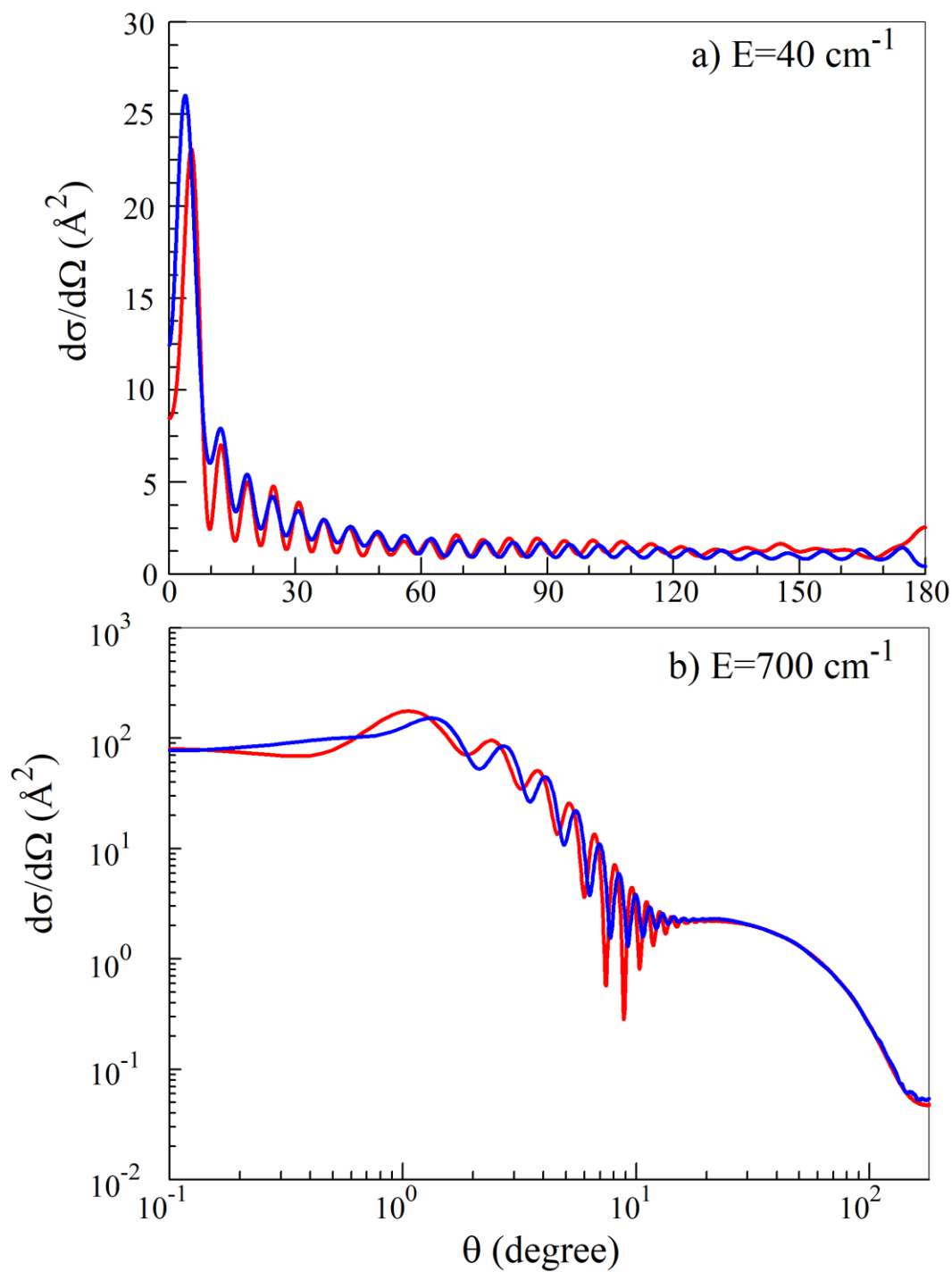


Figure 17: Differential cross sections for inelastic scattering channel into N_2 ($j = 2$), starting from N_2 ($j = 0$), at two collision energies with Na atom: a) $E = 40 \text{ cm}^{-1}$, and b) 700 cm^{-1} . Full-quantum data from Ref. 56 are shown by red line, whereas MQCT results are shown by blue line.

More insight was also obtained in how, within the MQCT framework, phase information can be utilized to describe interference between different values of l , and how the phase can be employed to determine differential and elastic integral scattering cross sections. These observables represent quantum properties of the system, since both rely on interference between different values of l . Phase appears to be a dominant factor in the elastic scattering cross section. A simplified expression is proposed for computationally affordable (single-channel) MQCT calculations of the elastic cross sections. Differential cross sections for inelastic scattering were reported here for the first time, but only for the initial rotational level $j = 0$. In the future, it would be interesting to carry out similar MQCT calculations of the differential inelastic cross sections for $j > 0$ initial states, for those molecules where the full-quantum results are available for comparison (since they are not available for $\text{N}_2 + \text{Na}$).

Finally, we explored in detail the range of very small collision energies dominated by quantum scattering resonances. MQCT calculations produce qualitatively similar spiky energy dependence of cross section, due to the looping and orbiting trajectories. We studied properties of these trajectories, and found that at each collision energy there is, typically, only one value of l that leads to looping or orbiting. Removing such resonance from deflection function (by interpolating between the neighboring points) works and permits to restore phase-dependence in the entire range of l . Accuracy of MQCT is lower in this regime, compared to the high energy regime.

In the future, the developments of this work could be expanded onto other more complicated molecular systems, for example, onto the dipole dominated scattering, such as found in $\text{CO} + \text{CO}$ or in $\text{H}_2\text{O} + \text{H}_2\text{O}$ collisions.

CHAPTER 5. ADIABATIC TRAJECTORY APPROXIMATION WITHIN THE FRAMEWORK OF MIXED QUANTUM/CLASSICAL THEORY

5.1. Introduction

Inelastic collisions of molecules with atomic gasses^{125–128}, with other gas-phase molecules^{129–133} or with solid surfaces^{134–139} lead to the energy exchange between translational, rotational and vibrational degrees of freedom, which is a fundamentally important phenomenon in the field of Chemical Physics. On the applied side, the inelastic molecular collisions play critical roles in many processes that span a huge range of sizes and time scales, from the man-made micro-traps^{140–143} to the galaxies and extra-galactic sizes^{8,42,43,96,144}. Therefore, theoretical prediction of inelastic cross sections has been and still is actively pursued, including practical applications of the well-known codes to more and more complex molecular processes^{15,48,52,127,128,142}, development of new computational tools^{1,86,145,146} and exploration of new theoretical methodologies^{6,71,97,147–149}.

During the last decade we developed the mixed quantum/classical theory of inelastic molecular scattering^{78,79,96,150–152} and implemented this method in a recently released ready-to-use code named MQCT¹. Our method is approximate, but it appears to work well in a wide range of collision regimes and for a broad variety of molecular systems^{16,75,79,94,96}. It offers significant computational advantages in both the overall CPU cost required to solve the inelastic scattering problem (due to a simplified physics) and in the user's wall-clock time (enabled by efficient massive parallelization).

Within the framework of MQCT, the internal molecular degrees of freedom are treated quantum mechanically using the time-dependent Schrodinger equation. Therefore, this method takes into account many quantum features of molecular rotations and vibrations, such as state quantization and zero-point energy preservation³, symmetry restrictions on allowed and forbidden transitions¹, propensities of state-to-state transition cross section⁹⁷, quantum interference effects¹⁵³ and several other quantum features that we keep investigating. At the same time, the translational motion of colliding partners, responsible for their scattering in space, is treated classically within the Ehrenfest mean-field trajectory approach^{17,107}. This simplification was found to work well even for the lightest collision partners such as He atom and H₂ molecule, in a broad range of collision energies^{1,75,94,151}. Since the quantum treatment of scattering is avoided, the mixed quantum/classical method enables an affordable computational treatment of heavier collision partners and/or at higher collision energies – the limits when the standard full-quantum methods are not affordable computationally anymore.

During the last few years, our efforts were focused mainly on proving, to ourselves and to the community, that the mixed quantum/classical methodology can be sufficiently accurate, and thus practically useful. Namely, we demonstrated that for many molecules the results of MQCT calculations become nearly identical to the full-quantum results in the range of high collision energies^{78,151,152}, which is a theoretically important limiting case and a practically important collision regime. Moreover, we showed that the results of MQCT remain reasonably accurate even at low scattering energies, near the excitation threshold¹, which historically was thought of as a quantum scattering regime, not amenable to any semi-classical treatment. At this point it becomes clear that MQCT

represents a generally reliable method, with a potential of becoming a practical alternative to the full quantum description of molecular inelastic scattering (except, perhaps, in the ultracold physics conditions).

One interesting feature of the MQCT formalism is that it includes the Coriolis coupling effect, in a mixed quantum/classical fashion, through transitions between the (quantum) states with different projections of molecular angular momentum that are driven by the (classical) orbital angular momentum of the relative motion of collision partners. This most rigorous version of MQCT calculations was named CC-MQCT, by analogy with a well-known quantum coupled-channel method which is considered to be exact. Besides CC-MQCT, we also developed and tested an approximate version of MQCT, in which the Coriolis coupling is neglected, leading to a simpler set of equations of motion propagated at a reduced numerical cost. This is a mixed quantum/classical analog of a well-known coupled-states (CS) approximation^{85,101,154–156}, and therefore we named our approximate MQCT version as CS-MQCT¹⁵¹. We found that it gives acceleration by an order of magnitude, which is quite attractive. Unfortunately, we also found that for some molecules the results of CS-MQCT deviate appreciably from the results of more rigorous CC-MQCT, and more so at low collision energies¹⁵¹. Again, this is analogous to the performance of the full-quantum coupled-states method, that is known to be less reliable at lower collision energies.

Therefore, it makes sense to examine other alternative methods for the computational treatment of inelastic molecular scattering (and for the description of rotational-vibrational-translational energy exchange in general) still within the MQCT framework, but such that solve the problem in an approximate way, and hopefully at a

fraction of the computational cost. At the moment this territory is largely unexplored, and we envision a development of a hierarchy of approximate methods of solving the MQCT equations of motion.

In this chapter we introduce one such option that we want to name AT-MQCT, where the prefix stands for the *adiabatic trajectory* version of MQCT. This approximation is specific to the time-dependent mixed quantum/classical theory, and thus it does not have any direct quantum analogue, to our best knowledge. In this method the classical and quantum equations of motion are decoupled in a sense, by conducting MQCT calculations in two consecutive steps. During the first step the molecular basis size is restricted to the degenerate states of the initial rotational channel only (with different projections of the molecular angular momentum). This information is recorded and used during the second run, to propagate the quantum equations of motion along this pre-computed adiabatic path. The Coriolis-like coupling terms are included during both steps of such calculations, which preserves an important physical effect, in contrast to the CS approximation where it is entirely neglected.

In the Theory section we review the formalism of MQCT and introduce the AT-MQCT version of the method. In the section Results we apply this theory to the $\text{H}_2\text{O} + \text{H}_2$ system and demonstrate that it produces the systematically reliable and rather accurate results. New method is benchmarked *vs* the well-established CC-MQCT version, but also *vs* the full-quantum CC calculations of Dubernet and coworkers for the same system⁴². In the Discussion section we determine acceleration due to the adiabatic trajectory approximation, which approaches the factor of $\times 200$, making these mixed quantum/classical calculations relatively cheap. Opportunities for further development of

a hierarchy of approximations within MQCT are also discussed. Summary is presented in the final section of the chapter.

5.2. Theory

Rigorous derivation and detailed discussion of the MQCT equations of motion can be found in the recent literature,^{1,79} and a brief summary is provided in section 3.2.1. Efficient methodologies for generation of the initial conditions for MQCT trajectories, and for constructing cross sections from the final values of probability amplitudes a_{mn} , have been discussed earlier and will not be repeated here^{1,79,96,150,153}.

5.2.1. Adiabatic Trajectory Approximation

Formula (13)-(17) represent a system of coupled differential equations of first order. Note that the classical system of Eqs. (13)-(16) and the quantum system of Eqs. (17) contain the same variables and thus are coupled. In the most rigorous MQCT treatment they are propagated in time all together. Such straightforward approach was implemented in the released version of MQCT¹.

Although the mixed quantum/classical treatment is more affordable than the full quantum treatment, there are still molecular systems and collision conditions where even the MQCT calculations become computationally demanding. Let's consider the $\text{H}_2\text{O} + \text{H}_2$ system covered in this research. Assume that in the basis for para- H_2O molecule we want to include lowest 45 rotational states, with the upper state $j_1 = 8$ at 1442.095 cm^{-1} ($k_a = 6, k_c = 2$) and the largest value of $j_1 = 11$ at 1332.166 cm^{-1} ($k_a = 1, k_c = 11$), whereas for the para- H_2 we want to include two rotational states, with upper state $j_2 = 2$ at

365.118 cm^{-1} . This gives us 90 energetically non-degenerate asymptotic rotational states overall in the basis for the $\text{H}_2\text{O} + \text{H}_2$ system. Within each of these asymptotic states, the complete basis contains all j_{12} states in the range $|j_1 - j_2| \leq j_{12} \leq j_1 + j_2$, that here we will call *the channels*. In the example above, the largest value of the total molecular angular momentum is $j_{12} = 13$, and there are 264 channels overall. Within each molecular channel there are $2j_{12} + 1$ projection states with different values of m . Altogether this gives 3486 unique quantum states in the basis, and a huge state-to-state transition matrix $M_n^{n'}(R; m)$. In the MQCT code¹, zero matrix elements are identified and excluded, but still, for the example above the number of unique non-zero matrix elements included in the triple-summation of Eqs. (15) and (16) is 336595, which represents a numerical challenge since these summations need to be re-computed at each time step (several times) along each trajectory. Indeed, from the extensive profiling of MQCT calculations we found that over 50% of the total numerical effort was used to compute the right-hand sides of Eqs. (15) and (16), and over 65% to propagate Eqs. (15) and (16), despite the fact that these are just two equations in a huge system of coupled differential equations (6976 equations total in our example, out of which 4 are for the classical degrees of freedom while 6972 are for the real and imaginary parts of 3486 quantum probability amplitudes).

It is also important to realize that, when computed, the triple-summations in the right-hand sides of the classical equations produce just two numbers – the average gradient for Eq. (15) and the average torque for Eq. (16). How sensitive are these average values to the contribution of each term in the sum? Do we really need to take into account all these terms? Can we neglect the contributions of some terms? Which terms contribute

more and thus must be retained? Clearly, more than one truncation scenario is possible here, depending on the answers to these questions, and we will discuss various alternatives in detail further below (see Discussion). Here we will propose and test a simple solution that, in a sense, goes to the extreme. It is discussed next.

It is clear that the largest contributions to the right-hand sides of Eqs. (15) and (16) will normally come from the most populated states, those with larger values of probability amplitudes $a_{mn}(t)$. For many molecular systems and many collision conditions the inelastic transition probabilities are relatively small, and thus the survival probability (in the initial channel) is dominant. Therefore, one simple way to truncate the sum in Eqs. (15) and (16) is to retain only the states of the initial channel. This can include all the degenerate m -states, since the number of such states within one channel is usually manageable, $2j_{12} + 1$. With this choice, the MQCT trajectories will be driven by the potential energy surface associated with one quantum channel only (the initial channel), rather than by the average Ehrenfest potential. Such trajectories are not sensitive to excitation or quenching of the initial state and, strictly speaking, are not the mean-field trajectories anymore. These are *adiabatic trajectories*, which suggests the name AT-MQCT for this approximation.

Using truncation of the right-hand sides in Eqs. (15) and (16) one could still hold the overall system of MQCT equations (13)-(17) coupled as before, to propagate in time all the equations of motion together. Or, alternatively, one could go beyond just truncation and, following the spirit of the adiabatic ansatz, try to completely decouple the propagation of four classical equations of motion, Eqs. (13)-(16), from the huge system of quantum coupled equations, Eq. (17). In practice, this can be implemented as follows:

- In the first run, propagate all MQCT equations of motion rigorously coupled, as before, but using an *adiabatic* basis that includes only $2j_{12} + 1$ states (labelled by m in Eqs.(13)-(17) above) of the initial quantum channel. Since the basis is small, such MQCT calculations would be trivial for any molecular system, without any other approximations. The existing MQCT code can be used without modifications. These would be adiabatic MQCT calculations, since no rotational excitation or quenching of the internal molecular states is possible within such basis, but the goal is to record the trajectory data as a function of time, to use this information during the second run. For example, one can record all classical variables: $R(t)$, $\Phi(t)$, $P_R(t)$ and $P_\Phi(t)$, or one can record only $R(t)$ and $\dot{\Phi}(t)$ that are specifically needed in the second run. As you will see, it is also beneficial to record average potential $V(t)$ along the trajectory.
- In the second run the basis is increased to the desired size, in order to describe all the state-to-state excitation and quenching transitions (*e.g.*, 90 states in the $\text{H}_2\text{O} + \text{H}_2$ example above), but now only the quantum system of coupled equations is propagated in time, using Eq. (17), to determine the evolution of probability amplitudes $a_{mn}(t)$. The value of R for the state-to-state transition matrix $M_n^{n'}(R; m)$ and the value of $\dot{\Phi}$ for the Coriolis coupling (in the first and second terms of Eq. (17), respectively) are “borrowed” from the adiabatic trajectory data saved during the first run (*e.g.*, using a 1D spline along the trajectory, which is a computationally cheap trick). Only minor technical modifications to the code are needed.

Of course, such decoupling of classical and quantum degrees of freedom in the AT-MQCT method is an approximation which needs to be tested by numerical simulations (see next Section). One downside of this assumption is that the total energy of the system is not conserved anymore. However, the norm of the wavefunction is still conserved and can be monitored to ensure the convergence of numerical integration. One important advantage of this method, compared to the CS-MQCT approximation, is that the Coriolis coupling terms in Eqs. (16) and (17) are included during both steps of the AT-MQCT calculations: during the first adiabatic step as well as during the second non-adiabatic step.

5.2.2. Adiabatic Step-Size Predictor

The previously released version of MQCT¹ had 4th order Runge-Kutta integrator built in, for the propagation of the total system of coupled equations: the classical Eqs. (13)-(16) and the quantum Eq. (17), altogether. By default, the constant step-size was used, with an option of adaptive step-size control from Numerical Recipes¹⁵⁷. We found, however, that the adaptive step-size control routine gave advantage only for the molecular systems with long-range interaction potential, such as $\text{H}_2\text{O} + \text{H}_2\text{O}$ ^{1,79,97}. For other cases, such as $\text{H}_2\text{O} + \text{H}_2$ system considered here, the “black-boxed” step-size control gave no noticeable increase of performance. But, we realized that the adiabatic trajectory approximation introduced above gives us opportunity to implement a very efficient method for the variable-step integration of the quantum system of equations, Eq. (17), propagated during the second step of the AT-MQCT calculations (which is the only

costly part of new method). For this, we can take advantage of the $V(t)$ dependence, recorded along the adiabatic trajectory during the first step of AT-MQCT calculations.

Indeed, the form of the right-hand side of Eq. (17) suggests that the time-evolution of probability amplitudes $a_{mn}(t)$ is driven by the magnitudes of matrix elements $M_n^{n'}(R; m)$ as molecule-molecule separation $R(t)$ first decreases and then increases along the trajectory. Although individual matrix elements $M_n^{n'}$ change slightly differently as a function R , the potential $V(t)$ recorded during the first step gives us a reasonable prediction of their overall behavior (as they increase from the asymptotic region to the interaction region). Importantly, the numerical error of integration is also expected to depend on the magnitude of matrix elements $M_n^{n'}$, and therefore the variable integration step-size Δt may be efficiently predicted using the $V(t)$ dependence.

If we keep using 4th order Runge-Kutta method, in which the integration error I is proportional to Δt^4 , and also take into consideration that numerical error is proportional to the interaction potential $V(t)$, we can write:

$$I = \alpha \cdot \tilde{V} \cdot \Delta t^4 \quad (40)$$

where α is a proportionality coefficient that takes care of units, and \tilde{V} is the average value of $V(t)$ during the time step Δt . This average can be computed, for example, by taking N tiny steps τ through the interval Δt , from t to $t + \Delta t$:

$$\tilde{V} = \frac{1}{N} \sum_{i=1}^N V(t + [i - \frac{1}{2}]\tau) \quad (41)$$

Then, $\Delta t = N\tau$. The goal is to vary Δt as \tilde{V} changes along the trajectory in such a way that the numerical error remains constant, for example, does not exceed a specified value of I_{\max} . This is achieved by setting, based on Eq. (40):

$$\Delta t = \sqrt[4]{\frac{I_{\max}}{\alpha \cdot \tilde{V}}} \quad (42)$$

From Eqs. (40) and (41) it follows that this can be implemented by taking tiny steps τ along the trajectory, accumulating the predicted value of error:

$$\frac{I}{\alpha} = (N\tau)^4 \cdot \frac{1}{N} \sum_{i=1}^N V(t + [i - 1/2]\tau) \quad (43)$$

and monitoring that within each time step it does not exceed I_{\max}/α . The value of I_{\max} can be defined by considering a hypothetic trajectory with very weak interaction such that the potential remains negligibly small at any moment of time: $V(t) < V_{\text{tiny}}$. In this case the integration of entire trajectory can be done in one step, $\Delta t = T$, where T is the duration of trajectory (the time t when the molecule-molecule separation reaches R_{\max} , also determined during the first step of AT-MQCT propagation). From these considerations, and using Eq. (40), we obtain:

$$\frac{I_{\max}}{\alpha} = T^4 \cdot V_{\text{tiny}} \quad (44)$$

It is more convenient to introduce a unitless measure of precision:

$$\epsilon = \sqrt[4]{\frac{V_{\text{tiny}}}{U}} \quad (45)$$

where U is a characteristic value energy, say the kinetic energy of collision. The values of kinetic energy in typical MQCT calculations vary in range from 1 cm^{-1} to $10,000 \text{ cm}^{-1}$. The typical values of ϵ are 0.01 and below, say down to 10^{-5} . With these definitions, the final formula for the variable time-step is obtained from Eqs. (42), (44), and (45):

$$\Delta t = \epsilon T \cdot \sqrt[4]{\frac{U}{\tilde{V}}} \quad (46)$$

We checked by extensive calculations and confirmed that this method of step-size prediction works efficiently along the entire trajectory (as it goes from the asymptotic range to the interaction region and back), and for all trajectories in the batch (from the most intense head on collisions, to more typical side-scattering, forward scattering, and the asymptotic trajectories that barely touch the interaction region). Varying one convergence parameter ϵ permits to achieve monotonic convergence for all trajectories in the batch, which is very convenient and numerically efficient.

We checked and found that our step-size prediction works for a broad range of collision energies, but the value of ϵ needs to be adjusted. Namely, at higher energies the collision is faster, so the time step needs to be reduced, according to $\Delta t \sim 1/\sqrt{U}$. This relationship occurs simply because $\Delta t = \Delta R/v$ where velocity depends on collision energy as $v = \sqrt{2mU}$. Thus, if we want the integration to proceed with roughly the same steps through space (through the potential energy surface) at different energies, we have to adjust the time-step accordingly. This adjustment is analytic, and we found a simple way to scale the value of ϵ inside the code (without user's intervention), to take this effect into account. We also found, by trial and errors, that at the very low collision energies a higher accuracy is needed and the value of ϵ has to be reduced too. Based on our experimentations with the $\text{H}_2\text{O} + \text{H}_2$ system we derived an empirical dependence of this effect and have also hardcoded it into the MQCT program. As it stands now, the user can enter one single value of ϵ that will guarantee the same level of accuracy for all AT-MQCT trajectories at all collision energies. For the $\text{H}_2\text{O} + \text{H}_2$ system we observed that, as

the value of ϵ is reduced, all AT-MQCT trajectories converge monotonically. We hope that this behavior is general, and plan checking the performance of adiabatic step-size predictor for other molecular systems, in the near future.

To avoid confusion, we would like to stress one more time that this adiabatic predictor scheme is *not* used to propagate the classical-like equations of motion (13)-(16). This method is used only for the quantum-like Eq. (17) for evolution of probability amplitudes $a_{mn}(t)$ along the precomputed trajectories. While classical equations of motion include the gradient of potential (the force), the quantum time-dependent Schrödinger equation includes the potential itself. This difference manifests in Eqs. (15) vs. (17), where the right-hand side of the first (classical-like) formula contains gradients of matrix elements, while the right-hand side of the second (quantum-like) formula contains matrix elements themselves.

5.3. Results

In order to benchmark the accuracy and performance of the newly developed approximate AT-MQCT methodology, we carried out a series of calculations for a reasonably complex real molecular system of astrophysical importance, $\text{H}_2\text{O} + \text{H}_2$. It was studied in the past by various groups^{42,158} and a fair amount of data are available from literature. In order to make the comparison meaningful we used the same potential energy surface⁴².

5.3.1. Comparison of AT-MQCT vs CC-MQCT

The initial distance between the collision partners was set to $R_{max} = 30 a_0$, and the maximum impact parameter was selected as $b_{max} = R_{max}$ at all collision energies (which automatically defines the maximum value of the orbital angular momentum at each collision energy). The range of collision energies covered in this test was from 20 cm^{-1} to 7000 cm^{-1} . The rotational basis incorporates 20 asymptotic rotational states of $\text{H}_2\text{O} + \text{H}_2$ with energies below 500 cm^{-1} , which includes 4 states with hydrogen molecule excited to $j_2 = 2$. For water, the upper rotational state in this test was 4_{40} , where two subscripts stand for $k_a = 4$ and $k_c = 0$, of $j_1 = 4$. The standard CC-MQCT calculations, that are expected to serve as a reference and thus need to be perfectly converged, were carried out in a standard way, using the RK4 integrator with a constant time-step set to a rather small value, $\Delta t = 10 a.u.$ Convergence of the approximate AT-MQCT calculations with adiabatic step-size predictor was also rigorously checked, by varying the value of ϵ . The results presented in Figure 18 and Figure 19 are found to be entirely converged when $\epsilon = 10^{-3}$.

First, we looked at the excitations from the ground rotational state of the system, $\text{H}_2\text{O} (j_1 = 0) + \text{H}_2 (j_2 = 0)$, which we denote here as $0_{00}0$. Figure 18 reports cross sections for 20 transitions, including the elastic channel, for eight values of collision energies (one may notice that at lower collision energies some channels are closed). One can see that results of the approximate AT-MQCT (green symbols, dashed lines) follow closely the trend of the benchmark CC-MQCT data (red symbols, solid lines), through all transitions and all collision energies, systematically. We did not see even one transition when the adiabatic trajectory approximation would fail miserably. It should be

emphasized that the values of cross sections vary through seven orders of magnitude, still, the results of the approximate AT-MQCT method remain very close to the results of the original CC-MQCT method. At higher energies the agreement is generally better, which is somewhat counterintuitive, since one would expect that the error of adiabatic trajectory approximation (single-state) may increase together with possibilities of multiple state excitations, enabled by higher collision energies. But this does not happen. Higher errors are found at lower collision energies, when only a few channels are open, and for lower rotational states, which is also somewhat unexpected.

Next, we looked at the quenching and excitations of the first excited rotational state of water, $\text{H}_2\text{O}(j_1 = 1, k_a = 1, k_c = 1) + \text{H}_2(j_2 = 0)$, which we denote here as $1_{11}0$. Figure 19 reports cross sections for transitions into the same 20 states of the basis, at the

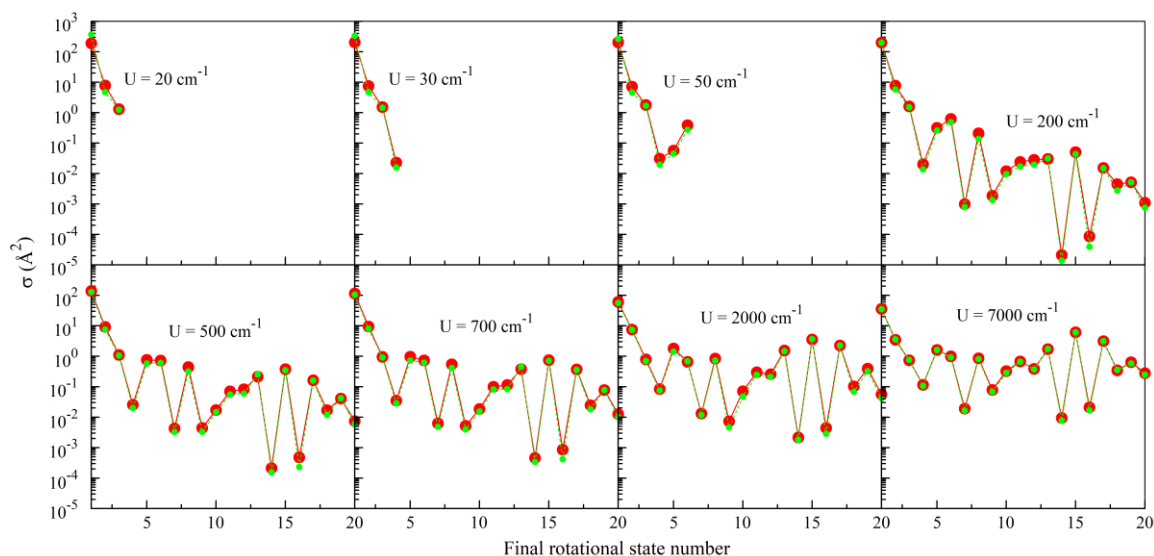


Figure 18: Comparison of results of the new approximate AT-MQCT method (green dots) against the full-coupled CC-MQCT calculations (red symbols) for the initial state $0_{00}0$ of the $\text{H}_2\text{O} + \text{H}_2$ system. Final states are listed along the horizontal axis. The values of collision cross sections are plotted along the vertical axis using log scale. Eight frames correspond to eight values of the kinetic energy, as indicated. Twenty rotational states of the basis include both ground and excited rotational states of H_2 .

same collision energies as in Figure 18 (with all the same convergence parameters chosen). These data again indicate an excellent systematic agreement between the approximate AT-MQCT method (green symbols, dashed lines) and the benchmark CC-MQCT method (red symbols, solid lines), through all transitions, all collision energies, and seven orders of magnitude of cross section values.

A different viewpoint is obtained by plotting the values of cross sections as a function of collision energy. This is done in Figure 20 for transitions into the five lower energy states of $\text{H}_2\text{O} + \text{H}_2$, starting from the ground state $0_{00}0$, and in Figure 21 for the rotationally excited initial state $1_{11}0$. In these figures different colors correspond to different transitions. Vertical dashed lines indicate energy thresholds of the individual processes. From Figure 20 and Figure 21 we can see clearly that the results of the adiabatic trajectory approximation do approach monotonically the results of the full-coupled MQCT calculations as collision energy is increased. Larger deviations are found

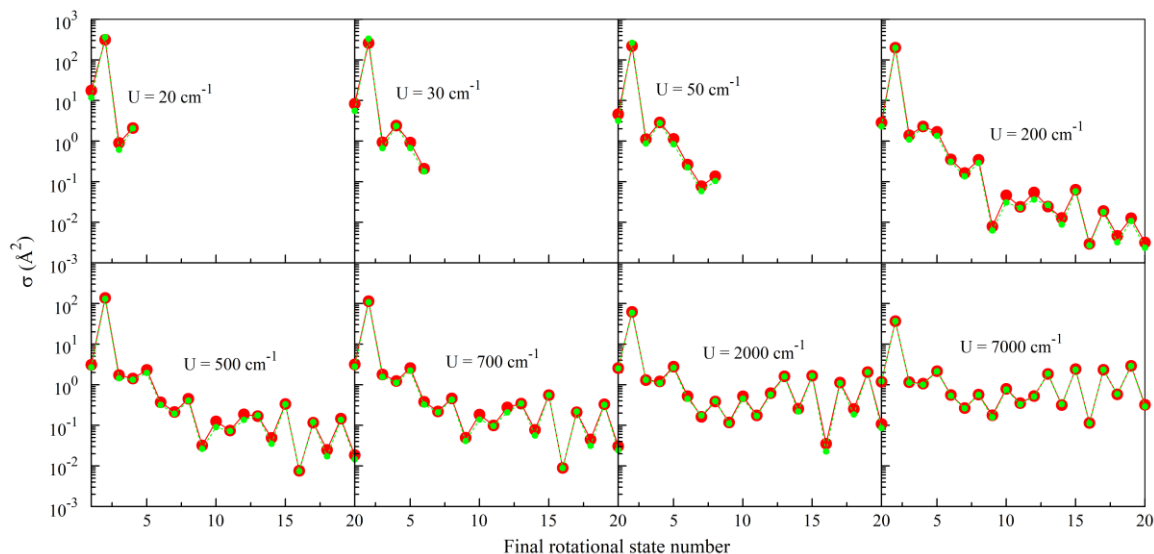


Figure 19: Same as Fig. 1, but for the initial state $1_{11}0$ of the $\text{H}_2\text{O} + \text{H}_2$ system, which is first excited rotational state.

at lower collision energies, often at threshold. The positions of thresholds are correctly captured by the approximate AT-MQCT method, but the values of cross sections just above the threshold are usually underestimated. For the transitions plotted in Figure 20 and Figure 21 the largest underestimations of this kind are by about 40%, found for transitions $0_{00} \rightarrow 1_{11}$ and $1_{11} \rightarrow 2_{02}$ near their thresholds, at collision energies 37.158 and about 33.001 cm^{-1} , respectively.

To summarize, the results of adiabatic-trajectory approximation, within the MQCT framework, appear to be systematically accurate, particularly at higher collision

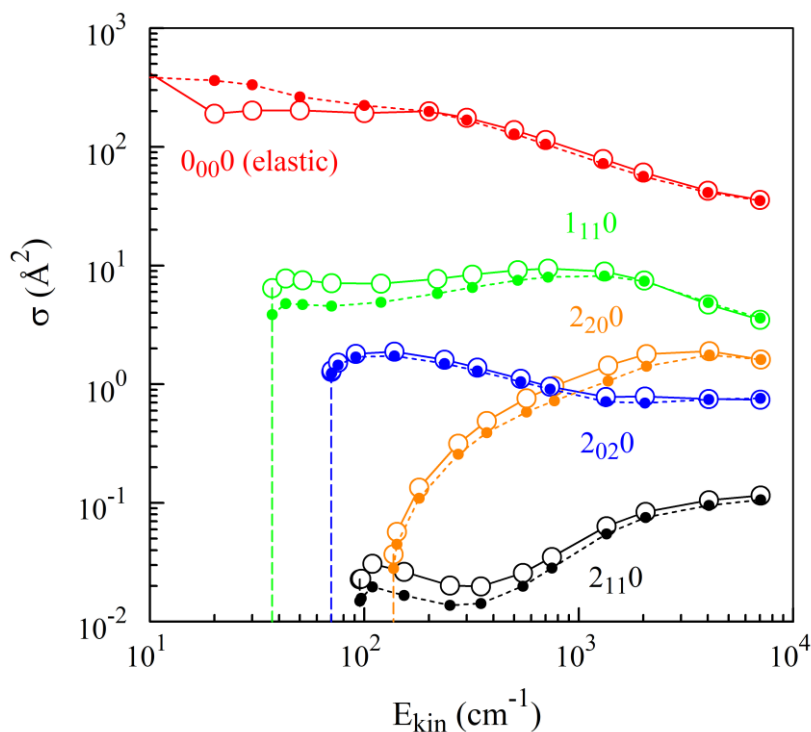


Figure 20: Comparison of results of the new approximate AT-MQCT method (empty circles, solid line) against the full-coupled CC-MQCT calculations (filled symbols, dashed lines) for the initial state $0_{00}0$ of the $\text{H}_2\text{O} + \text{H}_2$ system. The values of collision cross sections are plotted along the vertical axis using log scale. Kinetic energy of collision (including Billing's correction) is plotted along the horizontal axis. Color corresponds to five different final rotational states, as indicated in the picture. Excitation thresholds are shown by the vertical dashed lines.

energies. When it concerns only the trajectory of collision, we do not lose much by restricting the basis size to include only the states of the initial quantum channel. Such approach is found to be less accurate at the limit of low collision energies, near the process threshold, but this collision regime is often amenable to the full-quantum treatment of scattering, which we discuss next.

5.3.2. Comparison of AT-MQCT vs full-quantum CC method

For the $\text{H}_2\text{O} + \text{H}_2$ system, the results of full-quantum coupled-channel calculations are available from the detailed work of Dubernet and coworkers⁴². Besides thermal rate coefficients they also reported the energy dependencies of cross sections for a number of individual state-to-state transitions. Their results are reproduced in Figure 22

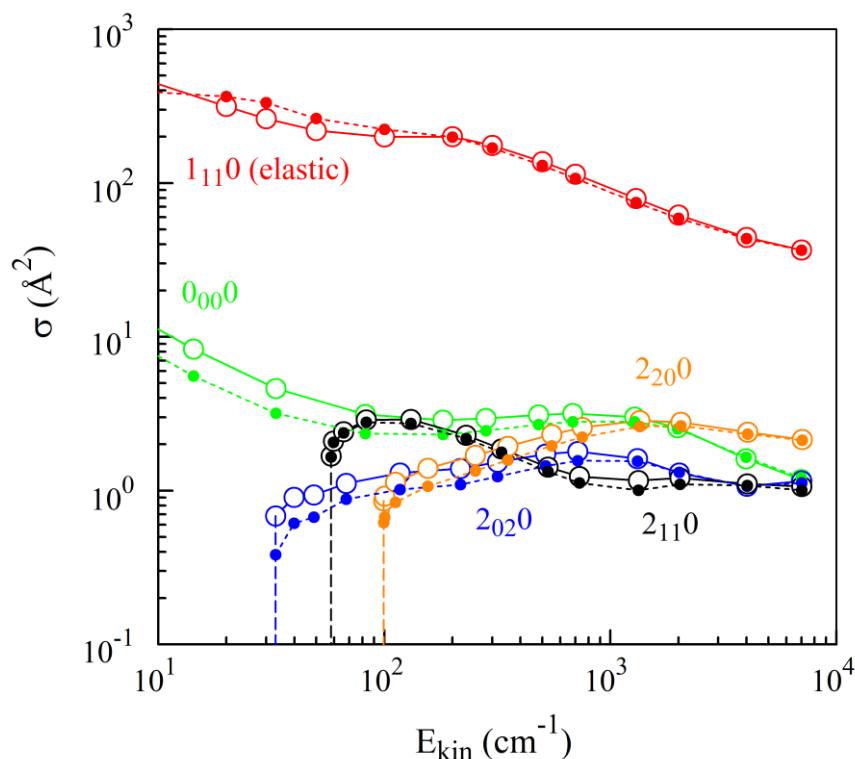


Figure 21: Same as Fig. 3 but for the first excited state $1_{11}0$ of H_2O as the initial channel.

(with permission of the author). For the same transitions, we carried out the approximate AT-MQCT calculations. In those, all the convergence parameters were kept as in the previous test, except that the rotational basis size was dramatically increased, to match the basis size in the calculations of Dubernet and coworkers at higher collision energies. Namely, 90 asymptotic rotational states of $\text{H}_2\text{O} + \text{H}_2$ with energies below 1810 cm^{-1} were included, with two states of the hydrogen ($j_2 = 0, 2$) and the states of water up to 8_{62} . In Figure 22 four colors correspond to four state-to-state processes in H_2 , two elastic ones: $0 \rightarrow 0$ (black) and $2 \rightarrow 2$ (blue), one quenching $2 \rightarrow 0$ (green) and one excitation $0 \rightarrow 2$ (red). Three initial states of water are considered: 2_{11} (three frames on the left side), 3_{22} (three frames in the middle of the picture), and 4_{40} (three frames on the right side). The final states of water are different for each frame, as indicated in the figure caption, and include 0_{00} , 1_{11} , 2_{02} , 2_{11} , 3_{31} and 5_{24} .

Overall, Figure 22 contains energy dependencies of 36 transitions, which is a rather comprehensive set of data for the benchmarking of new methods. In all these cases the results of our AT-MQCT method show very good systematic agreement with the full-quantum results of Dubernet and coworkers⁴². Some differences are present, but they are relatively small and typically vanish at high collision energies. One possible source of small differences at higher energies is likely to originate in the fact that a Kyrö-type Hamiltonian for water molecule was used by Dubernet and co-workers, while we employ a simpler rigid-rotor model. Also, given the difficulty of achieving convergence of the full-quantum calculations at high energies, we would cautiously assume that some of these differences may originate in the full quantum calculations too. The AT-MQCT results are expected to be quite reliable in the high energy regime.

Moreover, it is also quite encouraging that in the low collision energy regime the results of AT-MQCT remain close to the full-quantum results that are considered to be exact. Out of 36 state-to-state transition processes in this figure, we spotted only one transition (frame 1a, dashed vs solid black lines) where the results of AT-MQCT calculations deviate significantly from the full-quantum results: $2_{11}0 \rightarrow 0_{00}0$ at collision energies below 10 cm^{-1} . Note that this particular process has a number of narrow

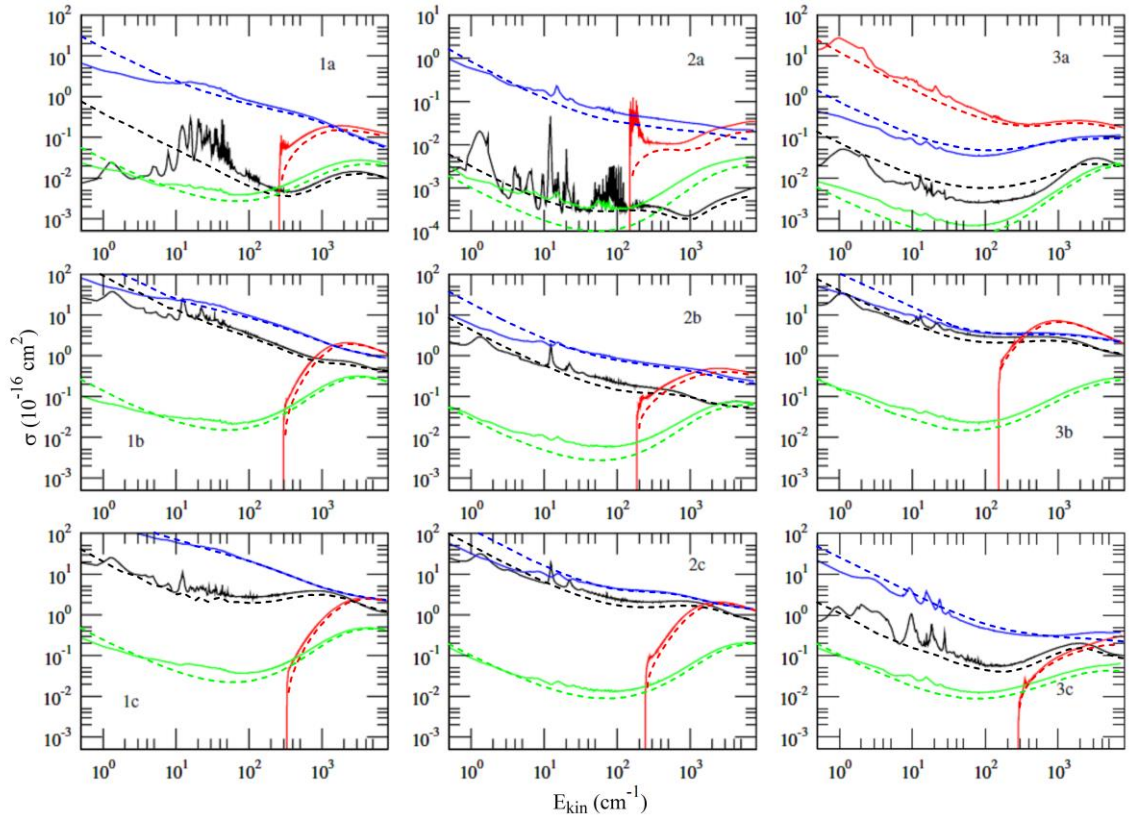


Figure 22: Comparison of results of the new approximate AT-MQCT method (dashed lines) against the full-coupled quantum calculations (solid lines) of Ref. [42] for the $\text{H}_2\text{O} + \text{H}_2$ system. The values of collision cross sections are plotted along the vertical axis, while the kinetic energy of collision is plotted along the horizontal axis, both in log scale. Black, red, green, and blue color is for $0 \rightarrow 0$, $0 \rightarrow 2$, $2 \rightarrow 0$ and $2 \rightarrow 2$ transitions in H_2 , respectively. In H_2O the transitions are from state 2_{11} to states: 1a) 0_{00} , 1b) 1_{11} , 1c) 2_{02} ; from state 3_{22} to states: 2a) 0_{00} , 2b) 1_{11} , 2c) 2_{11} ; from state 4_{40} to states: 3a) 1_{11} , 3b) 3_{11} , 3c) 5_{24} .

resonances densely packed in the range of collision energies between 10 cm^{-1} and 100 cm^{-1} . These quantum features cannot be described within AT-MQCT method, which may explain the asymptotic difference observed at very low collision energies in the frame 1a of Figure 22.

5.3.3. Time-dependent insight from AT-MQCT

Indeed, quantum resonances are entirely absent in our calculations, but this is expected since the adiabatic trajectory approximation, by construct, prohibits energy transfer during the first step of AT-MQCT calculations, and therefore disables the mechanism of Feshbach resonance formation¹⁵³. If the resonant behavior is present in the low energy range and happens to be important, then the full-quantum calculations are probably indispensable.

However, there are number of interesting phenomena where the MQCT results appear to capture the physics correctly. Take a closer look at the frame 3a, red lines, that describe the $4_{40}0 \rightarrow 1_{11}2$ transition. Notice that among nine processes represented by red lines in Figure 22 this is the only one that has no energy threshold! The value of cross section keeps increasing as collision energy is decreased, and our AT-MQCT method (dashed red line) reproduces this behavior very well in comparison with the full-quantum result (solid red line). This particular process can be thought of as a direct energy exchange between the two collision partners: the hydrogen molecule is excited, $0 \rightarrow 2$, while the water molecule is quenched, $4_{40} \rightarrow 1_{11}$. Energy released by one molecule is sufficient to excite the other molecule directly, without using the kinetic energy of collision.

Since MQCT offers a useful time-dependent picture, we tried to gain more insight into this quasi-resonant energy-exchange process. In Figure 23 we plotted the values of state populations along a typical AT-MQCT trajectory with impact parameter $b = 4.602 a_0$, which corresponds to the orbital angular momentum $L = 6$ at collision energy $U = 56.5 \text{ cm}^{-1}$. Population of the elastic channel (survival probability) corresponds to the initial state $4_{40}0$ of the $\text{H}_2\text{O} + \text{H}_2$, *i.e.*, hydrogen is in the ground state whereas water is excited. Figure 23 shows that population of this state (black) drops quickly as two molecules start colliding, then it slightly oscillates right after the collision, and finally goes to an asymptotic value close to ~ 0.8 . Population of the final state $1_{11}2$ (red in Figure 23), shows a roughly opposite trend but is not a mirror image of the initial state

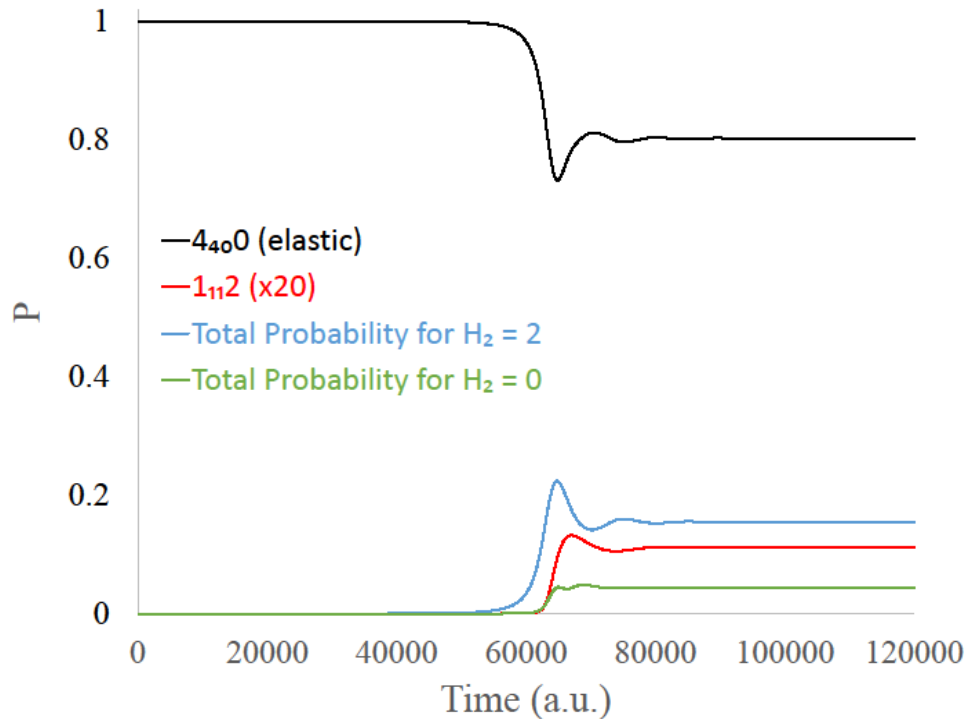


Figure 23: Time evolution of state probabilities along a typical MQCT trajectory (see text) that indicate a direct exchange of populations between the excited water state and the excited hydrogen state – a quasi-resonance energy exchange process $4_{40}0 \rightarrow 1_{11}$.

population, and the final probability in the $1_{11}2$ state is only $\sim 5.63 \times 10^{-3}$ (notice the scale factor). So, where does the rest of the initial state population go?

We inspected time evolution of all probability amplitudes $a_{mn}(t)$ and computed the total probability for the excitation of hydrogen to $j_2 = 2$ (summed over all states of water molecule, namely: $0_{00}2$, $1_{11}2$, $2_{02}2$, $2_{11}2$, *etc.*) This dependence is shown in blue in Figure 23 and we see that it is closer to the mirror image of the survival probability. The remaining small contribution is a probability for hydrogen to survive in the ground state $j_2 = 0$, while the water molecule is quenched and/or excited. This missing piece is plotted in Figure 23 in green. Now we see that in a time-dependent picture all these energy exchange processes happen synchronously.

5.4. Discussion

5.4.1. Numerical speed-up

Now let's address the question of computational speed-up of the MQCT method due to the adiabatic trajectory approximation, AT-MQCT. The overall speed-up is very substantial, but it comes from two separate sources. The cost of running the first (adiabatic) step of the AT-MQCT calculations is insignificant since the size of the adiabatic basis is rather small. Associated numerical cost can be neglected for the sake of transparency.

One substantial contribution to the speed-up comes from the fact that in the second part of AT-MQCT calculations we only need to propagate the quantum system of equations for the probability amplitudes, Eq. (17), instead of the Eqs. (13)-(17) propagated together in the original CC-MQCT method. As explained above, when the

basis size is large, the cost of computing the average gradient and torque in the right-hand sides of Eqs. (15) and (16) is dominant, and the overall cost associated with these two classical-like equations is about 65% (in the original version of the MQCT method). But this is not anymore required in the AT-MQCT, so, the numerical gain of the approximate method is expected to be on the order of $\times 3$. We carefully monitored the numerical cost of the full-coupled CC-MQCT (the original method) and of the AT-MQCT calculations (new approximate method) and confirmed that the acceleration close to the factor of three is indeed achieved in our code.

The second contribution to the speed-up comes from the efficient adiabatic step-size predictor, used to accelerate integration of the quantum-like system of equations, Eq. (17), during the second step of the AT-MQCT calculations. Associated computational

Table 8. Computational speed-up due to employment of the adiabatic step-size predictor in the AT-MQCT calculations, at different values of the kinetic energy of collision, for $\text{H}_2\text{O} + \text{H}_2$ system.

U (cm^{-1})	Speed-up
20	22.5
30	25.8
50	32.2
200	49.5
500	69.5
700	63.7
2000	48.0
7000	33.1

speed-up can be obtained by determining the number of time steps taken by the older version of integrator with constant step-size, and by new version with an adjustable step-size predictor, and then dividing one by the other (note that both versions use the RK4 integrator with the same numerical cost of one time step). We collected such data in a series of the numerical tests, making sure that both the constant step-size and the variable step-size calculations converge to about the same accuracy. We found that the numerical speed-up is sensitive to the collision energy, and these data are presented in Table 8. They indicate that the numerical gain associated with adiabatic step-size predictor is very substantial. The largest acceleration, by a factor of close to $\times 70$, is found at intermediate collision energies. At higher collision energies this is reduced to the factor of about $\times 33$.

Overall, taking into account both sources of the computational speed-up, the AT-MQCT calculations appear to be faster than the original MQCT method by a factor ranging from about $\times 200$ at intermediate scattering energies, to about $\times 100$ at high scattering energies. Since MQCT is more reliable at high collision energies, and the intended use of this approximate method is at high collision energies, we can deduce, as a take-home message, that the adiabatic trajectory approximation within MQCT framework reduces the numerical cost of scattering calculations by two orders of magnitude.

This makes many previously expensive calculations quite affordable now. As example, we want to report the cost of two runs we made during this work, at collision energies 500 cm^{-1} and 2000 cm^{-1} (the initial rotational state was $2_{11}2$ in both cases). These calculations were performed on Cori computer at NERSC¹⁵⁹, using only one node with 32 processors (2.3 GHz Intel Xeon). The wall-clock time of the run at $U = 500 \text{ cm}^{-1}$ was about 9 minutes, while at $U = 2000 \text{ cm}^{-1}$ it was about 23 minutes. It should also be taken

into account that out of this CPU time, only about 60% was spent on the actual propagation of the MQCT equations of motion, while about 40% is an overhead of the code associated with distribution of the initial data (array allocation, *etc.*) and collection of the final results (including MPI barrier). These costs can be substantially reduced by code optimization. It should also be kept in mind that the cost of MQCT calculations depends on the level of rotational excitation, since the number of initial states to be sampled, and the basis size itself, both depend on j_{12} . The corresponding cost scales linearly as $2j_{12} + 1$.

5.4.2. On a hierarchy of the approximate MQCT methods

The adiabatic trajectory approximation considered here, AT-MQCT, can be thought of as one member of the family of approximate solutions of the MQCT equations of motion (13)-(17). Indeed, in the second step of AT-MQCT calculations the quantum-like system of coupled equations (17) for the probability amplitudes $a_{mn}(t)$ is propagated decoupled from the classical-like trajectory, pre-computed during an independent first run. However, using the same overall two-step approach, we could explore various options for pre-computing the MQCT trajectory. Indeed, it does not necessarily have to be an adiabatic single-state trajectory. One can include more than one rotational state in the basis during the first run! Of course, this would increase the numerical cost of the first run, but hopefully not by much.

If we have a good physical intuition about what quantum states need to be included into the molecular basis to pre-compute the trajectory, we could include these states into the basis of the first run right away. Then, in a sense, we would operate with

two basis sizes: one relatively small (reduced) basis for pre-computing the mean-field trajectories and recording the $R(t)$, $\dot{\Phi}(t)$ and $V(t)$ dependencies, and the second (complete) basis for the propagating the probability amplitudes $a_{mn}(t)$ and computing the state-to-state transition cross sections. One can recall that similar algorithms of varying the basis size between different stages of calculations are routinely used in the electronic structure theory.

If we don't know *a priori* what molecular states need to be included into the trajectory calculations, we can either experiment by including several states energetically close to the initial state (since transition probabilities normally decrease as $\varepsilon_n^{n'}$ increases) or, we could simply run the adiabatic AT-MQCT calculations (both first and second steps, since their cost is relatively low), and analyze its results to identify the most important molecular states. Then, the basis for the mean-field trajectory could be increased by including these states, and a new set of trajectory calculations is re-run with a meaningful (still reduced) basis, followed by the final propagation of the quantum Eqs. (17) to determine $a_{mn}(t)$ and calculate the cross sections. If needed, this procedure could be repeated in an iterative fashion. Again, the exclusion of unnecessary states from the basis is often done in the electronic structure calculations.

In order to demonstrate this general approach, we carried out some of such iterative calculations. The results are presented in Figure 24 for the initial ground state of the $\text{H}_2\text{O} + \text{H}_2$ system, $0_{00}0$, with twenty rotational states in the basis, same as in the calculations reported in Figure 18. Collision energy here was $U = 200 \text{ cm}^{-1}$. Three sets of calculations are compared in Figure 24. Green bars correspond to the AT-MQCT method, with only one rotational state included into the basis to pre-compute the trajectory info

(the adiabatic trajectory approach). From these calculations one can see that besides the initial ground state #1, six excited rotational states gain significant populations during the collision. Large cross sections are found for the states #2, 3, 5, 6, 8 and 15. In particular, state #15 at high energy corresponds to the excitation of H_2 to the $j_2 = 2$ state. It makes sense to include these six excited states for pre-computing the mean-field trajectory data. The results of such calculations, with seven rotational states in the basis (expanded relative to the adiabatic trajectory case, but still reduced relative to the overall basis of 20 states) are presented in Figure 24 by blue bars. They indicate a consistent trend towards the results of the full-coupled CC-MQCT calculations shown by red bars (where all states are included, and all equations of motion are propagated together in a coupled fashion).

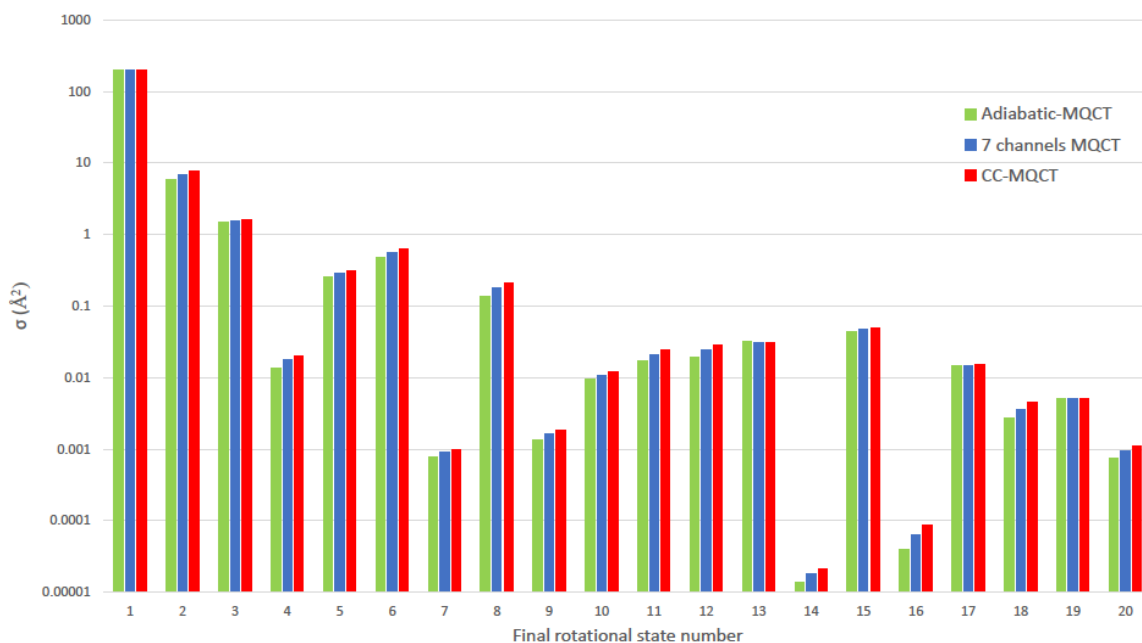


Figure 24: Comparison of results of the single-state AT-MQCT method (green bars) with calculations where seven rotational states are included in the trajectory prediction (blue bars), and with the full-coupled CC-MQCT calculations in a basis of twenty rotational states (red bars). The initial state is the ground state $0_{00}0$ of the $\text{H}_2\text{O} + \text{H}_2$ system. Collision energy is 200 cm^{-1} . Final states are listed along the horizontal axis. The values of collision cross sections are plotted along the vertical axis using log scale.

Therefore, we conclude that, in principle, one could employ a hierarchy of the approximate treatments that converge monotonically to the most accurate solution, and thus one can always achieve the desired degree of accuracy, if needed. The single-state AT-MQCT method is a limiting case in this hierarchy, which is also the fastest to run and the simplest to implement. Moreover, the results of calculations presented in this work indicate that AT-MQCT is accurate enough for many applications, and thus is a good starting point of exploration of any molecular system. It may become the “work horse” within the MQCT series of methods.

We also want to note that a similar hierarchy of approximations can be formulated without decoupling the classical-like equations of motion (13)-(16) from the quantum-like equations for probability amplitudes (17). In this case we would only talk about truncation of the triple sum in the right-hand sides of the Eq. (15) for the average gradient and Eq. (16) for the average torque. In a limiting case, the summation would be restricted to the m -states of one rotational channel that corresponds to the initial state of collision partners (*aka* adiabatic). Or one could expand this summation to include more rotational states into the estimate of the right-hand sides of Eqs. (15) and (16). And, in principle, one could do this iteratively, monitoring convergence. We tried some of such calculations too, and found that they also work, and give some computational advantage relative to the full-coupled CC-MQCT. However, without decoupling it is harder to take the full advantage of the computational speed up enabled by the adiabatic step-size predictor.

Therefore, we have chosen to stick with the decoupled AT-MQCT method. This option is now coded and will be made available to users in the new release of the program that will happen later this year.

5.5. Summary

In this chapter we reviewed the formalism of the mixed quantum/classical theory (MQCT) for calculations of molecular inelastic scattering and proposed a hierarchy of the approximate methods for solutions of the corresponding equations of motion. In the simplest limiting case, which we named AT-MQCT, we decouple the classical-like equations of motion from the quantum like equations for the propagation of probability amplitudes. The MQCT trajectories are pre-computed during the first step of calculations, where the driving forces are determined by the potential energy surface of the entrance channel alone, which is an adiabatic trajectory (AT) approach. The quantum state-to-state transition probabilities are computed during the second step, with an expanded basis and using the precomputed trajectory information for an efficient variable step-size integration.

This method was applied to a real system $\text{H}_2\text{O} + \text{H}_2$ and it was found that a very significant acceleration, by two orders of magnitude, is obtained at high collision energies. The results of the approximate propagation scheme are still rather accurate, as determined by comparison against more rigorous CC-MQCT calculations, in which the quantum and classical equations of motion are propagated together in a coupled fashion, but also against the full-quantum CC calculations from the literature (using the same potential energy surface).

Therefore, we conclude that our new AT-MQCT method represents a practical option for solving the inelastic scattering problem at high collision energies and for complex molecular collision partners (heavy molecules with many internal states, and heavy collision partners), when the standard full-quantum calculations become

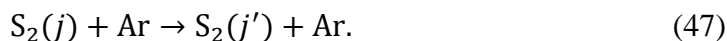
computationally unaffordable. The next step would be to apply this theory to much more demanding molecular systems and scattering processes, such as $\text{H}_2\text{O} + \text{H}_2\text{O}$ rotationally inelastic scattering. Another avenue of the research could be to replace the generic Runge-Kutta integrator by another more specific routine, such as a velocity-Verlet¹⁶⁰, a preconditioned Lanczos⁸³ or a symplectic^{161,162} integrator, in conjunction with the adiabatic step-size predictor.

CHAPTER 6. ON SYMMETRY-BREAKING IN THE RECOMBINATION REACTION OF TWO SULFUR ATOMS: ROTATIONAL ENERGY TRANSFER

6.1. Introduction

Sulfur is an element that plays key role in the cycle of matter on Earth, and is also important for other planets.^{163–168} It takes part in volcanic eruptions, microbiological respiration processes, water evaporation, decay of organisms, and industrial processes.^{169–175} During the period of volcanism billions years ago, huge amount of sulfur compounds was ejected into the atmosphere and the traces of that sulfur are still present in minerals and in surface deposits from that time.²⁹ The most important phenomenon is that sulfur stable isotopes preserved in these rocks exhibits unusual mass-independent fractionation (S-MIF) and the molecular level origin of this anomaly remains unexplained.^{29,34} The recombination reactions of sulfur are important in this context and here, we focus on the formation of the simplest sulfur allotrope by the energy transfer mechanism: $S + S \rightleftharpoons S_2^* \xrightarrow{+M} S_2$. The second step in this process is the energy transfer from the metastable intermediate to bath gas M. This step is the rate limiting step, and thus is important for this process. However, the second step has never been studied by anyone. Molecular symmetry is expected to play role in this process and this may help us to understand the origin of the mass-independent fractionation in sulfur (S-MIF).

The present work is focused on the collision of the S_2 molecule with argon as a bath gas:



The rotational energy transfer is being studied for the initial j in the broad range (up to $j = 51$), and the final j' in the range from $j' = 0$ (quenching) to $j' = 101$ (excitation). To study this rotational energy transfer, we need to build an accurate potential energy surface for $S_2 + Ar$ system.

6.2. Potential Energy Surface

Overall, our methodology for construction of the potential energy surface is similar to the methodology described by Peterson and co-workers,³⁴ but we made several improvements to it, as described below. The potential energy surface is represented as a sum of the pairwise interaction potentials of $S + S$ and $S + Ar$, plus the three-body interaction term:

$$U = U_{S_2} + U_{ArS} + U_{ArS} + U_{3b}. \quad (48)$$

The pairwise potentials, U_{S_2} of $S + S \rightarrow S_2$ and U_{ArS} of $S + Ar$, are determined using rather accurate methods while the three-body term, U_{3b} , is constructed using a simpler and numerically less expensive method, because the three-body interaction is expected to be smaller and has to be computed for a large number of points on the potential energy surface. All the *ab initio* calculations were done using MOLPRO^{176–178} suite.

6.2.1. *Ab Initio* Calculations of Pair Interactions for S_2 and $Ar + S$

The pairwise potentials were computed with an accurate method and a large basis set. The potential, U_{S_2} , was computed using two different methods. We used the multi-reference configuration interaction (MRCI)^{179–181} theory with Davidson correction (+Q). From the previous work on sulfur and ozone, O_2 , O_3 , S_2 , S_4 , it is known that the multi-

reference configuration interaction method is needed to describe the bond breaking.^{29,182,183} This is why we use the MRCI method for the potential energy curve for S_2 . We used one of the largest basis set available, aug-cc-pV(5+d)Z, for this calculation.^{184,185} The potential energy curve is shown in Figure 25 by red line.

Another method we used is the explicitly correlated coupled-cluster method and smaller basis set, CCSD(T)-F12/VTZ-F12.^{186–189} To be specific, we used unrestricted F12a method.¹⁸⁶ We considered this method because we decided to perform the three atom calculations using this method which will be discussed in the Section 6.2.2. The reason for choosing the F12 method was that it provides faster convergence towards the

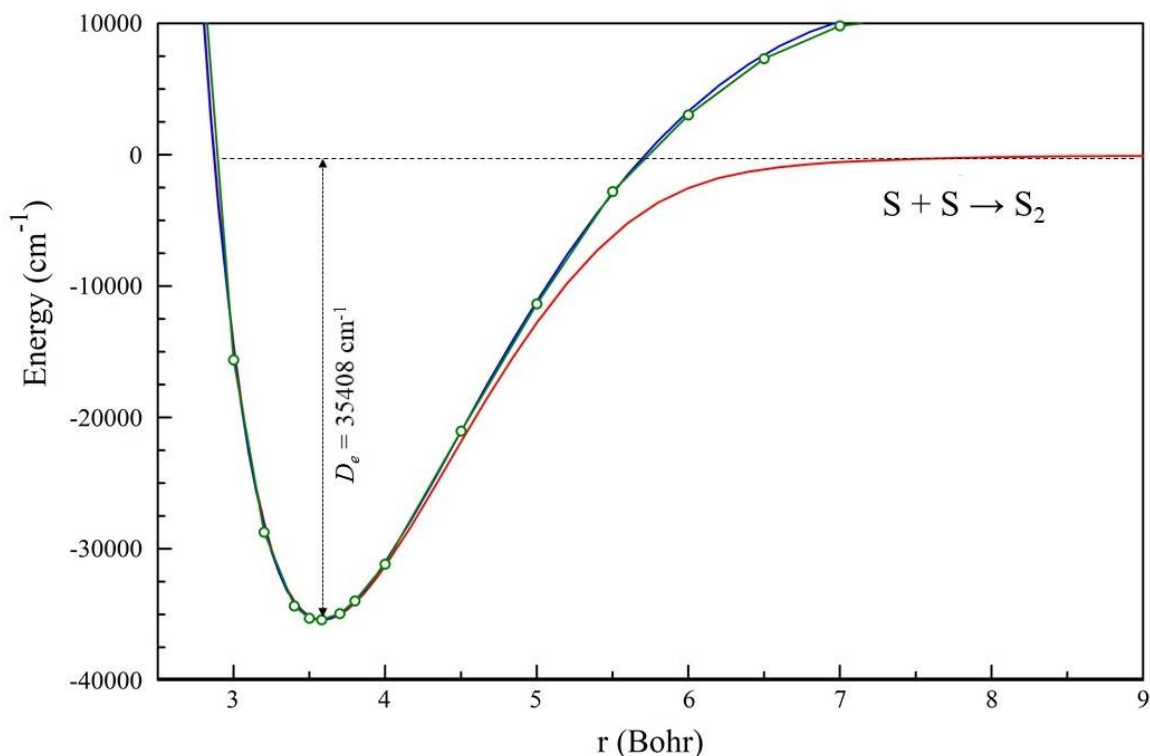


Figure 25: Potential energy curve of S_2 molecule computed using MRCI/aug-cc-pV(5+d)Z method is shown by the red line while the blue line represents the one computed with CCSD(T)-F12/VTZ-F12 method. The green line with circle is the S_2 curve computed by CCSD(T)-F12/VTZ-F12 method from three atom calculations of $S_2 + \text{Ar}$ system with Ar moved to a distance of 33.0 Bohr.

complete basis set limit even with a smaller basis set since the three-atom calculations are needed to be done for many points on the space. This calculation is represented as blue line in the same figure.

The equilibrium distance and dissociation energy are obtained by fitting Morse potential:¹⁹⁰

$$V(r) = -D_e + d[e^{-(r-r_e)/a} - 1]^2, \quad (49)$$

with different number of points in different energy range. These fitting coefficients were then used to compute the harmonic frequency and the anharmonicity parameter¹⁹⁰, as follows:

Table 9. Fitting of the *ab initio* data to obtain the spectroscopic and geometric parameters for S₂ molecule.

Method	Energy Range	Number of points used for fitting	r_e (Bohr)	ω_e (cm ⁻¹)	$\omega_e x_e$ (cm ⁻¹)	D_e (cm ⁻¹)
MRCI/ aug-cc-pV(5+d)Z	0.5 ω	4	3.587	724.74	1.97	35408.47
	1.5 ω	7	3.588	720.92	3.14	35408.64
	2.5 ω	9	3.588	720.68	3.05	35408.19
	3.5 ω	11	3.588	720.87	3.04	35408.61
CCSD(T)-F12/ VTZ-F12	0.5 ω	4	3.579	729.81	3.14	— —
	1.5 ω	7	3.579	730.35	3.07	— —
	2.5 ω	9	3.579	730.39	2.99	— —
	3.5 ω	11	3.579	730.77	2.97	— —
CCSD(T)-F12/ VTZ-F12 with Ar at R = 33.0 Bohr	1.5 ω	4	3.555	759.95	3.01	— —
	2.5 ω	6	3.555	760.50	3.01	— —

$$\omega_e = \frac{1}{a} \sqrt{\frac{2D_e}{m}}, \quad (50)$$

$$\omega_e \chi_e = \frac{1}{2ma^2},$$

where m is the reduced mass of $^{32}\text{S}^{32}\text{S}$. Table 9 summarizes the computed spectroscopic and geometric parameters obtained by fitting different number of points within different ranges of energy. The equilibrium distance and the dissociation energy did not change as we considered more points with different energy. The equilibrium bond distance is found to be $r_e = 3.59$ Bohr and the dissociation energy is $D_e = 35408.2 \text{ cm}^{-1}$. However, the harmonic frequency and anharmonicity parameter is more sensitive to the fitting with different energy range. The fit with smaller energy range of 0.5ω is less anharmonic, on the order of 2 cm^{-1} and shows slightly higher frequency, about 725 cm^{-1} which is the experimental value. But, the fit with larger energy shows more anharmonicity. Finally, the fit with 2.5ω was considered as the final results.

Table 10. Computed spectroscopic and thermochemical parameters of the S_2 molecule.

Reference	Method	r_e (Bohr)	ω_e (cm^{-1})	$\omega_e \chi_e$ (cm^{-1})	D_e (cm^{-1})	D_e (kcal/mol)
Peterson and co-workers ³⁴	ACPF/aV(T+d)Z	3.61	703.6	2.85	33377.1	95.43
	ACPF/aV(Q+d)Z	3.60	715.2	2.87	34748.2	99.35
	ACPF/aV(5+d)Z	3.59	718.0	2.84	35258.2	100.81
	ACPF/CBS	3.59	720.3	2.81	35680.0	102.00
Present work	MRCI/aV(5+d)Z	3.59	720.9	3.05	35408.2	101.24
	CCSD(T)-F12/VTZ-F12	3.58	730.4	2.99	--	--
Experiment ¹⁹¹		3.57	725.65	2.844	35601.6	101.79

The harmonic frequency is $\omega_e = 720.68 \text{ cm}^{-1}$ and the anharmonicity parameter has the value of $\omega_e \chi_e = 3.05 \text{ cm}^{-1}$.

The CCSD(T)-F12/VTZ-F12 method agrees reasonably well within the range of about 4.0 Bohr of S_2 distance. But, above 7.5ω , it starts deviating considerably. However, the similar fitting procedure was implemented with the data computed by CCSD(T)-F12/VTZ-F12 method and the spectroscopic and geometric parameters were obtained. The equilibrium bond length is different by 1 milli-Bohr. We cannot determine the dissociation energy because we cannot break the bond of the S_2 molecule by coupled cluster method. However, the frequency is about 10 cm^{-1} higher than the frequency computed by MRCI/aug-cc-pV(5+d)Z and the anharmonicity parameter is in the same order.

These data can be compared with previously available theoretical and experimental data¹⁹¹. The summary is presented in Table 10. The equilibrium distance of S_2 molecule deviates only by 0.02 Bohr. Our calculated harmonic frequency is very close to that of experiment and it deviates by only 4.97 cm^{-1} . The dissociation energy deviates by 193.4 cm^{-1} or 0.55 kcal/mol, which is about 0.5% of D_e . The data obtained by Peterson and co-workers using aug-cc-pV(5+d)Z basis set is pretty far from the experiment. The dissociation energy computed using aV(5+d)Z basis set is smaller from the experiment by almost 1 kcal/mol while the dissociations energy obtained by complete basis set extrapolation exceeds the experimental value by 0.21 kcal/mol. But our results of MRCI/aug-cc-pV(5+d)Z method is calculation with one basis set and the results are comparable. Although, CCSD(T)-F12/VTZ-F12 method cannot describe the dissociation energy, but the obtained frequency and anharmonicity parameter is pretty well.

Interaction of sulfur with argon was also computed using two different methods. The first one is the coupled cluster singles and doubles method with a perturbative treatment of triple excitations [CCSD(T)].^{192–195} Unrestricted CCSD(T) method was implemented for this calculation where the reference orbitals were determined from restricted Hartree-Fock calculations. The basis set chosen for this calculation was aug-cc-pV(5+d)Z. The reason for using this method and basis set is that Peterson and co-workers used the same. The result is shown in Figure 26 by the red line. The second method is CCSD(T)-F12/VTZ-F12. We decided to use it because it is known that F12 method converge faster to the complete basis set limit even with a smaller basis set. Our result shown in Figure 26 by the blue line do really demonstrate that.

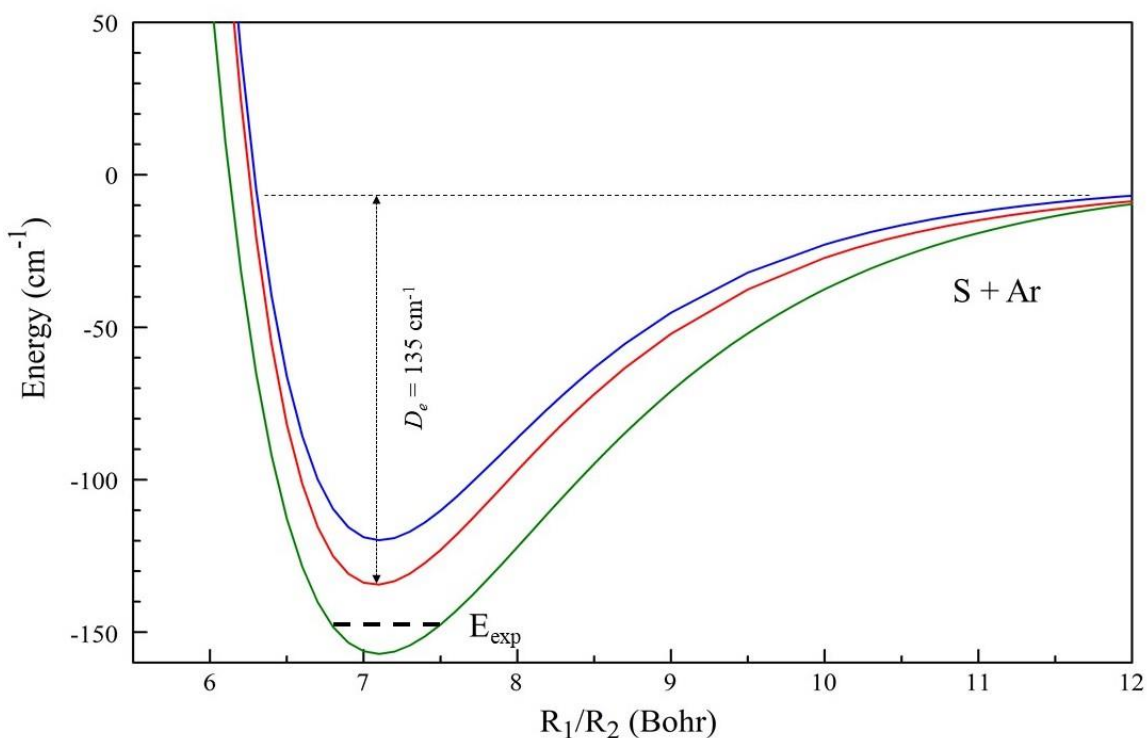


Figure 26: The red line represents the potential energy curve of S–Ar interaction computed by CCSD(T)/aug-CC-pV(5+d)Z method and blue line represents the potential interaction computed by CCSD(T)-F12/VTZ-F12 method.. The green line is representing the analytic fit of the S₂ + Ar data as discussed in section 6.2.3.

Various geometric and spectroscopic parameters were obtained by similar methodology as discussed above by using Eqs. (49) and (50). Table 11 summarizes the results of different fit within several energy range. The obtained results are not changing much for both methods. The equilibrium distance is found to be in the order of $r_e = 7.08$ Bohr. The harmonic frequency is in the order of $\omega_e = 36.4 \text{ cm}^{-1}$ and the anharmonicity on the order of $\omega_e \chi_e = 2.5 \text{ cm}^{-1}$. However, these two methods yield two different depths of the well. The depth of the well computed by CCSD(T)/aug-cc-pV(5+d)Z method is 14.6 cm^{-1} deeper than that of F12 method. The CCSD(T)/aug-cc-pV(5+d)Z method gives the dissociation energy closer to the experimental value.

Table 12 summarizes these results compared with previously available experimental results and theoretical results. The minimum energy point deviates from experimental data by 0.08 Bohr. The depth of the well is rather shallow and deviates from the experimental result by 13.9 cm^{-1} . There is no experimental data for the harmonic frequency and the anharmonicity parameter. However, these spectroscopic parameters are

Table 11. Fitting of the *ab initio* data to obtain the spectroscopic and geometric parameters for S + Ar interaction.

Method	Energy Range	Number of points used for fitting	r_e (Bohr)	ω_e (cm^{-1})	$\omega_e \chi_e$ (cm^{-1})	D_e (cm^{-1})
CCSD(T)/ aug-cc-pV(5+d)Z	0.5ω	9	7.083	36.22	2.44	134.43
	1.5ω	19	7.082	36.42	2.47	134.42
	2.5ω	24	7.082	36.40	2.46	134.39
CCSD(T)-F12/ VTZ-F12	0.5ω	9	7.103	34.68	2.51	119.83
	1.5ω	19	7.103	34.87	2.54	119.82
	2.5ω	24	7.103	34.85	2.53	119.80

in good agreement with previous theoretical data computed by Peterson and co-workers³⁴ using the same method and basis set. The harmonic frequency deviates by 0.83 cm^{-1} and the anharmonicity parameter deviates by 0.02 cm^{-1} . The attraction between sulfur and argon is relatively weak, resulting in a van der Waals interaction. The most significant part in this curve is the S–Ar repulsion region.

In principle, for a diatomic system like S + S or S + Ar, there is no problem to build a one-dimensional potential energy curve just by using a 1D spline interpolation of the *ab initio* data points. Such spline goes through the *ab initio* data points and between any two points it uses interpolation by a quadratic or cubic function, depending on the order of the spline. Here, cubic spline was used for interpolation. Let us assume that, one needs potential at the point r between points r_i and r_{i+1} . The method then considers four points, r_{i-1} , r_i , r_{i+1} , and r_{i+2} and four values of the potentials at those points $V(r_{i-1})$, $V(r_i)$, $V(r_{i+1})$, and $V(r_{i+2})$. Now, for a cubic spline, the method runs a function to fit these data, such as

Table 12. Computed spectroscopic and thermochemical parameters of the minimum energy point of the S–Ar interaction.

References	Method	$r_e(\text{Bohr})$	$\omega_e(\text{cm}^{-1})$	$\omega_e x_e(\text{cm}^{-1})$	$D_e(\text{cm}^{-1})$
Peterson and co-workers ³⁴	CCSD(T)/aV(T+d)Z	7.18	34.4	2.45	129.06
	CCSD(T)/aV(Q+d)Z	7.10	34.5	2.46	131.51
	CCSD(T)/aV(5+d)Z	7.07	35.6	2.44	136.4
	CCSD(T)/CBS	7.04	36.5	2.39	140.6
Present work	CCSD(T)/aV(5+d)Z	7.08	36.4	2.46	134.4
	CCSD(T)-F12/VTZ-F12	7.10	34.85	2.53	119.8
Experiment ²⁰⁴		7.16	— —	— —	148.3

$$V(r) = ar^3 + br^2 + cr + d, \quad (51)$$

to obtain four fitting parameters, a , b , c , and d by solving a linear system of equations.

The codes I used for this purpose are `SPLINE` and `SPLINT`, taken from the Numerical Recipes.^{80,196}

6.2.2. *Ab Initio* Calculation for the Three-Atom System $S_2 + Ar$

After exploring the pair potentials, we step forward to build the potential energy surface. In order to build the three-atom potential, we decided to take the less numerically expensive method, the explicitly correlated coupled-cluster method and a smaller basis set as CCSD(T)-F12/VTX-F12.^{186–189} We used unrestricted F12a method specifically.¹⁸⁶ As I mentioned earlier, the reason for choosing the F12 method was that it provides faster convergence towards the complete basis set limit even with a smaller basis set. For this calculation, Jacobi coordinates were used as in Figure 27. In this coordinate system, r is

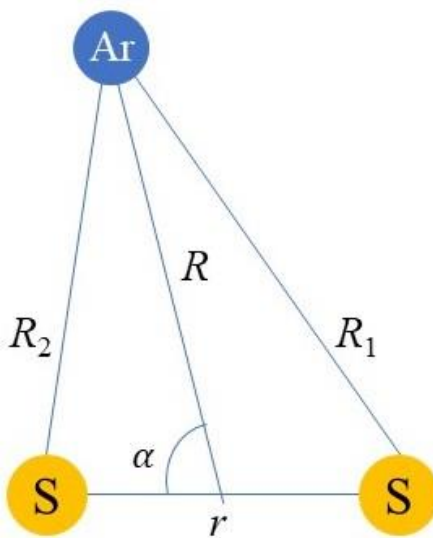


Figure 27: Jacobi coordinates of $S_2 + Ar$ system. Here, r is the distance between two sulfur atoms, R is the distance of argon atom from the geometric center of S_2 , and α is the angle of approach.

the interatomic distance of the S_2 molecule. The coordinate R represents the distance of Ar from the geometric center of S_2 , and α is the angle of approach. The bond distance of the S_2 molecule was fixed at its equilibrium distance, $r_e = 3.59$ Bohr. Thus, the S_2 molecule is considered in this subsection as rigid. The potential energy surface then was built for the remaining two degrees of freedom, R and α . The distance of argon from S_2 molecule was varied in the range $3.5 \leq R \leq 24.0$ Bohr (61 grid points) and the angular

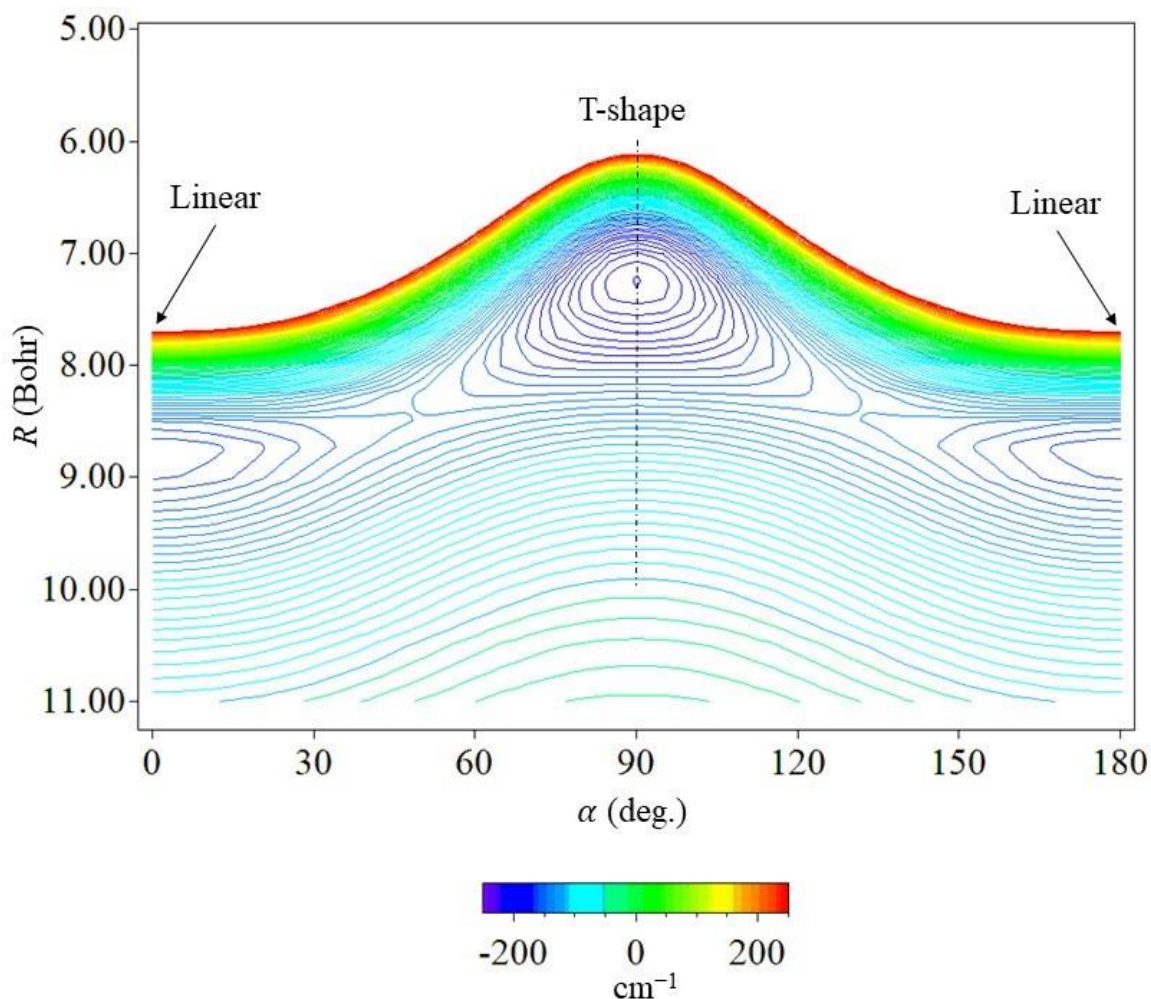


Figure 28: Potential energy surface of the $S_2 + \text{Ar}$ system in two degrees freedom. The S_2 bond distance is set fixed for this case at its equilibrium distance of 3.59 Bohr. The global minimum energy point was found to be in T-shaped geometry and the energy of this point is $V = -210.5 \text{ cm}^{-1}$ and the local minimum energy point was at linear geometry with energy $V = -166.1 \text{ cm}^{-1}$.

coordinate was changed in the range $0^\circ \leq \alpha \leq 90^\circ$ with a step of 5° . Symmetry was used to reflect the data into the range $90^\circ < \alpha \leq 180^\circ$. Thus, we have $N_1 = 61$ points along R coordinate and $N_2 = 19$ points along α coordinate. Overall, we have $61 \times 19 = 1159$ points for this 2D PES.

The potential energy surface is shown in Figure 28. The global minimum point is found in the T-shaped geometry (when the angle of approach is 90°) and the energy of

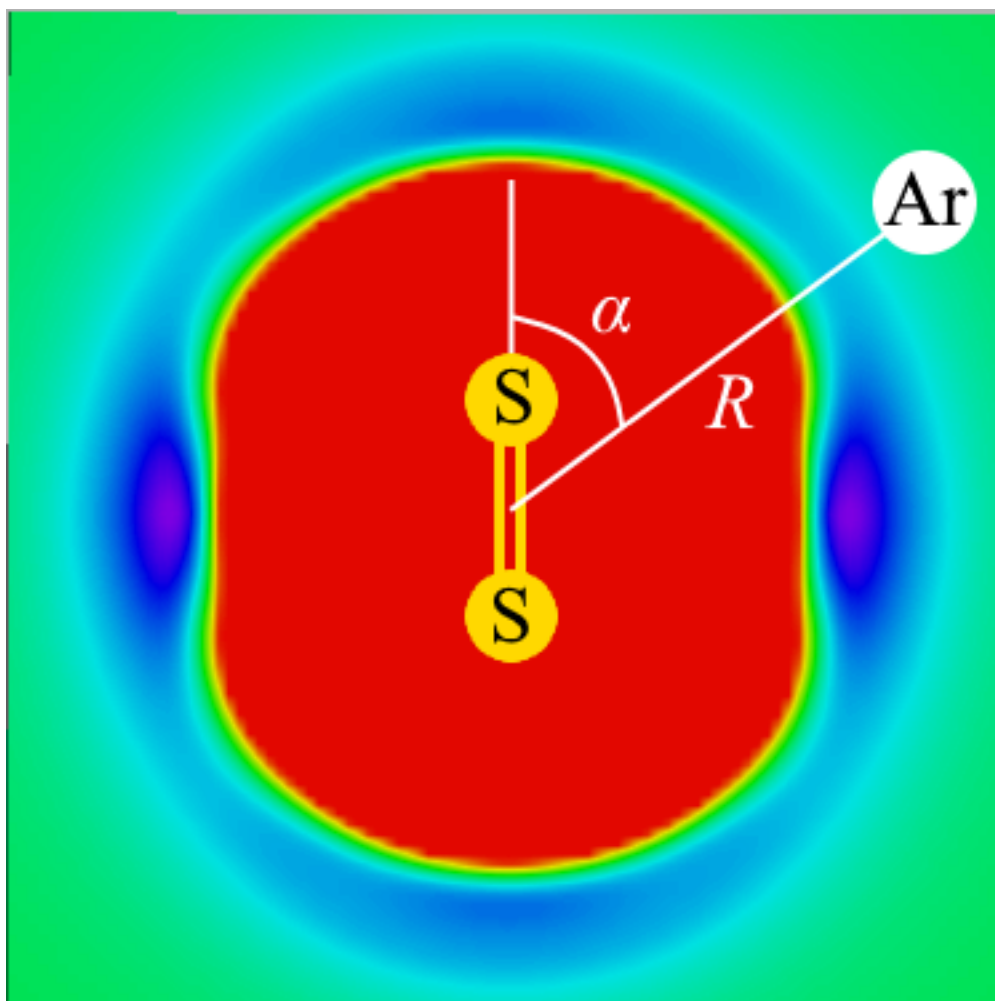


Figure 29: Potential energy surface of the $S_2 + Ar$ system with two degrees freedom. The S_2 bond distance is set fixed for this case at its equilibrium distance of 3.59 Bohr. The minimum energy point at T-shaped geometry and small wells at linear geometry is better reflected in this figure.

this point relative to the dissociation limit of $S_2 + Ar$ is about $V = -210.5 \text{ cm}^{-1}$. There are two more shallower wells in linear geometries when the angle of approach is either 0° or 180° . The energy of this secondary minima is about $V = -166.1 \text{ cm}^{-1}$ relative to dissociation limit. The transition point is found around the angle of approach of $\alpha = 45^\circ$ or 135° . The energy for the transition state was found as $V = -140.0 \text{ cm}^{-1}$.

An alternative, more intuitive way of showing the PES is presented in Figure 29. In this figure, Ar approaches the S_2 molecule from various direction. As I mentioned earlier, the global minimum (deeper well) is observed when Ar approaches S_2 in perpendicular direction and the local minima is in the linear direction. This image has 101×101 points generated from those *ab initio* data of Figure 28 using a two-dimensional spline interpolation to plot this figure.

6.2.3. Calculation of the Three-Body Interaction Term

The global potential energy surface requires one more degree of freedom, which is the bond distance of S_2 molecule, r , responsible for vibration. I computed $U(r, R, \alpha)$ potential energy surface on a three-dimensional grid of points, r, R, α using CCSD(T)-F12/VTZ-F12 method. We have $N_3 = 11$ points along S_2 bond distance (r coordinates) in the range $2.7 \leq r \leq 8.0$ Bohr, $N_1 = 19$ points along the distance of Argon from the S_2 molecule (coordinate R) ranged from $4.5 \leq R \leq 33.0$ Bohr and $N_2 = 7$ points the angular coordinate (α) is ranged from $0^\circ \leq \alpha \leq 90^\circ$. A total of 1463 *ab-initio* data points in 3D computed and out of which only 820 points were converged.

One reason of this convergence failure is that when the Ar atom approaches one of the sulfur atom, i.e. the value of R_1 and/or R_2 in Figure 27 getting smaller, then the

interaction of sulfur with argon changes its electronic state and the calculations start failing. So, we can see that there are “holes” in our potential energy surface. Another problem is that the coupled cluster method can give reasonable description of bond breaking, but within a limited range of S₂ bond distance, coordinate r . In Figure 25, the coupled cluster results are close to the MRCI results only within a very limited range up to $r = 4$ Bohr. Significant differences between these data observed between the range $5.0 < r \leq 8.0$ Bohr and beyond $r \geq 8$ Bohr, the calculations did not even converge. Thus, the coupled cluster method gives wrong shape of the surface and wrong dissociation energy. However, our goal is to build a potential energy surface up to dissociation limit. One can probably perform these *ab initio* calculations with MRCI method, but it will be numerically expensive since both sulfur and argon have many electrons.

Therefore, we followed a simplified methodology of Peterson and co-workers³⁴. The potential energy was expressed as a sum of pairwise additive potential and the three-body term:

$$U(r, R, \alpha) = U_{S_2}(r) + U_{ArS}(R_1) + U_{ArS}(R_2) + U_{3b}(r, R, \alpha). \quad (52)$$

Here as before, r is the distance between two sulfur atoms, as in Figure 27, R_1 and R_2 are the distance of Ar from two sulfur atoms respectively. In order to extract the three-body terms from the *ab initio* data one can use the expression that follows from Eq (52):

$$U_{3b}(r, R, \alpha) = U(r, R, \alpha) - U_{S_2}(r) - U_{ArS}(R_1) - U_{ArS}(R_2). \quad (53)$$

The behavior of the three-body term, U_{3b} , is shown in Figure 30. Here four different colors represent four different values of interatomic distances of the S₂

molecule. Black, green, red and blue circles correspond to S_2 molecule for $r = 3, 4, 5$ and 6 Bohr respectively. Three different curves for each color represents three different angles of approach, $\alpha = 0^\circ, 45^\circ$ and 90° . Note that the three-body term computed in this way changes its sign. It is positive in T-shape and near it, but becomes negative and very large in linear configurations (see Figure 30). Such anisotropic behavior of the three-body term is difficult to fit or spline. We tried two different methods described below, but neither of them worked satisfactorily.

We suppose that this approach of obtaining the three-body term worked for Peterson and did not work for us because our range of R is considerably broader than his

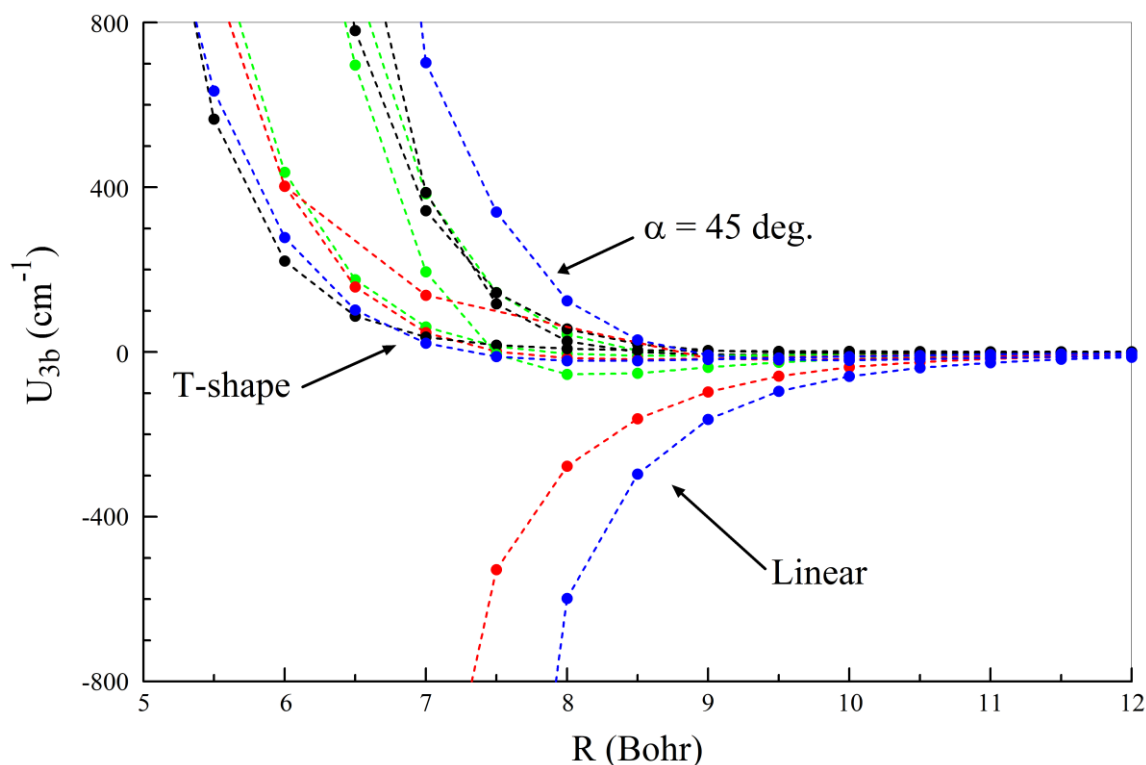


Figure 30: Slices of the three-body term $U_{3b}(R)$ were computed following the methodology of Peterson and co-workers is shown here. Black, green, red, and blue symbols correspond different S_2 distance: $r = 3.0, 4.0, 5.0$, and 6.0 Bohr respectively. Three different lines for each color corresponds to three different angles of approach: $\alpha = 0^\circ, 45^\circ$ and 90° .

range. In particular, it is extended further into the range of small values of R down to $R = 4.5$ Bohr while for his grid started much further, at $R = 10.02$ Bohr. Therefore, the values of R_1 and R_2 are smaller for our case while he was looking at the long range of the potential energy surface only where the interaction is not that strong. Therefore, our potential energy surface is expected to be more accurate in a broader range of values of the interatomic distances, but we have to find a way to deal with accurate representation of the three-body term.

What is the reason for this three-body term to be negative? Clearly, the S + Ar potentials are too repulsive at smaller values of R_1 and/or R_2 in linear configuration when the Ar–S interaction is important. So, instead of taking this potential from a separate *ab initio* calculation, why simply we don't try to obtain the alternative pairwise potentials from analysis of the *ab initio* data points, $U(r, R, \alpha)$, we computed. One possibility is to find the diatomic potential in a simple analytic form $U_{\text{ArS}}^{\text{Morse}}(R)$ that would give a good description of these pairwise interaction but would never exceed the value of PES, $U(r, R, \alpha)$:

$$U_{\text{ArS}}^{\text{Morse}}(R_1) + U_{\text{ArS}}^{\text{Morse}}(R_2) \lesssim U(r, R, \alpha) - U_{\text{S}_2}(r). \quad (54)$$

Thus, we want to reproduce the repulsive S–Ar interaction at short distance of R (smaller values of R_1 and R_2) without exceeding the actual values of potential so that the three-body term remains always positive. We considered a subset of points from the repulsive part of the potential at energies, $U(r, R, \alpha)$, in the range $200 < U \leq 2000 \text{ cm}^{-1}$. This range

Table 13. Morse parameters representing the interaction of S–Ar.

$D_e(\text{cm}^{-1})$	$R_e(\text{Bohr})$	$a(\text{Bohr})$
157.1	7.1	1.41

was chosen because at thermal energies majority of Ar + S₂ collision have energy above 200 cm⁻¹ and beyond 2000 cm⁻¹. There are 286 points in this energy regime. This subset of data was then used to tune parameters of two Morse functions:

$$U^{\text{Morse}}(R_1) = -D_e + D_e \left[e^{-(R_1 - R_e)/a} - 1 \right]^2. \quad (55)$$

The same function was used for R_2 as well. Root mean square deviation (RMSD) was computed in order to determine the set of parameters that provides the smallest possible error.

The fitted parameters found for this Morse potential with minimum RMSD are given in Table 13. The analytic Ar + S potential energy curve, U^{Morse} , obtained this way

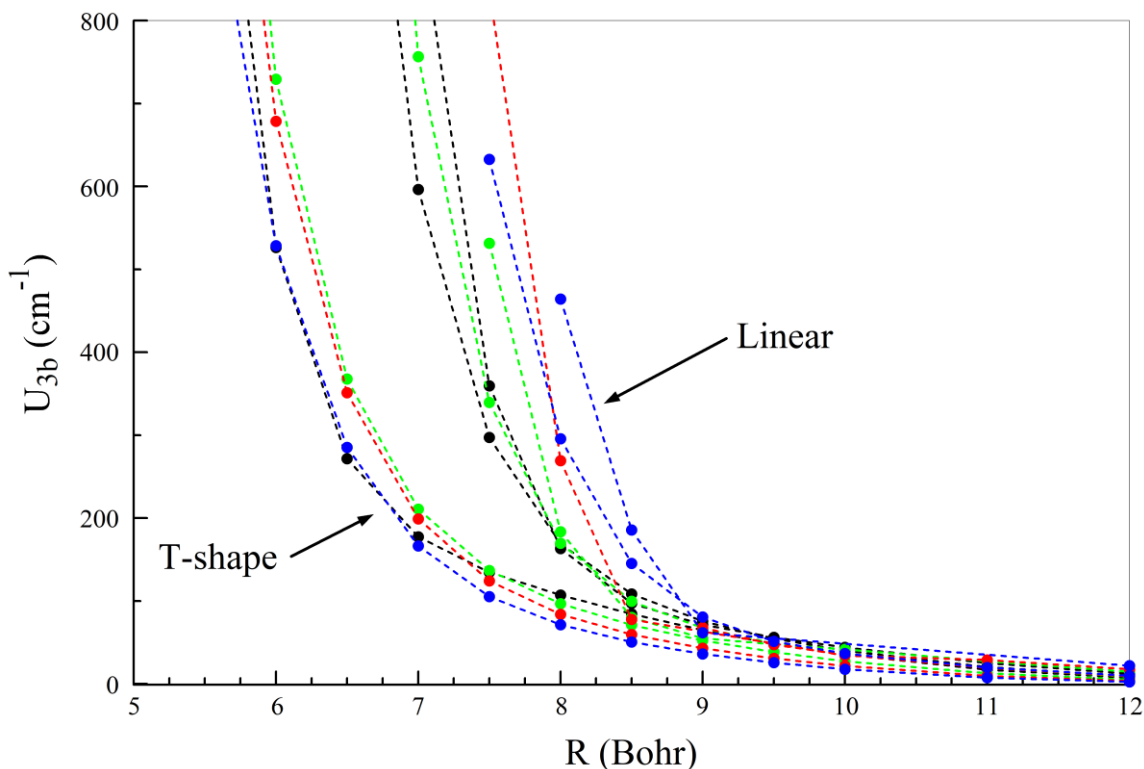


Figure 31: Three-body terms computed following our methodology. Here again, black, green, red, and blue lines correspond different S₂ distance, $r = 3.0, 4.0, 5.0$ and 6.0 Bohr respectively and three different lines for each color corresponds to three different angles of approach, $\alpha = 0^\circ, 45^\circ$ and 90° .

is also shown in Figure 26 by the green line. This curve indicates the minimum at approximately the same value S–Ar distance, $R_1 = 7.07$ Bohr. However, this curve is deeper by 22.67 cm^{-1} than the one computed with CCSD(T)/aV(5+d)Z. Although, the experimental dissociation energy is right in between of red line and green line. These two curves give similar energies beyond $R = 12.0$ Bohr. But most importantly, the analytic curve is less repulsive in the range of shorter distance of R_1 (S–Ar close approach). This is one difference from the approach of Peterson and co-workers.

We have also made the second modification to this procedure. Instead of subtracting the S_2 curve computed separately, we subtract our data. The S_2 potential was simply taken as the last slice of $U(r, R, \alpha)$:

$$U_{S_2}(r) = U(r; R = 33 \text{ Bohr}). \quad (56)$$

We checked that when Ar is very far from the S_2 molecule, then there is no change of potential due to the change of angle α , i.e. S_2 curve at the last slice ($R = 33.0$ Bohr) was isotropic with respect to the angle. So, from the *ab-initio* data, we subtracted the last slice of our *ab initio* data cube, $U(r; R = 33.0 \text{ Bohr})$, when Ar is very far which makes the difference of $U(r, R, \alpha) - U_{S_2}(r)$ zero asymptotically, $R \rightarrow \infty$. It is represented in Figure 25 by the green line.

Finally, the three-body term can be computed as:

$$U_{3b}(r, R, \alpha) = U(r, R, \alpha) - U_{S_2}(r, R \rightarrow \infty) - U_{\text{ArS}}^{\text{Morse}}(R_1) - U_{\text{ArS}}^{\text{Morse}}(R_2). \quad (57)$$

This gives us an alternative description of the three-body term and it is represented in Figure 31. From the figure, we can see that this form of the three-body term is always positive in all slices. The R dependence is monotonic, and the α dependence is less

anisotropic and is smooth. The value of U_{3b} is now always positive in all slices. So, these data are much easier to fit.

6.2.4. Representation of the Three-Body Term by Fitting

We tried fitting the three-body term data points with the following functional form:

$$U_{3b}^{\text{fit}}(R_1, R_2, R_3) = \sum_{l=0}^L \sum_{ijk}^M d_{ijkl} \rho_1^i \rho_2^j \rho_3^k \left(1 + \sum_{n=1}^3 \cos(\theta_n) \right)^l \quad (58)$$

suggested by Peterson.¹⁹⁷ Here, d_{ijkl} is a set of fitting coefficients, θ_1, θ_2 and θ_3 represent three angles between three atoms (as represented in Figure 32 below). R_1, R_2 , and R_3 are three distances between the atoms and $\rho_1^i(R_1), \rho_2^j(R_2)$ and $\rho_3^k(R_3)$ are the basis functions of the distance coordinate:

$$\rho_m(R_m) = e^{-\frac{R_m^0}{R_m}} e^{-\beta_m(R_m - R_m^0)}, \quad (59)$$

where, $m = 1, 2$ or 3 . The R_m^0 is the reference interatomic distance which was set to be equal to the minimum energy point of each pair potential. For S – S bond distance, $m = 1$, the value is $R_1^0 = 3.59$ Bohr, and for S – Ar distance, $m = 2$ and 3 , it is $R_2^0 = R_3^0 = 7.08$ Bohr. In the Eq (59) the β_m is a nonlinear fitting parameter. The values of L and M in Eq. (58) determine the size of the basis set. There are two constraints on the choice of the basis set:

$$(i + j + k) \leq M \quad (60)$$

$$(i + j + k) \neq i \neq j \neq k \quad (61)$$

Equation (60) implies that M is the total number of functions. Equation (61) set the condition that any of i, j or k could be equal to zero, but any two cannot be zero at the same time.

A FORTRAN code was written for this fitting method which used Levenberg-Marquardt algorithm¹⁹⁶ for solving this non-linear system of equations. There were four different loops for each of i, j, k , and l and optimized value for each was found such that the value of root mean squared error (RMSE) is minimum. The maximum initial values up to $L = 8$ and $M = 5$ were tried. Finally, the best fit was found for the values of $L = 5$ and $M = 6$ for which the value of RMSE was 2.51 cm^{-1} . There was a total of 390 linear fitting parameters which is represented as d_{ijkl} in equation (58) and three nonlinear parameters, β_1, β_2 and β_3 , as in equation (59). We can see that the function chosen for this fitting is rather flexible. But we found that for configurations of small R_1 and R_2 near the linear geometry where we do not have enough *ab initio* points, the fit of $U_{3b}(r, R, \alpha)$ exhibits large-amplitude oscillation. The problem is shown in Figure 33 as a function of

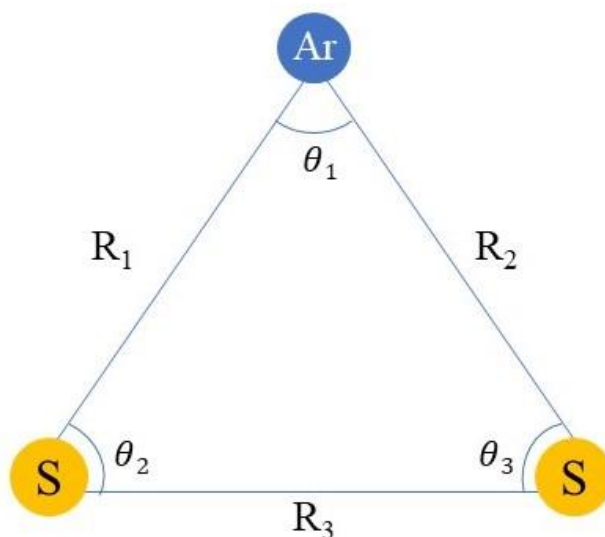


Figure 32: Graphical representation of the coordinates for the fitting function.

R . It goes to large negative numbers as you see in Figure 33. In fact, at smaller distances of R , it goes back again to large positive values and thus oscillates.

Although this fitting method is rather general and can be used even for larger molecules, it does not work for us, unfortunately, due to the insufficient number of points for the shapes of close Ar–S approach where R_1 and R_2 are small.

6.2.5. Representation of the Three-Body Term by Spline Interpolation

Alternatively, the three-body term can be interpolated using the Reproducing Kernel Hilbert Space (RKHS) method of Ho and Rabitz¹⁹⁸. The expression is as follows:

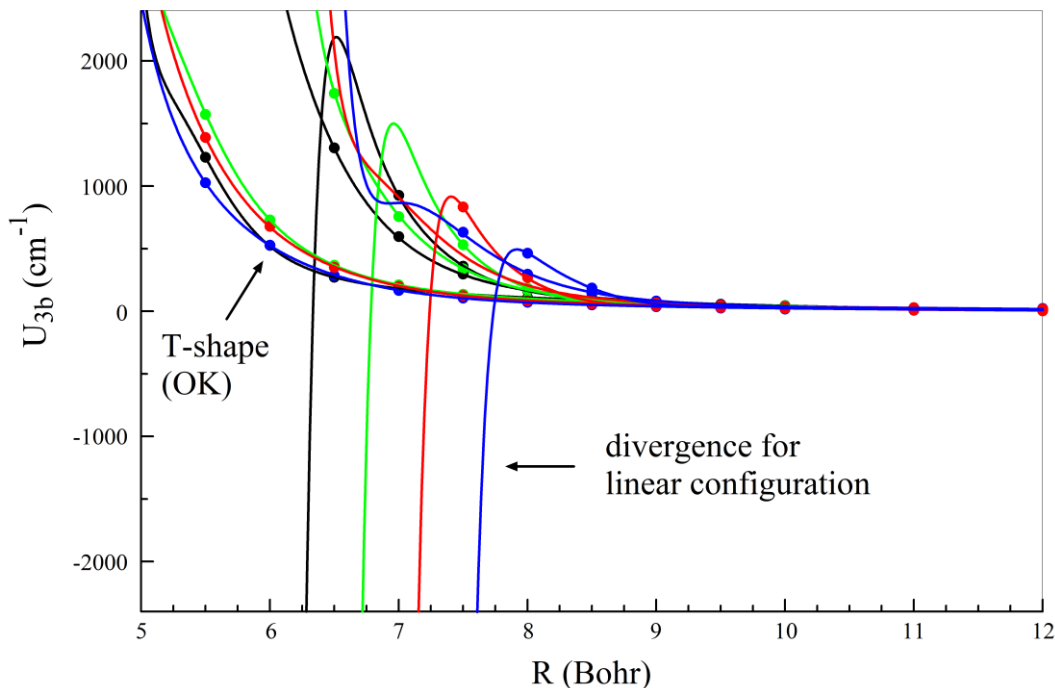


Figure 33: The fitted three-body term for the $S_2 + \text{Ar}$ system. The divergence behavior in linear configuration can be seen here. Black, green, red, and blue lines correspond different S_2 distance, $r = 3.0, 4.0, 5.0$ and 6.0 Bohr respectively. Three different lines for each color corresponds to three different angles of approach, $\alpha = 0^\circ, 45^\circ$ and 90° .

$$U_{3b}^{\text{spline}}(r, R, S) = \sum_i^{N_{\text{TOT}}} C_i q_1(r, r_i) q_2(R, R_i) q_3(S, S_i), \quad (62)$$

Here, N_{TOT} is total number of data points, C_i are a set of the RKHS coefficients that needs to be determined. The functions q_1 , q_2 and q_3 , which is called reproducing kernel, play role of the basis functions for three degrees of freedom, r , R and α . Let's consider the first one. It has the following form:¹⁹⁸

$$q_1(r, r_i) = \frac{1}{14r_{>}^7} \left(1 - \frac{7r_{<}}{9r_{>}} \right). \quad (63)$$

For each point r_i along the grid, one would have to define $r_{>} = \max$ of (r, r_i) and $r_{<} = \min$ of (r, r_i) where r is the arbitrary point where the potential energy surface has to be computed. For example, consider point r_1 in Figure 34. The grid point is located before the point r which is indicated by the red cross in the figure. So, $r_{>} = r$ since the value of r is larger than r_1 and $r_{<} = r_1$. From the figure, all the points in the blue region would correspond to $r_{<}$ with respect to point r and all the points in the pink region would correspond to $r_{>}$. Basically, for a given arbitrary point r , one can define the value of this kernel for each point on the grid r_i as shown in the figure. According to this definition we can construct the same number of kernels as the data points r_i . The value of this function

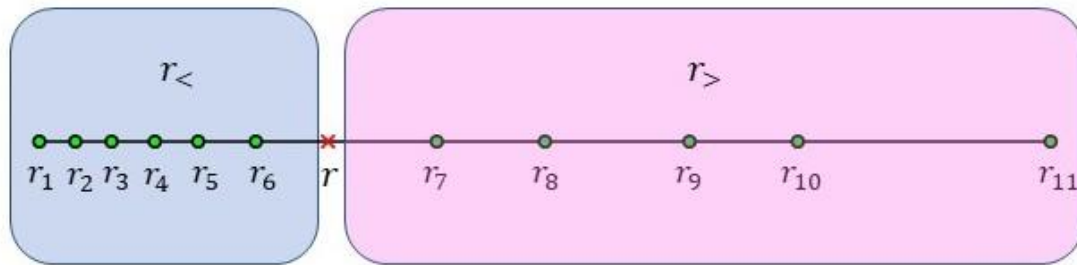


Figure 34: Dependence of kernel on the grid of coordinate. A schematic representation is also provided to determine $r_{<}$ and $r_{>}$.

is determined by the actual grid r_i and position of the point. Each of these kernels is computed at the corresponding point r and shows how different points in the grid affect the value here.

The kernel q_2 is same as kernel q_1 since both are the distance like coordinate:

$$q_2(R, R_i) = \frac{1}{14R_{>}^7} \left(1 - \frac{7R_{<}}{9R_{>}} \right). \quad (64)$$

The kernels q_1 and q_2 are defined in the range of interval $r \in [0, \infty)$ for the distance like coordinates r and R . The behavior of this distance kernel is illustrated by Figure 35. This picture shows that the set of kernels show large values only for the short distance approach between r and r_i . It corresponds to strong repulsion due to close approach of two atoms. The kernels exhibit the minimum at intermediate distances between r and r_i and then, it goes smoothly to zero in the asymptotic range when the atoms are far.

For the angular coordinate, the kernel q_3 is as follows:

$$q_3(S, S_i) = 1 + S_{<}S_{>} + 2S_{<}^2S_{>} \left(1 - \frac{S_{<}}{3S_{>}} \right). \quad (65)$$

The variable S :

$$S = (1 + \cos\alpha)/2. \quad (66)$$

represents the angle like coordinate scaled such that the values of the coordinates remain in the interval $[0,1]$.

The angle-like kernel is represented in Figure 36. This figure illustrates that at linear configurations, $S = 1$, the repulsion would be higher and then decreases smoothly towards the T-shape configuration. The value of the kernel q_3 changes in the limit $[1, 3.5]$ while the value of kernels q_1 or q_2 change form $[0, \infty)$.

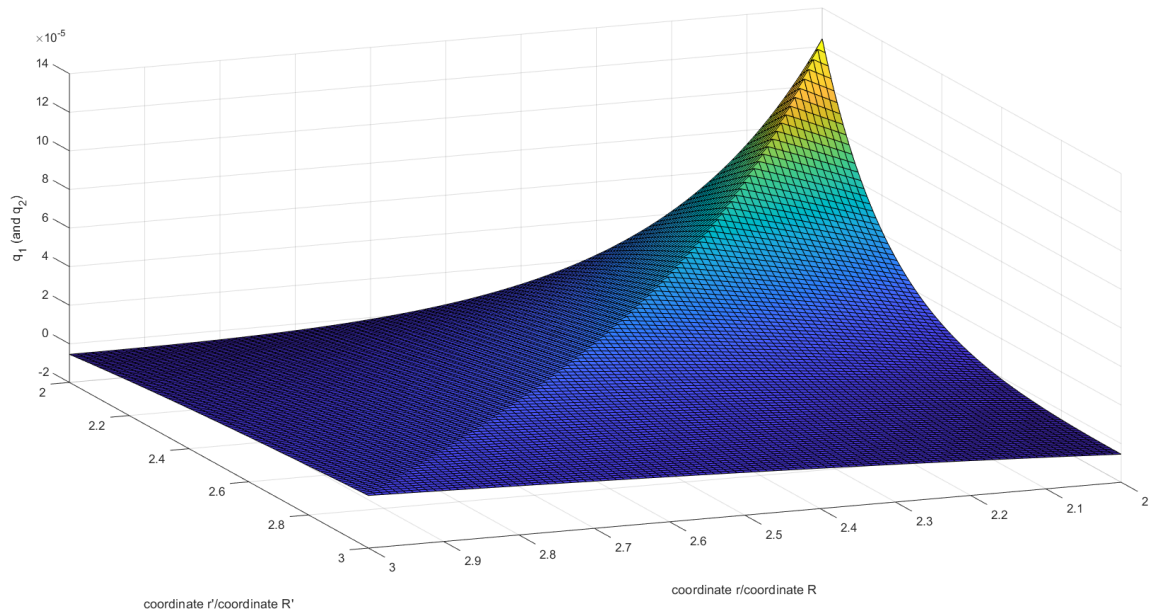


Figure 35: The reproducing kernel q_1 for the distance coordinate r . The kernel q_2 for the distance coordinate R is exactly the same.

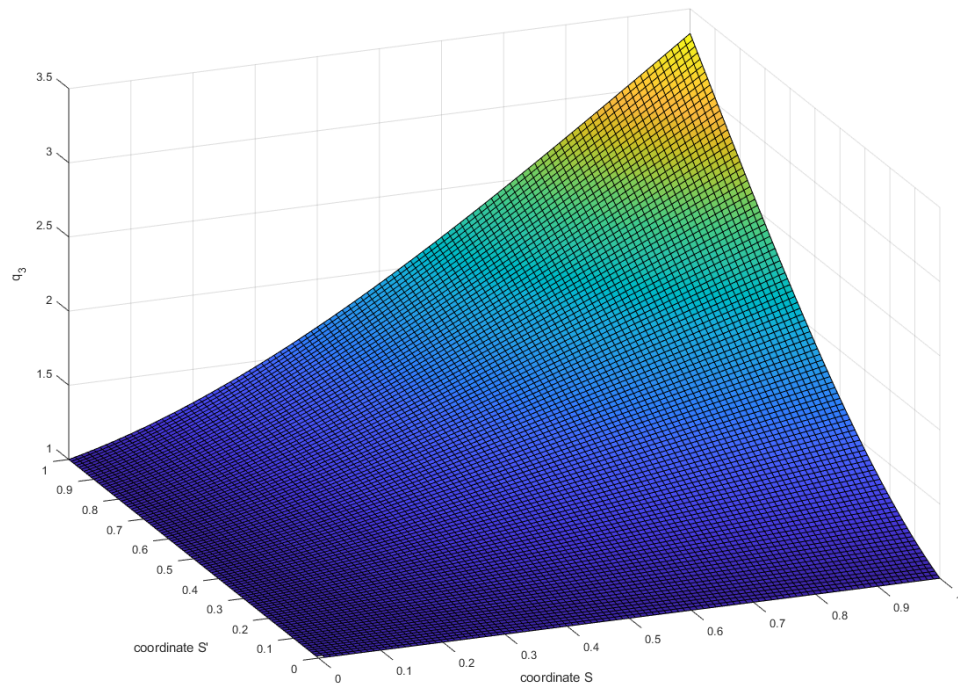


Figure 36: The reproducing kernel q_3 for the angle like coordinate S , where $S = (1 + \cos\alpha)/2$.

In equation (62), the three kernels for r , R and α are multiplied together to give the three-dimensional basis function. The coefficients C_i were computed by matrix inversion method. This computation of coefficients was done using the MATLAB¹⁹⁹ software package. The spline representation of the three-body term using this method is shown in Figure 37. The behavior is now rather smooth, and all the curves are positive representing the behavior of actual data even for linear configuration in contrast with Figure 33. Therefore, this method of RKHS spline interpolation worked well to represent the behavior of three-body term.

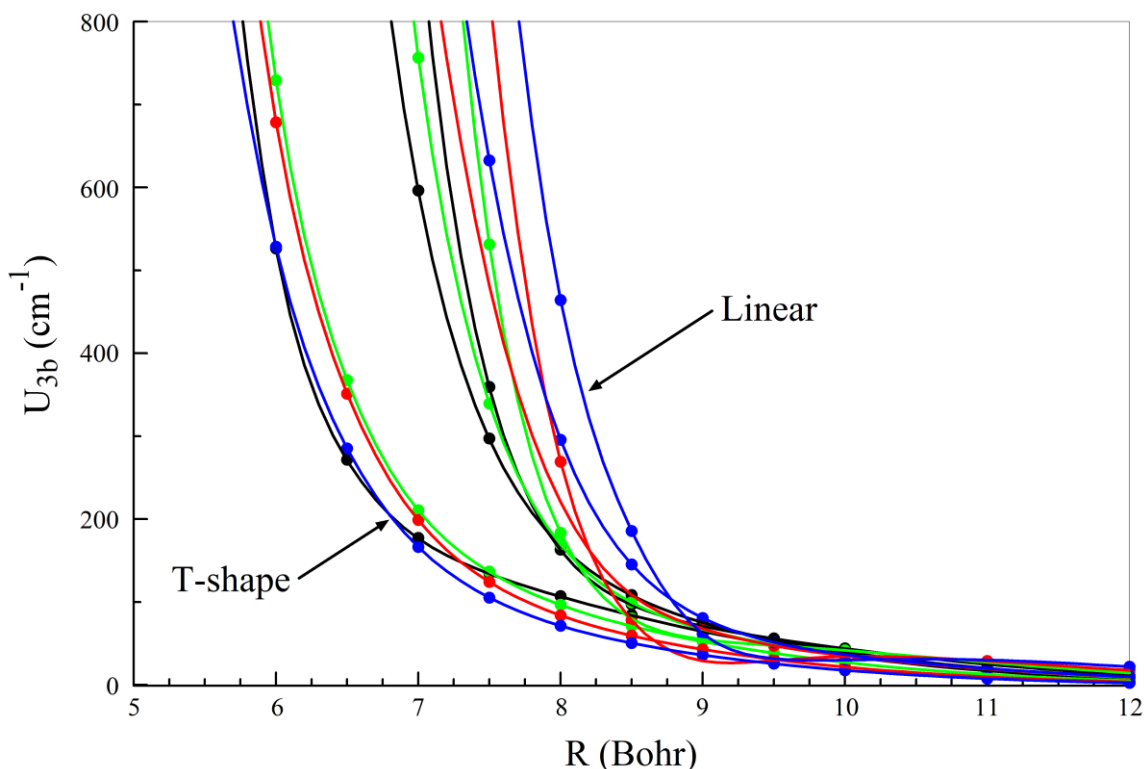


Figure 37: The fitted three-body term for the $S_2 + \text{Ar}$ system. Black, green, red, and blue lines correspond different S_2 distance, $r = 3.0, 4.0, 5.0$ and 6.0 Bohr respectively. Three different lines for each color corresponds to three different angles of approach, $\alpha = 0^\circ, 45^\circ$ and 90° . The behavior is same for all slices.

6.2.6. The Global 3D PES for the Reaction $S + S + Ar \rightarrow S_2 + Ar$

Finally, the three-dimensional potential energy surface is constructed as:

$$\begin{aligned}
 U(r, R, \alpha) = & U_{3b}^{\text{spline}}(r, R, \alpha) \\
 & + U_{S_2}^{\text{MRCI}}(r) \\
 & + U_{ArS}^{\text{Morse}}(R_1) + U_{ArS}^{\text{Morse}}(R_2).
 \end{aligned} \tag{67}$$

Note that, in this equation (67), besides the three-body term there are the pairwise interactions. For the S_2 potential, we are adding the MRCI/aV(5+D)/Z calculations which describes the dissociation. Although in the equation (57), we extracted the $S + S$ interaction computed using CCSD(T)-F12/VTZ-F12 in a limited range of r value, this equation (67) contains the global S_2 curve computed using MRCI/aug-cc-pV(5+d)/Z from Section 6.2.1 as shown in Figure 25 red line which is good in a broad range of r , $r \rightarrow \infty$, and thus describes the dissociation. So, the overall constructed surface is accurate up to dissociation limit.

Figure 38 shows the overall three-dimensional PES where one can see the dependence of the potential energy surface as the S_2 molecule is allowed to vibrate and eventually dissociate. One can see a similar picture as of Figure 29 which describe the interaction of Ar with the S_2 molecule and another coordinate shows the evolution of interaction as r is increased. On top of the figure, we can see a small interaction between one sulfur atom and Ar as both approaches closer to each other due to the extension of S_2 bond length. The potential behaves smooth in all parts of space (r, R, α) .

In the present version of PES, we included the points up to $r = 6.0$ Bohr because beyond that the coupled cluster calculations converged but we observed wrong behavior. However, in the range not covered by our grid, the three-body term is basically given by

extrapolation by equation (62). The extrapolation is not necessarily physical because we observed that the three-body term does not die quickly. So, we decided to apply a damping cosine function to avoid this unphysical behavior. So, we made a small additional correction to the PES.

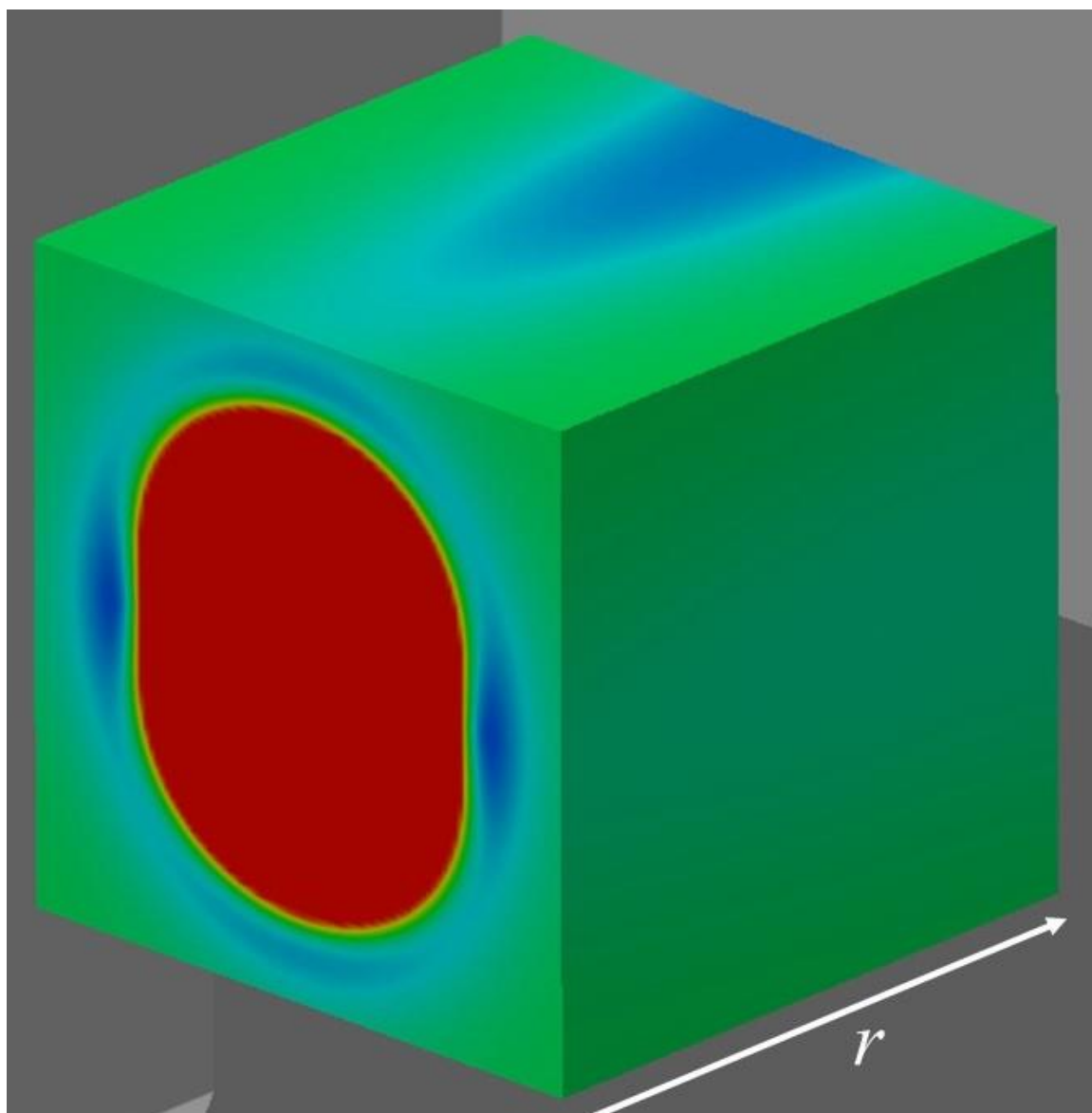


Figure 38: Potential energy surface of the $S_2 + Ar$ system with all degrees of freedom. The dependence of potential on S_2 bond distance can be seen on the top surface of the figure.

Our potential energy surface is better because we considered the three-body term in a broader range of space, particularly smaller distance of Ar–S distance R_1 and R_2 than the surface by Peterson and co-workers.³⁴ Also, his ab initio data points was restricted to the range of relatively large r distances, particularly he did not include the geometries for $r \lesssim 5.76$ Bohr. But the S_2 molecule is smaller than that. The equilibrium bond distance of S_2 was found to be 3.59 Bohr. We considered the r grid down to $r = 3.0$ Bohr. Hence, our surface is more general and better.

6.3. Study of the Rotational Energy Transfer

6.3.1. Inelastic Scattering Cross-Sections for Isotopically Substituted S_2

After the potential energy surface had been constructed, the method of mixed quantum/classical theory (MQCT) was applied to describe the process of energy transfer from the rotationally excited S_2 to the bath gas, argon. The collision energy is $E = 300.0$ cm^{-1} , which is typical at room temperature. Figure 39 reports collisional cross sections $\sigma(j, j')$ for transitions to various possible final values of j' starting from $j = 51$ in the most abundant (usual) isotopomer of S_2 , symmetric $^{32}\text{S}^{32}\text{S}$, which has only odd rotational states. Cross section for the elastic scattering channel ($j' = 51$) is larger by almost two orders of magnitude, as represented by the red point in the figure. The frame (a) represents the collisional cross section, σ , as a function of final rotational level, j' . Transitions to $j' < 51$ correspond to quenching, while transitions to $j' > 51$ correspond to excitation. These two wings of this dependences are clearly seen in Figure 39. As the magnitude of Δj :

$$\Delta j = j' - j, \quad (68)$$

increases, the value of cross section drops, and it drops faster for excitation. For example, for excitation, with Δj on the order of 20, the cross section decreases by a factor of 7. But for quenching, with $\Delta j \sim 20$, the value of the cross section drops by only a factor of 5.

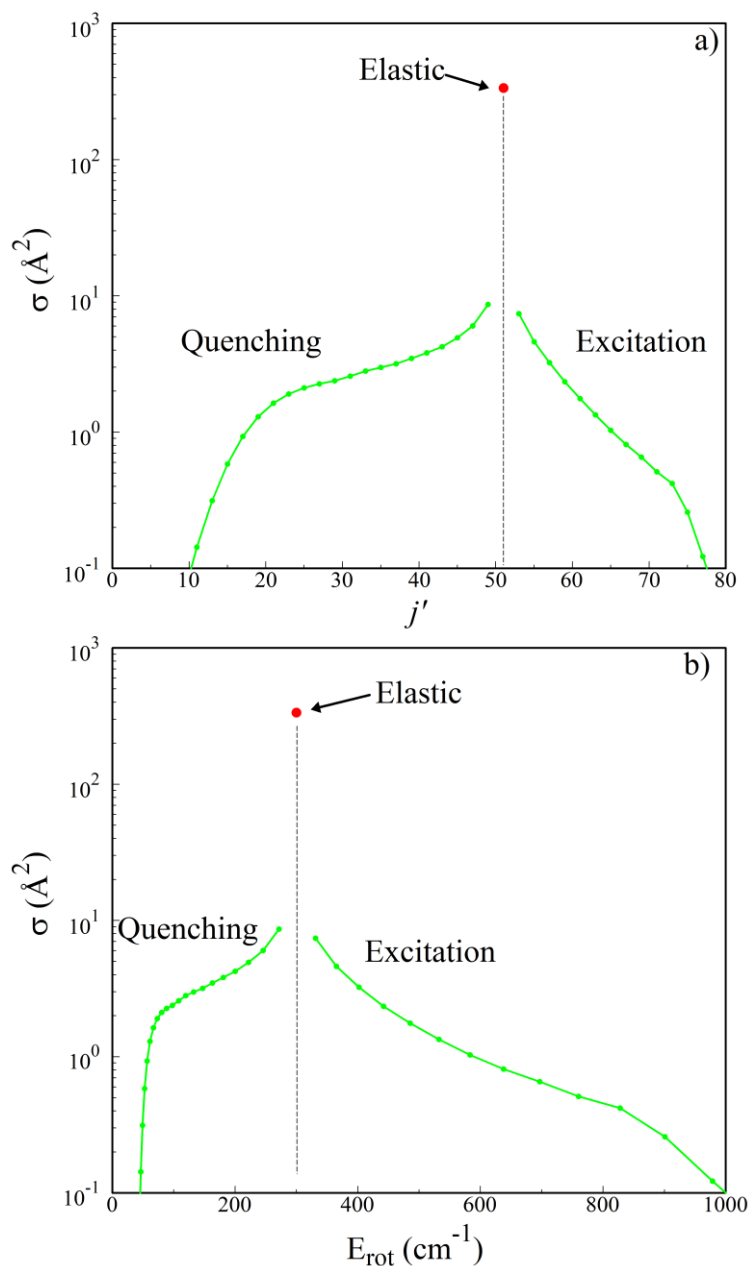


Figure 39: Energy transfer of rotationally excited S_2 molecule at initial rotational level $j = 51$ as a function of final rotational state (a) and final rotational energy (b).

A different version of this plot is shown in frame (b), where the horizontal line represents the final rotational energy, E_{rot} :

$$E_{\text{rot}} = \frac{j(j+1)}{2\mu r_e^2}. \quad (69)$$

The excitation wing drops sharper than quenching in this figure too, similar to the frame (a). As the magnitude of ΔE :

$$\Delta E = E_{\text{rot}}(j') - E_{\text{rot}}(j), \quad (70)$$

reaches 200 cm^{-1} , the value of cross section drops by a factor of 10 for excitation, while it drops by a factor of 4 for quenching.

Similar calculations were done using MQCT for several initial rotational states: $j = 21, 31, 41$ and 51 , and are presented all together in Figure 40. The black, blue, green, and red circles represent cross sections for initial rotational level $j = 51, 41, 31$, and 21 , respectively. One trend we see is that when the value of the initial j is increased, the

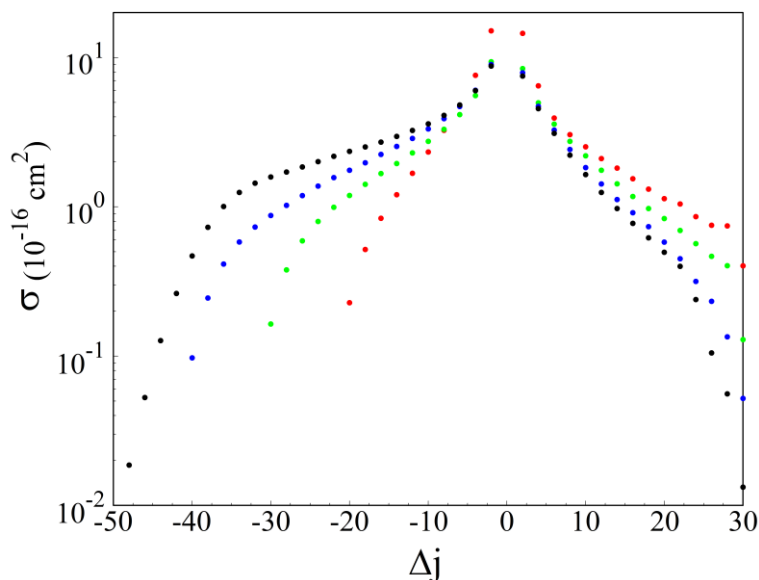


Figure 40: Energy transfer of rotationally excited S_2 molecule for initial rotational level $j = 51, 41, 31$, and 21 in black, blue, green, and red respectively as a function of Δj .

quenching cross section also increases, but the excitation cross section drops, and these variations are larger for the quenching process (the data are further apart) than for the excitation (the data are closer together). The second observation is that at the far end of the quenching wing the value of cross section drops faster, especially for lower values of the initial rotational excitation such as $j = 21$.

Calculations of the same sorts were done for S_2 molecule with several different isotopic compositions, namely for symmetric $^{34}S^{34}S$ and asymmetric $^{32}S^{34}S$. Cross sections were computed for both excitation and quenching for several values of the initial rotational excitation. The state-to-state transitions cross sections for isotopically substituted symmetric S_2 molecule, $^{34}S^{34}S$ (Figure 41), has similar behavior to $^{32}S^{32}S$ (Figure 40). However, for the asymmetric molecule, $^{32}S^{34}S$, where the rotational states with even j are allowed, the dependence of cross section exhibits a qualitatively different

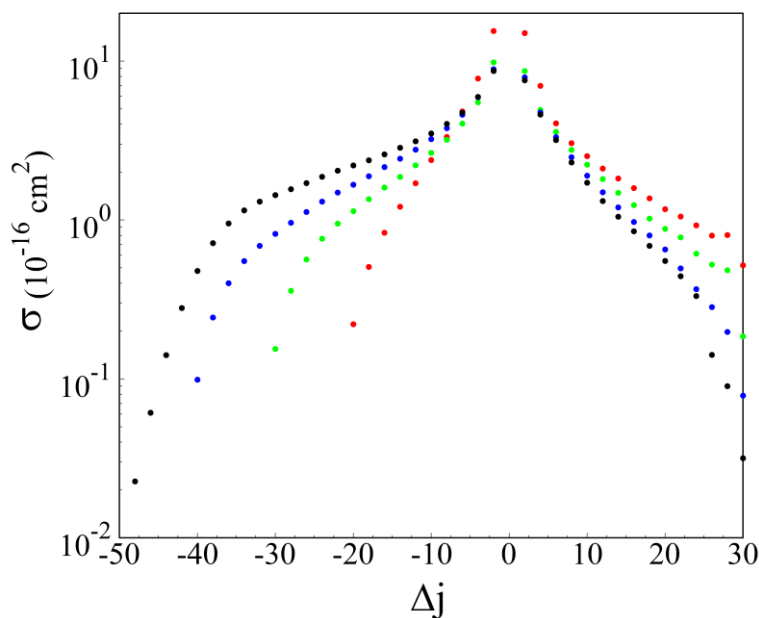


Figure 41: Same as Figure 40, but for isotopically substituted symmetric rotationally excited S_2 molecule $^{34}S^{34}S$.

behavior. Figure 42 reports the cross sections for the initial rotational level $j = 21$ in asymmetric $^{32}\text{S}^{34}\text{S}$ as an example. One could notice from the previous figures (Figure 40 and Figure 41) that only transitions for the even values of $\Delta j = \pm 2, 4, 6, \dots$ are allowed. This is the case for the homonuclear molecules ($^{32}\text{S}^{32}\text{S}$ and $^{34}\text{S}^{34}\text{S}$), and it is caused by the fact that the center of mass is exactly at the geometric center of the molecule. But, for the heteronuclear molecules, such as $^{32}\text{S}^{34}\text{S}$, the center of mass is shifted, the symmetry is broken, and thus $\Delta j = \pm 1, 3, 5, \dots$ show up. Although, the magnitudes of cross sections for transitions with odd Δj values are still much smaller than those with even Δj , they are not negligible. In particular, cross sections for transitions with odd Δj are larger than the difference of cross sections in two considered homonuclear molecules, $^{32}\text{S}^{32}\text{S}$ and $^{34}\text{S}^{34}\text{S}$,

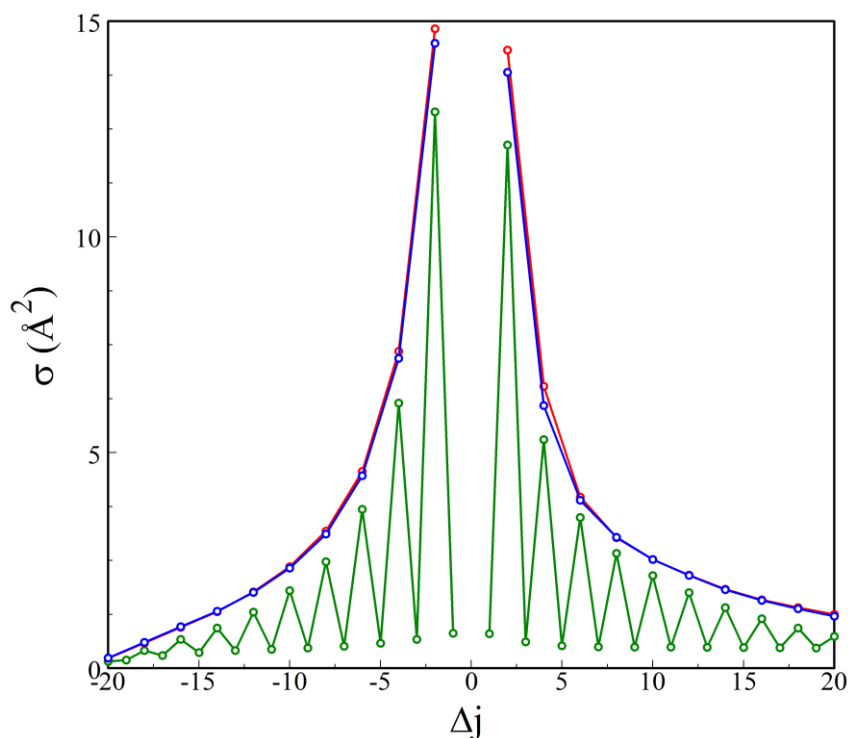


Figure 42: Energy transfer of rotationally excited asymmetric S_2 molecule ($^{32}\text{S}^{34}\text{S}$) for initial rotational level $j = 21$ as a function of shift of final rotational state is shown here by green, while blue and red represents symmetric S_2 molecule $^{32}\text{S}^{32}\text{S}$ and $^{34}\text{S}^{34}\text{S}$, respectively.

with even Δj . So, these smaller allowed cross sections must be computed and included into the kinetics of energy transfer.

6.3.2. Rotational Energy Transfer Model

The analytical energy transfer models are often exponential.⁴⁰ However, one can notice from Figure 40 and Figure 41 (plotted in the exponential scale) that the slope for the cross section dependence changes as we go from the elastic peak further towards the wings. Therefore, a double-exponential model is more appropriate, in which one of the exponents describe the behavior near the elastic peak, while the second exponent represents the results near the wing⁴⁰:

$$\sigma_{excite} = \sigma_0 \left(e^{-\frac{|\Delta j|}{\gamma}} + c e^{-\frac{|\Delta j|}{d}} \right). \quad (71)$$

Equation (71) can be applied to describe the excitation wing reasonably well in Figure 40 and Figure 41. But the quenching cross sections show a sharp drop for transitions with large Δj values. In order to describe that behavior using our analytic model, we incorporated the hyperbolic sine function as an argument into one of the exponents of the analytic expression:

$$\sigma_{quench} = \sigma_0 \left(e^{-\frac{|\Delta j|}{\gamma}} + c e^{-\frac{\sinh \{|\Delta j|/e\}}{d}} \right). \quad (72)$$

Furthermore, one can notice from Figure 40 and Figure 41, that the curves are different for different initial rotational states, which means that one needs separate sets of parameters for each data set. In order to capture this dependence of the fitting parameters on the initial rotational state, j , we introduced a Taylor-like expansion up to the 3rd order for σ_0 , γ , c , and d as given below:

$$\sigma_0 = a_0 + a_1j + a_2j^2 + a_3j^3. \quad (73)$$

$$\gamma = b_0 + b_1j + b_2j^2. \quad (74)$$

$$c = c_0 + c_1j + c_2j^2. \quad (75)$$

$$d = d_0 + d_1j + d_2j^2. \quad (76)$$

The values of these fitting parameters, determined by iterative procedure for quenching and excitation cross sections are listed in Table 14 and Table 15, respectively. Low values of RMSE, on the order of 0.1 \AA^2 and 0.03 \AA^2 for quenching and excitation wings

Table 14. Fitting parameters for the cross sections of quenching wing of S₂ molecules.

Parameters	³² S ³² S	³⁴ S ³⁴ S	³² S ³⁴ S (even Δj)	³² S ³⁴ S (odd Δj)
RMSE	9.89E-02	1.01E-01	4.57E-02	4.68E-02
<i>a</i>₀	1.83E+02	1.79E+02	1.46E+02	2.72E+01
<i>b</i>₀	-1.39E+00	1.26E-01	1.63E+00	1.82E-01
<i>c</i>₀	2.23E-01	2.11E-01	1.98E-01	4.60E-02
<i>d</i>₀	-3.83E-01	1.05E-01	-1.92E-01	3.42E+03
<i>a</i>₁	-1.26E+01	-1.18E+01	-9.46E+00	-6.16E-01
<i>b</i>₁	1.73E-01	6.52E-02	-2.22E-02	5.16E-03
<i>c</i>₁	3.24E-03	3.80E-03	6.56E-03	-5.16E-04
<i>d</i>₁	1.26E-02	-1.01E-02	2.58E-02	-2.92E+02
<i>a</i>₂	3.03E-01	2.80E-01	2.24E-01	-9.50E-03
<i>b</i>₂	-1.67E-03	-1.21E-04	6.22E-04	-1.36E-04
<i>c</i>₂	0.00E+00	0.00E+00	0.00E+00	0.00E+00
<i>d</i>₂	1.56E-03	1.33E-03	-1.24E-04	6.19E+00
<i>a</i>₃	-2.41E-03	-2.21E-03	-1.79E-03	5.93E-04
<i>e</i>	1.41E+01	1.60E+01	2.15E+01	4.48E+00

respectively, attest for sufficient flexibility of the fitting function and good quality of the fit.

The fitted function is shown in Figure 43 by the orange line, while black, blue, green, and red circles represent the cross sections for initial rotational level $j = 51, 41, 31, \text{ and } 21$ respectively. The agreement between cross sections computed using MQCT method and the analytical fit is good enough for the purpose of describing the energy transfer model.

Table 15. Fitting parameters for the cross sections of excitation wing of S_2 molecules.

Parameters	$^{32}\text{S}^{32}\text{S}$	$^{34}\text{S}^{34}\text{S}$	$^{32}\text{S}^{34}\text{S}$ (even Δj)	$^{32}\text{S}^{34}\text{S}$ (odd Δj)
RMSE	2.90E-02	3.64E-02	2.91E-02	6.49E-02
a_0	2.60E+02	2.12E+02	2.23E+02	5.13E+03
b_0	1.75E+00	2.47E+00	3.09E+00	4.06E+01
c_0	-1.14E+00	-7.63E-01	-9.07E-01	-1.00E+00
d_0	2.59E+01	2.75E+01	1.85E+01	4.06E+01
a_1	-1.81E+01	-1.44E+01	-1.52E+01	-6.71E+01
b_1	-2.78E-02	-5.79E-02	-1.11E-01	-5.29E-01
c_1	7.99E-02	5.38E-02	6.29E-02	-2.21E-06
d_1	-7.76E-01	-7.92E-01	-5.30E-01	-5.28E-01
a_2	4.35E-01	3.43E-01	3.64E-01	-1.96E+00
b_2	7.25E-04	9.96E-04	1.62E-03	-2.50E-03
c_2	-9.08E-04	-5.32E-04	-6.04E-04	-1.85E-09
d_2	8.56E-03	8.31E-03	5.52E-03	-2.51E-03
a_3	-3.45E-03	-2.71E-03	-2.91E-03	1.15E-01

After successfully representing the cross sections by the analytic model, we step forward to apply this method to other isotopically substituted S_2 molecules. The same approach with the analytical function of equations (71)-(76) was used to fit both excitation and quenching for $^{34}S^{34}S$. The cross sections of even and odd Δj transitions for the asymmetric S_2 molecule ($^{32}S^{34}S$) were fitted separately since the magnitude of even Δj transition cross sections are larger compared to odd Δj . All these fitting parameters are provided in Table 14 and Table 15 for $^{32}S^{32}S$, $^{34}S^{34}S$, and $^{32}S^{34}S$. The analytical energy transfer model is plotted in Figure 43, Figure 44, and Figure 45 for $^{32}S^{32}S$, $^{34}S^{34}S$, and $^{32}S^{34}S$. The color scheme in all these pictures is the same as before. It can be concluded that the analytical model worked well to describe the energy transfer process in all isotopically substituted S_2 molecules.

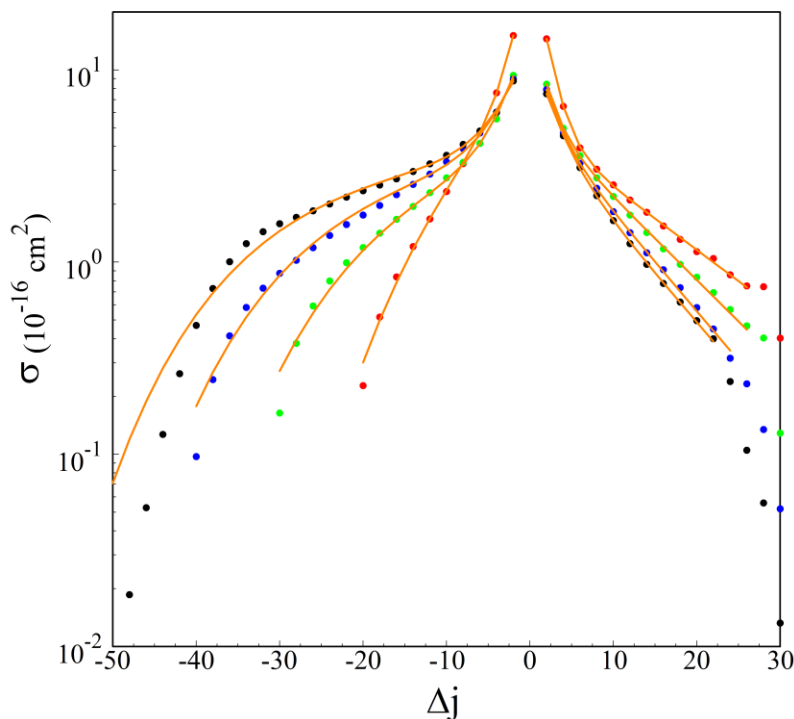


Figure 43: Analytic representation of the energy transfer of rotationally excited S_2 molecule ($^{32}S^{32}S$) for initial rotational level $j = 51, 41, 31$, and 21 in black, blue, green, and red respectively as a function of Δj . The orange line represents the analytic fit.

6.3.3. Kinetics of Energy Transfer and Symmetry-Driven Isotope Effect

From the review of the literature, it is found that the principle of microscopic reversibility is not automatically satisfied for the calculations of cross sections within the

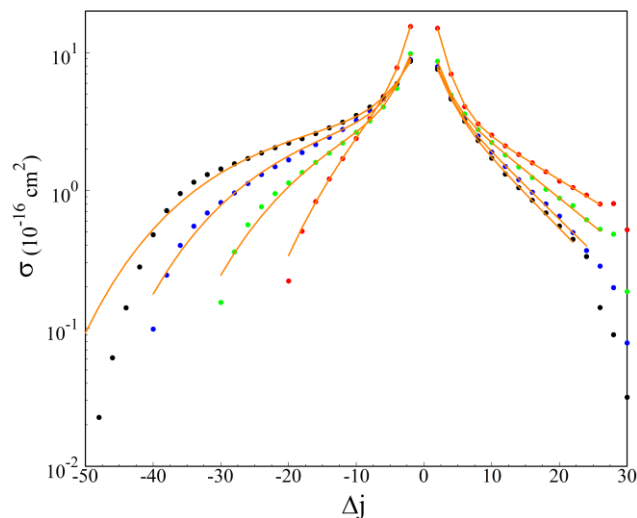


Figure 44: Analytic representation of the energy transfer of rotationally excited symmetric S_2 molecule ($^{34}S^{34}S$) as Figure 43.

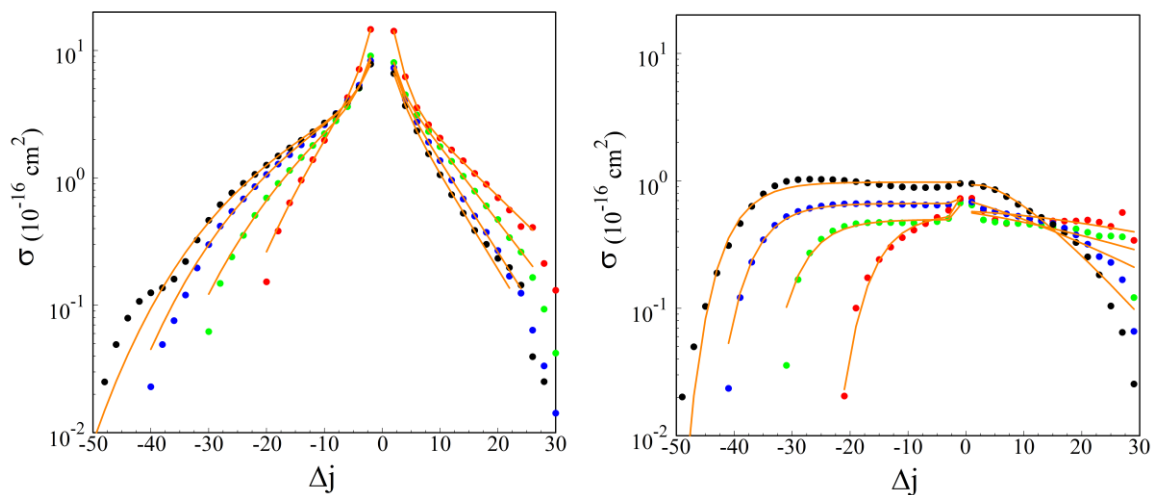


Figure 45: Analytic representation of the energy transfer of rotationally excited asymmetric S_2 molecule $^{32}S^{34}S$. The left frame and right frame represent data for even and odd Δj values respectively.

mixed quantum/classical approach.^{77,78,200} Literature survey from the previous research on CO + He⁷⁷, CO + CO²⁰⁰, N₂ + Na⁷⁸ concluded that MQCT could represent the state-to-state transition cross sections for excitation processes better compared to quenching. Therefore, we used the excitation cross sections computed for the S₂ + Ar collision and analytically fit using the double exponential model as described by equations (71)- (76) earlier. The energy transfer model for the state-to-state excitation transitions is built from ground rotational state $j = 1$ to $j = 81$ for symmetric molecule and $j = 0$ to $j = 81$ for the asymmetric molecule. Then the rate coefficients are computed using these excitation cross sections as:

$$k_{excite} = \sqrt{\frac{8k_B T}{\mu\pi}} \sigma_{excite}. \quad (77)$$

Here, k_B is the Boltzmann's constant, T is temperature corresponding to room temperature, 300 K, and μ is the reduced mass of the system S₂ + Ar.

Using the principle of microscopic reversibility, we computed the rate constants for the quenching process using the excitation rate constants as:

$$k_{stab} = k_{excite} * \frac{(2j+1)e^{-\frac{E_j}{k_B T}}}{(2j'+1)e^{-\frac{E_{j'}}{k_B T}}}. \quad (78)$$

Here, j and j' are initial and final rotational states, respectively. E_j and $E_{j'}$ are internal energy of the initial and final rotational state. The rate constant has the unit of $cm^3 s^{-1}$. A matrix of rate constants for 81 and 41 state-to-state transitions was built for asymmetric and symmetric S₂ molecules, to be used as an input for the study of kinetics for S₂ + Ar energy transfer.

After that, we needed the master equations to simulate the energy transfer process for the collisional event. We followed the steps suggested by Pack *et al.*^{39,201–203} for our system as described next. The concentrations of molecules in each quantum state $[i]$ are introduced and are assumed to be affected (decreased/increased) by state-to-state transitions (to/from) all other states $[f]$. The rate is assumed to follow the second order kinetics with a set of corresponding state-to-state rate coefficients:

$$R = \frac{d[i]}{dt} = - \sum_f k_{i \rightarrow f} [i][\text{Ar}] + \sum_f k_{f \rightarrow i} [f][\text{Ar}]. \quad (79)$$

Equation (79) can be transformed into a more useful expression where the unitless population of each state n_i is monitored as a function of time:

$$\frac{dn_i}{dt} = - \sum_f k_{i \rightarrow f} [\text{Ar}] n_i + \sum_f k_{f \rightarrow i} [\text{Ar}] n_f. \quad (80)$$

The population for each state is defined as $n_i = [i] / \sum [i]$, where summation runs through all states of the system.

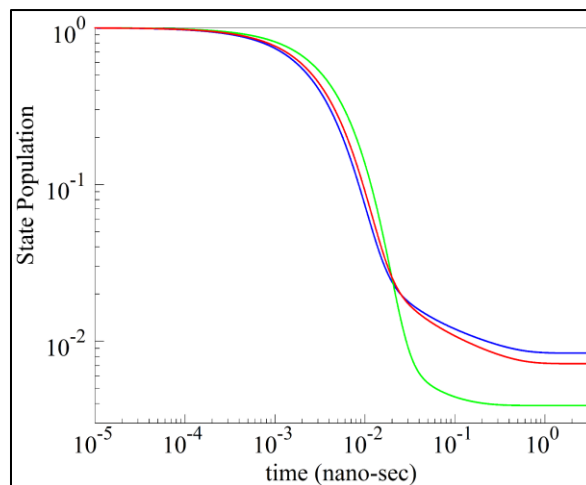


Figure 46: Decay of initially populated rotational state $j = 51$. Red, green, and blue line represents $^{32}\text{S}^{32}\text{S}$, $^{32}\text{S}^{34}\text{S}$, and $^{34}\text{S}^{34}\text{S}$ molecule.

We propagated equation (80) using the 4th order Runge-Kutta method (from Numerical Recipes) to solve the ordinary differential equation.¹⁹⁶ Initially, we populated a typical rotational state, such as $j = 51$, and started monitoring for 100 μsec . We found that during the early stage of simulation (up to about .01 μsec) the decay of the initial state is slower in the asymmetric $^{32}\text{S}^{34}\text{S}$ compared to symmetric $^{32}\text{S}^{32}\text{S}$ and $^{34}\text{S}^{34}\text{S}$ (Figure 46). This is because the asymmetric molecule has somewhat lower values of rate constants for even Δj transitions, compared to symmetric S_2 . However, after .01 μsec , the asymmetric molecules take over, due to the presence of odd Δj transitions, and relax to the equilibrium significantly faster compared to the symmetric S_2 molecules.

Overall, the time scale of energy equilibration is almost 2 times faster for the asymmetric molecule compared to the symmetric molecules. This is also reflected in Figure 47, where the evolution of the deviation of the average energy of the system from the Boltzmann energy is represented. One can notice that the energy relaxation process

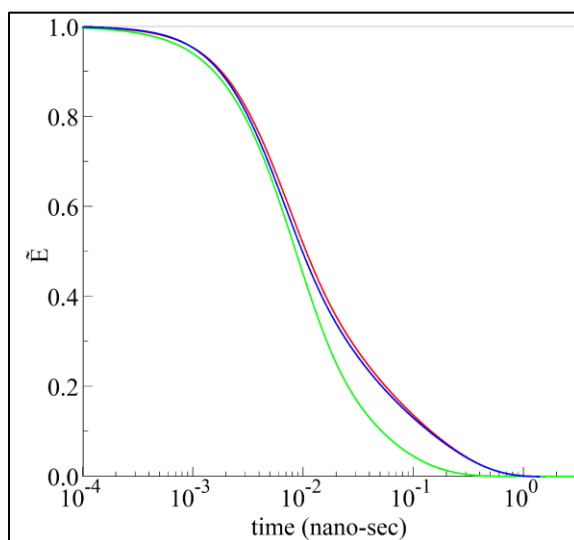


Figure 47: Comparison of energy relaxation for several isotopic composition of S_2 molecule. Red, green, and blue line represents $^{32}\text{S}^{32}\text{S}$, $^{32}\text{S}^{34}\text{S}$, and $^{34}\text{S}^{34}\text{S}$ molecule.

for the asymmetric molecule is way faster compared to the symmetric molecules. The reason for the quicker stabilization for the asymmetric S_2 molecule is the presence of the odd Δj valued transitions. Although, the magnitude of these transitions is significantly smaller compared to even Δj , but the presence of these transitions in between even Δj works as intermediate steps and thus, reaching the equilibrium becomes easier. In conclusion, stabilization of metastable S_2^* is faster for asymmetric molecule and the presence of odd Δj states facilitate the energy transfer process by making the energy gap less.

6.4. Summary

In this chapter, our focus was to apply MQCT methodology to study the energy transfer process during $S_2 + \text{Ar}$ collision, a system with relevance to atmospheric chemistry. For this purpose, the potential energy surface for the $S_2 + \text{Ar}$ system was built, valid up to the dissociation limit. This surface is better than the one available from the literature because it considers a broader range of geometries of the molecule, particularly in the range of smaller S-Ar distances. We also used an explicitly correlated method CCSDT-F12/VTZ-F12 for the computation of the three-body terms, and MRCI/aug-cc-pV(5+d)Z was used for S_2 . The smooth representation of the three-body term $U_{3b}(r, R, \alpha)$ was obtained using RKHS spline interpolation by Ho and Rabitz. The global PES was constructed by adding up the pair-wise potential with the three-body term.

The PES was then used to carry out the computational study of S_2 colliding with bath gas Ar using MQCT methodology. Rotational excitation and quenching cross sections were computed for the energy exchange between the rotationally excited S_2

molecule to argon. Several isotopically substituted S_2 molecule was studied to understand the symmetry driven isotope effect. An analytic model for the description of the energy transfer process was built using a double exponential function. Using this model and the principle of microscopic reversibility, a matrix of 41 and 82 state-to-state transitions was built to serve as the input for the kinetics study. Then simulation of the energy transfer process was conducted to find the role of symmetry in the process of energy transfer. It is found that the symmetry-driven isotope effect in the stabilization of metastable S_2^* molecule is significantly larger than mass induced isotope effect. The S_2 molecule with one sulfur substituted by a rare isotope, namely asymmetric $^{32}S^{34}S$, reaches thermal equilibrium faster than symmetric molecules $^{32}S^{32}S$ and $^{34}S^{34}S$. It happens because of the presence of transitions with odd Δj values, which facilitates the energy transfer process in the asymmetric molecule by reducing the energy gap between the even Δj values of rotational states on the contrary to the symmetric S_2 molecules, namely $^{32}S^{32}S$ and $^{34}S^{34}S$, where only even Δj values of states are present. It helps the $^{32}S^{34}S$ molecule to reach equilibrium almost twice faster than $^{32}S^{32}S$ or $^{34}S^{34}S$.

The rotational energy transfer for the ground vibrational state considering highly excited rotational states was performed in the current study. In the future, one can perform calculations including the vibrational states of the S_2 molecule to study the stabilization step of the recombination reaction $S + S \xrightarrow{+Ar} S_2$ up to dissociation threshold, with a focus on the isotopic effect.

CHAPTER 7. SUMMARY AND FUTURE WORK

The study of surface sediments from the Archean eon of Earth identifies a significant amount of sulfur. This sulfur exhibits mass-independent isotope fractionation (S-MIF) specific to the gas phase recombination reactions in the anoxic atmosphere of early Earth. It is assumed that sulfur would participate in a chain of recombination reactions in the anoxic atmosphere to form several sulfur allotropes, such as S_2 , S_3 , S_4 , S_6 , and S_8 . But it is impossible to study these recombination reactions experimentally in sufficient detail. In terms of theoretical approach, we are also limited to the exploratory models that address some aspects of the overall problem. In this work, we studied the energy transfer for the collision of S_2 with bath gas argon for several isotopic compositions to study the mass-independent isotope effect.

Mixed quantum/classical theory (MQCT) was developed, as a methodology and a code, to serve as a practical tool for calculations of energy transfer processes during an inelastic scattering applicable to astrophysics and atmospheric chemistry. A diagram is presented in Figure 48 to compare performance of several methodologies within the MQCT framework vs. full quantum code, MOLSCAT. One can notice that a calculation with a basis set of about 150 channels took more than two months using MOLSCAT, while the full-coupled version of MQCT (named CC-MQCT) took only a few hours. Moreover, we also demonstrated that a simplified version of MQCT (named AT-MQCT) is even more affordable by finishing this calculation within few minutes. Calculation of a more complicated system, like the collision of methyl formate CH_3COOH with He at

temperatures around $T \approx 20$ K with about 400 quantum channels included, would take years to finish using MOLSCAT (i.e., computationally unaffordable), while AT-MQCT makes it possible within few hours. It is clear that MQCT proves to be a very useful tool for computational chemists.

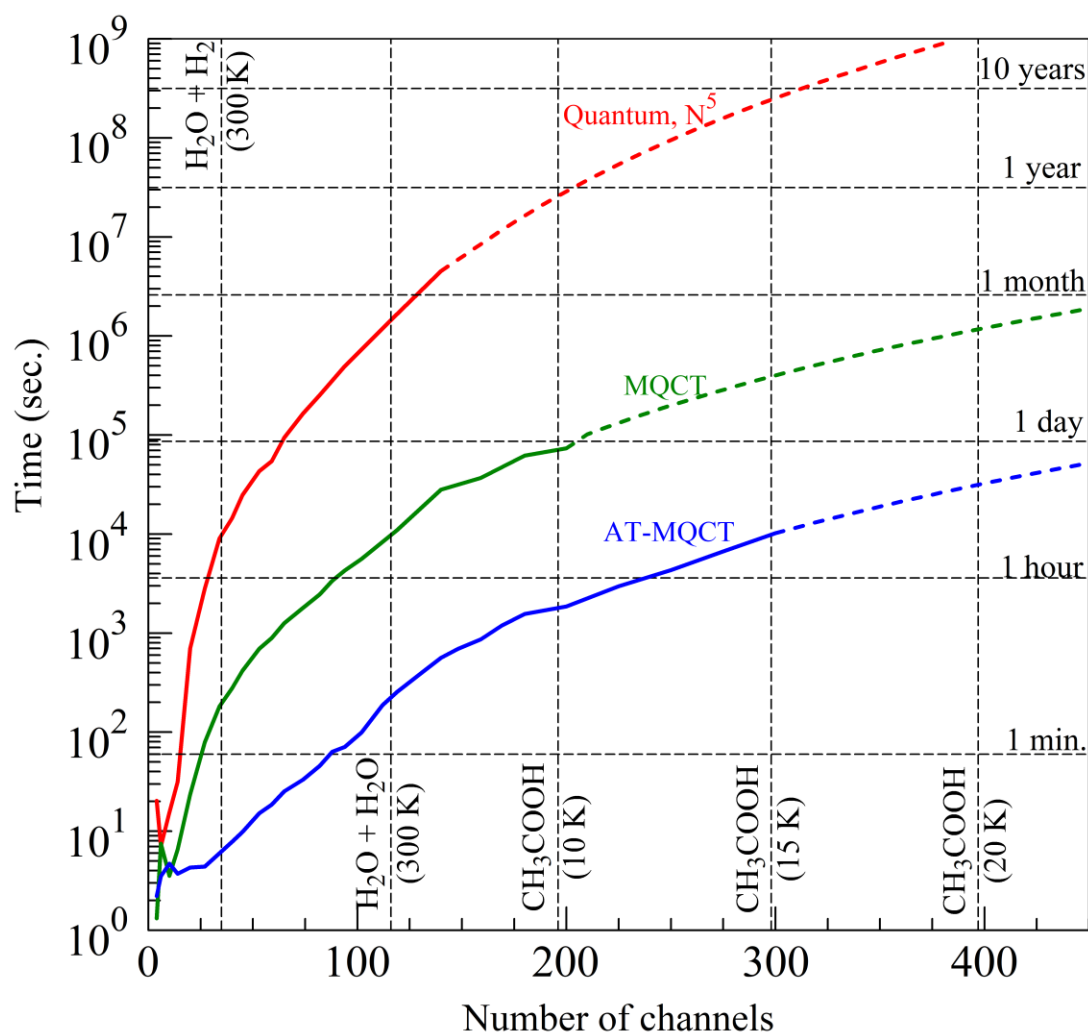


Figure 48: Comparison of complexity of calculations as performed by different codes and methods. The full-quantum code, MOLSCAT, can perform calculations for collision of two water molecules in several months. The CC-MQCT method outperforms MOLSCAT easily and extend the opportunity for users. Finally, the AT-MQCT, as the most efficient methodology, can perform efficiently quite heavy calculations in reasonable amount of time.

The MQCT code we developed is capable to study various complicated systems, such as two asymmetric top rotors, which was not possible before because no other code in the community can perform the calculation of this type of molecular collision. The diatomic vibrational system is also included in this version of the code. It is easy to set up calculations using MQCT as the input is simple since it has almost all the default values for the keywords. There are many options available within the code for expert calculations. The code takes parallel computing advantage using message passing interface (MPI), which enables massive speed-up. The code is publicly available for other scientists to use in the following link:

<https://github.com/MixedQuantumClassicalTheory/MQCT>.

MQCT is becoming noticed by the scientific community rather quickly, and several researchers have started using it. Last year, we published a collaborative study for the collision of two water molecules with Prof. Marie-Lise Dubernet from Paris Observatory, France. Recently, we received invitations to collaborate with Prof. Cecilia Coletti from D'Annunzio University, Chieti-Pescara, Italy to study the reactive scattering of N_2 colliding with oxygen, and with Prof. Ad van der Avoird, Radboud University Nijmegen, The Netherlands to study the collision of $ND_3 + D_2$ (deuteride NH_3 and H_2) and $ND_3 + NO$. Fellow students from the Center for Astrophysics of Harvard & Smithsonian at Massachusetts, ICTP-EAIFR at Rwanda, and Institute of Mechanics of Chinese Academy of Sciences at China have contacted us for a consultation to perform their research using MQCT. The code has been published for about a year now and has already been downloaded 27 times. We plan to release the second version in 2021

including important updates like AT-MQCT, parallel input-output (I/O), new manual, and more examples of the collision of different system types.

Another important aspect of MQCT is the study of differential cross sections. It was achieved within our methodology by sampling the integer values of the orbital angular momentum l , by analogy to the full-quantum calculations. It resulted in excellent agreement with full quantum results for the collision of $\text{Na} + \text{N}_2$, a system of astrochemical interest. An improved sampling procedure of the initial condition was also embedded. This new approach of MQCT requires fewer trajectories with respect to the previous method of the Monte-Carlo random sampling procedure. The only convergence parameter is now l_{max} in MQCT, which is very similar to the full quantum framework where J_{max} is the convergence parameter.

The significant role of the phase information was also demonstrated. It has been shown that the phase can be used to trace the interference behavior between different orbital angular momentum. The phase information can also be applied to compute the differential cross section and the elastic integral cross section. In this work, the differential inelastic cross section was reported for the first time within the MQCT framework. This was done for the initial rotational level $j = 0$. Another important aspect is the quantum phenomena of resonance. The low collisional energy regime was explored in detail to reproduce within the MQCT framework the highly oscillatory behavior of the cross-section dependence. The reason behind this behavior is the energy exchange between the colliding partners, which led to trapping and orbiting of the quencher.

The methodology is further advanced by decoupling the classical-like equations of motion for the translational degrees of freedom (scattering) from the quantum-like

equations for time-evolution of the internal molecular states (rotational, vibrational). Application of this method (AT-MQCT) to $\text{H}_2\text{O} + \text{H}_2$ rotationally inelastic scattering shows a significant computational speed-up, by two orders of magnitude. The results of this approximate propagation scheme are still accurate, as demonstrated by benchmarking against more rigorous calculations in which the quantum and classical equations of motion are held coupled, and against the full-quantum coupled-channel calculations from literature. It is concluded that AT-MQCT method represents a promising tool for the computational treatment of molecular collisions and energy exchange. It is important to stress out here that AT-MQCT has been applied to compute the thermally averaged cross section for $\text{H}_2\text{O} + \text{H}_2\text{O}$ collisions. An excellent agreement is observed with the CC-MQCT results, as shown in Figure 49 while achieving speed up of more than a factor of 150.

As for the application of MQCT to systems relevant to atmospheric chemistry, we carried out calculations for the simplest sulfur allotrope, S_2 , with several isotopic compositions using an improved potential energy surface (PES) that was built to describe the collision of the $S_2 + Ar$ system. The electronic structure calculation for the three-atom system, $S_2 + Ar$, employed the explicitly correlated method CCSD(T)-F12/VTZ-F12. This method is faster computationally and gives better convergence towards the complete basis set limit. For the description of S_2 dissociation, MRCI/aug-cc-pV(5+d)Z method was used. The three-body interaction term is considered in a broader range of S_2 bond

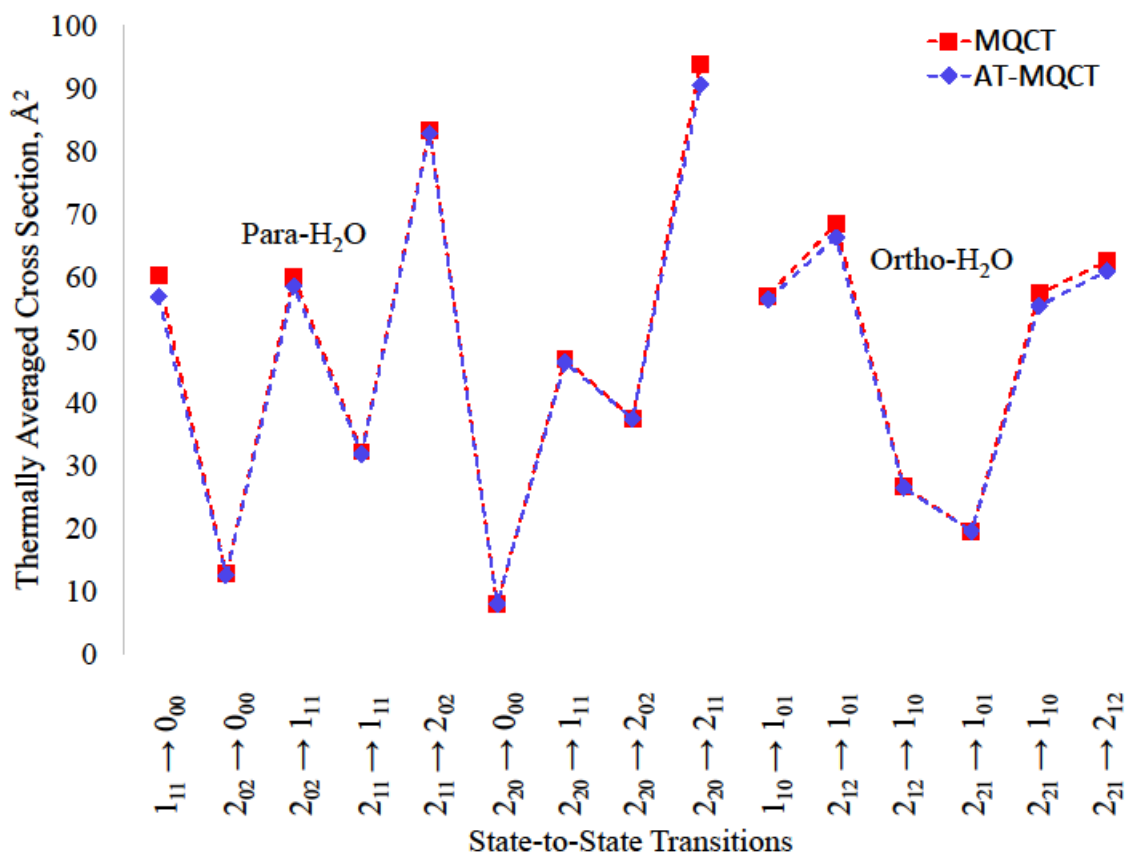


Figure 49: Comparison of thermally averaged cross-sections obtained by the AT-MQCT (blue) vs. the CC-MQCT method (red) for para-H₂O (left) and ortho-H₂O (right).

distance (r), particularly r goes to 3.0 Bohr and the distance of Ar from S_2 (R) down to 4.5 Bohr.

The PES was then used to study the collision dynamics using MQCT methodology. The energy transfer process was studied between the rotationally excited S_2 molecule ($j > 0, v = 0$) and the Ar atom as bath gas. Both quenching and excitation processes were considered. The effect of isotopic substitution was also studied during the energy transfer process. One or both of the ^{32}S atoms in the S_2 molecule is replaced by ^{34}S . It is confirmed that for the homonuclear S_2 molecule ($^{32}\text{S}^{32}\text{S}$ or $^{34}\text{S}^{34}\text{S}$), the transition with odd Δj values is forbidden due to symmetry. But for the heteronuclear S_2 molecule ($^{32}\text{S}^{34}\text{S}$), the transitions with odd Δj show up. The values for these transitions are not as large as the transitions of even Δj , but they are significant and play an important role. A model was built to describe the rotational energy transfer analytically for three different isotopically substituted S_2 molecules, two symmetric molecules ($^{32}\text{S}^{32}\text{S}$ & $^{34}\text{S}^{34}\text{S}$) and one asymmetric molecule ($^{32}\text{S}^{34}\text{S}$). The asymmetric S_2 molecule facilitates the stabilization steps almost by a factor of 2 faster compared to symmetric isotopic variants due to the presence of odd Δj states, which shows the mass-independent isotope effect in S_2 recombination.

In this work, we studied the rotational energy transfer in a broad range of initial rotational excitations, including highly excited species near the dissociation threshold (up to $j = 81$) but without the vibrational excitation. In the future, one can expand this research by including vibrationally excited states in addition to the rotational excitation simultaneously and go above the dissociation threshold to the scattering resonances. The rate constant for the stabilization step of the recombination reaction $S + S \leftrightarrow S_2^* + \text{Ar} \rightarrow$

S_2 can be computed to study S-MIF with vibrational levels included. In further perspective one can potentially look at larger sulfur allotropes, such as S_3 and S_4 . An accurate description of the potential energy surface is needed for these systems of molecules to study the energy transfer processes.

In terms of the development of the current MQCT program, it can be done in two major directions. First avenue is to make the code more efficient numerically. During the development phase, I made the program about 7 times faster by incorporating efficient memory access and matrix operations. To make it numerically even more efficient, the following implementations can be done.

Although the calculations for individual state-to-state transitions for a complex system, such as $H_2O + H_2O$, are possible within fully-coupled MQCT methodology, they are too costly when many rotational states are needed, to compute thermally averaged cross sections, and to produce the data suitable for the modelling of kinetics.⁹⁷ The AT-MQCT method needs to be made more general and applicable to other systems, namely $H_2O + H_2O$ and other complicated molecules. It needs to be rigorously tested for different system types and incorporated within the code for users.

MQCT has a significant bottleneck when it comes to writing and reading files for large, complicated systems, namely the state-to-state transition matrix. The matrix file is reusable for the same system to perform calculations for different initial states, several collision energies, and even smaller basis set sizes. The current version of the code reads and writes the matrix file sequentially, which takes a significant amount of time. To solve this problem, one can implement parallel input-output procedures. Moreover, one can exploit the fact that the transitions with the same value of helicity quantum number are

different only by a sign (phase) to reduce the size of state-to-state transition matrix, roughly by a factor of two, and boost the performance significantly.

The current version uses RK4 to solve the differential equations of motion, which is a 4th order method. Within an approximated theory, such as the adiabatic trajectory method, it is more convenient to use some simple propagator to reduce the total number of calls to the integrator within each time-step. To solve this issue, the code requires the addition of another propagator, such as preconditioned Lanczos method, for the propagation of the Ehrenfest trajectories of motion and solution of the time-dependent quantum equation of motion.

The second direction for the development of MQCT code is to expand the theory to more system types. As of now, the vibrational motion is limited to diatomic molecules only. It is important to include another mode, bending, for triatomic molecules, crucial for linear triatomic systems, such as CO₂, or other molecules of astrophysical importance, such as H₂O. One can incorporate another level of parallelization within the code using MPI to propagate trajectories and calculations of many collisional energies in parallel.

The present version of the code was focused on the collision of the water molecule with several background gases typical to the interstellar medium. Therefore, the input files were prepared for H₂O + He (asymmetric top rotor + atom), H₂O + H₂ (asymmetric top rotor + diatom), and H₂O + H₂O (asymmetric top rotor + asymmetric top rotor). We were contacted by potential users and asked to provide more example files, such as vibrating diatom + atom, vibrating diatom + vibrating diatom, symmetric top rotor + diatom, symmetric top rotor + symmetric top rotor.

One of our future goals is to produce collisional data that would be useful for astronomers to model kinetics. So far, our work was mostly focused on methodology development and serve the scientific community by providing MQCT as an efficient computational tool. Now we are ready to make a database consisting of collisional rates of sulfur recombination to model the atmosphere of planets and water calculations to be used for cometary applications.

BIBLIOGRAPHY

- (1) Semenov, A.; Mandal, B.; Babikov, D. MQCT: User-Ready Program for Calculations of Inelastic Scattering of Two Molecules. *Comput. Phys. Commun.* **2020**, 107155.
- (2) Ivanov, M. V.; Babikov, D. Mixed Quantum-Classical Theory for the Collisional Energy Transfer and the Rovibrational Energy Flow: Application to Ozone Stabilization. *J. Chem. Phys.* **2011**, 134, 144107.
- (3) Ivanov, M. V.; Babikov, D. On Molecular Origin of Mass-Independent Fractionation of Oxygen Isotopes in the Ozone Forming Recombination Reaction. *Proc. Natl. Acad. Sci.* **2013**, 110, 17708–17713.
- (4) Ivanov, M. V.; Schinke, R. Recombination of Ozone via the Chaperon Mechanism. *J. Chem. Phys.* **2006**, 124, 104303.
- (5) Ivanov, M. V.; Schinke, R. Temperature Dependent Energy Transfer in Ar -- O₃ Collisions. *J. Chem. Phys.* **2005**, 122, 234318.
- (6) Ivanov, M. V.; Babikov, D. Efficient Quantum-Classical Method for Computing Thermal Rate Constant of Recombination: Application to Ozone Formation. *J. Chem. Phys.* **2012**, 136, 184304.
- (7) Johnston, D. T. Multiple Sulfur Isotopes and the Evolution of Earth's Surface Sulfur Cycle. *Earth-Science Reviews*. May 2011, pp 161–183.
- (8) Roueff, E.; Lique, F. Molecular Excitation in the Interstellar Medium: Recent Advances in Collisional, Radiative, and Chemical Processes. *Chem. Rev.* **2013**, 113, 8906–8938.

- (9) Yang, B.; Nagao, M.; Satomi, W.; Kimura, M.; Stancil, P. C. Rotational Quenching of Rotationally Excited H₂O in Collisions with He. *Astrophys. J.* **2013**, 765, 77.
- (10) Schewe, H. C.; Ma, Q.; Vanhaecke, N.; Wang, X.; Klos, J.; Alexander, M. H.; van de Meerakker, S. Y. T.; Meijer, G.; van der Avoird, A.; Dagdigian, P. J. Rotationally Inelastic Scattering of OH by Molecular Hydrogen: Theory and Experiment. *J. Chem. Phys.* **2015**, 142, 204310.
- (11) Kirste, M.; Wang, X.; Schewe, H. C.; Meijer, G.; Liu, K.; van der Avoird, A.; Janssen, L. M. C.; Gubbels, K. B.; Groenenboom, G. C.; van de Meerakker, S. Y. T. Quantum-State Resolved Bimolecular Collisions of Velocity-Controlled OH with NO Radicals. *Science (80-.)*. **2012**, 338, 1060–1063.
- (12) Tkáč, O.; Ma, Q.; Rusher, C. A.; Greaves, S. J.; Orr-Ewing, A. J.; Dagdigian, P. J. Differential and Integral Cross Sections for the Rotationally Inelastic Scattering of Methyl Radicals with H₂ and D₂. *J. Chem. Phys.* **2014**, 140, 204318.
- (13) Dagdigian, P. J.; Alexander, M. H. Exact Quantum Scattering Calculations of Transport Properties: CH₂ ($\tilde{X}^3 B_1$, $\tilde{a}^1 A_1$)--Helium. *J. Chem. Phys.* **2013**, 138, 164305.
- (14) Balakrishnan, N.; Groenenboom, G. C.; Krems, R. V.; Dalgarno, A. The He--CaH ($^2 \Sigma^+$) Interaction. II. Collisions at Cold and Ultracold Temperatures. *J. Chem. Phys.* **2003**, 118, 7386–7393.
- (15) Mack, A.; Clark, T. K.; Forrey, R. C.; Balakrishnan, N.; Lee, T.-G.; Stancil, P. C. Cold He + H₂ Collisions near Dissociation. *Phys. Rev. A* **2006**, 74, 52718.
- (16) Semenov, A.; Babikov, D. Mixed Quantum/Classical Theory for Molecule-

Molecule Inelastic Scattering: Derivations of Equations and Application to $\text{N}_2 + \text{H}_2$ System. *J. Phys. Chem. A* **2015**, *119*, 12329–12338.

- (17) Billing, G. D. *The Quantum Classical Theory*; Oxford University Press, 2003.
- (18) Caselli, P.; Ceccarelli, C. Our Astrochemical Heritage. *Astron. Astrophys. Rev.* **2012**, *20*, 56.
- (19) Dubernet, M.-L.; Alexander, M. H.; Ba, Y. A.; Balakrishnan, N.; Balanço, C.; Ceccarelli, C.; Cernicharo, J.; Daniel, F.; Dayou, F.; Doronin, M.; et al.
BASECOL2012: A Collisional Database Repository and Web Service within the Virtual Atomic and Molecular Data Centre (VAMDC). *Astron. Astrophys.* **2013**, *553*, A50.
- (20) Lique, F.; Spielfiedel, A.; Cernicharo, J. Rotational Excitation of Carbon Monosulfide by Collisions with Helium. *Astron. Astrophys.* **2006**, *451*, 1125–1132.
- (21) Dayou, F.; Balanço, C. Rotational Excitation of SiO by Collisions with Helium. *Astron. Astrophys.* **2006**, *459*, 297–305.
- (22) Sakai, N.; Ceccarelli, C.; Bottinelli, S.; Sakai, T.; Yamamoto, S. DISTRIBUTION OF CH_3OH IN NGC 1333 IRAS4B. *Astrophys. J.* **2012**, *754*, 70.
- (23) Hammami, K.; Owono, L. C. O.; Stäuber, P. Rotational Excitation of Methylidyne (CH^+) by a Helium Atom at High Temperature. *Astron. Astrophys.* **2009**, *507*, 1083–1086.
- (24) Semenov, A.; Babikov, D. Mixed Quantum/Classical Approach for Description of Molecular Collisions in Astrophysical Environments. *J. Phys. Chem. Lett.* **2015**, *6*, 1854–1858.

- (25) Babikov, D.; Semenov, A. Recent Advances in Development and Applications of the Mixed Quantum/Classical Theory for Inelastic Scattering. *J. Phys. Chem. A* **2016**, *120*, 319–331.
- (26) Claire, M. W. Advances in Quantifying the Composition of the Ancient Atmosphere. **2018**.
- (27) Harman, C. E.; Pavlov, A. A.; Babikov, D.; Kasting, J. F. Chain Formation as a Mechanism for Mass-Independent Fractionation of Sulfur Isotopes in the Archean Atmosphere. *Earth Planet. Sci. Lett.* **2018**, *496*, 238–247.
- (28) Kasting, J. F. The Rise of Atmospheric Oxygen. *Science (80-.)*. **2001**, *293*, 819–820.
- (29) Babikov, D.; Semenov, A.; Teplukhin, A. One Possible Source of Mass-Independent Fractionation of Sulfur Isotopes in the Archean Atmosphere of Earth. *Geochim. Cosmochim. Acta* **2017**, *204*, 388–406.
- (30) Pavlov, A. A.; Kasting, J. F. Mass-Independent Fractionation of Sulfur Isotopes in Archean Sediments: Strong Evidence for an Anoxic Archean Atmosphere. *Astrobiology* **2002**, *2*, 27–41.
- (31) Fair, R. W.; Thrush, B. A. Mechanism of S₂ Chemiluminescence in the Reaction of Hydrogen Atoms with Hydrogen Sulphide. *Trans. Faraday Soc.* **1969**, *65*, 1208–1218.
- (32) Nicholas, J. E.; Amodio, C. A.; Baker, M. J. Kinetics and Mechanism of the Decomposition of H₂S, CH₃SH and (CH₃)₂S in a Radio-Frequency Pulse Discharge. *J. Chem. Soc. Faraday Trans. 1 Phys. Chem. Condens. Phases* **1979**, *75*, 1868–1875.

- (33) Lyons, J. R. Mass-Independent Fractionation of Sulfur Isotopes by Isotope-Selective Photodissociation of SO₂. *Geophys. Res. Lett.* **2007**, *34*.
- (34) Du, S.; Francisco, J. S.; Shepler, B. C.; Peterson, K. A. Determination of the Rate Constant for Sulfur Recombination by Quasiclassical Trajectory Calculations. *J. Chem. Phys.* **2008**, *128*, 204306.
- (35) Du, S.; Germann, T. C.; Francisco, J. S.; Peterson, K. A.; Yu, H.-G.; Lyons, J. R. The Kinetics Study of the S + S₂ → S₃ Reaction by the Chaperone Mechanism. *J. Chem. Phys.* **2011**, *134*, 154508.
- (36) Domagal-Goldman, S. D.; Poirier, B.; Wing, B. A. Mass-Independent Fractionation of Sulfur Isotopes: Carriers and Sources; 2011.
- (37) Teplukhin, A. Theoretical Study of Ozone Forming Recombination Reaction and Anomalous Isotope Effect Associated with It, Marquette University, 2017.
- (38) Forrey, R. C.; Balakrishnan, N.; Lee, T.-G.; Stancil, P. H₂ Dissociation Due to Collision with He. In *APS Division of Atomic, Molecular and Optical Physics Meeting Abstracts*; 2007.
- (39) T Pack, R.; Walker, R. B. Some Symmetry-Induced Isotope Effects in the Kinetics of Recombination Reactions. *J. Chem. Phys.* **2004**, *121*, 800–812.
- (40) Ivanov, M. V; Babikov, D. Collisional Stabilization of van Der Waals States of Ozone. *J. Chem. Phys.* **2011**, *134*, 174308.
- (41) Du, S.; Germann, T. C.; Francisco, J. S.; Peterson, K. A.; Yu, H.-G.; Lyons, J. R. The Kinetics Study of the S + S₂ → S₃ Reaction by the Chaperone Mechanism. *J. Chem. Phys.* **2011**, *134*, 154508.
- (42) Daniel, F.; Dubernet, M.-L.; Grosjean, A. Rotational Excitation of 45 Levels of

- Ortho/Para-H₂O by Excited Ortho/Para-H₂ from 5 K to 1500 K: State-to-State, Effective, and Thermalized Rate Coefficients. *Astron. Astrophys.* **2011**, 536, A76.
- (43) Faure, A.; Wiesenfeld, L.; Scribano, Y.; Ceccarelli, C. Rotational Excitation of Mono- and Doubly-Deuterated Water by Hydrogen Molecules. *Mon. Not. R. Astron. Soc.* **2012**, 420, 699–704.
- (44) Ma, Q.; Dagdigian, P. J.; Alexander, M. H. Theoretical Study of the Vibrational Relaxation of the Methyl Radical in Collisions with Helium. *J. Chem. Phys.* **2013**, 138, 104317.
- (45) Brown, N. J.; Bastien, L. A. J.; Price, P. N. Transport Properties for Combustion Modeling. *Prog. Energy Combust. Sci.* **2011**, 37, 565–582.
- (46) Schiffman, A.; Chandler, D. W. Experimental Measurements of State Resolved, Rotationally Inelastic Energy Transfer. *Int. Rev. Phys. Chem.* **1995**, 14, 371–420.
- (47) Hartmann, J.-M.; Boulet, C.; Robert, D. *Collisional Effects on Molecular Spectra: Laboratory Experiments and Models, Consequences for Applications*; Elsevier, 2008.
- (48) Wiesenfeld, L.; Faure, A. Ab Initio Computation of the Broadening of Water Rotational Lines by Molecular Hydrogen. *Phys. Rev. A* **2010**, 82, 40702.
- (49) McGuire, P.; Micha, D. A. Coupled-Channel Investigation of Rotationally and Vibrationally Inelastic Collisions between He and H₂. *Int. J. Quantum Chem.* **1972**, 6, 111–132.
- (50) Arthurs, A. M.; Dalgarno, A. The Theory of Scattering by a Rigid Rotator. *Proc. R. Soc. Lond. A* **1960**, 256, 540–551.
- (51) Kendrick, B. K.; Hazra, J.; Balakrishnan, N. The Geometric Phase Controls

- Ultracold Chemistry. *Nat. Commun.* **2015**, *6*, 7918.
- (52) Kendrick, B. K.; Hazra, J.; Balakrishnan, N. Geometric Phase Appears in the Ultracold Hydrogen Exchange Reaction. *Phys. Rev. Lett.* **2015**, *115*, 153201.
- (53) Hutson, J. M.; Green, S. Molscat Computer Code, Version 14, Distributed by Collaborative Computational Project No. 6 of the Engineering and Physical Sciences Research Council. *Swindon, UK* **1994**.
- (54) Alexander, M. H.; Manolopoulos, D. E.; Werner, H. J.; Follmeg, B. Hibridon. University of Maryland: College Park, MD 2011.
- (55) Balakrishnan, N.; Dalgarno, A.; Forrey, R. C. Vibrational Relaxation of CO by Collisions with ^4He at Ultracold Temperatures. *J. Chem. Phys.* **2000**, *113*, 621–627.
- (56) Loreau, J.; Zhang, P.; Dalgarno, A. Elastic Scattering and Rotational Excitation of Nitrogen Molecules by Sodium Atoms. *J. Chem. Phys.* **2011**, *135*, 174301.
- (57) Green, S. Rotational Excitation of Symmetric Top Molecules by Collisions with Atoms: Close Coupling, Coupled States, and Effective Potential Calculations for $\text{NH}_3\text{--He}$. *J. Chem. Phys.* **1976**, *64*, 3463–3473.
- (58) Yang, B.; Zhang, P.; Wang, X.; Stancil, P. C.; Bowman, J. M.; Balakrishnan, N.; Forrey, R. C. Quantum Dynamics of CO--H_2 in Full Dimensionality. *Nat. Commun.* **2015**, *6*, 6629.
- (59) dos Santos, S. F.; Balakrishnan, N.; Forrey, R. C.; Stancil, P. C. Vibration-Vibration and Vibration-Translation Energy Transfer in $\text{H}_2\text{--H}_2$ Collisions: A Critical Test of Experiment with Full-Dimensional Quantum Dynamics. *J. Chem. Phys.* **2013**, *138*, 104302.

- (60) Yang, C.-H.; Sarma, G.; Parker, D. H.; Ter Meulen, J. J.; Wiesenfeld, L. State-to-State Differential and Relative Integral Cross Sections for Rotationally Inelastic Scattering of H₂O by Hydrogen. *J. Chem. Phys.* **2011**, *134*, 204308.
- (61) Faure, A.; Szalewicz, K.; Wiesenfeld, L. Potential Energy Surface and Rotational Cross Sections for Methyl Formate Colliding with Helium. *J. Chem. Phys.* **2011**, *135*, 24301.
- (62) Walker, K. M.; Lique, F.; Dumouchel, F.; Dawes, R. Inelastic Rate Coefficients for Collisions of C₆H⁺ with H₂ and He. *Mon. Not. R. Astron. Soc.* **2016**, *466*, 831–837.
- (63) Walker, K. M.; Dumouchel, F.; Lique, F.; Dawes, R. The First Potential Energy Surfaces for the C₆H⁺--H₂ and C₆H⁺--He Collisional Systems and Their Corresponding Inelastic Cross Sections. *J. Chem. Phys.* **2016**, *145*, 24314.
- (64) Faure, A.; Wiesenfeld, L.; Wernli, M.; Valiron, P. The Role of Rotation in the Vibrational Relaxation of Water by Hydrogen Molecules. *J. Chem. Phys.* **2005**, *123*, 104309.
- (65) Faure, A.; Josselin, E. Collisional Excitation of Water in Warm Astrophysical Media-I. Rate Coefficients for Rovibrationally Excited States. *Astron. Astrophys.* **2008**, *492*, 257–264.
- (66) Agg, P. J.; Clary, D. C. Infinite Order Sudden Calculation of Raman Q-Branch Linewidths for H₂O+ H₂O. *J. Chem. Phys.* **1991**, *95*, 1037–1048.
- (67) Buffa, G.; Tarrini, O.; Scappini, F.; Cecchi-Pestellini, C. H₂O-H₂O Collision Rate Coefficients. *Astrophys. J. Suppl. Ser.* **2000**, *128*, 597.
- (68) Wernli, M.; Wiesenfeld, L.; Faure, A.; Valiron, P. Rotational Excitation of HC₃N

- by H₂ and He at Low Temperatures. *Astron. Astrophys.* **2007**, *464*, 1147–1154.
- (69) Troscompt, N.; Faure, A.; Wiesenfeld, L.; Ceccarelli, C.; Valiron, P. Rotational Excitation of Formaldehyde by Hydrogen Molecules: Ortho-H₂CO at Low Temperature. *Astron. Astrophys.* **2009**, *493*, 687–696.
- (70) Rabli, D.; Flower, D. R. The Rotational Excitation of Methanol by Molecular Hydrogen. *Mon. Not. R. Astron. Soc.* **2010**, *406*, 95–101.
- (71) Semenov, A.; Babikov, D. Equivalence of the Ehrenfest Theorem and the Fluid-Rotor Model for Mixed Quantum/Classical Theory of Collisional Energy Transfer. *J. Chem. Phys.* **2013**, *138*, 164110.
- (72) Semenov, A.; Babikov, D. Mixed Quantum/Classical Theory of Rotationally and Vibrationally Inelastic Scattering in Space-Fixed and Body-Fixed Reference Frames. *J. Chem. Phys.* **2013**, *139*, 174108.
- (73) Semenov, A.; Babikov, D. Accurate Calculations of Rotationally Inelastic Scattering Cross Sections Using Mixed Quantum/Classical Theory. *J. Phys. Chem. Lett.* **2013**, *5*, 275–278.
- (74) Semenov, A.; Babikov, D. Mixed Quantum/Classical Calculations of Total and Differential Elastic and Rotationally Inelastic Scattering Cross Sections for Light and Heavy Reduced Masses in a Broad Range of Collision Energies. *J. Chem. Phys.* **2014**, *140*, 44306.
- (75) Semenov, A.; Babikov, D. Inelastic Scattering of Identical Molecules within Framework of the Mixed Quantum/Classical Theory: Application to Rotational Excitations in H₂ + H₂. *J. Phys. Chem. A* **2016**, *120*, 3861–3866.
- (76) Semenov, A.; Dubernet, M.-L.; Babikov, D. Mixed Quantum/Classical Theory for

- Inelastic Scattering of Asymmetric-Top-Rotor + Atom in the Body-Fixed Reference Frame and Application to the $\text{H}_2\text{O} + \text{He}$ System. *J. Chem. Phys.* **2014**, *141*, 114304.
- (77) Semenov, A.; Ivanov, M.; Babikov, D. Ro-Vibrational Quenching of CO ($v = 1$) by He Impact in a Broad Range of Temperatures: A Benchmark Study Using Mixed Quantum/Classical Inelastic Scattering Theory. *J. Chem. Phys.* **2013**, *139*, 74306.
- (78) Babikov, D.; Semenov, A. Recent Advances in Development and Applications of the Mixed Quantum/Classical Theory for Inelastic Scattering. *J. Phys. Chem. A* **2015**, *120*, 319–331.
- (79) Semenov, A.; Babikov, D. A. MQCT. I. Inelastic Scattering of Two Asymmetric-Top Rotors with Application to $\text{H}_2\text{O} + \text{H}_2\text{O}$. *J. Phys. Chem. A* **2017**.
- (80) Press, W. H.; Press, W. H.; Flannery, B. P.; Flannery, B. P.; Teukolsky, S. A.; Vetterling, W. T.; Vetterling, W. T. *Numerical Recipes in Pascal: The Art of Scientific Computing*; Cambridge University Press, 1989; Vol. 1.
- (81) Kobeissi, H. On Testing Diatomic Vibration-Rotation Wavefunction for High Levels. *J. Comput. Phys.* **1985**, *61*, 351–358.
- (82) Mandal, B.; Semenov, A.; Babikov, D. Calculations of Differential Cross Sections Using Mixed Quantum/Classical Theory of Inelastic Scattering. *J. Phys. Chem. A* **2018**, *122*, 6157–6165.
- (83) Stancil, P. C.; You, H.; Cook, A.; Sornborger, A. T.; Geller, M. R. Towards Quantum Simulation of Chemical Dynamics with Prethreshold Superconducting Qubits. *arXiv Prepr. arXiv1602.00063* **2016**.

- (84) Arthurs, A. M.; Dalgarno, A. The Mobilities of Ions in Molecular Gases. *Proc. R. Soc. London. Ser. A. Math. Phys. Sci.* **1960**, 256, 552–558.
- (85) Heil, T. G.; Green, S.; Kouri, D. J. The Coupled States Approximation for Scattering of Two Diatoms. *J. Chem. Phys.* **1978**, 68, 2562–2583.
- (86) Alexander, M. H.; Manolopoulos, D. E.; Werner, H. J.; Follmeg, B. The HIBRIDON Package. 2014.
- (87) Grosjean, A.; Dubernet, M.-L.; Ceccarelli, C. Collisional Excitation Rates of H₂O with H₂. *Astron. Astrophys.* **2003**, 408, 1197–1203.
- (88) Loreau, J.; Kalugina, Y. N.; Faure, A.; Van Der Avoird, A.; Lique, F. Potential Energy Surface and Bound States of the H₂O-HF Complex. *J. Chem. Phys.* **2020**, 153.
- (89) Roueff, E.; Lique, F. Molecular Excitation in the Interstellar Medium: Recent Advances in Collisional, Radiative, and Chemical Processes. *Chem. Rev.* **2013**, 113, 8906–8938.
- (90) Lee, H.-H.; Bettens, R. P. A.; Herbst, E. Fractional Abundances of Molecules in Dense Interstellar Clouds: A Compendium of Recent Model Results. *Astron. Astrophys. Suppl. Ser.* **1996**, 119, 111–114.
- (91) Tielens, A.; Allamandola, L. J. Evolution of Interstellar Dust. In *Physical processes in interstellar clouds*; Springer, 1987; pp 333–376.
- (92) Tielens, A. G. G. M.; Allamandola, L. J. Composition, Structure, and Chemistry of Interstellar Dust. In *Interstellar processes*; Springer, 1987; pp 397–470.
- (93) Graff, M. M.; Dalgarno, A. Oxygen Chemistry of Shocked Interstellar Clouds. II- Effects of Nonthermal Internal Energy on Chemical Evolution. *Astrophys. J.* **1987**,

317, 432–441.

- (94) Semenov, A.; Dubernet, M. L.; Babikov, D. Mixed Quantum/Classical Theory for Inelastic Scattering of Asymmetric-Top-Rotor + Atom in the Body-Fixed Reference Frame and Application to the H₂O + He System. *J. Chem. Phys.* **2014**, *141*.
- (95) Bunker, P. R.; Jensen, P. *Fundamentals of Molecular Symmetry*; CRC Press, 2004.
- (96) Semenov, A.; Babikov, D. Mixed Quantum/Classical Approach for Description of Molecular Collisions in Astrophysical Environments. *J. Phys. Chem. Lett.* **2015**, *6*, 1854–1858.
- (97) Boursier, C.; Mandal, B.; Babikov, D.; Dubernet, M. L. New H₂O–H₂O Collisional Rate Coefficients for Cometary Applications. *Mon. Not. R. Astron. Soc.* **2020**, *498*, 5489–5497.
- (98) Buffa, G.; Tarrini, O.; Scappini, F.; Cecchi-Pestellini, C. H₂O–H₂O Collision Rate Coefficients. *Astrophys. J. Suppl. Ser.* **2000**, *128*, 597–601.
- (99) Levine, R. D. *Quantum Mechanics of Molecular Rate Processes*; Courier Corporation, 2011.
- (100) Schatz, G. C.; Kuppermann, A. Quantum Mechanical Reactive Scattering for Three-Dimensional Atom plus Diatom Systems. II. Accurate Cross Sections for H + H₂. *J. Chem. Phys.* **1976**, *65*, 4668–4692.
- (101) McGuire, P.; Kouri, D. J. Quantum Mechanical Close Coupling Approach to Molecular Collisions. j_z-Conserving Coupled States Approximation. *J. Chem. Phys.* **1974**, *60*, 2488–2499.
- (102) Schatz, G. C.; Kuppermann, A. Quantum Mechanical Reactive Scattering for

- Three-Dimensional Atom plus Diatom Systems. I. Theory. *J. Chem. Phys.* **1976**, *65*, 4642–4667.
- (103) McCabe, P.; Connor, J. N. L.; Sokolovski, D. Nearside--Farside Analysis of Differential Cross Sections: Ar + N₂ Rotationally Inelastic Scattering Using Associated Legendre Functions of the First and Second Kinds. *J. Chem. Phys.* **1998**, *108*, 5695–5703.
- (104) Billing, G. D. Semi-Classical Calculations of Rotational/Vibrational Transitions in He-H₂. *Chem. Phys.* **1975**, *9*, 359–369.
- (105) Billing, G. D. Comparison of Quantum Mechanical and Semiclassical Cross Sections and Rate Constants for Vibrational Relaxation of N₂ and CO Colliding with ⁴He. *Chem. Phys.* **1986**, *107*, 39–46.
- (106) Billing, G. D. *The Quantum-Classical Theory*; Oxford University Press, 2002.
- (107) Billing, G. D. The Semiclassical Treatment of Molecular Roto/Vibrational Energy Transfer. *Comput. Phys. Reports* **1984**, *1*, 239–296.
- (108) Sørensen, G. D. B. Semiclassical Three-Dimensional Model for Vibrational Relaxation. *J. Chem. Phys.* **1972**, *57*, 5241.
- (109) Edmonds, A. R. *Angular Momentum in Quantum Mechanics*; Princeton University Press, 2016.
- (110) Coletti, C.; Billing, G. D. Quantum-Classical Calculation of Cross Sections and Rate Constants for the H₂ + CN → HCN + H Reaction. *J. Chem. Phys.* **2000**, *113*, 11101–11108.
- (111) Balakrishnan, N.; Billing, G. D. A Mixed Quantal/Classical Study of the Reaction OH + H₂ → H₂O + H. *Chem. Phys. Lett.* **1995**, *233*, 145–153.

- (112) Balakrishnan, N.; Billing, G. D. Integral Cross Sections and Rate Constants for the Reaction $\text{OH} + \text{H}_2 \rightarrow \text{H}_2\text{O} + \text{H}$: A Semiclassical Wave Packet Approach. *J. Chem. Phys.* **1994**, *101*, 2785–2792.
- (113) Martí, C.; Pacifici, L.; Laganà, A.; Coletti, C. A Quantum-Classical Study of the $\text{OH} + \text{H}_2$ Reactive and Inelastic Collisions. *Chem. Phys. Lett.* **2017**, *674*, 103–108.
- (114) Thompson, W. H. A General Method for Implementing Vibrationally Adiabatic Mixed Quantum-Classical Simulations. *J. Chem. Phys.* **2003**, *118*, 1059–1067.
- (115) Whittier, G. S.; Light, J. C. Quantum/Classical Time-Dependent Self-Consistent Field Treatment of $\text{Ar} + \text{HCO}$ Inelastic and Dissociative Scattering. *J. Chem. Phys.* **1999**, *110*, 4280–4290.
- (116) Tully, C.; Johnson, R. E. Semiclassical Calculation of Collisional Dissociation Cross Sections for $\text{N} + \text{N}_2$. *J. Chem. Phys.* **2002**, *117*, 6556–6561.
- (117) Babikov, D.; Aguillon, F.; Sizun, M.; Sidis, V. Fragmentation of Na_2^+ Dimer Ions in Kilo-Electron-Volt Collisions with He: A Coupled Wave-Packet Study. *Phys. Rev. A* **1999**, *59*, 330.
- (118) Chen, F.; McCoy, A. B. Multiple-Configuration Quantum/Classical Studies of the Photodissociation Dynamics of H_2O . *J. Phys. Chem. A* **2003**, *107*, 7220–7229.
- (119) Ermoshin, V. A.; Kazansky, A. K.; Engel, V. A Novel Mixed Quantum/Classical Method for the Dynamics of Molecules in a Gas Environment with an Application to Femtosecond Time-Resolved Spectroscopy. *Chem. Phys. Lett.* **1999**, *302*, 20–26.
- (120) Aguillon, F.; Sizun, M.; Sidis, V.; Billing, G. D.; Marković, N. Semiclassical Coupled Wave Packet Study of the Nonadiabatic Collisions $\text{Ar}^+(\text{J}) + \text{H}_2$: Zero

- Angular Momentum Case. *J. Chem. Phys.* **1996**, *104*, 4530–4543.
- (121) Sizun, M.; Aguillon, F.; Sidis, V.; Zenevich, V.; Billing, G. D.; Marković, N. Theoretical Investigation of the $\text{Ar}^+(\text{J}) + \text{H}_2 \rightarrow \text{ArH}^+ + \text{H}$ Reaction: Semiclassical Coupled Wavepacket Treatment. *Chem. Phys.* **1996**, *209*, 327–353.
- (122) Bala, P.; Lesyng, B.; McCammon, J. A. Extended Hellmann-Feynman Theorem for Non-Stationary States and Its Application in Quantum-Classical Molecular Dynamics Simulations. *Chem. Phys. Lett.* **1994**, *219*, 259–266.
- (123) Garraway, B. M.; Suominen, K.-A. Wave-Packet Dynamics: New Physics and Chemistry in Femto-Time. *Reports Prog. Phys.* **1995**, *58*, 365.
- (124) Yang, B.; Perera, H.; Balakrishnan, N.; Forrey, R. C.; Stancil, P. C. Quenching of Rotationally Excited CO in Cold and Ultracold Collisions with H, He and H₂. *J. Phys. B At. Mol. Opt. Phys.* **2006**, *39*, S1229.
- (125) Sharples, T. R.; Leng, J. G.; Luxford, T. F. M.; McKendrick, K. G.; Jambrina, P. G.; Aoiz, F. J.; Chandler, D. W.; Costen, M. L. Non-Intuitive Rotational Reorientation in Collisions of NO ($A^2\Sigma^+$) with Ne from Direct Measurement of a Four-Vector Correlation. *Nat. Chem.* **2018**, *10*, 1148–1153.
- (126) Goldberg, N. T.; Zhang, J.; Koszinowski, K.; Bouakline, F.; Althorpe, S. C.; Zare, R. N. Vibrationally Inelastic H + D₂ Collisions Are Forward-Scattered. *Proc. Natl. Acad. Sci.* **2008**, *105*, 18194–18199.
- (127) Faure, A.; Dagdigian, P. J.; Rist, C.; Dawes, R.; Quintas-Sánchez, E.; Lique, F.; Hochlaf, M. Interaction of Chiral Propylene Oxide (CH₃CHCH₂O) with Helium: Potential Energy Surface and Scattering Calculations. *ACS Earth Sp. Chem.* **2019**, *3*, 964–972.

- (128) Khalifa, M. Ben; Quintas-Sánchez, E.; Dawes, R.; Hammami, K.; Wiesenfeld, L. Rotational Quenching of an Interstellar Gas Thermometer: CH₃CN...He Collisions. *Phys. Chem. Chem. Phys.* **2020**.
- (129) Denis-Alpizar, O.; Stoecklin, T.; Dutrey, A.; Guilloteau, S. Rotational Relaxation of HCO⁺ and DCO⁺ by Collision with H₂. *Mon. Not. R. Astron. Soc.* **2020**.
- (130) Chen, J.; Li, J.; Bowman, J. M.; Guo, H. Energy Transfer between Vibrationally Excited Carbon Monoxide Based on a Highly Accurate Six-Dimensional Potential Energy Surface. *J. Chem. Phys.* **2020**, *153*, 54310.
- (131) Chefdeville, S.; Kalugina, Y.; van de Meerakker, S. Y. T.; Naulin, C.; Lique, F.; Costes, M. Observation of Partial Wave Resonances in Low-Energy O₂-H₂ Inelastic Collisions. *Science (80-.)*. **2013**, *341*, 1094–1096.
- (132) Perreault, W. E.; Mukherjee, N.; Zare, R. N. Cold Quantum-Controlled Rotationally Inelastic Scattering of HD with H₂ and D₂ Reveals Collisional Partner Reorientation. *Nat. Chem.* **2018**, *10*, 561–567.
- (133) Sun, Z.-F.; van Hemert, M. C.; Loreau, J.; van der Avoird, A.; Suits, A. G.; Parker, D. H. Molecular Square Dancing in CO-CO Collisions. *Science (80-.)*. **2020**, *369*, 307–309.
- (134) Lau, J. A.; Choudhury, A.; Chen, L.; Schwarzer, D.; Verma, V. B.; Wodtke, A. M. Observation of an Isomerizing Double-Well Quantum System in the Condensed Phase. *Science (80-.)*. **2020**, *367*, 175–178.
- (135) Chen, L.; Lau, J. A.; Schwarzer, D.; Meyer, J.; Verma, V. B.; Wodtke, A. M. The Sommerfeld Ground-Wave Limit for a Molecule Adsorbed at a Surface. *Science (80-.)*. **2019**, *363*, 158–161.

- (136) Chang, H.-C.; Ewing, G. E. Infrared Fluorescence from a Monolayer of CO on NaCl (100). *Phys. Rev. Lett.* **1990**, *65*, 2125.
- (137) Jiang, B.; Yang, M.; Xie, D.; Guo, H. Quantum Dynamics of Polyatomic Dissociative Chemisorption on Transition Metal Surfaces: Mode Specificity and Bond Selectivity. *Chem. Soc. Rev.* **2016**, *45*, 3621–3640.
- (138) Jiang, B.; Guo, H. Dynamics in Reactions on Metal Surfaces: A Theoretical Perspective. *J. Chem. Phys.* **2019**, *150*, 180901.
- (139) Alkoby, Y.; Chadwick, H.; Godsi, O.; Labiad, H.; Bergin, M.; Cantin, J. T.; Litvin, I.; Maniv, T.; Alexandrowicz, G. Setting Benchmarks for Modelling Gas--Surface Interactions Using Coherent Control of Rotational Orientation States. *Nat. Commun.* **2020**, *11*, 1–8.
- (140) Rui, J.; Yang, H.; Liu, L.; Zhang, D.-C.; Liu, Y.-X.; Nan, J.; Chen, Y.-A.; Zhao, B.; Pan, J.-W. Controlled State-to-State Atom-Exchange Reaction in an Ultracold Atom--Dimer Mixture. *Nat. Phys.* **2017**, *13*, 699–703.
- (141) Morita, M.; Krems, R. V.; Tscherbul, T. V. Universal Probability Distributions of Scattering Observables in Ultracold Molecular Collisions. *Phys. Rev. Lett.* **2019**, *123*, 13401.
- (142) Kendrick, B. K.; Li, H.; Li, M.; Kotochigova, S.; Croft, J. F. E.; Balakrishnan, N. Non-Adiabatic Quantum Interference Effects and Chaoticity in the Ultracold Li + LiNa \rightarrow Li₂ + Na Reaction. *arXiv Prepr. arXiv2006.15238* **2020**.
- (143) Hazra, J.; Kendrick, B. K.; Balakrishnan, N. Geometric Phase Effects in Ultracold Hydrogen Exchange Reaction. *J. Phys. B At. Mol. Opt. Phys.* **2016**, *49*, 194004.
- (144) Wiesenfeld, L.; Faure, A.; Lique, F.; Dumouchel, N.; Feautrier, N.; Spielfiedel, A.;

- Scribano, Y. Analyzing Observations of Molecules in the ISM: Theoretical and Experimental Studies of Energy Transfer. *EAS Publ. Ser.* **2012**, 58, 267–270.
- (145) Hutson, J. M.; Le Sueur, C. R. MOLSCAT: A Program for Non-Reactive Quantum Scattering Calculations on Atomic and Molecular Collisions. *Comput. Phys. Commun.* **2019**, 241, 9–18.
- (146) Hutson, J. M.; Le Sueur, C. R. MOLSCAT, BOUND, and FIELD, Version 2020.0. 2020.
- (147) Bonnet, L. Semiclassical Initial Value Theory of Rotationally Inelastic Scattering: Some Remarks on the Phase Index in the Interaction Picture. *J. Chem. Phys.* **2018**, 148, 194104.
- (148) Loreau, J.; Faure, A.; Lique, F. Scattering of CO with H₂O: Statistical and Classical Alternatives to Close-Coupling Calculations. *J. Chem. Phys.* **2018**, 148, 244308.
- (149) Sur, S.; Ndengué, S. A.; Quintas-Sánchez, E.; Bop, C.; Lique, F.; Dawes, R. Rotationally Inelastic Scattering of O₃--Ar: State-to-State Rates with the Multiconfigurational Time Dependent Hartree Method. *Phys. Chem. Chem. Phys.* **2020**, 22, 1869–1880.
- (150) Semenov, A.; Babikov, D. Mixed Quantum/Classical Theory of Rotationally and Vibrationally Inelastic Scattering in Space-Fixed and Body-Fixed Reference Frames. *J. Chem. Phys.* **2013**, 139.
- (151) Semenov, A.; Babikov, D. Mixed Quantum/Classical Calculations of Total and Differential Elastic and Rotationally Inelastic Scattering Cross Sections for Light and Heavy Reduced Masses in a Broad Range of Collision Energies. *J. Chem.*

- Phys.* **2014**, *140*.
- (152) Semenov, A.; Babikov, D. Accurate Calculations of Rotationally Inelastic Scattering Cross Sections Using Mixed Quantum/Classical Theory. *J. Phys. Chem. Lett.* **2014**, *5*, 275–278.
- (153) Mandal, B.; Semenov, A.; Babikov, D. Calculations of Differential Cross Sections Using Mixed Quantum / Classical Theory of Inelastic Scattering. **2018**.
- (154) Pack, R. T. Space-Fixed vs Body-Fixed Axes in Atom-Diatomic Molecule Scattering. Sudden Approximations. *J. Chem. Phys.* **1974**, *60*, 633–639.
- (155) Pack, R. T. Coordinates for an Optimum CS Approximation in Reactive Scattering. *Chem. Phys. Lett.* **1984**, *108*, 333–338.
- (156) Kouri, D. J.; Goldflam, R.; Shimoni, Y. On the Coupled States and Infinite Order Sudden Approximations to the Body Frame Wavefunction. *J. Chem. Phys.* **1977**, *67*, 4534–4544.
- (157) Press, W. H.; Teukolsky, S. A.; Flannery, B. P.; Vetterling, W. T. *Numerical Recipes in Fortran 77: Volume 1, Volume 1 of Fortran Numerical Recipes: The Art of Scientific Computing*; Cambridge university press, 1992.
- (158) Yang, C. H.; Sarma, G.; Parker, D. H.; Ter Meulen, J. J.; Wiesenfeld, L. State-to-State Differential and Relative Integral Cross Sections for Rotationally Inelastic Scattering of H₂O by Hydrogen. *J. Chem. Phys.* **2011**, *134*.
- (159) Cori System - NERSC Documentation <https://docs.nersc.gov/systems/cori/>.
- (160) Kong, X.; Markmann, A.; Batista, V. S. Time-Sliced Thawed Gaussian Propagation Method for Simulations of Quantum Dynamics. *J. Phys. Chem. A* **2016**, *120*, 3260–3269.

- (161) Gray, S. K.; Manolopoulos, D. E. Symplectic Integrators Tailored to the Time-Dependent Schrödinger Equation. *J. Chem. Phys.* **1996**, *104*, 7099–7112.
- (162) Manolopoulos, D. E.; Gray, S. K. Symplectic Integrators for the Multichannel Schrödinger Equation. *J. Chem. Phys.* **1995**, *102*, 9214–9227.
- (163) McCarthy, M. C.; Thorwirth, S.; Gottlieb, C. A.; Thaddeus, P. The Rotational Spectrum and Geometrical Structure of Thiozone, S₃. *J. Am. Chem. Soc.* **2004**, *126*, 4096–4097.
- (164) Glassgold, A. E.; Mamon, G. A. Chemistry and Spectroscopy of Interstellar Molecules, Edited by DK Bohme et Al. *Herbst, N. Kaifu, S. Saito Univ. Tokyo Press. Tokyo* **1992**, 261–266.
- (165) Prinn, R. G. On the Possible Roles of Gaseous Sulfur and Sulfanes in the Atmosphere of Venus. *Geophys. Res. Lett.* **1979**, *6*, 807–810.
- (166) Lewis, J. S.; Kreimendahl, F. A. Oxidation State of the Atmosphere and Crust of Venus from Pioneer Venus Results. *Icarus* **1980**, *42*, 330–337.
- (167) Lellouch, E. Urey Prize Lecture. Io's Atmosphere: Not yet Understood. *Icarus* **1996**, *124*, 1–21.
- (168) Moses, J. I.; Zolotov, M. Y.; Fegley Jr, B. Photochemistry of a Volcanically Driven Atmosphere on Io: Sulfur and Oxygen Species from a Pele-Type Eruption. *Icarus* **2002**, *156*, 76–106.
- (169) Meyer, B. Solid Allotropes of Sulfur. *Chem. Rev.* **1964**, *64*, 429–451.
- (170) Meyer, B. Elemental Sulfur. *Chem. Rev.* **1976**, *76*, 367–388.
- (171) Cotton, A. F.; Wilkinson, G.; Bochmann, M.; Murillo, C. A. *Advanced Inorganic Chemistry*; Wiley, 1999.

- (172) Miessler, G. L.; Tarr, D. A. *Inorganic Chemistry*. 2003. Upper Saddle River, NJ: Pearson Prentice Hall.
- (173) Yen, T. F. *Environmental Chemistry: Chemistry of Major Environmental Cycles*; World Scientific, 2005.
- (174) VanLoon, G. W.; Duffy, S. J. *Environmental Chemistry: A Global Perspective*; Oxford university press, 2017.
- (175) Mason, B. *Meteorites*, 274 Pp. Wiley, New York 1962.
- (176) Werner, H.-J.; Knowles, P. J.; Knizia, G.; Manby, F. R.; Schütz, M.; Celani, P.; Györfy, W.; Kats, D.; Korona, T.; Lindh, R.; et al. MOLPRO, Version 2015.1, a Package of Ab Initio Programs.
- (177) Werner, H.-J.; Knowles, P. J.; Knizia, G.; Manby, F. R.; Schütz, M. Molpro: A General-Purpose Quantum Chemistry Program Package. *Wiley Interdiscip. Rev. Comput. Mol. Sci.* **2012**, 2, 242–253.
- (178) Werner, H. J.; Knowles, P. J.; Knizia, G.; Manby, F. R.; Schütz, M.; Celani, P.; Györfy, W.; Kats, D.; Korona, T.; Lindh, R.; et al. Molpro, Version 2015.1, a Package of Ab Initio Programs, See [Http://Www. Molpro. Net](http://www.molpro.net), 2015. *Google Sch.*
- (179) Werner, H.-J.; Knowles, P. J. An Efficient Internally Contracted Multiconfiguration-Reference Configuration Interaction Method. *J. Chem. Phys.* **1988**, 89, 5803–5814.
- (180) Shamasundar, K. R.; Knizia, G.; Werner, H.-J. A New Internally Contracted Multi-Reference Configuration Interaction Method. *J. Chem. Phys.* **2011**, 135, 054101.
- (181) Knowles, P. J.; Werner, H. An Efficient Method for the Evaluation of Coupling

- Coefficients in Configuration Interaction Calculations. *Chem. Phys. Lett.* **1988**, *145*, 514–522.
- (182) Ayouz, M.; Babikov, D. Improved Potential Energy Surface of Ozone Constructed Using the Fitting by Permutationally Invariant Polynomial Function. *Adv. Phys. Chem.* **2012**, *2012*, 1–9.
- (183) Ayouz, M.; Babikov, D. Global Permutationally Invariant Potential Energy Surface for Ozone Forming Reaction. *J. Chem. Phys.* **2013**, *138*, 164311.
- (184) Woon, D. E.; Dunning Jr, T. H. Gaussian Basis Sets for Use in Correlated Molecular Calculations. III. The Atoms Aluminum through Argon. *J. Chem. Phys.* **1993**, *98*, 1358–1371.
- (185) Dunning Jr, T. H.; Peterson, K. A.; Wilson, A. K. Gaussian Basis Sets for Use in Correlated Molecular Calculations. X. The Atoms Aluminum through Argon Revisited. *J. Chem. Phys.* **2001**, *114*, 9244–9253.
- (186) Werner, H.-J.; Knizia, G.; Manby, F. R. Explicitly Correlated Coupled Cluster Methods with Pair-Specific Geminals. *Mol. Phys.* **2011**, *109*, 407–417.
- (187) Adler, T. B.; Knizia, G.; Werner, H.-J. A Simple and Efficient CCSD(T)-F12 Approximation. *J. Chem. Phys.* **2007**, *127*, 221106.
- (188) Peterson, K. A.; Adler, T. B.; Werner, H.-J. Systematically Convergent Basis Sets for Explicitly Correlated Wavefunctions: The Atoms H, He, B--Ne, and Al--Ar. *J. Chem. Phys.* **2008**, *128*, 84102.
- (189) Hill, J. G.; Peterson, K. A. Correlation Consistent Basis Sets for Explicitly Correlated Wavefunctions: Valence and Core--Valence Basis Sets for Li, Be, Na, and Mg. *Phys. Chem. Chem. Phys.* **2010**, *12*, 10460–10468.

- (190) Babikov, D. Accuracy of Gates in a Quantum Computer Based on Vibrational Eigenstates. *J. Chem. Phys.* **2004**, *121*, 7577–7585.
- (191) Huber, K.-P. *Molecular Spectra and Molecular Structure: IV. Constants of Diatomic Molecules*; Springer Science & Business Media, 2013.
- (192) Knowles, P. J.; Hampel, C.; Werner, H.-J. Erratum:“Coupled Cluster Theory for High Spin, Open Shell Reference Wave Functions”[*J. Chem. Phys.* 99, 5219 (1993)]. *J. Chem. Phys.* **2000**, *112*, 3106–3107.
- (193) Knowles, P. J.; Hampel, C.; Werner, H.-J. Coupled Cluster Theory for High Spin, Open Shell Reference Wave Functions. *J. Chem. Phys.* **1993**, *99*, 5219–5227.
- (194) Hampel, C.; Peterson, K. A.; Werner, H.-J. A Comparison of the Efficiency and Accuracy of the Quadratic Configuration Interaction (QCISD), Coupled Cluster (CCSD), and Brueckner Coupled Cluster (BCCD) Methods. *Chem. Phys. Lett.* **1992**, *190*, 1–12.
- (195) Deegan, M. J. O.; Knowles, P. J. Perturbative Corrections to Account for Triple Excitations in Closed and Open Shell Coupled Cluster Theories. *Chem. Phys. Lett.* **1994**, *227*, 321–326.
- (196) Vetterling, W. T.; Teukolsky, S. A.; Press, W. H. *Numerical Recipes: Example Book (FORTRAN)*; Cambridge university press, 1992.
- (197) Peterson, K. A.; Skokov, S.; Bowman, J. M. A Theoretical Study of the Vibrational Energy Spectrum of the HOCl/HClO System on an Accurate Ab Initio Potential Energy Surface. *J. Chem. Phys.* **1999**, *111*, 7446–7456.
- (198) Ho, T.-S.; Rabitz, H. A General Method for Constructing Multidimensional Molecular Potential Energy Surfaces from Ab Initio Calculations. *J. Chem. Phys.*

1996, *104*, 2584–2597.

- (199) Guide, M. U. The Mathworks. *Inc., Natick, MA* **1998**, *5*, 333.
- (200) Semenov, A.; Babikov, D. Three Sources of Errors in the Ehrenfest Treatment of Inelastic Scattering and Possible Ways of Resolving Them. *J. Chem. Phys.* **2017**, *146*, 224107.
- (201) T Pack, R.; Walker, R. B.; Kendrick, B. K. Three-Body Collision Contributions to Recombination and Collision-Induced Dissociation. I. Cross Sections. *J. Chem. Phys.* **1998**, *109*, 6701–6713.
- (202) T Pack, R.; Walker, R. B.; Kendrick, B. K. Three-Body Collision Contributions to Recombination and Collision-Induced Dissociation. II. Kinetics. *J. Chem. Phys.* **2002**, *109*, 6714–6724.
- (203) Babikov, D.; Kendrick, B. K.; Walker, R. B.; Schinke, R.; Pack, R. T. Quantum Origin of an Anomalous Isotope Effect in Ozone Formation. *Chem. Phys. Lett.* **2003**, *372*, 686–691.
- (204) Kłos, J.; Chałasiński, G.; Krems, R. V; Buchachenko, A. A.; Aquilanti, V.; Pirani, F.; Cappelletti, D. Ab Initio Potentials for the $S(^3P_J)$ --Rare Gas Dimers: Implementation for Elastic and Inelastic Collisions and Comparison with Scattering Potentials. *J. Chem. Phys.* **2002**, *116*, 9269–9280.